UNIVERSITY OF LEEDS

Investigating the basal and englacial properties of a West Antarctic ice rise with novel active-source seismic methods

Ronan Agnew

Submitted in accordance with the requirements for the degree of Doctor of Philosophy

The University of Leeds

Faculty of Environment

School of Earth and Environment

May 2024

Acknowledgements

There are many people I must thank for enabling me to complete this thesis. Firstly, huge thanks to my supervisors, Adam Booth, Roger Clark and Alex Brisbourne, for their supervision and support over the last 4 years, often in difficult circumstances. You have all really helped me find my feet and find a way through this project. I gratefully acknowledge the NERC PANORAMA DTP (grant NE/S007458/1) for financially supporting me in this research. The Korff data were collected as part of the British Antarctic Survey programme Polar Science for Planet Earth with the support of British Antarctic Survey Operations.

Many thanks go to Carlos Martín for the temperature model and many ice rise discussions. Thanks to Rob Arthern and James Smith for valuable discussions which helped with the interpretation. Thanks to Steve Colwell for providing the AWS data, and to Phil Livermore for advising on the inversion scheme. I am particularly grateful to Andy Smith for acquiring the Korff data with Alex, and for moral support while stuck at McMurdo!

I have been extremely lucky to do two field seasons during my PhD. I'd like to acknowledge the support of the ITGC TIME project in supporting me to join that fieldwork, and to BAS and USAP for making it happen.

Thanks to Emma Smith for introducing me to the delights of Antarctic fieldwork, moral support, answering my stupid questions and helping me decide to stick with it. The Eggs on Toast team - Emma P, TJ, Madeline, Meghana, and Marianne, for reigniting my enthusiasm for science when I needed it. To Andrew for being a great McMurdo roommate and general pal. To the residents of Wingfield Road + Norwich friends, you have always been there when I needed it, for a heart to heart or a game of bar billiards.

I would not have even started this PhD if it were not for my family, Mum, Dad, Tansy, and Remco. Thank you for encouraging me to look outwards at the world. Grandpa, you have been my inspiration ever since I can remember. Karan, thanks so much for having me to stay whenever I needed. John, Lyndall and Conni (and Dylan), I am so grateful for your company, support and encouragement, and not taking me too seriously. Finally, to Esther, thank you for your support through the frequent ups and downs - I truly appreciate you (and Rosie of course).

Abstract

Seismic observations of glacier beds are key to understanding processes of basal slip and incorporating these processes into ice sheet models, which in turn inform predictions of global sea level rise. Observations of seismic reflection amplitude are a powerful tool for identifying glacier bed materials. Amplitude-versus-angle (AVA) analysis is a technique commonly used to identify glacier substrates whereby the amplitude of the basal reflection is measured as a function of its incidence angle at the ice base. Glaciological AVA experiments conventionally consider only the compressional (P) wave component of the wavefield, ignoring the shear wave (S) component; however, three-component seismic acquisitions are proliferating in the glaciological community. To harness the full potential of three-component recording, analysis of PS converted waves (incident P waves converted to S waves at the glacier bed) is necessary. This thesis presents an investigation into the glaciological application of joint PP and PS AVA inversion.

Prior to inverting AVA data, amplitudes must be corrected for attenuation losses. The transition of snow to firn and glacial ice represents a challenge to seismic study due to the continuous transition in elastic properties with depth. I describe a method for measuring the seismic quality factor, Q, which enables more detailed characterisation of firn's attenuative structure than previous approaches allow. Q increases from 56 ± 23 in the uppermost firn to 570 ± 450 between 55 and 77 m depth. This method offers a strategy of constraining attenuation in seismic reflection experiments which do not record multiples, also enabling improved constraint of source amplitude when compared with conventional methods.

I present an inversion scheme which jointly inverts PP and PS AVA data for the properties of the ice-bed interface. Using synthetic AVA data, I investigate the improvement joint inversion of PP and PS amplitudes makes to constraint of bed properties when compared with PP inversion. In general, joint inversion improves upon PP inversion in both precision and accuracy over the same angular range. In many cases joint inversion of data over $0 - 30^\circ$ performs favourably with single inversion of data over $0 - 60^\circ$. Joint inversion therefore has the potential to reduce ambiguity in substrate identification and reduce the logistical requirements of glaciological AVA surveys.

The inversion scheme is applied to PP and PS data from Korff ice rise (KIR), in the Weddell Sea sector of West Antarctica. Analysis of PP and PS AVA responses at KIR shows the reflection to arise from a material with a P wave velocity of $\alpha = 4.03 \pm 0.05$ km s^{-1}, an S wave velocity of $\beta = 2.16 \pm 0.06$ km s^{-1} and a density of $\rho = 1.44 \ \pm 0.06$ g cm^{-3}. The inverted properties are consistent with a reflection from a layer of basal debris overlying frozen sediments, with a poorly-defined boundary between the two. I propose that this results from a previous episode of flow as an ice rumple, followed by grounding on the lee side of the bathymetric high occupied by KIR and subsequent freezing of basal sediments. The indication of a reflection from a basal debris layer raises questions about whether conventionally-interpreted basal reflections can truly be considered as such, and whether these interpretations may mask the true nature of the underlying subglacial material.

Intellectual Property

The candidate confirms that the work submitted is his/her own, except where work which has formed part of jointly-authored publications has been included. The contribution of the candidate and the other authors to this work has been explicitly indicated below. The candidate confirms that appropriate credit has been given within the thesis where reference has been made to the work of others.

The work presented in Chapter 2 of this thesis appears in the publication:

Agnew, R. S., Clark, R. A., Booth, A. D., Brisbourne, A. M., and Smith, A. M. (2023). "Measuring seismic attenuation in polar firn: method and application to Korff Ice Rise, West Antarctica". In: *Journal of Glaciology*, FirstView, pp. 1–12. doi: 10.1017/jog.2023.82.

RSA processed the data, developed the error analysis method, interpreted the results and wrote the manuscript. RAC devised the Q in firn method. AMB and AMS acquired the data. ADB, RAC and AMB advised on processing, interpretation, and writing the manuscript. All authors commented on early drafts of the manuscript.

Contents

List of Figures

List of Tables

Chapter 1

Introduction

1.1 Motivation: Glacier bed properties and ice dynamics

Understanding the dynamics of the world's glaciers and ice sheets is a matter of pressing global importance: future sea level rise must be predicted to enable coastal communities to adapt (Hinkel et al. 2018). Ice sheet models are used to understand the contributions to global sea level rise of each part of the cryosphere and predict how this will evolve in the coming centuries, but these models require field observations to verify and constrain input parameters.

The West Antarctic Ice Sheet (WAIS) contains enough fresh water to raise global sea level by 4.3 m (Fretwell et al. 2013), with an average global sea level rise resulting from a collapse of the WAIS estimated at 3.2 m (Bamber et al. 2009). A large proportion of the WAIS' bed is below sea level, which means that the WAIS is potentially vulnerable to future ocean warming and feedbacks such as the marine ice-sheet instability (MISI), which has been hypothesised to trigger irreversible collapse of the WAIS (Mercer 1978). Understanding how the WAIS responds to climatic conditions is therefore extremely important for predicting sea level rise.

There are three fundamental mechanisms of glacier flow: internal deformation of ice, sliding at the ice-bed interface, and deformation of the subglacial material (Cuffey and Paterson 2010). In ice sheet models, the relationship between slip resistance and slip velocity is determined by the slip law (e.g. Weertman 1957; Zoet and Iverson 2020), which takes different forms depending on the subglacial material properties. Flow velocities depend on a complex interaction between bed topography, hydrology and material properties; in many of the ice streams which drain West

Antarctica, the presence and distribution of saturated, deforming subglacial till and 'sticky spots' of unsaturated tills are important controls on ice stream flow velocities and ice sheet stability (e.g. Anandakrishnan and Alley 1997; Catania et al. 2006; Parizek et al. 2013; Peters et al. 2006; Siegert et al. 2016; A. M. Smith 1997b). Ice sheet models are typically initialised with basal conditions inverted from ice surface velocities; however, inverted bed conditions can be contradicted by field observations (e.g. Bougamont et al. 2014; Harper et al. 2017). Model predictions are highly sensitive to the distribution and type of bed material (Parizek et al. 2013). This highlights the need of continued field observations to inform model processes.

Furthermore, studying a glacier's basal conditions can help to better understand the physical origins of subglacial landforms. This can both provide information about the history of a particular glacier (e.g. Alley et al. 2021) and help to inform theories of the formation processes of subglacial landforms. Studying the formation of subglacial landforms in situ (e.g. Schlegel et al. 2022; A. M. Smith et al. 2007) can aid in interpreting these landforms as they exist in the geological record, providing key information to constrain reconstructions of palaeo ice sheets (e.g. C. D. Clark et al. 2000). Inferring the response of the WAIS to past changes in climate can therefore aid predictive models of future ice sheet dynamics (e.g. DeConto and Pollard 2016).

The work presented in this thesis has two main purposes. The first is to explore novel methods of seismic analysis and determine whether these new methods can provide better constraint on subglacial material properties than conventional methods. The second is to improve understanding of the recent history of the WAIS in the Weddell Sea sector, by applying these methods to data from Korff ice rise (KIR).

In this introduction, I will give an overview of the application of active-source seismic methods to glaciological problems and describe the theory of amplitude-versus-angle (AVA) methods. I will introduce the motivation for my methodological improvements concerning multicomponent AVA analyses and advanced attenuation corrections. I will summarise previous work in the Weddell Sea region and place work at KIR within this context. Finally, I will provide a road map of this thesis, describing aims, objectives, and questions I hope to answer.

1.2 Seismic reflection as a means of investigating subglacial conditions

Active source seismic methods are concerned with measuring seismic waves emitted from a controlled source (e.g. an explosive charge), rather than detecting waves produced by a geological or glaciological event, or ambient noise. They form part of a suite of geophysical techniques available to glaciologists interested in basal conditions, which includes complementary techniques such as radio-echo-sounding (RES, e.g. Bingham and Siegert 2007), electromagnetic methods (e.g. Killingbeck et al. 2020) and passive seismic monitoring of icequakes (e.g. Kufner et al. 2021; E. C. Smith et al. 2015). Borehole measurements of basal conditions can provide essential information; however, these methods are inevitably spatially limited, and basal conditions have been shown to vary significantly within individual ice streams (e.g. Muto et al. 2019b; A. M. Smith 1997b). Furthermore, hot-water drilling to the bed of very thick ice can be costly and logistically extremely difficult (Siegert et al. 2014). Geophysical methods hold the key to understanding variations in basal conditions and their effect on ice flow, being able to measure bed topography and material properties, as well as detect changes in hydrology (e.g. Kulessa et al. 2017; Nolan and Echelmeyer 1999).

Controlled-source seismic studies are particularly responsive to the material properties of the subglacial environment. Where data are of sufficient quality to observe subglacial layers, direct measurement of interval velocity can help determine the glacier substrate (Blankenship et al. 1987). Where subglacial layering is not clear, the substrate can be determined by measuring the amplitudes of wavelets reflected at the ice-bed interface. Commonly, these measurements aim to distinguish materials by measurement of the bed's acoustic impedance, Z, via the reflection coefficient R. This is a well-established technique for identifying subglacial materials, and has frequently been applied to Antarctic ice streams (e.g. Brisbourne et al. 2017; Clyne et al. 2020; Muto et al. 2019b; A. M. Smith 1997a; A. M. Smith 1997b; A. M. Smith et al. 2013). At normal incidence, the amplitude reflection coefficient R_0 of a P wave is given by:

$$R_0 = \frac{Z_2 - Z_1}{Z_2 + Z_1}, \tag{1.1}$$

where Z_1 is the acoustic impedance in the first medium and Z_2 is the acoustic impedance in the second medium (Sheriff and Geldart 1995). If Z_1 of ice is assumed to be known it is

straightforward to calculate Z_2 in the subglacial material from the reflection coefficient.

It is common to measure R_0 from the normal-incidence primary reflection and its first multiple using a method by Röthlisberger (1972). This technique has been used to distinguish bedrock from stiff tills and those that are likely deforming, (e.g., Brisbourne et al. 2017; A. M. Smith 1997a; A. M. Smith 1997b; A. M. Smith et al. 2002; A. M. Smith 2007; A. M. Smith et al. 2013; Vaughan et al. 2003), as well as identify areas of frozen and unfrozen subglacial sediment (Peters and Anandakrishnan 2007). Where multiples are not clearly present, R_0 can be determined by measuring the amplitude of the primary ice-bed reflection, and making a correction for source amplitude (Clyne et al. 2020; Muto et al. 2019b). Similar methods have also been used to investigate the sediments within subglacial lakes (e.g. Brisbourne et al. 2023; A. M. Smith et al. 2018).

Normal-incidence techniques are particularly useful as they enable measurement of basal properties at many points along a seismic line, providing a means of assessing the distribution of subglacial materials and determining the distribution of subglacial water (Muto et al. 2019b; A. M. Smith 1997b). However, incorporating acoustic impedance directly into ice-sheet models is difficult (Kyrke-Smith et al. 2017), and in many cases it can be beneficial to further constrain subglacial properties by measurement of Poisson's ratio, σ, which is related to porosity. This can help to distinguish materials which may have similar acoustic impedances, but whose Poisson's ratios may have differing effects on ice flow. Amplitude-versus-offset (AVO), or amplitude-versus-angle (AVA) techniques can deliver more comprehensive measurements of the bed's material properties due to their sensitivity to both Z and σ. This comes at the expense of surveying over a more limited spatial area; AVA and normal-incidence measurements are therefore complementary.

AVA techniques quantify the reflection coefficient R as a function of incidence angle θ. Glaciologically, they have been used to identify basal materials underneath ice streams and outlet glaciers in Antarctica (Anandakrishnan 2003; Horgan et al. 2021; Peters et al. 2007) and Greenland (Booth et al. 2012; Hofstede et al. 2018; Hofstede et al. 2023; Kulessa et al. 2017; Peters 2009), as well as mountain glaciers in Alaska (Gonzalez 2020; Zechmann et al. 2018). They can be used to identify thinly layered substrates by consideration of interference effects (Booth et al. 2012), and have also been used to detect changes in subglacial hydrology (Kulessa et al. 2017; Nolan and Echelmeyer 1999). Their sensitivity to subglacial water also makes them excellent

methods for investigating possible subglacial lake locations (Hofstede et al. 2023; Horgan et al. 2012; Peters et al. 2008); in some cases, inference of subglacial lakes from RES may be refuted by seismic measurements owing to the latter technique's greater capability for measuring basal properties (Hofstede et al. 2023).

AVA methods are a powerful tool for quantifying subglacial conditions. However, P wave AVA inversions are highly nonunique (Castagna and Backus 1993). As three-component recording and joint active- and passive-source experiments using technologies such as seismic nodes increase in popularity in the glaciological community (e.g. Labedz et al. 2022; Veitch et al. 2021; Young et al. 2023), datasets which include high-quality records of P to S wave mode conversions (converted waves) will become more common. Converted wave AVA has been applied to characterisation of hydrocarbon reservoir wells (e.g. Kurt 2007; Lu et al. 2015; Ramos and Castagna 2001), and joint inversion approaches have been shown to be more accurate than sole analysis of PP amplitudes (Ursenbach 2005); however to date, the extent to which the inclusion of converted waves may mitigate nonuniqueness in glaciological AVA inversions has been unexplored.

Recent work has demonstrated that the ice-bed interface can be significantly more complex than is conventionally assumed in glaciological seismic studies, with thin layers of deforming sediment observed overlying stiffer sediment (e.g. Booth et al. 2012; Brisbourne et al. 2017; Kulessa et al. 2017). This influences the interpretation of geophysical measurements, as composite AVA responses arise from interference at the thin layer, and the glaciological processes associated with the characteristics of the glacier bed. Furthermore, the presence of basal debris is known to affect glacier sliding (Zoet et al. 2013), and may have a significant effect on the sliding of Antarctic ice streams (Hudson et al. 2023). Improved methods of seismic analysis may therefore improve our understanding of the fundamental properties of the ice-bed interface, and enable ice sheet models to better capture its complexity.

In this thesis, I address these knowledge gaps by presenting an inversion scheme for jointly inverting PP and PS wave amplitudes, and investigate thoroughly the extent to which this improves over conventional methods (Chapter 3). I then implement the method on data from Korff ice rise (Chapter 4), discussing the glaciological implications of the observed response, which is indicative of a basal debris layer.

Accurate constraint of attenuation losses is essential for AVA and normal-incidence methods.

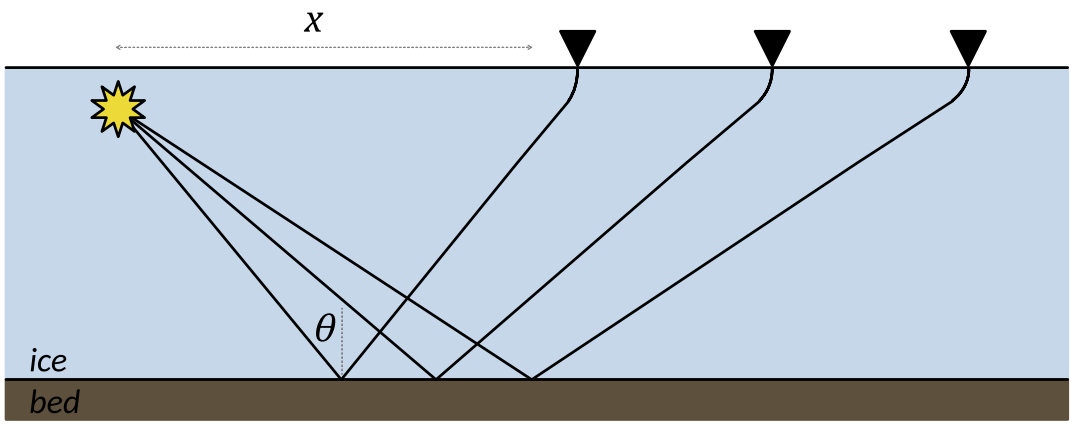

Figure 1.1: Schematic of an active-source seismic survey. The yellow star represents the seismic source and the triangles represent the receivers. Curved ray paths result from continuous refraction in the firn. x denotes source-receiver offset and θ refers to incidence angle.

However, in cases where multiple ice-bed reflections are not observed, attenuation is often poorly constrained or must be assumed. This thesis (Chapter 2) also addresses this shortfall by presenting a method for measuring seismic attenuation in firn from continuously refracted diving waves. This method, since it does not rely on measurements from reflections, is applicable even where multiples are not present, and allows the measurement of attenuation as a function of depth in the firn column, also aiding seismic studies of the upper portions of glaciers and ice sheets. In addition, the measurement of attenuation in firn aids accurate measurement of source amplitude, which is necessary for correcting absolute basal reflection amplitudes.

1.3 Amplitude-versus-angle (AVA) analysis: theory

1.3.1 Measuring seismic amplitude

Figure 1.1 shows a schematic of a glaciological seismic survey. A seismic source is usually buried and geophones laid out at increasing distances from the source. The amplitude A of a wavelet arriving at a receiver a distance x from the source is:

$$A(x, f) = A_0(f)R(x)\gamma(x)e^{-a(f)r(x)}. \tag{1.2}$$

Here, A_0 is the source amplitude, f is frequency, and R describes the effect of reflectivity along the ray path, which has length $r(x)$. γ describes geometrical spreading factors and a is the absorption coefficient:

$$a(f) = \frac{\pi f}{Qv}. \tag{1.3}$$

Q is the seismic quality factor and v the velocity of the wavelet. Throughout this thesis I make the common assumption that Q is independent of frequency (Kjartansson 1979); furthermore, I assume a low-loss formulation of Q (O'Connell and Budiansky 1978; Toverud and Ursin 2005). For the purposes of making amplitude corrections when Q and v vary over the ray path, it is useful to make the substitution

$$t^* = \frac{t}{Q}, \tag{1.4}$$

where t is propagation time. t^* is called the attenuated time (Carpenter et al. 1966) and is cumulative along the ray path r', i.e.:

$$t^*_{\text{ray}} = \int_{r'=0}^{r'=r} \frac{t(r')}{Q(r')} \mathrm{d}r', \tag{1.5}$$

where r is the total ray path distance. For a ray travelling through n discrete homogeneous isotropic layers:

$$t^*_{\text{ray}} = \sum_{i=1}^{n} t^*_i = \sum_{i=1}^{n} \frac{t_i}{Q_i}. \tag{1.6}$$

Substituting Equation 1.4 into Equation 1.2 and rearranging for R gives:

$$R = \frac{A}{A_0} \frac{1}{\gamma} e^{\pi f t^*} \tag{1.7}$$

where t^* is the attenuated time of the entire ray.

Glaciological seismic reflection experiments often aim to make an accurate measurement of R in order to identify the material underlying a glacier and measure its properties. This requires the measured amplitude A to be corrected for source amplitude A_0, geometric spreading γ, and attenuative effects. R is dependent on the elastic properties of the bed, and varies with angle of incidence θ. The reflection coefficient at normal incidence, R_0, can be used to calculate the

acoustic impedance of the bed using Equation 1.1. At non-normal incidence, AVA methods can be used.

In Chapter 3, I assume $R(\theta)$ can be measured perfectly and discuss experiments using numerical synthetics. Chapter 2 details a novel method for measuring Q which is applicable where conventional methods may not be available. I discuss the attenuation, source amplitude and geometric corrections in more detail as I apply them to real-world AVA data in Chapter 4.

1.3.2 Partition of energy at an interface: angular dependence of R

When a seismic wave is incident on an interface between two media, the energy is partitioned into reflected and transmitted waves. This partitioning was described in terms of potentials by Knott (1899), and subsequently in terms of displacement amplitudes by Zoeppritz (1919). When a P wave is obliquely incident on an interface, some energy is converted into transmitted and reflected shear waves; these are called converted waves. The proportion of energy partitioned into each of the reflected and transmitted P and S phases is dependent on the incidence angle θ and the elastic properties of the two media. Figure 1.2 shows a schematic of a P wave incident at an interface of contrasting properties, and the resulting reflected and transmitted waves. The fundamental principle of amplitude-versus-offset (AVO) and amplitude-versus-angle (AVA) techniques is to deduce the elastic properties from measurements of the offset- or angle-dependence of $R(\theta)$.

The Knott-Zoeppritz equations describe $R(\theta)$ in terms of the the elastic properties of the media on either side of the interface. These are the P wave velocities α_1 and α_2, the S wave velocities β_1 and β_2, and the densities ρ_1 and ρ_2. The Knott-Zoeppritz equations are stated as four equations with four unknowns R_P, R_S, T_P and T_S:

$$\begin{bmatrix} R_P \\ R_S \\ T_P \\ T_S \end{bmatrix} = \begin{bmatrix} -\sin(\theta_1) & -\cos(\phi_1) & \sin(\theta_2) & \cos(\theta_2) \\ \cos(\theta_1) & -\sin(\phi_1) & \cos(\theta_2) & -\sin(\phi_2) \\ \sin(2\theta_1) & \frac{\alpha_1}{\beta_1}\cos(2\phi_1) & \frac{\rho_2\beta_2^2\alpha_1}{\rho_1\beta_1^2\alpha_2}\sin(2\theta_2) & \frac{\rho_2\beta_2\alpha_1}{\rho_1\beta_1^2}\cos(2\phi_2) \\ -\cos(2\phi_1) & \frac{\beta_1}{\alpha_1}\sin(2\phi_1) & \frac{\rho_2\alpha_2}{\rho_1\alpha_1}\cos(2\phi_2) & -\frac{\rho_2\beta_2}{\rho_1\alpha_1}\sin(2\phi_2) \end{bmatrix}^{-1} \begin{bmatrix} \sin\theta_1 \\ \cos\theta_1 \\ \sin 2\theta_1 \\ \cos 2\phi_1 \end{bmatrix}. \quad (1.8)$$

R_P and R_S are the P and S wave reflection coefficients and T_P and T_S are the P and S wave

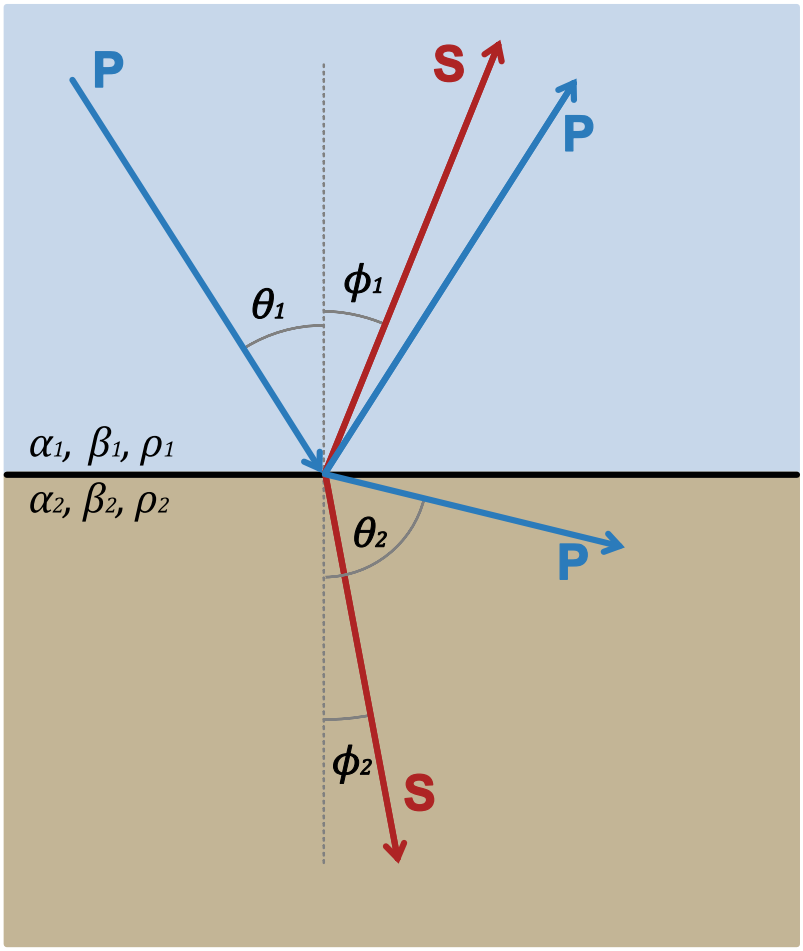

Figure 1.2: Partition of obliquely incident planar P wave energy at a planar interface between two materials (e.g. the ice-bed interface).

transmission coefficients, respectively. θ_1 is the (P wave) angle of incidence, and θ_2 is the angle of refraction. ϕ_1 and ϕ_2 are the S wave reflection and transmission angles, respectively (Figure 1.2). θ_2, ϕ_1 and ϕ_2 are determined by Snell's law. At normal incidence to the interface, the Knott-Zoeppritz equations reduce to Equation 1.1 and $R(\theta)$ is determined by the acoustic impedances of the two media.

Z is related to the density and P wave velocity of a material by

$$Z = \rho\alpha. \tag{1.9}$$

Poisson's ratio is related to the P and S wave velocities of a material by (Mavko et al. 2009):

$$\sigma = \frac{\alpha^2 - 2\beta^2}{2(\alpha^2 - \beta^2)}. \tag{1.10}$$

The Knott-Zoeppritz equations can therefore be recast in terms of acoustic impedance and Poisson's ratio, which can aid in interpreting the results of AVA inversions.

It should be noted here that the term 'converted wave' in general applies to any mode conversion, whether transmitted or reflected, P to S or S to P. From here on I use it to refer to the reflected PS wave only.

1.3.3 Glaciological AVA responses

In this section, I use the Knott-Zoeppritz equations to model AVA responses for hypothetical subglacial materials, discussing the qualitative characteristics of the AVA responses as basal acoustic impedance and Poisson's ratio are varied, after Booth et al. (2012). I extend the qualitative analysis of Booth et al. (2012) to consider characteristics of PS and SS AVA responses. I then show AVA responses for a variety of real and previously observed subglacial materials, discussing their characteristics, and extending previous work (e.g. Peters 2009) to consider PS and SS AVA responses of these subglacial materials.

Thin layering can complicate analyses of seismic reflectivity. In particular, series of thin layers can enhance the amplitude of reflected waves over transmitted waves, and act as a low pass filter (Ziolkowski and Fokkema 1986). Booth et al. (2012) present an in depth exploration of the effect of thin layering at the bed on glaciological AVA responses. A full consideration of thin

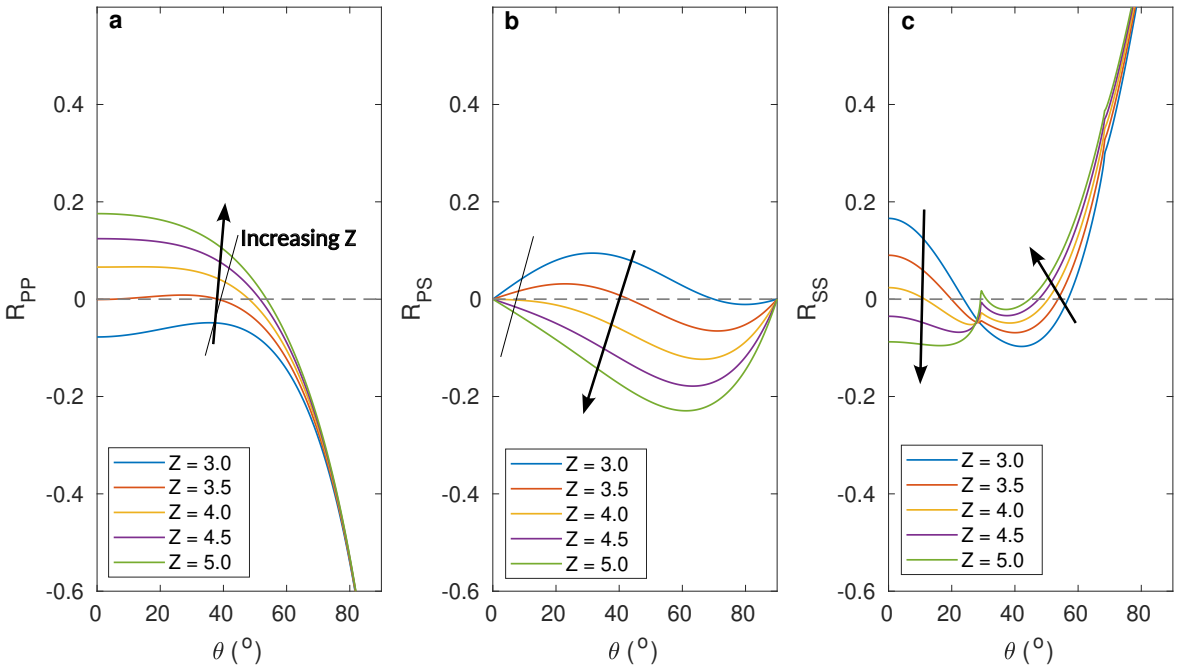

Figure 1.3: Varying basal acoustic impedance Z (units 10^6 kg m^{-2}s^{-1}) while basal Poisson's ratio is kept constant at $\sigma = 0.4$. Arrows are marked in the direction of increasing acoustic impedance. (a) PP reflection coefficient, (b) PS reflection coefficient, (c) SS reflection coefficient as a function of incidence angle θ. Units of Z are 10^6 kg m^{-2}s^{-1}.

layering is beyond the scope of this section, as I intend to highlight some qualitative aspects of glaciological AVA interpretation. Implications of thin layering on the interpretation of the data acquired at Korff Ice Rise are discussed in Section 5.2.4.

Effect of acoustic impedance and Poisson's ratio on PP, PS and SS AVA responses

The character of an AVA response depends on the change in acoustic impedance Z and Poisson's ratio σ across the interface. Figures 1.3 and 1.4 show examples of modelled AVA responses for glacial ice ($Z = 3.5 \times 10^6$ kg m^{-2}s^{-1}, $\sigma = 0.34$) over a variety of theoretical basal materials, after Booth et al. 2012. Shuey (1985) simplified the Knott-Zoeppritz equations for incidence angles less than 30°, separating the effects of acoustic impedance and Poisson's ratio into intercept and gradient terms. While I do not follow Shuey's approximation in this thesis, it can aid qualitative interpretation to look at examples of AVA responses within this framework. Booth et al. (2012) presented hypothetical PP AVA responses for subglacial materials, keeping one of Z or σ constant while varying the other. I extend their observations to PS and SS AVA responses, using the same values for Z and σ.

Figure 1.3 shows the effect of varying Z in the basal material while keeping σ constant at

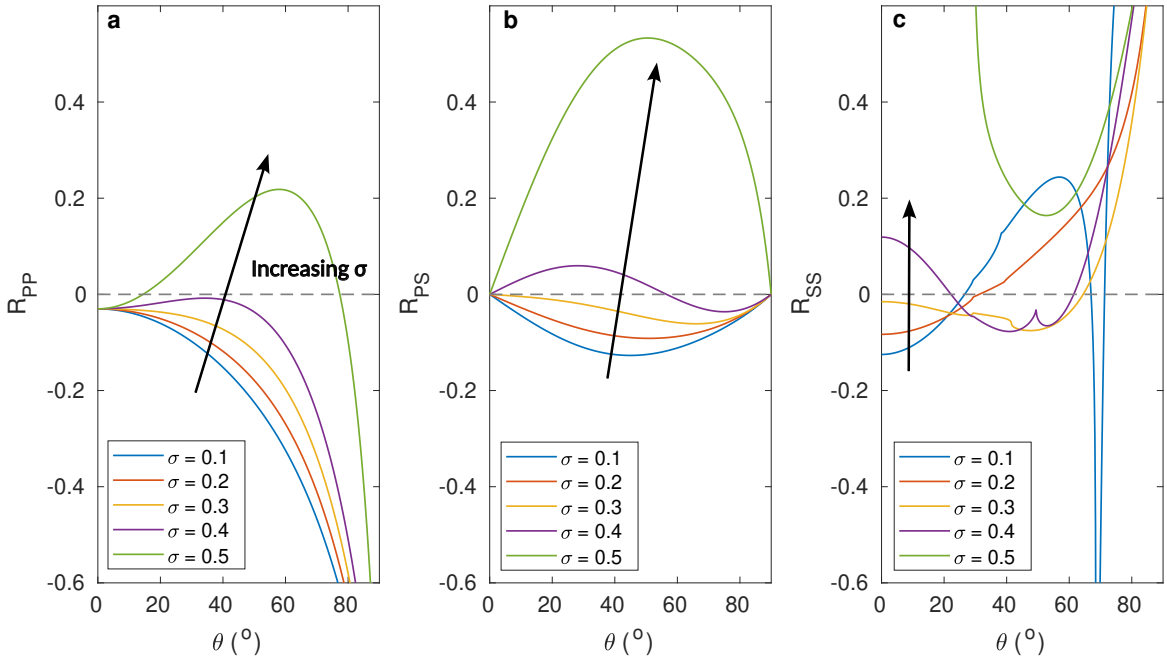

Figure 1.4: Varying basal Poisson's ratio σ while basal acoustic impedance is kept constant at $Z = 3.3 \times 10^6$ kg m^{-2}s^{-1}. Arrows indicate the direction of increasing Poisson's ratio. (a) PP reflection coefficient, (b) PS reflection coefficient, (c) SS reflection coefficient as a function of incidence angle θ. Units of Z are 10^6 kg m^{-2}s^{-1}.

$\sigma = 0.4$. Z is varied between 3×10^6 kg m^{-2}s^{-1} and 5×10^6 kg m^{-2}s^{-1}. The arrows indicate the direction of increasing Z. The primary effect on the PP AVA response of an increase in the basal material's acoustic impedance is that the intercept increases (Fig. 1.3a). A negative polarity at zero incidence is associated with a decrease in acoustic impedance across the interface and a positive polarity is associated with an increase in acoustic impedance. The linearised PS AVA gradient decreases with increasing basal Z at $\theta < 30°$ (Fig. 1.3b), and the SS intercept decreases with increasing Z (Fig. 1.3c).

At incidence angles $< 30°$ the PP AVA gradient is principally controlled by the contrast in σ across the interface. Figure 1.4 shows PP, PS and SS AVA responses for ice over a hypothetical subglacial material with Z fixed at $Z = 3.3 \times 10^6$ kg m^{-2}s^{-1} and σ varied between 0.1 and 0.5 at intervals of 0.1. A positive PP AVA gradient is associated with an increase in σ across the interface, with the gradient increasing as the contrast in σ increases (Fig. 1.4a). An increase in subglacial σ increases the PS AVA gradient, with the response associated with lowest σ subglacial materials having a strong negative gradient at $\theta < 30$ and that associated with the highest σ materials having a strong positive gradient (Fig. 1.4b). The SS intercept increases with increasing σ (Fig. 1.4c). At incidence angles increase, interpretation of SS AVA responses

Table 1.1: Seismic properties of bed materials simulated. a) properties taken from Peters et al. 2007. b) properties taken from Christensen 1989, after Peters et al. 2008. c) properties taken from Peters et al. 2008.

Material	α (m s^{-1})	β (m s^{-1})	ρ (kg m^{-3})	Z (10^6kg m^{-2} s^{-1})	σ
Ice[a,b]	3810	1860	920	3.5	0.34
Water[b]	1500	0	997	1.5	0.5
Basement[b]	5200	2800	2700	14	0.3
Stiff till[a]	1800 $\pm$ 150	1000 $\pm$ 100	1900 $\pm$ 150	3.42 $\pm$ 0.4	0.28 $\pm$ 0.08
Dilatant till[a,c]	1700 $\pm$ 150	200 $\pm$ 50	1800 $\pm$ 150	3.06 $\pm$ 0.4	0.49 $\pm$ 0.004
Lithified sediment[b]	3750	2450	2450	9.19	0.128

becomes difficult due to their complexity.

Qualitative interpretation of PS and SS AVA responses is less straightforward than interpretation of PP AVA responses because Z and σ can not be separated into intercept and gradient terms; they both act on the PS gradient and the SS intercept. However, since for many real-world subglacial materials increasing acoustic impedance is often associated with decreasing Poisson's ratio (Booth et al. 2012; Peters et al. 2008), these effects may amplify each other; in combination with a qualitative interpretation from PP amplitudes, a quantitative evaluation of PS and/or SS wave amplitudes may provide useful constraint on basal properties.

AVA responses of typical glacier bed materials

Figure 1.5 shows the AVA responses for previously reported glacial substrates 1.5. The AVA responses are computed from the properties detailed in Table 1.1, after Peters et al. (2008). Together, these materials represent the full range of subglacial materials a glacial AVA survey is likely to encounter. Subglacial water may be measured under ice shelves (e.g. Horgan et al. 2021), at subglacial lakes (e.g Brisbourne et al. 2023), or in other locations where the subglacial hydrological system allows water pooling (e.g. Muto et al. 2019b). 'Basement' refers to crystalline bedrock. 'Stiff till' is used to mean a dry till which is not deforming (e.g. Peters et al. 2007). During streaming flow, saturated subglacial till dilates, causing an increase in till porosity (e.g. A. M. Smith 1997a). This saturated, deforming material is referred to as dilatant till. Finally, lithified sediment can be interpreted as sedimentary rock.

The characters of these AVA responses follow the general observations of the previous section. The PP intercept (Fig. 1.5a) is strongly negative for an ice/water interface, there being a strongly decreasing acoustic impedance across the interface. The intercept is strongly positive for an ice-basement or ice/lithified sediment interface, because of the strong increase in Z across

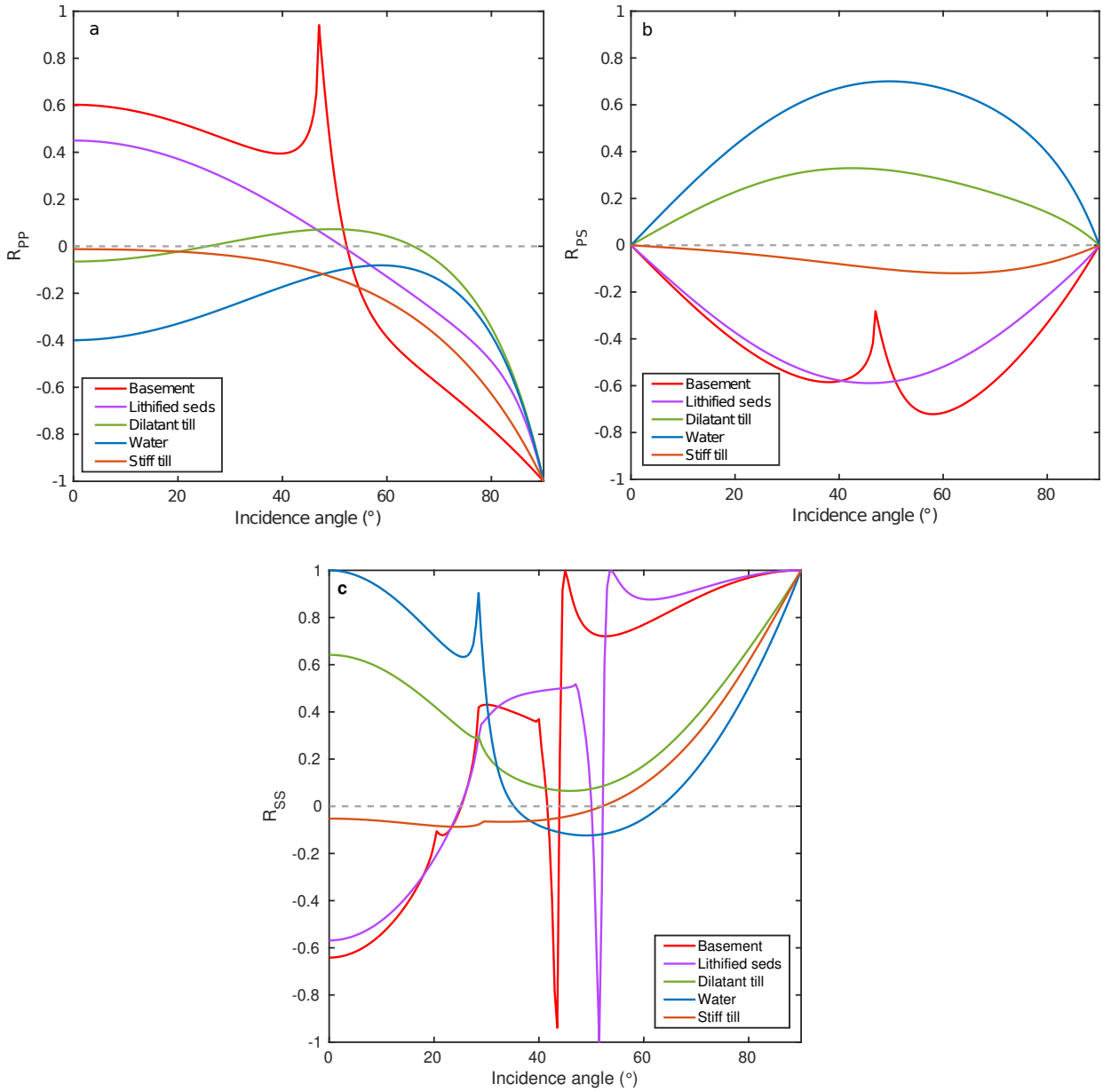

Figure 1.5: (a) PP, (b) PS and (c) SS AVA responses for the glacier bed materials detailed in Table 1.1

the interface. The PP intercepts for beds of stiff and dilatant till are weakly negative, as they have acoustic impedances only slightly less than that of ice.

The (linearised) AVA gradient associated with the PP response is strongly negative for beds of lithified sediments or basement, and strongly positive where there is subglacial water. The AVA responses of some substrates (e.g. dilatant till, lithified sediments) display a polarity reversal, which is a highly diagnostic feature which can be used to classify glacial substrates. Anandakrishnan (2003) identified a dilatant till layer at Ice Stream C (Kamb Ice Stream) by measuring the angle at which this polarity reversal occurred. The angle of polarity reversal, or crossing angle, supplies key information about the Poisson's ratio of the material. If the polarity reversal is not captured by the angular range of the survey (e.g. if $\sigma < 25^\circ$ only), beds of stiff and dilatant till may be difficult to distinguish from the PP response alone. However, analysis of PS responses (Fig. 1.5b) jointly with PP responses (Fig. 1.5a) may enable identification of these materials, as their PS responses are better separated than their PP responses.

The PS AVA gradient decreases with both increasing Z and decreasing σ: water, which has the lowest Z and highest σ of a typical subglacial material, has the most strongly positive PS AVA gradient. In general, a higher acoustic impedance is associated with a lower Poisson's ratio, so these effects amplify each other in the AVA gradients, leading to progressively decreasing gradients as materials become stronger and stiffer (Figure 1.5b). However, when this is not the case, it can lead to nonuniqueness: at $\theta < 40^\circ$, the PS responses of lithified sediments and crystalline basement are very similar. This is because basement has a higher Z but also higher σ than lithified sediments, so the decrease in gradient associated with higher Z and increase in gradient associated with higher σ trade off against each other. These materials are indistinguishable from PS amplitudes at $\theta < 40^\circ$ alone; however, consideration of PP and PS responses together may enable identification.

The SS AVA intercept is most strongly positive for an ice/water interface and most strongly negative for basement and lithified sediments; here a strongly positive intercept is associated with a decrease in Z/increase in σ across the interface, and a strongly negative intercept associated with an increase in Z/decrease in σ across the interface (Figure 1.5c). As seen with the PS gradient, increasing Z and decreasing σ in the subglacial material have the same effect - a decrease in the SS intercept. These AVA responses therefore exhibit the same tradeoff between Z and σ which results in similarity between the responses for basement and lithified sediments.

A qualitative interpretation from the SS intercept may have some value but is fundamentally limited by this property. At incidence angles of $\theta = 30^\circ$ the SS responses become complicated, making interpretation difficult.

The sharp peaks in the AVA responses represent the critical angle θ_{crit} of the incident wave. For example, a P wave incident at an ice/basement interface goes critical at $\theta_{\text{crit}} \sim 45^\circ$, which is clearly visible as a peak in the PP and PS AVA responses (Figs. 1.5a and b). Since the Knott-Zoeppritz equations do not account for head waves, amplitudes at $\theta \geqslant \theta_{\text{crit}}$ should not be used, as the Knott-Zoeppritz equations do not accurately describe these amplitudes (Červený 1966). The SS responses show that for these glaciological substrates, the critical angle of an incident S wave is at relatively small angles compared to the critical angle of the incident P wave (Figure 1.5c). This means that only a small part ($\theta < 20^\circ$) of the SS AVA response can be used.

Typically, glaciological AVA inversions look for the basal properties which give the minimum misfit to a PP AVA response. However, these inversions are highly nonunique, especially when the available angular range of data is limited; commonly, $\theta < 30^\circ$ (e.g. Booth et al. 2012; Horgan et al. 2021). Jointly inverting PP and PS AVA data may help to reduce this nonuniqueness as the PP and PS AVA responses contain different information about the substrate. Furthermore, the converted wave detected at a given source-receiver offset is incident at a larger angle than the PP wave received, due to the slower S wave velocity resulting in an asymmetric ray path (Figure 1.6). Therefore analysing PS waves is a means of extending the angular coverage of incident waves at the glacier bed, and offers an independent subset of seismic data with which to constrain material properties.

While in principle SS wave AVA responses can be included in these inversions, in practice their measurement is more challenging, due to the requirement of S wave sources and the greater difficulty of measuring S wave source amplitude and attenuation. Therefore this thesis is mainly focused on exploring the potential for PS converted waves to improve AVA inversions. I also investigate the hypothetical value of joint inversion including SS amplitudes using numerical synthetics. However, this does not form the main focus of the work.

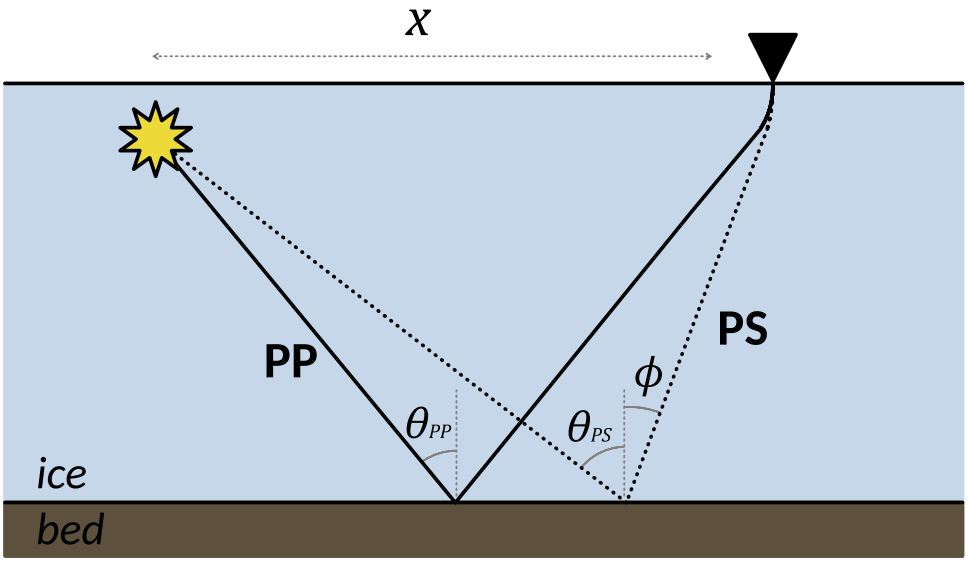

Figure 1.6: Schematic ray paths of a PP reflection (solid line) and converted-wave PS reflection (dotted line). For waves incident at the same receiver, the PS incidence angle, θ_{PS} is larger than the PP incidence angle, θ_{PP}, due to the slower S wave velocity.

1.3.4 Converted-wave AVA processing

To calculate the reflection coefficient of a P-to-S converted wave, the P wave and S wave portions of the propagation path are dealt with separately, and Equation 1.7 becomes:

$$R_{PS} = \frac{A}{A_0}\frac{1}{\gamma_P \gamma_S} e^{\pi f t_P^*} e^{\pi f t_S^*}, \tag{1.11}$$

where γ_P is the geometric spreading factor applied to the P wave portion of the ray path, γ_S is the geometric spreading factor applied to the S wave portion, t_P^* is the wavelet's attenuated time as a downgoing P wave, and t_S^* is its attenuated time as an upgoing S wave.

Analysis of converted wave amplitudes is more challenging when compared with PP wave analysis due to the independent constraint needed for S wave velocity and attenuation. Furthermore, the reflection points for PP and PS waves recorded at a single receiver are different (Figure 1.6), so either the ice-bed interface must be assumed homogeneous or the spatial variability of reflection points must be accounted for.

1.4 Seismic attenuation in snow, firn and ice

Seismic Q is a main source of uncertainty in AVA studies (Luh 1993; Peters 2009). This thesis is also concerned with the development of a method to measure Q in firn, with a view to improving

attenuation corrections and better constraining glacier bed reflectivity.

As a seismic wave propagates, it loses energy in four generic ways: geometric spreading, partial reflection at interfaces, scattering, and by conversion of kinetic energy to heat due to the internal friction of the propagating medium (Section 1.3.1). The lattermost is termed anelastic attenuation, and is quantified using the dimensionless seismic quality factor Q. Q is inversely proportional to the fractional energy loss per wave cycle (Aki and Richards 2002; Sheriff and Geldart 1995), with higher Q materials associated with more efficient propagation. A wide range of P wave quality factors (Q_p) have been found in both polar ice sheets and mountain glaciers; field-based measurements have ranged from $Q_p = 6 \pm 1$ in warm ice (Gusmeroli et al. 2010), to $Q_p > 500$ in cold polar ice (C. R. Bentley and Kohnen 1976). A dependence of Q_p on temperature has been demonstrated both in the laboratory (Kuroiwa 1964), and in the field (Peters et al. 2012, using a method by Dasgupta and Clark 1998). Clee et al. (1969) measured both Q_p and the shear-wave quality factor, Q_s, in ice near its melting point, finding $Q_p/Q_s \sim 3$.

Attenuation measurements have been made across various depth ranges in glacial ice, with some authors measuring Q over the entire ice column from the spectra of pairs of primary/multiple reflections (e.g. C. R. Bentley 1971; Booth et al. 2012; Jarvis and King 1993; Robin 1958). Others have measured Q within narrower depth ranges, either by using strong basal and englacial reflections (e.g. Jarvis and King 1993; Peters et al. 2012) or by measuring the amplitude decay of the direct P wave in a vertical seismic profile (Booth et al. 2020).

The upper portions of polar glaciers are characterised by the gradual compaction of snow into ice. The intermediate material, called firn, exhibits a continuous transition in elastic properties with depth, presenting a challenge for seismic studies (Schlegel et al. 2019). Q has been measured in the uppermost ice of a snow-free glacier (Gusmeroli et al. 2010), and at a single depth at the base of the firn column (Peters 2009); however little attention has been paid to the depth-dependence of attenuation at intermediate depths in the firn column. Measurements of Q are therefore desirable to both provide further insight into the structure of the firn itself, and correct seismic reflection amplitudes for attenuation losses.

Chapter 2 of this thesis focuses on the development of a new method of measuring seismic attenuation in polar firn, preparatory to the AVA experiments. The method is applicable in cases where conventional multiple-based methods may not be available, and provides a more detailed model of the depth-dependence of Q than has previously been resolved. Correction for

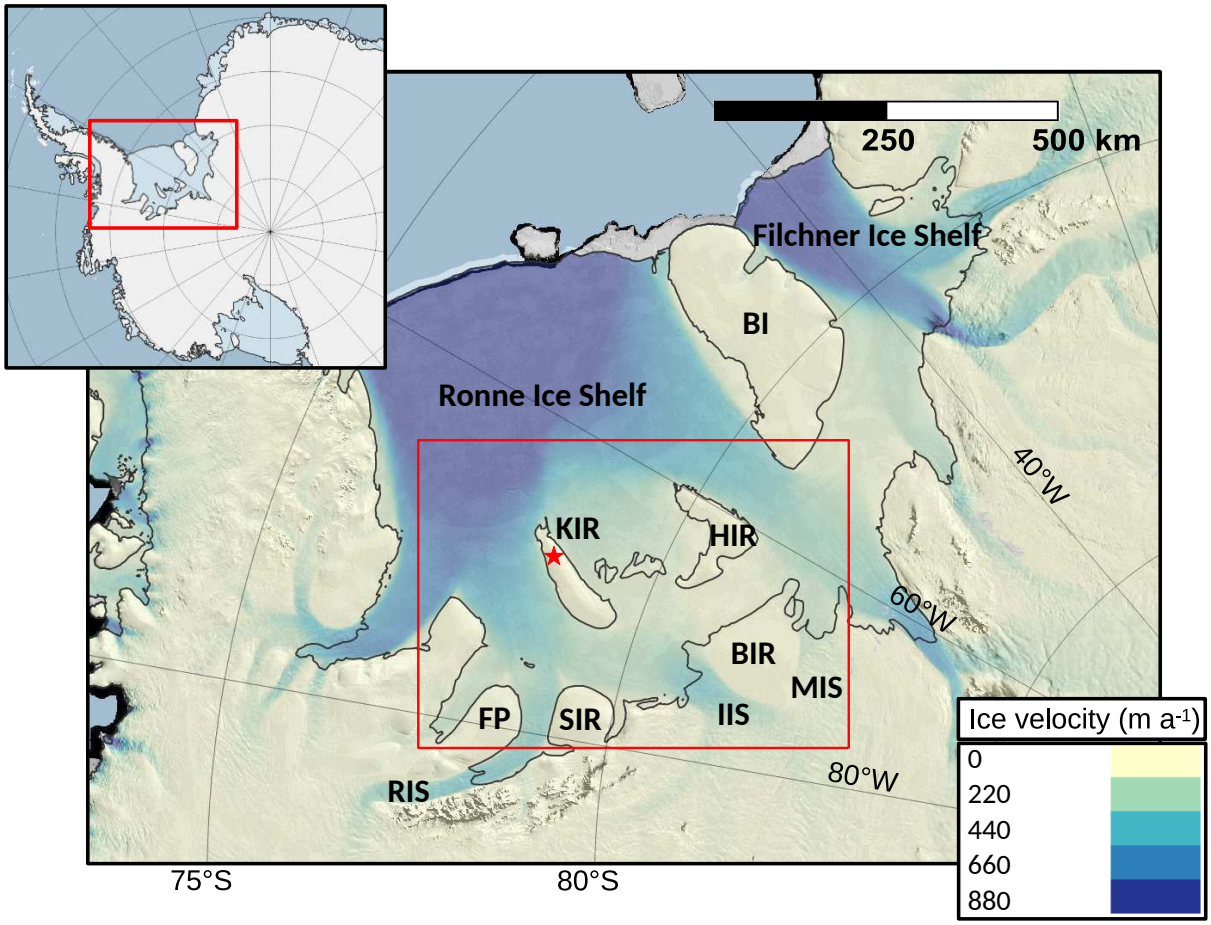

Figure 1.7: Location of the field site (red star) on Korff ice rise (KIR) in the Ronne Ice Shelf. HIR = Henry ice rise, BIR = Bungenstock ice rise, SIR = Skytrain ice rise, FP = Fletcher Promontory, BI = Berkner Island. IIS = Institute ice stream, MIS = Möller ice stream, RIS = Rutford ice stream. Inset shows the location within Antarctica. MODIS imagery (Scambos et al. 2007) is overlain by MEaSUREs flow velocities (Mouginot et al. 2012; Mouginot et al. 2017; Rignot et al. 2017), accessed through Quantarctica (Matsuoka et al. 2021). Red box in main figure indicates the region shown in Fig. 1.8a.

depth-varying Q in firn can also aid with accurately measuring the source amplitude, necessary for correcting absolute reflection amplitudes.

1.5 The study site: Korff ice rise, West Antarctica

Korff ice rise (KIR) is an ice rise in the Weddell Sea Sector of West Antarctica, which lies in the Ronne Ice Shelf. Figure 1.7 shows the location of KIR within the Ronne Ice Shelf and the Antarctic continent, showing the locations of other ice rises and rumples in the region - Bungenstock ice rise (BIR), Henry ice rise (HIR) and Skytrain ice rise (SIR). Also marked are the ice streams Rutford ice stream (RIS), Institute ice stream (IIS) and Möller ice stream (MIS). The ice surrounding KIR flows from RIS and IIS.

(a)

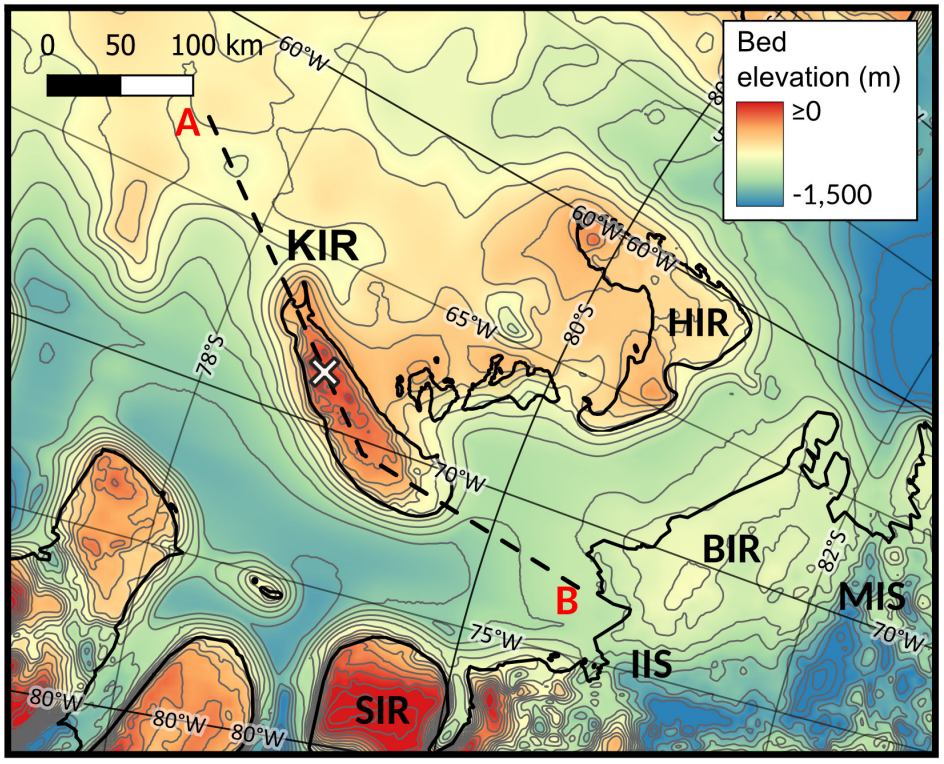

(b)

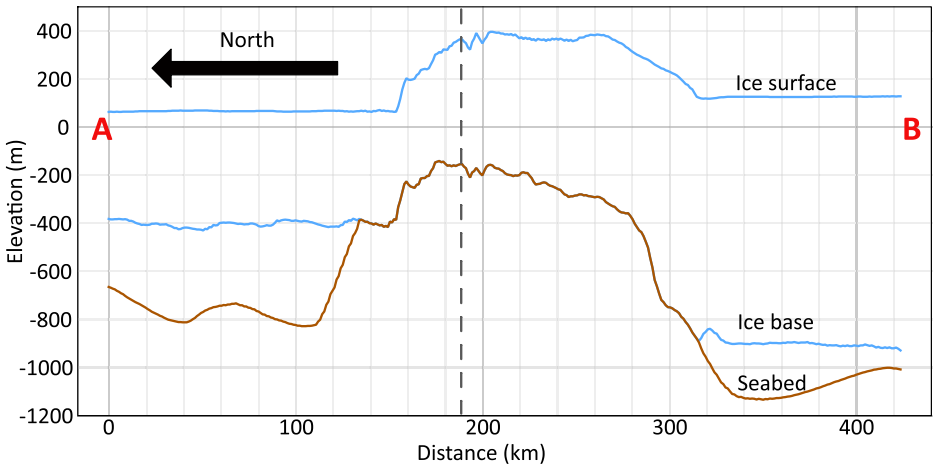

Figure 1.8: (a) Bed topography of the region surrounding KIR, from Bedmap 2 (Fretwell et al. 2013), showing the location of the field site (white cross) and present day grounding line (black solid line). Bed elevation is with reference to sea level. Contours are at intervals of 100 m. The dotted line from A to B indicates the location of the profile in (b). (b) profile showing bed elevation, surface elevation and the ice base, from A to B. The South end of the ice rise is the stoss side and the North end is the lee side. Ice is thicker on the stoss side. The vertical grey dotted line shows the location of the field site. Reverse bed slopes of IIS and MIS are visible in the basal topography.

Figure 1.8a shows the regional bed topography around KIR, from Bedmap 2 (Fretwell et al. 2013), with the field site marked by the white cross. The region displayed in Figure 1.8a is indicated by the red box in Fig. 1.7. Figure 1.8b shows a cross section of KIR's basal topography, as well as the ice surface and ice base, along its divide axis, indicated by the dashed line AB in Fig. 1.8a. The field site is at the apex of the subglacial mound; the ice is thicker on the upstream (stoss) side of the ice rise, and thinner on the downstream (lee) side. Stoss (South) and lee (North) sides are defined with respect to the flow of the surrounding ice shelf, which flows from South to North.

1.5.1 Ice rises and rumples: formation and temperature

Ice rises and rumples are areas of locally grounded ice within ice shelves. They play an important role in buttressing ice shelves and thus regulating discharge from the Antarctic Ice Sheet (Favier and Pattyn 2015; Reese et al. 2018; Thomas 1979). Furthermore, ice rises encode information about past ice flow and are extremely valuable in constraining ice sheet history (Matsuoka et al. 2015). Ice rises and rumples are distinguished from each other in that at an ice rumple, flow is coincident with the surrounding ice shelf, whereas an ice rise has a flow regime independent of the surrounding shelf (A. M. Smith 1986). Ice rumples can be a precursor to ice rise formation or be stable features in and of themselves (Matsuoka et al. 2015).

Ice rises can form in a number of ways, illustrated in Figure 1.9, reproduced from Matsuoka et al. (2015). An ice rise or rumple can form following ice sheet thinning and retreat of a grounding zone to upstream of the bedrock high, leaving the ice rise grounded (deglacial emergent, Fig. 1.9b). Alternatively, following grounding zone retreat, the ice may unground from the local high and subsequently reground either as a result of glacial isostatic adjustment (GIA emergent, Fig. 1.9c) or ice shelf thickening (glaciological emergent, Fig. 1.9d). Depending on the scenario of formation and its timing, signatures are left in englacial structures (e.g. Kingslake et al. 2016; Siegert et al. 2013) and structures arising from basal processes (Wearing and Kingslake 2019). Observing these structures geophysically can help to inform about the glacial history of an ice rise and aid in the reconstruction of the wider region's past glaciation.

Ice at the base of a floating ice shelf is relatively warm, as it is in contact with ocean water and thus fixed at the pressure melting point. On grounding, the ice base and bed cool towards a geothermal equilibrium temperature due to the ocean cavity no longer being a source of

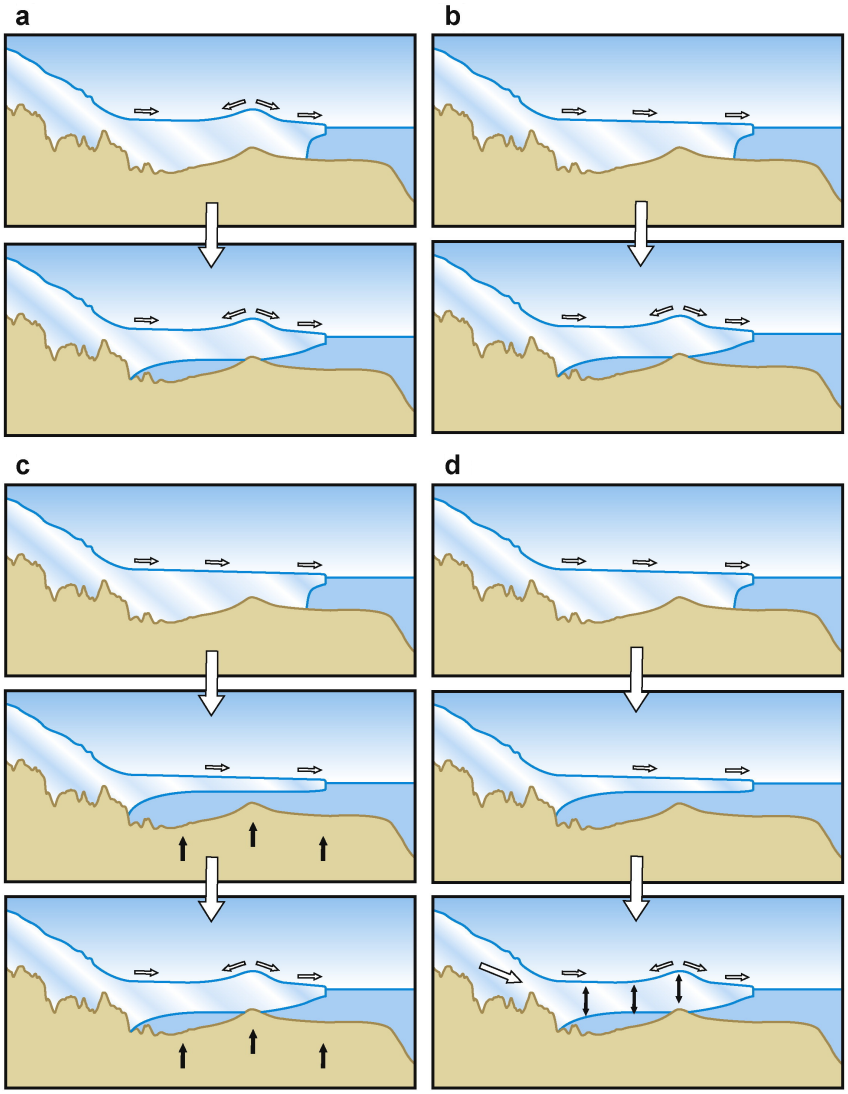

Figure 1.9: Formation mechanisms of ice rises, reproduced from Matsuoka et al. 2015. a) Long-term stable, b) deglacial emergent, c) GIA emergent, d) glaciological emergent. Figure reproduced from Matsuoka et al (2015).

heat (Lyons et al. 1972; MacAyeal and Thomas 1980), with the englacial temperature profile eventually reaching steady state. Temperature profiles at ice rises measured from boreholes have been used to date the formation of ice rises and can provide useful constraint on the glacial history of a region (e.g. Bindschadler et al. 1990; Montelli and Kingslake 2023). Seismic measurements of the ice-bed interface may help in drawing inferences of bed temperature, since frozen and unfrozen ice-bed interfaces will have different elastic properties. Identifying whether the bed at KIR is frozen may therefore provide information about the temperature regime, and inform the history of the Weddell Sea sector more broadly.

1.5.2 Grounding line retreat in the Weddell Sea sector following the last glacial maximum

In order to project the future evolution of the Antarctic ice sheet, models must be constrained based on our understanding of past ice sheet processes. Accurate reconstructions of the history of the West Antarctic Ice Sheet (WAIS) are necessary to understand its past response to ocean and climate forcings, and consequently its past contribution to sea level rise. The Weddell Sea Sector is a key part of this puzzle, having undergone large changes in glaciation since the last glacial maximum (LGM), $\sim$ 20 ka before the present day (e.g. M. J. Bentley et al. 2014). A number of ice streams which drain the WAIS in this region (e.g. Institute and Möller ice streams) rest on reverse bed slopes, meaning that the WAIS may be vulnerable to marine ice sheet instability in the Weddell Sea sector (Siegert et al. 2019; Ross et al. 2012). Loss of ice shelf buttressing from the Filchner-Ronne Ice Shelf may lead to accelerated ice flow from the region's ice streams and outlet glaciers and an increase in its future contribution to sea level rise. In recent years, there has been considerable interest in this region; observations aimed at constraining ice sheet history here have included studies focussing on cosmogenic nuclides (e.g. Hodgson et al. 2012), ice core drilling (Mulvaney et al. 2007; Mulvaney et al. 2014; Mulvaney et al. 2021), marine sediment sampling (e.g. Hillenbrand et al. 2012; Stolldorf et al. 2012) and geophysical investigations (Brisbourne et al. 2019; Kingslake et al. 2016; Ross et al. 2012; Siegert et al. 2013; Wearing and Kingslake 2019; Winter et al. 2015).

These measurements have greatly improved our understanding of the WAIS' recent history in the Weddell Sea sector. At the LGM, the WAIS had a far greater extent than it does today, with grounded ice extending to the continental shelf break (M. J. Bentley et al. 2010; M. J. Bentley

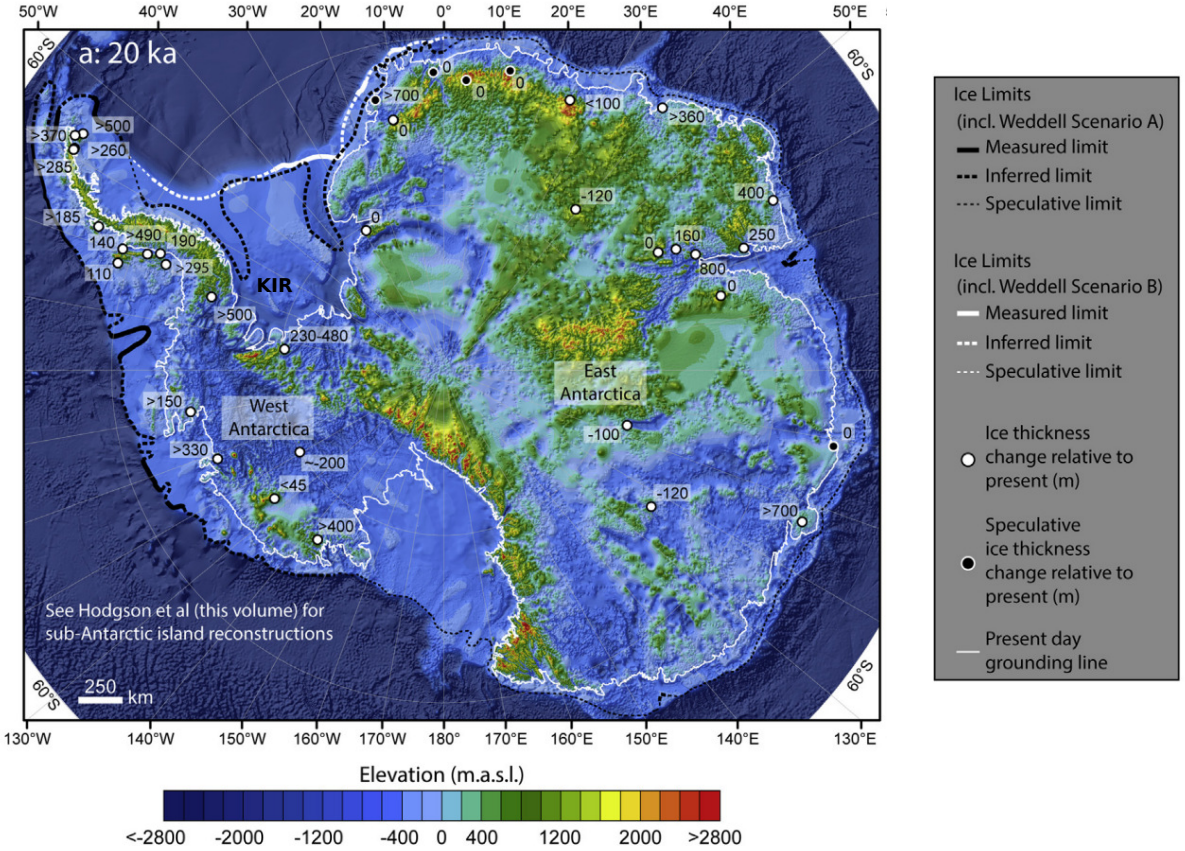

Figure 1.10: Maximum extent of the Antarctic Ice Sheet at the last glacial maximum, 20 ka before present, modified from Bentley et al. (2014). The location of KIR is marked. Weddell scenarios A and B are two possible scenarios of the ice sheet's maximum extent in the Weddell Sea embayment. The colour scale indicates bed elevation, which is taken from Bedmap2 (Fretwell et al. 2013).

et al. 2014; Hillenbrand et al. 2014; Le Brocq et al. 2011). Figure 1.10, modified from Bentley et al. (2014) shows the likely extent of the Antarctic Ice Sheet at the LGM. The white and black outlines describe two scenarios, A and B, which represent the maximum and minimum extents of the grounding line at the LGM consistent with observations. The two prominent inlets in scenario A coincide with bathymetric troughs.

While the extent of the grounded ice sheet at the LGM is now well understood, consensus has yet to be reached on the evolution of the grounding line from its LGM extent to its present position. Some authors have proposed monotonic retreat of the grounding line to its present day position after the LGM (e.g. Hillenbrand et al. 2014; Siegert et al. 2013). The mechanism by which the grounding line would stabilise on a retrograde slope is not clear due to the generally unstable geometry (Schoof 2007); however some authors have demonstrated that grounding lines can stabilise on retrograde slopes in particular circumstances (Gudmundsson et al. 2012;

Jamieson et al. 2012). In this scenario, KIR and its neighbouring ice rises may be deglacial emergent ice rises.

An alternative hypothesis is that of rapid grounding line retreat to a position significantly inland of the current grounding zone. This is followed by GIA resulting from the widespread ungrounding of ice, in turn leading to a readvance of the grounding line to the present day position (Bradley et al. 2015; Kingslake et al. 2018; Siegert et al. 2013). The ice rises and rumples in the Ronne ice shelf may have partially or completely ungrounded and subsequently regrounded as GIA emergent ice rises. This hypothesis offers an explanation for the current stability of the grounding line stability, as this would represent an advancing grounding line reaching stability on a reverse bed slope.

Previous geophysical measurements imply Holocene flow reorganisation at KIR from englacial layering (Kingslake et al. 2016) and observations of crystal orientation fabric (Brisbourne et al. 2019). Kingslake et al. (2016) inferred a change in flow at KIR 2.5 ka ago, observing from internal stratigraphy that the current ice flow regime is not in steady state. Brisbourne et al. (2019) observed a change in ice fabric below 230 m depth inconsistent with present-day divide flow, but consistent with a previous episode of ice flow from the South. Observations from Bungenstock ice rise (Siegert et al. 2013; Winter et al. 2015) also imply flow reorganisation in the Holocene, consistent with previous streaming flow either leading to stagnation and divide formation (in monotonic retreat) or grounding following GIA (retreat/readvance).

Basal crevasses observed at Henry ice rise (HIR) support the retreat/readvance hypothesis, and formation of the ice rise has been dated to 6 ± 2 ka before present (Wearing and Kingslake 2019). The absence of basal crevasses at KIR appears to contradict this, implying either that KIR has not ungrounded during the Holocene or that grounding occurred sufficiently long ago that signs of basal crevassing have been advected away (Kingslake et al. 2016). However, a weak ungrounding of KIR after the LGM and progression to a rumple, followed by GIA and divide formation, can not be ruled out. In this scenario, the downstream (lee) side of the present day ice rise would have ungrounded during rumple formation, and the grounding line may have retreated to the stoss side of the basal high point (Henry et al. 2022). Following this, GIA emergent ice rise formation and grounding of the lee side would represent progression to the present-day flow regime.

A recent date of grounding at KIR raises the possibility that the bed might not yet be frozen.

Mulvaney et al. (2021) report measurements of cold beds from three sites in the southern Weddell sea embayment, of $-11.6°C$, $-18°C$ and $-14.9°C$ at Berkner Island, Fletcher Promontory and Skytrain ice rise, respectively. However, Berkner Island is known to be long-term stable and has maintained a flow regime separate from that of the ice shelf during the last glacial cycle (Matsuoka et al. 2015). Fletcher Promontory and Skytrain ice rise are promontory-type ice rises connected to the main ice sheet, which are less likely to have ungrounded after the LGM than KIR or HIR.

Observations of the basal properties of KIR may therefore provide additional constraint on the timing and nature of this flow reconfiguration. Inferences about the material underlying the bed, its temperature and degree of freezing, may help to constrain the date of grounding at this location and inform our understanding of the ice rise's history to the present day; this in turn will add to our understanding of the wider Weddell Sea embayment's history.

1.6 Data

In the austral summer season of 2014/15, seismic surveys were carried out at KIR to investigate the location as a potential drill site. Data were acquired along a line parallel to the ice divide (the boundary separating opposing flow directions). Here, I give an overview of the dataset used for the work described in this thesis.

Prior to the AVA experiments, a 4km long seismic reflection profile was acquired along the divide to investigate bed topography. Figure 1.11 shows this reflection profile, courtesy of Alex Brisbourne, who processed the data. The bed is planar and homogeneous along the divide axis.

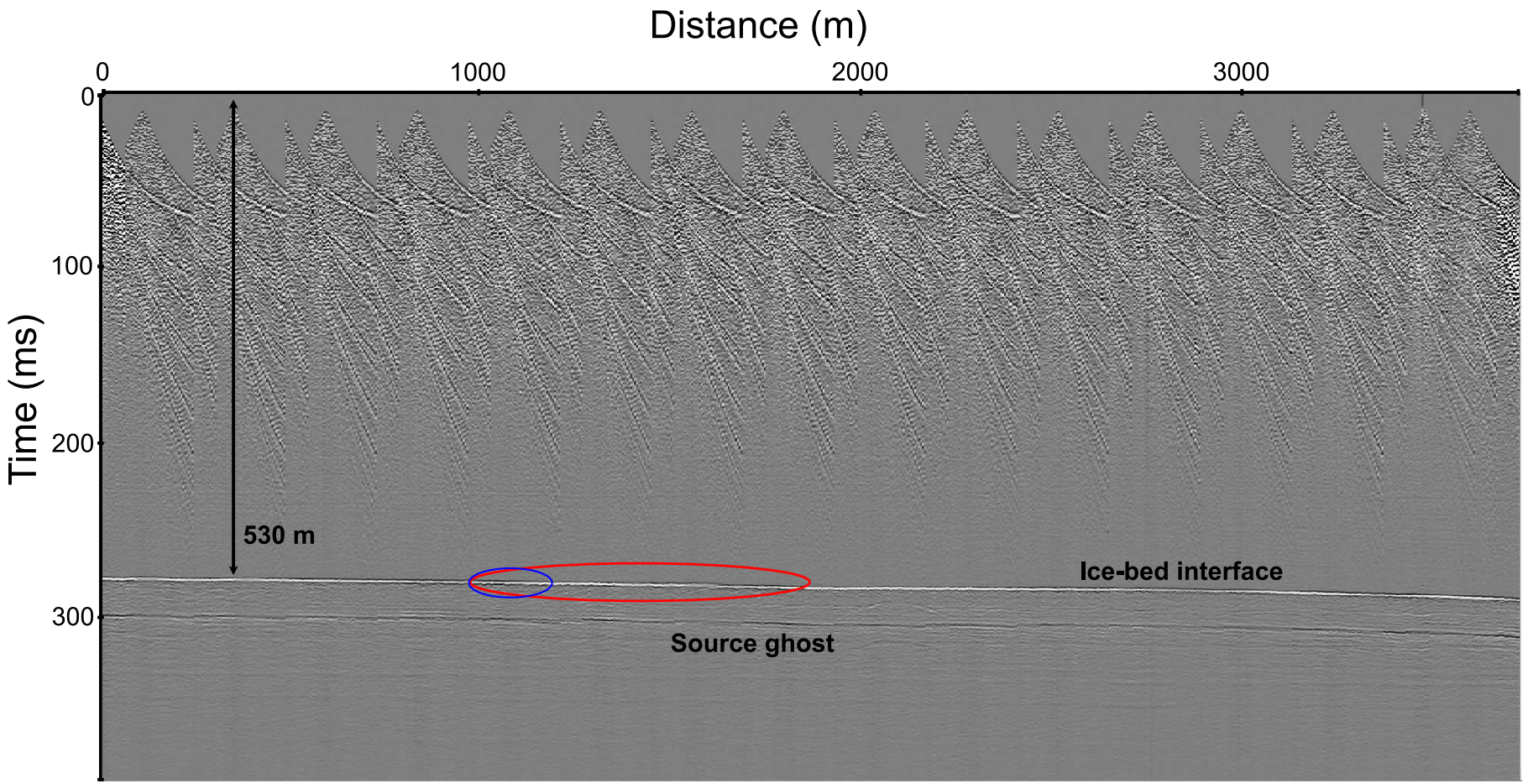

Figure 1.11: Reflection profile acquired along the divide axis. Data processed by and displayed courtesy of Alex Brisbourne. Approximate location of PP reflection points are marked by the blue ellipse and approximate location of PS reflection points is marked by the red ellipse (see Chapter 4 for more detailed analysis).

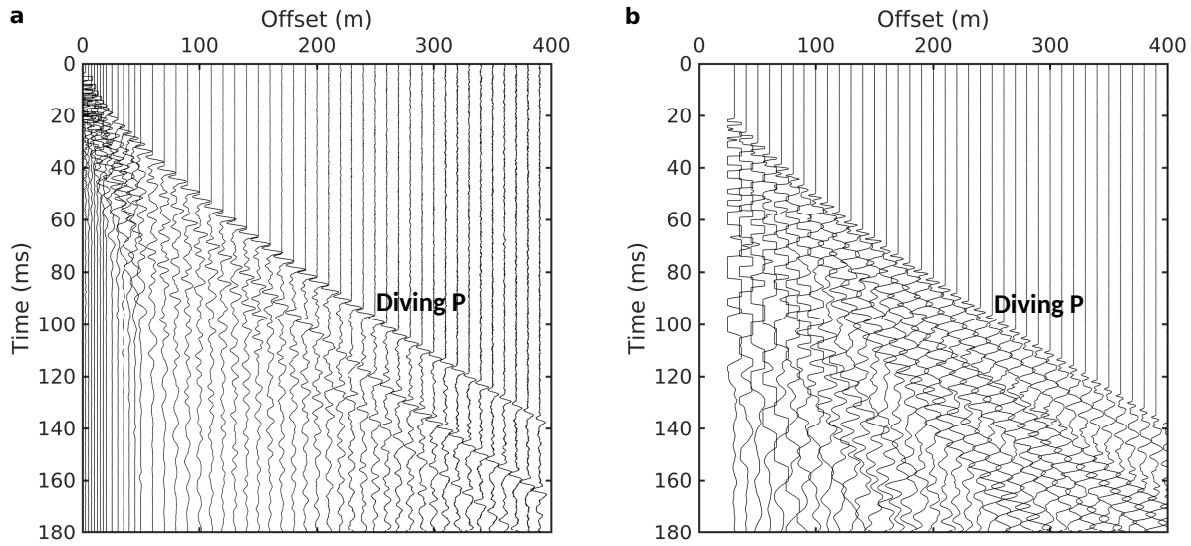

Figure 1.12: a) Diving wave first breaks from the expanding spread refraction experiment (Acquisition A1), used to constrain v and Q near the surface. Source: seismic detonator at surface. b) First 400 m of diving wave first breaks from Acquisiton A2 used for the layer stripping computation. Source: 150 g Pentolite at surface. Traces are normalised in both a) and b).

1.6.1 Surface-source data (Acquisitons A1 and A2)

To constrain seismic velocity and Q in the uppermost firn, a line of vertically-oriented georods (Voigt et al. 2013) was deployed with offset intervals progressively increased: 2.5 m between offsets of 2.5 m and 20 m, 5 m to 50 m and 10 m thereafter to a maximum offset of 390 m. A seismic detonator was used as the source. I call this Acquisition A1; data are shown in Figure 1.12a.

To constrain Q deeper in the firn, I use data from a second acquisition, which I call A2: a line of vertically oriented georods, deployed at 10 m offset intervals between 30 m and 980 m. A 150 g Pentolite source was used, and 2 s of data were recorded with a 16 kHz sampling rate (data are shown in Figure 1.12b). These measurements are described in Chapter 2.

1.6.2 Buried source data (Acquisitions B and C)

In addition to the layouts with the source at the surface, data were acquired from a line of vertically oriented georods at 10 m intervals, installed between 30 m and 1940 m offset, with a 150 g Pentolite source buried in a 20 m deep borehole. These data were recorded with an 8 kHz sampling rate. I call this Acquisition B, and use these data to measure Q using the primary, multiple, source ghost and critical refraction, described in Chapter 2. I also use data

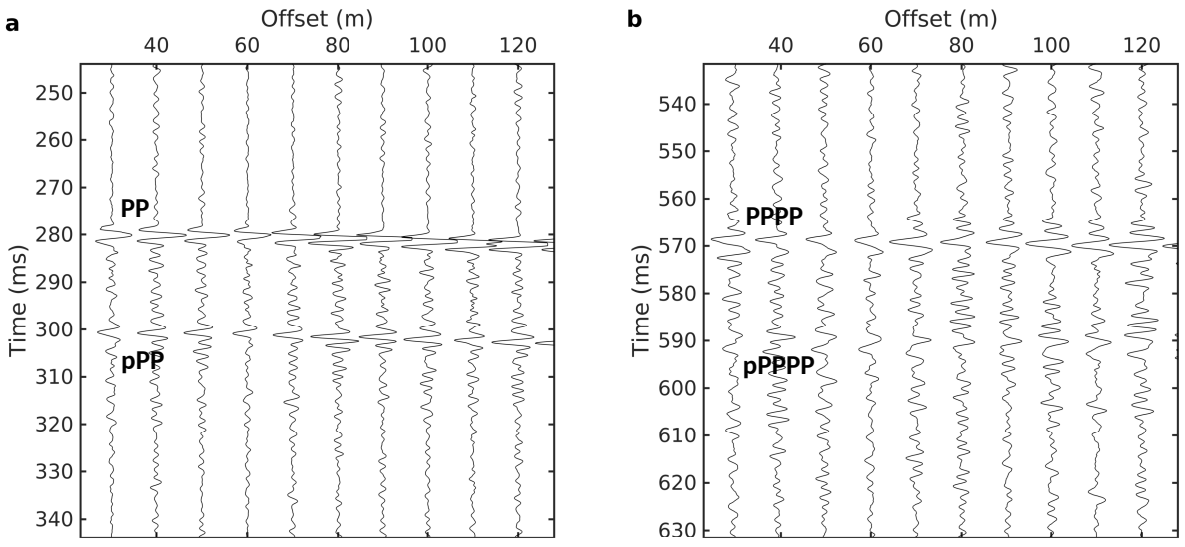

Figure 1.13: Normal incidence traces from buried source data, acquired in Acquisition B. a) The primary reflection (PP) and its source ghost reflection (pPP) are used to measure Q above the source. b) The primary and first multiple (PPPP) are used to measure Q from surface to bed. The source ghost (pPPPP) is also present.

recorded from acquisition B for the P wave AVA measurements described in Chapter 4. Four separate shots were recorded, which are combined into the supergather shown in Figure 1.15, with more detailed views of the normal-incidence primary, multiple and ghost wavelets used for the attenuation measurements shown in Figure 1.13.

To record shear and converted waves, data were recorded in a third acquisition, which I call Acquisiton C. While in a homogeneous, isotropic medium an explosive source produces only compressional waves, in a layered medium such as firn, shear waves are produced by mode conversions close to the source. To produce these mode conversions, which were needed for measurements of crystal orientation fabric (Brisbourne et al. 2019), a 600 g Pentolite source was used, buried at 20 m depth. Georods were installed at 10 m intervals, between 30 m and 1940 m offset, alternating between radial and transverse orientations. Data were recorded with an 8 kHz sampling rate. Again, four separate shots were recorded and combined into a supergather. The radial and transverse components of these data are shown separately in Figures 1.16 and 1.14, respectively. For the converted-wave AVA measurements (Chapter 4, I use only the radial component; I show the transverse component here for completeness.

A summary of Acquisitions A1, A2, B and C is given in Table 1.2.

Acquisition name	Source	Sample rate (kHz)	Receiver spread	Measurement
A1	Seismic detonator at surface	16	Spread from 2.5 m - 390 m; progressively increasing georod intervals: 2.5 m between 2.5 m and 20 m, 5 m between 20 and 50 m, and 10 m between 50 m and 390 m.	Q and v in uppermost firn
A2	150 g Pentolite at surface	16	Offsets from 30 m - 710 m, 10 m georod interval	Q in deep firn
B	150 g Pentolite buried at 20 m depth	8	Offsets from 30 m - 1940 m, 10 m georod interval, vertically oriented	Q from reflections, R_{PP}
C	600 g Pentolite buried at 20 m depth	8	Offsets from 30 m - 1940 m, 10 m georod interval, alternating radial and transversely oriented	R_{PS}

Table 1.2: Summary of acquisition geometries A1, A2, B and C, and the measurements for which each acquisition was used

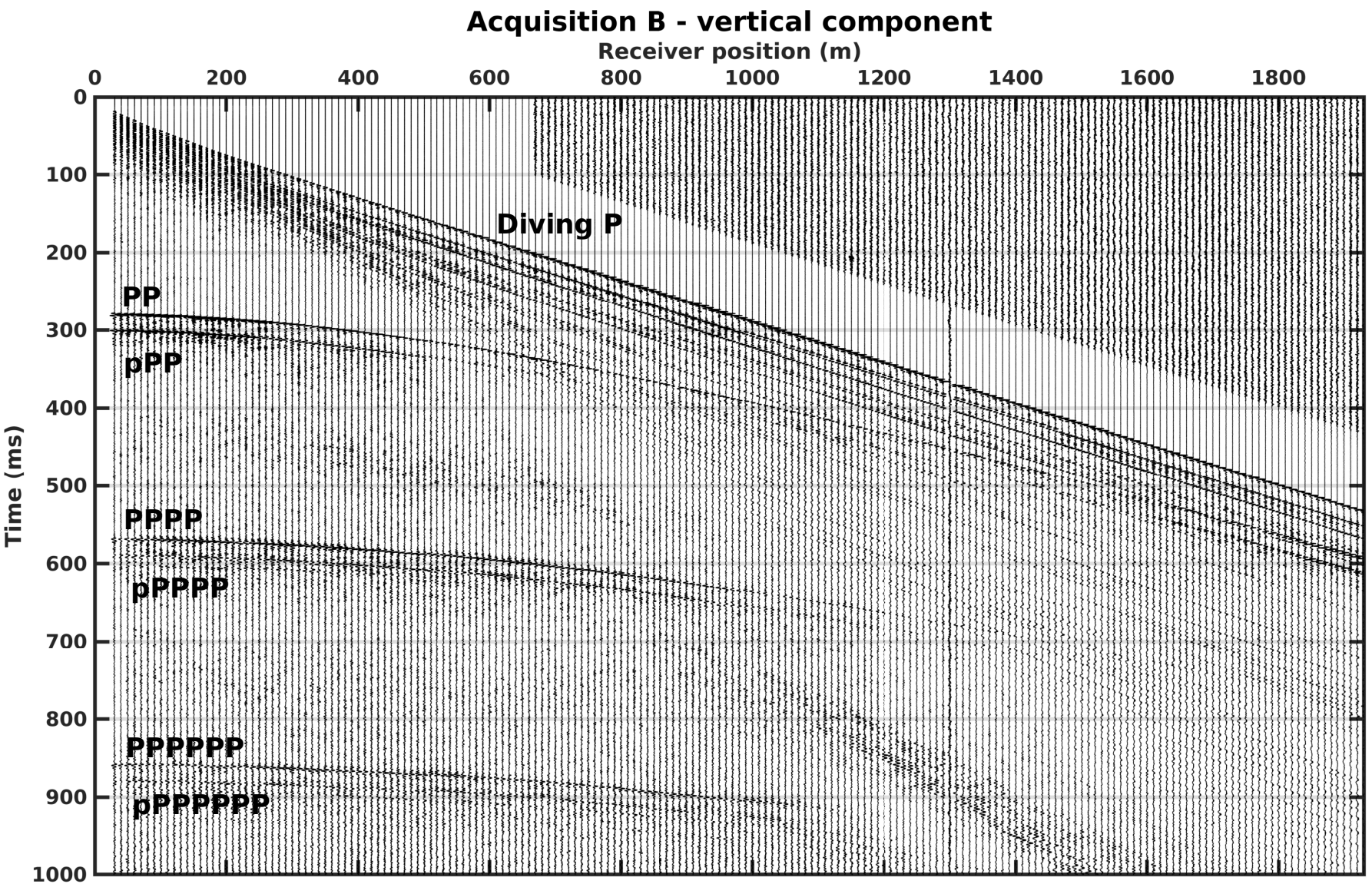

Figure 1.14: Data recorded in acquisition B, shown with an automatic gain control (window length: 200 ms) applied, for visual purposes only. Clearly visible are the diving wave first breaks, primary (PP), first multiple (PPPP) and second multiple bed reflections (PPPPPP), and their source ghosts (pPP, pPPPP, pPPPPPP).

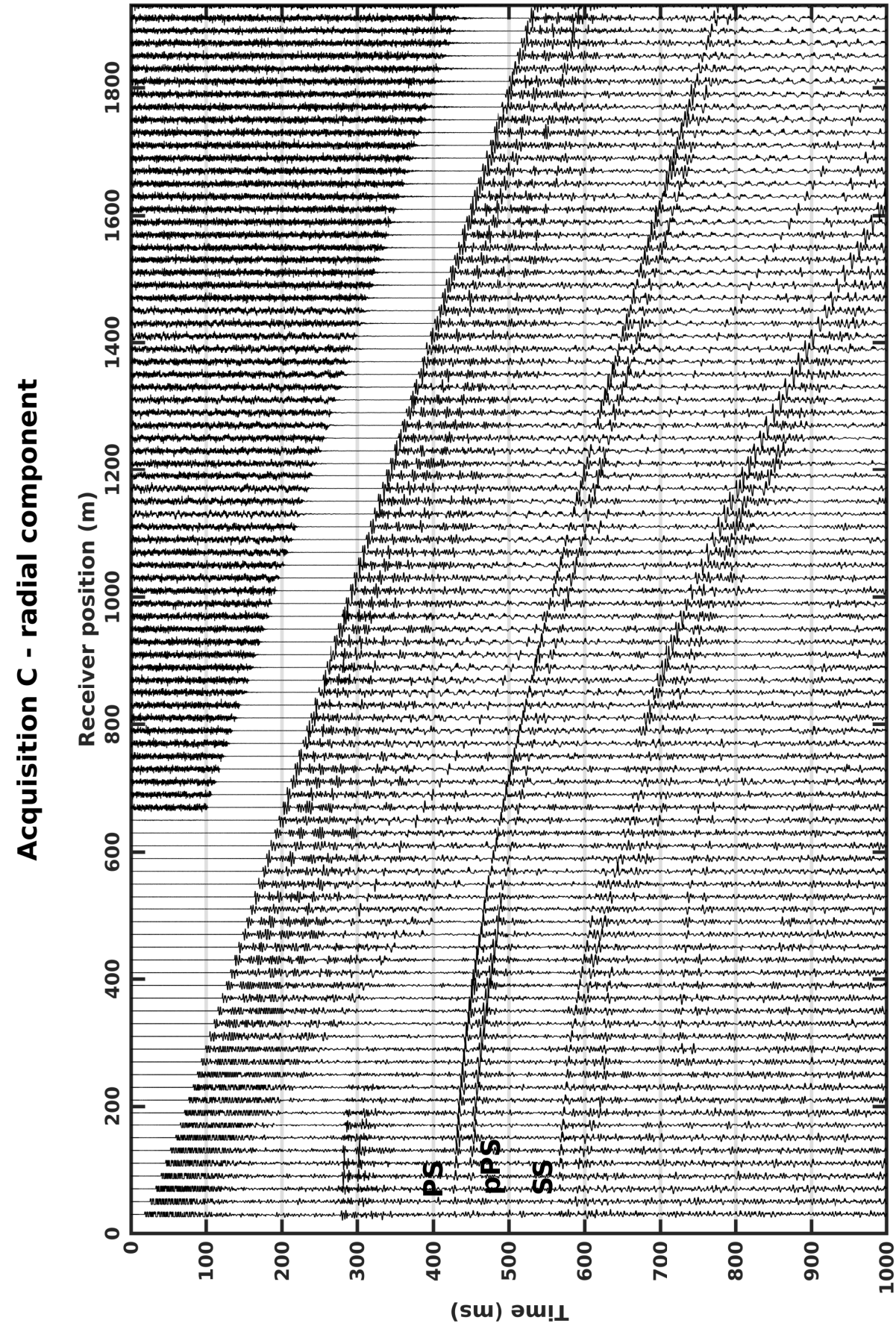

Figure 1.15: Radial component data recorded in acquisition C, shown with an automatic gain control (window length: 200 ms) applied, for visual purposes only. Labelled are the converted (PS) and shear wave (SS) reflections. These data were used for joint inversion as described in Chapter 4.

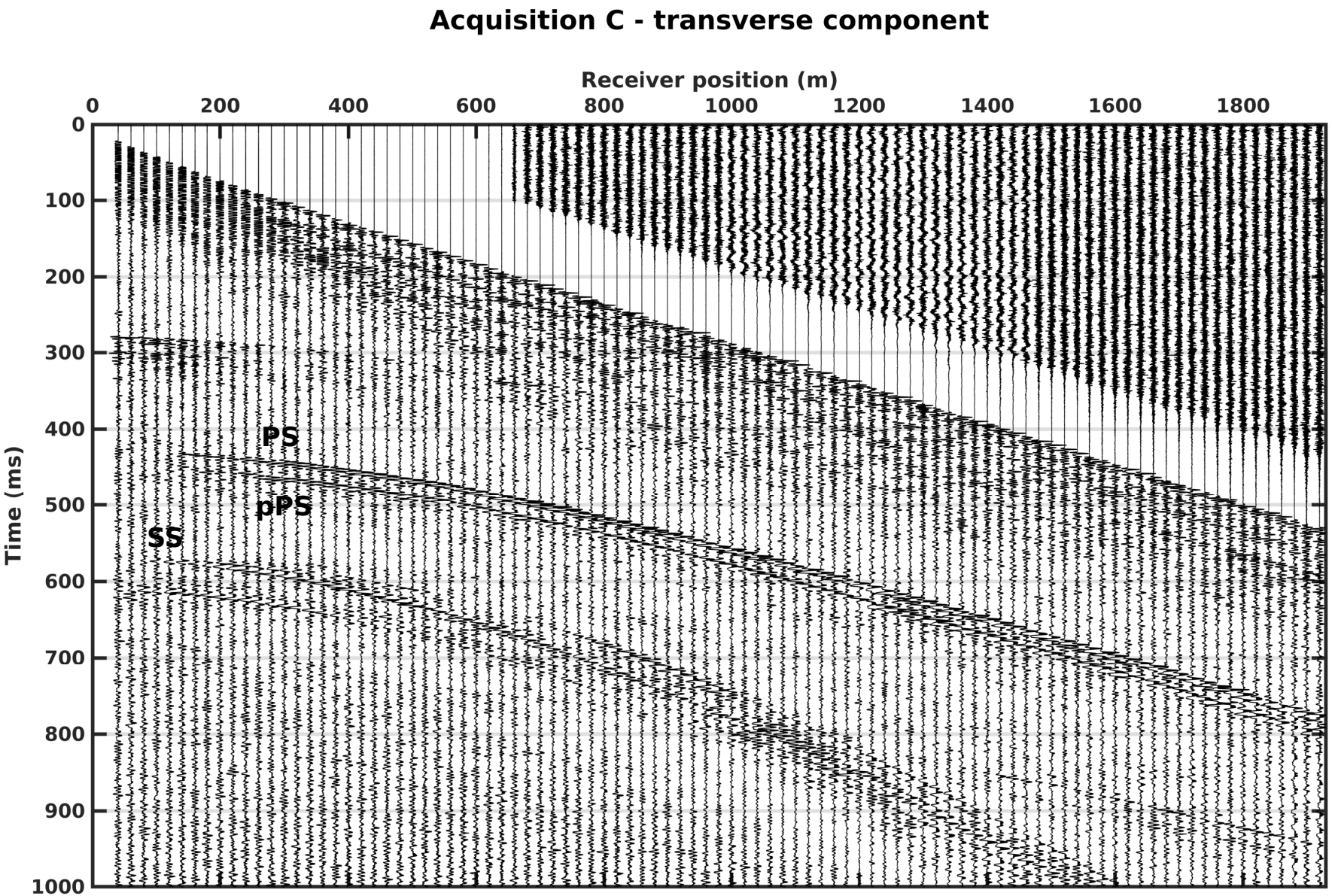

Figure 1.16: Data recorded in acqusition C, shown with an automatic gain control (window length: 200 ms) applied, for visual purposes only. Converted (PS) and shear wave (SS) reflections are labelled. These data were not used but are shown here for completeness.

1.7 Road map of thesis

This thesis has two main aims, which are methodological and glaciological.

Firstly, I aim to explore how glaciological AVA inversions can be improved, a) by using advanced methods of attenuation correction (Chapter 2) and b) by the inclusion of PS and SS wave amplitudes in AVA inversion (Chapters 3 and 4). I will develop these methods, assess their feasibility for use in glaciology, and evaluate their effectiveness when compared with existing methods of glaciological seismic analysis.

The second aim of this project is to provide constraint on the dynamics of the Weddell Sea sector in West Antarctica. This will be achieved through application of the improved methods of analysis to data from Korff ice rise. The main question I aim to answer is whether the bed at KIR is frozen. This will help inform our picture of the West Antarctic Ice Sheet's response to climate change over the Holocene.

Chapter 2 describes a novel method of measuring seismic attenuation in firn and comprises material published in the *Journal of Glaciology* (Agnew et al. 2023). This method is motivated by the requirement to better constrain attenuation in order to correct seismic reflection amplitudes prior to AVA analysis.

Chapter 3 details the inversion scheme I use for converted-wave AVA analysis and describes synthetic experiments aimed at investigating the potential improvement of joint PP/PS and PP/PS/SS inversion over conventional P wave analysis.

Chapter 4 is concerned with the application of the PP/PS joint inversion method described in Chapter 3 to data from KIR. I describe the processing of the AVA data and interpretation of the results, as well as discussing interpretive difficulties and geophysical implications of the converted wave analysis.

In Chapter 5 I expand on the geophysical interpretation of the results obtained in Chapter 4 and make glaciological interpretations, placing them in the context of the broader Weddell Sea sector using approaches from rock physics and synthetic temperature modelling. I then synthesise the findings of the previous chapters, discussing the geophysical experiments and recommending best practice for future acquisitions. Finally, I discuss future work necessary to improve our understanding of the geophysical techniques and the glacial history of the Weddell

Sea sector.

1.7.1 Aims and objectives

The main questions I aim to answer in each of the chapters are laid out here.

Chapter 2 (Seismic attenuation in firn):

1. How does seismic attenuation vary with depth in firn?
2. How can uncertainties in attenuation measurement be accurately modelled?
3. Can advanced attenuation analyses improve AVA analysis?

Chapter 3 (AVA method and synthetic experiments):

1. To what extent do PS and SS wave AVA analysis improve constraint of subglacial material properties when compared with conventional PP wave AVA?
2. Can interpretations of subglacial properties be made less ambiguous with joint inversion?
3. What sort of acquisition will deliver maximum value from a field campaign?

Chapter 4 (Bed conditions at Korff ice rise):

1. What are the bed conditions at KIR?
2. Does joint inversion improve constraint of bed properties at this site when compared with PP inversion?
3. How can analysis of converted waves improve our interpretation of this dataset?

Chapter 5 (Synthesis):

1. Can observations of basal properties at KIR constrain estimates of its age?
2. What are the possible glaciological explanations for the observed bed properties? What can this tell us about the Weddell Sea sector's recent history?
3. How should an acquisition be planned for joint inversion?
4. What are the implications of these experiments for glaciological studies of seismic reflection amplitudes?

Chapter 2

Measuring seismic attenuation in polar firn

In this chapter, I present a method of measuring the seismic quality factor, Q, in polar firn. I present seismic measurements of the firn column at Korff Ice Rise, West Antarctica, including measurements of compressional-wave velocity and attenuation. I describe a modified spectral-ratio method of measuring the seismic quality factor (Q) based on analysis of diving waves, which, combined with a stochastic method of error propagation, enables a more detailed characterisation of the attenuative structure of firn than has previously been possible. Q increases from 56 ± 23 in the uppermost firn to 570 ± 450 between 55 and 77 m depth. I corroborate the method with consistent measurements obtained via primary reflection, multiple, source ghost, and critically refracted waves. Using the primary reflection and its ghost, I find $Q = 53 \pm 20$ in the uppermost 20 m of firn. From the critical refraction, I find $Q = 640 \pm 400$ at 90 m depth. The method aids the understanding of the seismic structure of firn and benefits characterisation of deeper glaciological targets, providing an alternative means of correcting seismic reflection amplitudes in cases where conventional methods of Q correction may be impossible.

This chapter comprises work included in the publication:

Agnew, R. S., Clark, R. A., Booth, A. D., Brisbourne, A. M., and Smith, A. M. (2023). "Measuring seismic attenuation in polar firn: method and application to Korff Ice Rise, West Antarctica". In: *Journal of Glaciology*, FirstView, pp. 1–12. doi: 10.1017/jog.2023.82.

2.1 Introduction

Investigating the structure of polar firn is important for understanding the response of glaciers and ice sheets to a warming climate. Modelling firn density is necessary for calculating ice sheet mass balance from altimetry measurements (e.g. Alley et al. 2007; Wingham 2000). The mechanical properties of firn are key to understanding processes of crevasse formation (e.g. Rist et al. 1996), and potentially have implications for ice shelf rifting and hydrofracture (e.g. Hubbard et al. 2016; Kuipers Munneke et al. 2014; Kulessa et al. 2019).

Interpreting these physical properties from a seismic dataset requires wavelet velocities and amplitudes to be considered. Methods of measuring seismic velocity are well-developed: seismic velocity can be used as a proxy for density (Kohnen 1972)) and can be used to estimate the thickness of the firn column (e.g. Hollmann et al. 2021)). Combined estimates of compressional (P) and shear (S) wave velocities can also be used to evaluate mechanical properties such as Poisson's ratio (King and Jarvis 2007) and elastic moduli (Schlegel et al. 2019). In contrast, tools for quantifying attenuation, derived from amplitude losses, are less well developed. Attenuation is caused by both intrinsic mechanisms (elastic wave energy conversion) and apparent mechanisms (e.g., tuning and scattering); their combined effect is measured using the dimensionless seismic quality factor, or Q (O'Doherty and Anstey 1971; Schoenberger and Levin 1974).

Measuring Q is desirable for two main reasons. The first is that correcting for attenuation through firn is an essential part of many glaciological measurements of seismic amplitude. These include amplitude-versus-offset measurements, which are important for identifying glacial substrates (e.g. Booth et al. 2012; Horgan et al. 2021; Peters et al. 2007; Peters et al. 2008), as well as normal-incidence methods (e.g. Muto et al. 2019b; A. M. Smith 1997a). However, current methods of measuring attenuation do not take into account the complex attenuative structure of firn, and often rely on the presence of multiple reflections, which are not always present with a sufficient signal-to-noise ratio (e.g. Dow et al. 2013; Muto et al. 2019b).

Second, because Q is influenced by the physical properties of the propagating medium, measuring it has the potential to give further insight into the physical structure of firn. For example, the relationship between the compressional- and shear-wave quality factors and velocities in sands has been observed to be influenced by fluid saturation (Prasad and Meissner 1992), so measuring Q in firn may have implications for characterising firn hydrology. Recent obser-

Table 2.1: Summary of the survey layout used for each of the velocity and attenuation measurements.

Measurement	Depth (m)	Acquisition	Offset range used
Velocity	0 - 90	A1	0 - 390 m
Q in uppermost firn from direct waves (Q_{1d})	0 - 12	A1	Reference trace at 17.5 m offset; Comparison traces at 30, 35 and 40 m offset.
Q in firn from layer stripping (Q_{2-4})	27 - 77	A2	110 m - 710 m
Q in uppermost firn from source ghost Q_{1pg}, Q_{1mg}	0 - 20	B	30 m - 140 m (normal incidence traces).
Surface-to-bed Q from primary and multiple (Q_{tot})	0 - 530	B	40 m - 140 m (normal incidence traces).
Q at base of firn from critical refraction (Q_{crit})	90	B	990 m - 1460 m

vations of complex firn structure (Hollmann et al. 2021) and large ice lenses within the firn column (Hubbard et al. 2016) highlight the need for continued in-situ characterisation of firn and improvement of existing methods.

While the continuous increase in seismic velocity with depth enables the velocity-depth structure to be measured in detail by relatively simple methods such as Wiechert-Herglotz inversion (Herglotz 1907; Slichter 1932; Wiechert 1910), constraining the attenuation structure is less straightforward, due to the lack of convenient collinear raypaths. In this paper, we present a novel process of measuring the depth-dependence of Q in the firn from diving waves (downgoing direct waves continuously refracted back towards the surface). We apply the process to data from Korff Ice Rise, West Antarctica, providing a more complete description of the firn's attenuative structure than has previously been possible. We complement these results with measurements made using primary and multiple reflections, their source ghosts, and direct waves, to validate the firn Q model and obtain a complete Q vs depth model for the entire glacier.

2.2 Methods

The fundamental method we use is the spectral ratio method (Section 3.1), which we apply in different ways to measure Q in various portions of the ice column. The process we present to measure Q vs depth in the firn is layer stripping (Section 3.3). Layer stripping requires Q at the surface, Q_1, to be constrained independently, so we measure this using direct waves (Section

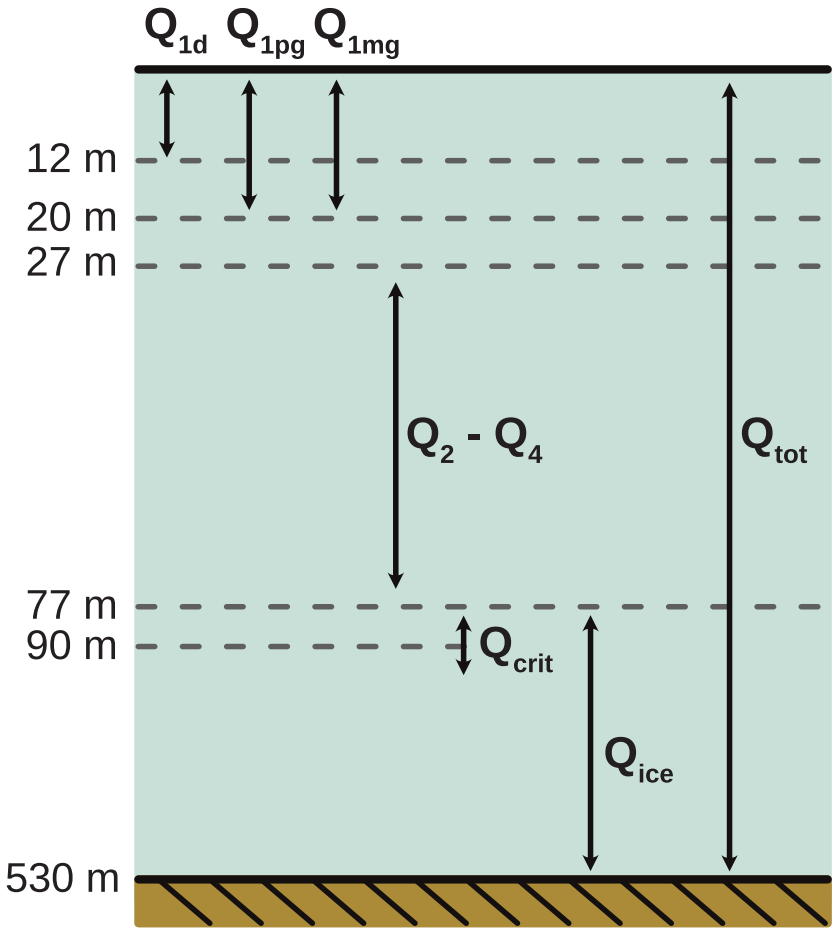

Figure 2.1: Schematic of measurements made and their depths. Note that depths are not to scale.

3.4.1), calling the result Q_{1d}. By initialising the layer stripping process with Q_{1d}, we obtain a full Q profile of the firn.

The other measurements we present corroborate our firn Q results. We measure Q from the surface to the bed, Q_{tot}, using the primary reflection and first multiple (Section 3.2). By combining Q_{tot} with our firn Q profile, we obtain Q in the section between the base of the firn and the bed, Q_{ice}. We compare this to a measurement made in the uppermost solid ice from critically refracted waves, Q_{crit} (Section 3.5). Additionally, we independently measure Q in the upper firn from the source ghosts of primary and first multiple phases, giving the results Q_{1pg} and Q_{1mg} (Section 3.4.2). We compare these to the direct wave result, Q_{1d}.

A summary of each measurement, its depth, acquisition type and offset range is given in Table 2.1; Figure 2.1 shows a schematic of the measurements and their depths.

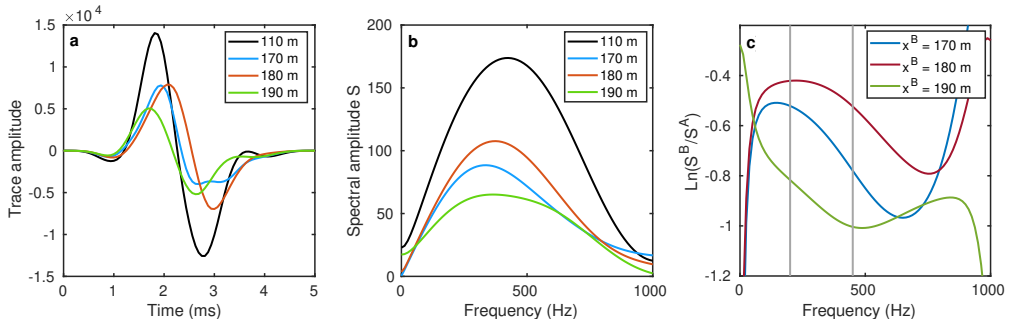

Figure 2.2: a) Wavelets, and b) spectra of diving waves used for the calculation of Q in the second layer of the firn, Q_2. Legends a) and b) indicate the source-receiver offsets of the traces and spectra. The trace at 110 m offset (black) is used as the reference trace, with spectrum S^A. c) Logarithmic spectral ratios used for the calculation. The comparison trace has spectrum S^B and source-receiver offset x^B. The spectral ratios are considered to be sufficiently linear within the chosen bandwidth of $200 - 450$ Hz, indicated by the grey vertical lines.

2.2.1 Spectral ratio method

Seismic attenuation is routinely measured using the spectral ratio method (Båth 1974; Teng 1968). The amplitude spectrum $S(f, r)$ of a seismic wavelet of frequency f which has propagated a distance r with no transmission or reflection at interfaces is given by:

$$S(f, r) = S_0(f)G(r)e^{-a(f)r} \tag{2.1}$$

where $S_0(f)$ is the initial spectrum, $G(r)$ describes geometric spreading and a is the attenuation rate, related to Q by $a = \pi f/Qv$ at frequency f and velocity v. The spectral ratio method compares the spectrum $S^A(f)$ of a reference wavelet A to that of a second wavelet B, $S^B(f)$, which travels for an additional time δt. The logarithmic ratio of the spectra is

$$\ln \frac{S^B(f)}{S^A(f)} = \frac{-\pi \delta t}{Q} f + \text{constant} \tag{2.2}$$

Linear regression of the spectral ratio's logarithm against frequency allows a measurement of Q to be made from the slope m:

$$m = -\pi \frac{\delta t}{Q} \tag{2.3}$$

Figure 2.2 shows examples of wavelets, their spectra and associated logarithmic spectral ratios used for a calculation of Q in the firn (Section 3.3.1). In all spectral ratio measurements, a

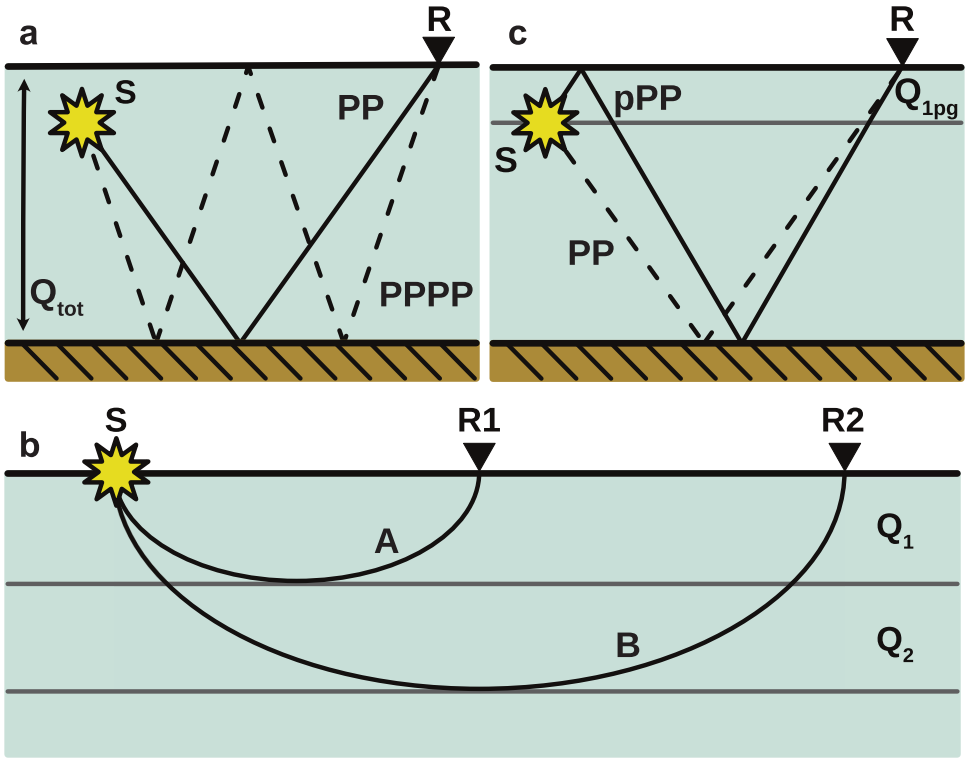

Figure 2.3: a) The primary reflection (solid, PP) and first multiple (dashed, PPPP) are used to measure effective Q across the glacier's entire depth, Q_{tot}. b) Diving waves travelling between source S and receivers R1, R2. We define layers of constant Q and take the bottoming depth of the rays to be the layer boundaries. c) The spectral ratio of the primary reflection (dotted, PP) and source ghost (solid, pPP) can be used to calculate Q in the uppermost layer, above a buried source. Note that this is schematic, and a) and c) do not show refraction of ray paths due to the firn's velocity gradient.

bandwidth must be chosen over which the spectral ratios are considered sufficiently linear; m is the curve's gradient within this bandwidth.

We use the common assumption that Q is independent of frequency (Kjartansson 1979). We assume a low-loss formulation and definition of Q (e.g. O'Connell and Budiansky 1978; Toverud and Ursin 2005) and a non-dispersive velocity (Kjartansson 1979; Liner 2012); we also assume that Q is isotropic.

Appendix A.2 contains examples of traces, spectra and spectral ratios used for each application of the spectral ratio method.

2.2.2 Surface-to-bed Q measurement (Q_{tot})

A common process for measuring Q to correct for attenuation in seismic reflection studies is to use the spectral ratio of the primary reflection and its multiples (e.g. Booth et al. 2012) with Equation 3. This gives the effective Q from surface to bed, Q_{tot}, which includes the firn and its

underlying ice (Figure 2.3a). We select non-clipped normal incidence traces from Acquisition B for our measurement (Figure 1.13), taking incidence angles $< 10^{\circ}$ as normal (A. M. Smith 2007). These wavelets and their spectra are shown in detail in Appendix A.2.

2.2.3 Deriving Q in the firn

The spectral ratio method usually measures the difference in frequency content of a propagating wavelet at different locations on an otherwise collinear path. We use a modified process which takes advantage of the firn's continuous velocity gradient and the resulting diving wave paths (e.g. Alsuleiman 2018; Crane et al. 2018; Hepburn 2016). We use Wiechert-Herglotz inversion to obtain a velocity model (WHI: Herglotz 1907; Slichter 1932; Wiechert 1910); WHI has been widely described for application to firn (e.g. Hollmann et al. 2021; Horgan et al. 2011; Jarvis and King 1993; King and Jarvis 2007; Kirchner and C. R. Bentley 1990; Schlegel et al. 2019).

Layer stripping

For the purposes of this method, we represent the firn column as a sequence of layers of uniform Q; the stated quality factor for an individual quasi-layer describes the aggregated effect of attenuation over a defined vertical interval. Layer stripping is an established technique in seismic tomography and attenuation analysis (e.g. Quan and Harris 1997; Yilmaz 2001), and it is the process by which we calculate the quality factor of an individual quasi-layer in the firn. This combines spectral ratio measurements of wavelets passing through that layer with an evaluation of the cumulative attenuation through all overlying layers.

Figure 2.3b shows two diving waves A and B arriving at receivers R1 and R2, having passed through different portions of the firn column. We trace these rays to find their depths of maximum penetration, and interpret layers of uniform Q between these depths, discretising what we assume to be a gradual change in attenuative properties with depth as the firn compacts. The attenuated time t^*, defined as $t^* = t/Q$, is cumulative along each ray (Carpenter et al. 1966); i.e. for a ray which travels through n layers:

$$t^*_{\text{ray}} = \sum_{i=1}^{n} t^*_i = \sum_{i=1}^{n} \frac{t_i}{Q_i} \tag{2.4}$$

where t_i is the time a ray spends in layer i, and Q_i is the quality factor in that layer. A wavelet's

attenuated time is not measured directly; however, the difference in t^* between two wavelets, δt^*, can be measured from their spectral ratio gradient $m = -\pi\delta t^*$. Ray-tracing is used to determine the time each ray spends in each layer; combined with the measured spectral ratio gradients, this is used to calculate Q in each successive layer. Q_n in layer n is calculated using the spectral ratio gradient of two rays A and B, which penetrate to the bottom of layers $n-1$ and n, respectively:

$$Q_n = t_n^B \left[\frac{-m^{B,A}}{\pi} + \sum_{i=1}^{n-1} \frac{t_i^A - t_i^B}{Q_i} \right]^{-1} \tag{2.5}$$

Here, the superscripts denote the ray and the subscripts denote the layer; i.e., Q_n is the quality factor in layer n, t_i^A is the time ray A spends in layer i, and $m^{B,A}$ is the gradient of the spectral ratio $S^B(f)/S^A(f)$. A derivation of this equation is given in Appendix A.1.

It is apparent from Equation 5 that the calculation of Q in each successive layer depends on the calculation of Q in all of the shallower layers. This process requires Q in the uppermost layer to be known before the others can be calculated; we measure this using near-offset direct waves (Section 3.4.1).

In principle, an attenuation-depth profile as smooth as the velocity-depth profile could be constructed using each successive offset pair; however, in practice, a vertical interval must be thick and/or attenuative enough that its Q contribution is detectable above noise. To obtain more robust results, we use clusters of 3 adjacent traces which, taken together, define the layer boundaries (Figure 2.3b), calculating and averaging nine $1/Q_i$ results for each layer. Figure 2.2 shows examples of traces, spectra and spectral ratios for the calculation of Q in the second layer. We choose traces and bandwidths based on inspection of individual spectra, avoiding traces with notched or unstable spectra.

We construct a 4-layer Q_p model based on available stable spectra with sufficiently large offset differences for a reliable measurement to be made, using data from the line of georods offset at 10 m intervals with a 150 g Pentolite source at the surface (Acquisition A2).

Stochastic error analysis

We estimate uncertainties in velocities by applying Gaussian perturbations to wavelet travel times before Wiechert-Herglotz inversion, repeating the process to obtain distributions of veloc-

ities as a function of depth. We then calculate the mean and standard deviation of the output distributions to obtain velocity-depth curves.

To estimate the propagation of errors through the layer stripping process, we implement a stochastic framework of error analysis. After Q_i is calculated for layer i, a Gaussian perturbation is applied to $1/Q_i$ consistent with the uncertainty on the spectral ratio slope, and this perturbed Q_i is used to calculate the Q_{i+1} of the next layer. We repeat this process 1,000 times to obtain a large number of credible models to analyse statistically. In order to ensure that each generated $Q(z)$ model is physically plausible, we assume two conditions, and accept only models which satisfy these. We require that Q increases with depth (i.e., $Q_{i+1} > Q_i$), and that $Q > 0$ always. We assume that the uncertainty is dominated by the spectral ratios, and that the uncertainty from the travel-time measurement is comparatively small. While these assumptions do not allow all theoretically possible results, we consider them necessary in order to obtain a large enough number of usable models from which statistics can be robustly calculated, given our computational constraints. All statistics are computed from distributions of the quantity $\rho = 1/Q$, and results and uncertainties are quoted as the mean and standard deviation of the output distributions. The uncertainty in Q is then derived from $\epsilon_Q = \epsilon_\rho/\rho^2$, where ϵ_Q is the error in Q and ϵ_ρ is the error in ρ (Topping, 1972).

2.2.4 Constraining near-surface Q

$Q(z)$ profiles output from layer stripping reveal relative variations, but evaluating absolute values requires Q in the shallowest layer, Q_1, to be constrained. We initialise our layer stripping process with a measurement of Q_1 from direct waves, which we call $Q_{1\mathrm{d}}$, and use measurements from primary and multiple source ghosts ($Q_{1\mathrm{pg}}$ an d$Q_{1\mathrm{mg}}$) to support this result.

Direct wave measurement, $Q_{1\mathrm{d}}$

This measurement allows Q_1 to be found without a buried source being necessary. Approximating near-offset diving waves as direct waves, we calculate $Q_{1\mathrm{d}}$ using their spectral ratios. The layer thickness d is the maximum thickness of the ray's first Fresnel volume, given by

$$d(x) = \sqrt{3\lambda x}/4, \tag{2.6}$$

where λ is the wavelength and x the source-receiver offset of the further offset ray in the pair (Gusmeroli et al. 2010; Spetzler and Snieder 2004). For the direct wave calculation, we use data acquired with a seismic detonator as source, which for our selected rays gives $Q_{1\mathrm{d}}$ in a layer 12 m thick. We initialise our layer stripping computation with $Q_{1\mathrm{d}}$. For layer stripping, we use the nearest-offset non-clipped traces from Acquisition A1; these rays reach 27 m depth, requiring that we assume $Q_1 = Q_{1\mathrm{d}}$ to 27 m.

Source ghost measurement, $Q_{1\mathrm{pg}}$, $Q_{1\mathrm{mg}}$

These results are used to corroborate the direct wave measurement of $Q_{1\mathrm{d}}$. We acquired data with a buried source (20 m depth, Acquisition B) which generates a discrete source ghost. We use these data to provide an independent measurement of Q in the upper 20 m. Figure 2.3c shows the ray paths of the primary reflection and its source ghost. The spectral ratio gradient for these two wavelets at normal incidence is used with Equation 3 to calculate Q, which we call $Q_{1\mathrm{pg}}$. The traces used to calculate $Q_{1\mathrm{pg}}$ are shown in Figure 1.13a.

Shown in Figure 1.13b are the normal incidence first multiple (PPPP) and its source ghost (pPPPP). Measuring Q using these wavelets also gives Q in the firn above the shot, which we call $Q_{1\mathrm{mg}}$. Ideally, we would expect $Q_{1\mathrm{pg}}$ and $Q_{1\mathrm{mg}}$ to be equal.

2.2.5 Constraining Q in the ice from multiples and critical refractions

Critical refraction, Q_{crit}

To validate the layer stripping approach to calculating Q, we make an independent measurement of Q in the uppermost solid ice, Q_{crit}, using critically refracted waves (Peters, 2009). At this depth, Q_{crit} can be straightforwardly measured using the spectral ratio of two critically refracted arrivals and Equation 3. For this measurement, we use data with a 150 g buried Pentolite shot (Acquisition B). We calculate the thickness of this quasi-layer using Equation 2.6.

Combining Q_{tot} with a firn-Q model

We combine our layer-stripping measurement with our measurement of Q_{tot} to provide an estimate of Q between the base of the firn and the bed, Q_{ice}:

$$Q_{\mathrm{ice}} = t_{\mathrm{ice}} \left[\frac{t_{\mathrm{tot}}}{Q_{\mathrm{tot}}} - \sum^{\mathrm{firn}} \frac{t_i}{Q_i} \right]^{-1}. \tag{2.7}$$

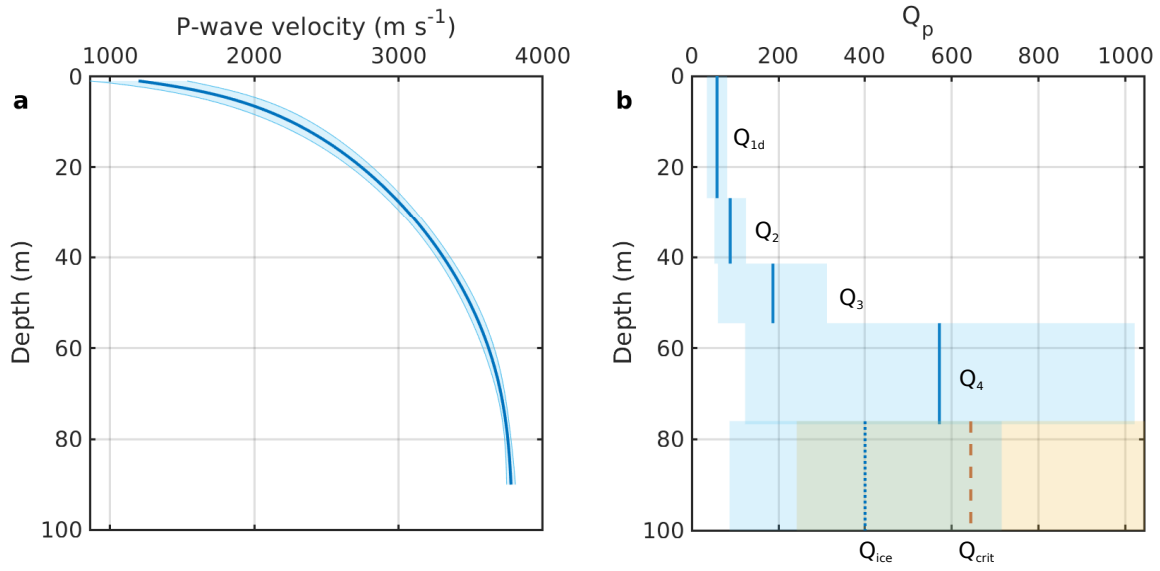

Figure 2.4: a) Results from Wiechert-Herglotz inversion, showing the depth-dependence of seismic velocity. b) $Q(z)$ model. $Q_{1\mathrm{d}}$ is measured from direct waves and assumed constant to 27 m. $Q_2 - Q_4$ result from the layer stripping process. The blue dotted line shows Q_{ice} resulting from combining the Q_{tot} measurement with the layered model $Q_1 - Q_4$. The red dashed line shows Q at the base of the firn, Q_{crit}, measured using the critical refraction. Shaded areas represent uncertainties.

Here, t_{ice} is the travel time of a normal-incidence reflection between the base of the firn and the bed, t_{tot} is the travel time between surface and bed, t_i is the travel time in a layer i of the firn, and Q_i is the quality factor of that layer.

Since the measurement of Q_{ice} is dependent on layer stripping, it is possible to validate the layer stripping process by evaluating the consistency of Q_{crit} and Q_{ice}.

2.3 Results

WHI yields the velocity-depth model shown in Figure 2.4a. The P- wave velocity increases with depth from 1200 ± 340 m/s at 1 m depth to 3779 ± 30 m/s at 90 m depth.

Measured using the primary and first multiple, the surface-to-bed Q is $Q_{\mathrm{tot}} = 250 \pm 100$.

The direct wave measurement of Q_1 gives $Q_{1\mathrm{d}} = 56 \pm 23$ in the uppermost 12 m of firn. From the primary reflection/ghost measurement, we find $Q_{1\mathrm{pg}} = 53 \pm 20$ for the uppermost 20 m, and from the first multiple/ghost, we find $Q_{1\mathrm{mg}} = 53 \pm 24$ for the uppermost 20 m.

The results of our layer stripping computation in combination with stochastic error analysis are shown in Figure 2.4b, which shows Q increasing to 570 ± 450 between 55 and 77 m depth. Table

Table 2.2: Q_p model from the layer stripping process, shown in Figure 2.4b. For the first layer, $0 - 27$ m, we take $Q_1 = Q_{1d}$ from the direct wave measurement.

Layer	Depth (m)	Q
Q_1 (from Q_{1d})	0 - 27	56 ± 23
Q_2	27 - 41	89 ± 36
Q_3	41 - 55	190 ± 130
Q_4	55 - 77	570 ± 450
Q_{ice} from layer stripping/multiple	77 - 530	400 ± 310

Table 2.3: Summary of measurements independent of layer stripping.

Measurement	Depth (m)	Q
Q_{tot} from primary/first multiple	0 - 530	250 ± 100
Surface Q from direct wave, Q_{1d}	0 - 12	56 ± 23
Surface Q from primary source ghost, Q_{1pg}	0 - 20	53 ± 20
Surface Q from first multiple source ghost, Q_{1mg}	0 - 20	53 ± 24
Uppermost solid ice Q from critical refraction, Q_{crit}	90	640 ± 400

2.2 presents the Q model resulting from the layer stripping process.

By measuring Q at the critical refraction, we obtain $Q = 640 \pm 400$ at 90 ± 14 m. This is indicated in Figure 2.4b by the dashed red line and shaded red area.

For a normal incidence reflection, our layered Q model, when combined with Q_{tot}, implies that for the entire ice column at depths greater than 77 m, $Q_{ice} = 400 \pm 310$. This result is dependent on layer stripping and is shown in Figure 2.4b as the deepest layer with a dotted blue line, with errors indicated by the shaded area. Table 2.3 summarises all Q measurements which are independent of layer stripping.

2.4 Discussion

We have shown an effective process of deriving the velocity and attenuation profiles through firn and ice, including a robust evaluation of uncertainties. Comparison of Q results obtained from layer stripping with independent measurements at similar depths shows consistency between methods. Our measurements of $Q_4 = 570 \pm 450$, $Q_{ice} = 400 \pm 310$ and $Q_{crit} = 640 \pm 400$ agree with each other within uncertainties, supporting the use of the layer stripping process.

In the shallow firn, our measurements of $Q_{1d} = 56 \pm 23$, $Q_{1pg} = 53 \pm 20$, and $Q_{1mg} = 53 \pm 24$ agree closely, despite the fact that the direct wave samples the top 12 m (Q_{1d}) and the source ghost samples the top 20 m of firn (Q_{1pg}, Q_{1mg}). This is suggestive of a shallow Q gradient in the upper firn.

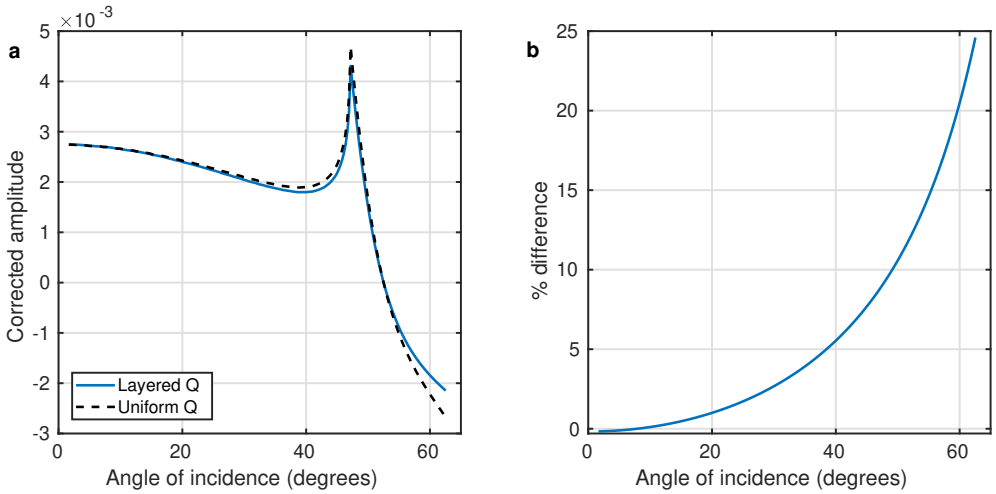

Figure 2.5: a) Bed reflectivities obtained from synthetic amplitude-versus-offset (AVO) data simulating a reflection from an ice-bedrock interface with a Korff-like geometry, correcting for attenutation with a layered Q model (solid blue line), and a uniform-Q assumption (dashed black line). Data are not corrected for synthetic source amplitude and the y-axis is consequently multiplied by a constant. b) Difference between layered-Q-corrected and uniform-Q-corrected AVO curves (%)

A key motivation for measuring Q in the firn is the need to compensate for Q losses when the amplitude of seismic waves is of interest, for example when using amplitude-versus-offset (AVO) analysis to identify a subglacial material (e.g. Booth et al. 2012; Peters et al. 2008). We assess the impact of a layered Q model by considering what difference such a model would make to an AVO measurement versus a model which assumes a uniform Q_{tot} throughout the whole glacier. We produce a synthetic AVO gather of a reflection from 530 m thick ice over bedrock, dominant frequency 200 Hz, which incorporates our detailed firn-Q model and velocity model. We then pick the amplitudes, and recalculate the bed reflection coefficient using a) our detailed Q model including Q_{ice}, and b) the assumption that $Q = 250$ everywhere. We correct the amplitudes for a single frequency, $f = 200$ Hz. Figure 2.5a shows the two corrected reflectivity curves, and Figure 2.5b shows the percentage difference between the layered-Q corrected and uniform-Q corrected curves. The difference is small compared with typical signal-to-noise ratios at angles $< 50°$, rising to $> 10\%$ at angles $> 50°$. Layer stripping could therefore in theory provide a small benefit to AVO surveys which have very high-quality and wide-angle data. However, for typical glaciological AVO experiments layer-stripping will provide minimal benefits if Q can be measured using the primary and first multiple.

There are circumstances in which it would be preferable to choose a layer stripping measurement

over a multiple-based one. First, for seismic experiments studying the firn itself, a measurement of Q in the firn is necessary, as clearly it is not valid to assume that Q at shallow depths is the same as the effective Q that would be measured using multiples. Second, thin layering at the ice-bed interface (Booth et al. 2012) can cause interference effects which change the apparent amplitudes of the primaries and multiples, making a multiple-based measurement inappropriate where a thinly layered bed is suspected. Third, multiples are not always clearly visible in a seismic dataset (e.g. Clyne et al. 2020; Dow et al. 2013; Muto et al. 2019b); in such a case Q would need to be estimated by layer stripping.

Our method has potential for improvement. A more detailed model could be produced if more closely spaced, or even all, traces were used, resulting in a model with very thin layers and providing a truer representation of the continuous nature of firn transformation; however, this would require an extremely good signal-to-noise ratio that was not achieved with our dataset. In principle, layer stripping could be used to measure the shear-wave quality factor; the acquisition would need to be designed with this in mind, with an S-wave source and closely spaced receivers at near offsets. In addition to our P-wave data, we acquired S-wave data using a 600 g Pentolite source; however the size of the source needed to generate S-waves caused a high degree of clipping and contamination with P-waves, rendering a Q-analysis impossible. In future, layer stripping could be combined with measurements relying on englacial reflections (e.g., Peters et al. 2012) in order to build up a more comprehensive englacial Q-profile; this could be supplemented by a dedicated microspread to resolve detail at very shallow depths (e.g. Gusmeroli et al. 2010). For complex firn structures such as those with ice lenses or hoar frost layers, WHI fails to capture the true velocity-depth relationship, and more advanced inversion methods such as full waveform inversion could be used to jointly invert for velocity and attenuation structures (e.g. Pearce et al. 2023a; Pearce et al. 2023b).

2.5 Conclusions

We have demonstrated a novel application of the spectral ratio method for the measurement of the seismic quality factor Q in firn, and applied the method to data from Korff Ice Rise in West Antarctica. We have therefore been able to resolve the compressional-wave attenuative structure of firn in greater detail than has previously been possible. We have combined our layer stripping method with a stochastic method of error propagation. Our results show Q

increasing from 56 ± 23 at the surface to 570 ± 450 between 55 and 77 m depth. We corroborate results from layer stripping with independent measurements using critically refracted waves, the source ghost and primary/multiple reflections. Using the primary reflection and source ghost shows $Q = 53 \pm 20$ in the uppermost 20 m of firn, and using critically refracted waves shows $Q = 640 \pm 400$ at 90 m depth. The layer stripping process can be used for seismic studies of firn or seismic reflection studies where conventional methods of measuring Q are not possible. Our results provide a fuller characterisation of firn's seismic properties than has previously been shown, and our methods will aid future seismic investigations of glaciological targets.

Chapter 3

Joint AVA inversion of PP, PS and SS wave amplitudes: method and synthetic experiments

In this chapter, I explore the potential of joint PP, PS, and SS wave inversion to improve glaciological amplitude-versus-angle (AVA) analysis. I present an inversion scheme which uses a Bayesian Markov chain Monte-Carlo framework to invert seismic amplitudes for the elastic properties of a glacier bed, namely the acoustic impedance Z and Poisson's ratio σ. I test the potential of converted and S wave data to improve glaciological AVA inversions using synthetically generated AVA amplitudes for a variety of bed properties and a range of imagined survey geometries. I find that joint inversion of PP and PS wave amplitudes is preferable to inverting solely from PP amplitudes, with the degree of improvement greatest for bed materials with high Poisson's ratios such as dilatant till. In general, joint inversion using PP and PS waves improves both inversion precision and accuracy, with joint inversion of data limited to incidence angles $< 30^{\circ}$ performing similarly to or better than PP only inversion of wider-angle data (where θ extends to 60°). There are exceptions to these general observations, notably in the case of AVA curves which display polarity reversals at large incidence angles; in this case ensuring that a single inversion captures the diagnostic polarity reversal gives a more accurate result than joint inversion. I extend the inversion scheme to include SS wave information, and find little meaningful improvement upon PP/PS joint inversion. In summary, jointly inverting

PP and PS wave amplitudes offers improved constraint of glacier bed properties in many cases, especially where the maximum offset in a survey is restricted by field conditions and where acquisition of three-component seismic data complements other survey aims.

First, I describe the experimental setup and inversion scheme. I give an example of the inversion output and demonstrate that it retrieves a known input model (Section 3.3). I then explore the extent to which jointly inverting PP and PS AVA data can reduce nonuniqueness, resulting in both improved precision and accuracy when compared with results from inverting PP data only (Section 3.4). I also demonstrate the effectiveness of the inversion scheme in reducing ambiguity when interpreting results from noisy datasets (Section 3.5), and investigate the robustness of the inversions to noise. Finally I investigate the hypothetical benefits of inverting PP, PS and SS waves (Section 3.6).

3.1 Synthetic experiments

All synthetic experiments were run using Mathworks MATLAB on a laptop computer. The synthetic AVA responses were generated using the Zoeppritz function from the CREWES MATLAB toolbox (Margrave and Lamoureux 2019, available from www.crewes.org), using material properties listed in Table 3.1, after Peters et al. (2007; 2008). MCMC inversions were carried out in MATLAB. Code can be accessed at github.com/rognew91/mcmc-ava.

3.1.1 Forward modelling of AVA data

I use synthetically generated AVA data to test the performance of the inversion. The data are generated from the exact Knott-Zoeppritz equations using the properties listed in Table 3.1. I generate synthetic AVA curves for ice overlying each of water, basement rock, stiff till, dilatant till and lithified sediment, after Peters et al. (2007; 2008). These represent a variety of likely bed conditions for locations in Antarctica, and their AVA responses are shown in Section 1.3.3. AVA inversions suffer from nonuniqueness resulting not only from noisy data, but also from the Knott-Zoeppritz equations themselves; there are many possible solutions to produce AVA curves which fit the data with an equal probability. This nonuniqueness arises partly from the linear tradeoff between density ρ and P wave velocity α as they combine in the acoustic impedance $Z = \rho\alpha$. In order to investigate the extent to which joint inversion reduces this nonuniqueness, I first use synthetic AVA data with no noise.

Material	α (m s^{-1})	β (m s^{-1})	ρ (kg m^{-3})	Z (10^6kg m^{-2} s^{-1})	σ
Ice[a,b]	3810	1860	920	3.5	0.34
Water[b]	1500	0	997	1.5	0.5
Basement[b]	5200	2800	2700	14	0.3
Stiff till[a]	1800 $\pm$ 150	1000 $\pm$ 100	1900 $\pm$ 150	3.42 $\pm$ 0.4	0.28 $\pm$ 0.08
Dilatant till[a,c]	1700 $\pm$ 150	200 $\pm$ 50	1800 $\pm$ 150	3.06 $\pm$ 0.4	0.49 $\pm$ 0.004
Lithified sediment[b]	3750	2450	2450	9.19	0.128

Table 3.1: Seismic properties of bed materials simulated. a) properties taken from Peters et al. 2007. b) properties taken from Christensen 1989, after Peters et al. 2008. c) properties taken from Peters et al. 2008. AVA responses of these materials are displayed in Section 1.3.

3.1.2 Experimental design

For the 5 chosen bed conditions, I run the inversion for 2 million iterations. I evaluate the performance of the inversions using two metrics: the distance of the medians from the true solution, and the width of the posterior distribution in the Z-σ directions, quantified by the inter-quartile range. I compare the performance of the inversion when given a) PP AVA curves only, b) PP and PS, and c) PP, PS, and SS AVA curves. Although I use noiseless synthetic AVA data, for the purposes of computing a likelihood (Section 3.2.2) I assume a standard deviation on the reflection coefficient $R(\theta)$ of ± 0.2. This corresponds with typical uncertainties in AVA data such as those presented in Chapter 4.

Real-world glaciological AVA datasets have been acquired using a variety of survey geometries. Although some datasets acquired over relatively thin ice, such as the one explored in Chapter 4, or those acquired with very large offsets (e.g. Peters et al. 2008), can obtain incidence angles up to 60°, it is common, especially for usual AVA targets such as ice stream beds, to obtain incidence angles $\leqslant 30^\circ$ (e.g., Booth et al. 2012; Kulessa et al. 2017; Peters et al. 2007). To investigate the extent to which jointly inverting using PS or SS waves improves the inversion for varying survey geometries, I test a) PP single inversion, b) PP/PS joint inversion and c) PP/PS/SS joint inversion for two survey geometries: i) a 'narrow-angle' survey, from $0 \leqslant 30^o$, and ii) a 'wide-angle' survey from $0 \leqslant 60^o$. If there is a critical refraction at the interface I exclude the post-critical amplitudes, such that $\theta < \theta_{\text{crit}}$. For example, a joint inversion of PP and PS waves for a wide-angle survey over basement rock would include incidence angles of $0 \leqslant \theta \leqslant 46^\circ$ for both PP and PS waves. If SS waves were included, $R_{SS}(\theta)$ would be truncated at the incident S wave critical angle of 20°. A summary of the extents of AVA curves used for the inversions is given in Table 3.2.

Bed material	Narrow-angle survey	Wide-angle survey
Water	PP, PS, SS: $0 - 30^\circ$	PP, PS: $0 - 60^\circ$; SS: $0 - 30^\circ$
Basement	PP, PS: $0 - 30^\circ$; SS: $0 - 20^\circ$	PP, PS: $0 - 46^\circ$; SS: $0 - 20^\circ$
Stiff till	PP, PS: $0 - 30^\circ$; SS: $0 - 27^\circ$	PP, PS: $0 - 60^\circ$; SS: $0 - 27^\circ$
Dilatant till	PP, PS, SS: $0 - 30^\circ$	PP, PS: $0 - 60^\circ$; SS: $0 - 30^\circ$
Lithified sediment	PP, PS: $0 - 30^\circ$; SS: $0 - 27^\circ$	PP, PS: $0 - 60^\circ$; SS: $0 - 27^\circ$

Table 3.2: Angle ranges used for each of the synthetic AVA curves. In general, a narrow-angle survey uses reflection amplitudes up to 30°, unless a critical angle is reached. A wide-angle survey uses amplitudes up to 60° unless a critical angle is reached. The SS angle ranges are the same for the narrow and wide surveys because incident S waves reach critical angles at $\theta < 30^\circ$ for all of the tested basal conditions.

Although I have tested the performance of the inversion scheme when given PP, PS and SS wave AVA data, I mainly focus my analysis on PP and PP/PS wave inversions (Section 3.4). Acquisition of good quality SS wave AVA data is more challenging due to the effects of increased travel times, attenuation, and the difficulties of measuring S wave source amplitude. Additionally, the effect of S wave critical refractions (see Section 1.3) means that in many cases a much smaller range of the SS AVA curve will be useable. Converted wave AVA will be easier to implement with real datasets than SS wave AVA, and therefore has greater potential to improve identification of glacial substrates at the present time.

Firstly, I present the details of the joint inversion scheme (Section 3.2). I then compare the performance of PP and joint PP/PS inversions (Section 3.4). Following this, I investigate the robustness of PP and PP/PS joint inversion to noisy AVA responses (Section 3.5). Finally, I compare the performance of joint PP/PS/SS inversion with that of PP/PS inversion (Section 3.6).

3.2 Inversion scheme

I use a Bayesian Markov chain Monte-Carlo (MCMC) inversion scheme similar to others reported for application to glaciological problems (e.g. Booth et al. 2012; Killingbeck et al. 2018) and hydrocarbon reservoir characterisation (e.g. He et al. 2022; Pan et al. 2017). Bayesian MCMC methods are a means of probabilistically evaluating proposed geophysical models in the context of observed data and *a priori* knowledge of a physical system, approximating the model space with an ensemble of models from which the solution can be statistically drawn and robust estimates of uncertainties can be made.

Bayes' Theorem relates the probabilities of two events A and B (Bayes 1764):

$$\mathrm{P}(A|B) = \frac{\mathrm{P}(A)\mathrm{P}(B|A)}{\mathrm{P}(B)}, \tag{3.1}$$

where $P(A)$ is the probability of event A, called the prior, and $P(B|A)$ is the probability of B given A, called the likelihood. $P(A|B)$ is termed the posterior probability, and $P(B)$ the evidence. I use the Metropolis-Hastings-Green algorithm (Green 1995; Hastings 1970; Metropolis et al. 1953), which is a commonly used framework for geophysical inverse problems. The algorithm evaluates posterior probabilities of models in relation to the neighbouring models so does not require the evidence, $\mathrm{P}(B)$ to be computed. I give here a brief overview of the algorithm as I apply it.

Bayes' theorem can be re-stated as

$$\mathrm{P}(\mathbf{m}|\boldsymbol{d}) \propto \mathrm{P}(\mathbf{m})\mathrm{P}(\boldsymbol{d}|\mathbf{m}), \tag{3.2}$$

i.e. the posterior probability $\mathrm{P}(\mathbf{m}|\boldsymbol{d})$ is proportional to the product of the prior $\mathrm{P}(\mathbf{m})$ and the likelihood $\mathrm{P}(\boldsymbol{d}|\mathbf{m})$. $\mathrm{P}(\mathbf{m}|\boldsymbol{d})$ can be interpreted as the probability of the model given the observed data. The aim of geophysical inversion is to determine a model $\mathbf{m}$ which, when physically simulated, produces an output of a forward model $\boldsymbol{g}(\mathbf{m})$ to maximise the posterior probability, given observed data $\boldsymbol{d}$ and reasonable priors. $\boldsymbol{d} = R(\theta)$ is a measured AVA curve. $\mathbf{m} = [\rho_1, \rho_2, \alpha_1, \alpha_2, \beta_1, \beta_2]$ contains information about the densities (ρ_1, ρ_2), P wave velocities (α_1, α_2) and S wave velocities (β_1, β_2) on either side of a reflective interface. $\boldsymbol{g}(\mathbf{m})$ is a synthetic AVA curve resulting from forward modelling of the Knott-Zoeppritz equations (see Section 1.3 for theoretical background).

First, a starting model $\mathbf{m}$ is defined. The Knott-Zoeppritz equations are used to forward model the seismic response of this model, resulting in the reflection coefficients $R(\theta)$. The likelihood of $\mathbf{m}$ is calculated based on the misfit of $R(\theta)$ to the observed data (further details are in section 3.2.2). The posterior probability $\mathrm{P}(\mathbf{m}|\boldsymbol{d})$ is then evaluated from Equation 3.2.

A Gaussian perturbation is applied to $\mathbf{m}$ to produce a new candidate model, $\mathbf{m}'$, and $\mathrm{P}(\mathbf{m}'|\boldsymbol{d})$ is computed. The Metropolis algorithm relies on acceptance-rejection sampling to produce a Markov chain, with the acceptance probability A determining whether a candidate model is accepted or rejected:

$$A = \frac{\mathrm{P}(\mathbf{m}'|\boldsymbol{d})}{\mathrm{P}(\mathbf{m}|\boldsymbol{d})} \tag{3.3}$$

If $A > 1$, the new model $\mathbf{m}'$ is accepted, saved and used as the starting point for the next perturbation. If $A < 1$, the new model is accepted with the probability $P(\mathbf{m}'|\boldsymbol{d})$. In other words, if a perturbation increases the posterior probability of the model, the new model is accepted (i.e., $\mathbf{m}_{i+1} = \mathbf{m}'$), and if a perturbation decreases the posterior probability, acceptance is dependent on the degree to which it decreases the probability. In this manner, a large ensemble of possible models is produced (the Markov chain), each with a measure of its posterior probability. In the limit of a large ensemble, the distribution of explored models converges to the posterior distribution, with regions of higher probability being explored with a greater frequency.

The Bayesian MCMC framework results in a posterior probability distribution of models. An interpretation can then be made from the posterior distribution and the statistical quantities by which it is characterised. The inversion program outputs the mean, standard deviation, median, 25th and 75th percentiles, and the best individual model found. It also calculates the basal acoustic impedance and Poisson's ratio for each model:

$$Z = \rho\alpha \tag{3.4}$$

$$\sigma = \frac{\alpha^2 - 2\beta^2}{2(\alpha^2 - \beta^2)}. \tag{3.5}$$

The median and quartiles of Z and σ are then computed from their marginal distributions (the distributions of Z or σ when summed over all other variables). Since the form of the posterior distribution is often unknown, I report the median and interquartile range as the most reliable standard measurement of the distributions; mean and standard deviation statistics would only be robust for normal distributions. The interquartile range is taken as the difference between the 25th and 75th percentiles.

3.2.1 Priors

I set flat priors between reasonable bounds for the subglacial material: the density must be in the range $920 \leqslant \rho_2 \leqslant 4000$ kg m^3, the P wave velocity in the range $0 \leqslant \alpha_2 \leqslant 8000$ m s^{-1} and the S wave velocity in the range $0 \leqslant \beta_2 \leqslant 5000$ m s^{-1}. I also specify that Poisson's ratio must

lie within $0 \leqslant \sigma_2 \leqslant 0.5$. If a model lies outside these ranges its posterior probability is zero. While materials can exist with Poisson's ratio outside of these bounds (Ting and Chen 2005), in practice these σ are unfeasible for a glaciological scenario since they mainly exist in engineered materials (e.g. Lakes 1987). Therefore it is reasonable to assume that the posterior probability of a model with σ_2 outside these bounds is zero.

The inversion is free to vary the basal ice properties somewhat, but they are constrained to previous measurements (after Peters et al. 2008) with assumed Gaussian probabilities: $\rho_1 = 920 \pm 20$ Kg m^{-3}; $\alpha_1 = 3810 \pm 20$ m s^{-1}; $\beta_1 = 1860 \pm 20$ m s^{-1}. These numbers can be changed for consistency with collocated measurements, if available.

Additionally, there is an option to force the modelled AVA curve to change polarity at a given angle, with specified Gaussian errors. This can help further constrain the inversion in the event that a clear change in polarity has been observed.

3.2.2 The likelihood and forward modelling

For forward modelling the AVA response, I use the exact Knott-Zoeppritz equations. Approximations such as the Aki-Richards (Aki and Richards 2002) and Shuey (Shuey 1985) approximations require that $\theta < 40^\circ$ and $\theta < 30^\circ$, respectively, and while they can be useful for making intuitive interpretations from AVA results (Booth et al. 2016), especially when available incidence angles $< 30^\circ$, their use is fundamentally unsuited to wide-angle surveys.

To explore the potential improvement from including converted- and S wave data in AVA analyses, the inversion can be run in three configurations. These are for inverting a) PP AVA data only; b) PP and PS AVA data jointly; and c) PP, PS and SS data. I define a likelihood $\mathcal{L}$ which depends on the error-weighted RMS misfit to the AVA curves in question. When inverting PP amplitudes only, I use the likelihood function:

$$\mathcal{L} = \exp\left(\sum_i \frac{R^i_{PP} - g^i_{PP}(\mathbf{m})}{\varepsilon^i_{PP}}\right). \tag{3.6}$$

Here, R^i_{PP} is the ith data point in a measured PP AVA curve (the data). $g^i_{PP}(\mathbf{m})$ is the ith data point in a synthetically generated AVA curve given the model $\mathbf{m}$. ε^i_{PP} is the uncertainty associated with the measurement of R^i_{PP}. When jointly inverting PP and PS AVA curves, the likelihood is given by:

$$\mathcal{L} = \exp\left(\sum_i \frac{R^i_{PP} - g^i_{PP}(\mathbf{m})}{\varepsilon^i_{PP}} + \sum_i \frac{R^i_{PS} - g^i_{PS}(\mathbf{m})}{\varepsilon^i_{PS}}\right). \tag{3.7}$$

Finally, when PP, PS and SS AVA curves are used for the inversion, the likelihood is:

$$\mathcal{L} = \exp\left(\sum_i \frac{R^i_{PP} - g^i_{PP}(\mathbf{m})}{\varepsilon^i_{PP}} + \sum_i \frac{R^i_{PS} - g^i_{PS}(\mathbf{m})}{\varepsilon^i_{PS}} + \sum_i \frac{R^i_{SS} - g^i_{SS}(\mathbf{m})}{\varepsilon^i_{SS}}\right). \tag{3.8}$$

In the above two equations, the subscripts PS and SS denote P-to-S converted waves and S waves, respectively. Otherwise the notation follows equation 3.6.

3.2.3 Convergence

The inversion outputs running means of bed acoustic impedance and S wave velocity to check for convergence. An inversion on noiseless synthetic data can converge to the posterior distribution in 1 million iterations see Section 3.3), while for noisy synthetic or real-world data $2-5$ million iterations are usually required. The inversion scheme requires a burn-in period from which the models are not included in the calculation of the posterior distribution; this is set to $10,000$ iterations.

3.3 Example of inversion output

To demonstrate the ability of the inversion scheme to retrieve known bed properties and illuminate some interpretive aspects, I give an example of the inversion output for a bed of lithified sediments (see Table 3.1), given noiseless synthetic PP and PS AVA responses. Figure 3.1 shows the input AVA responses, along with the PP and PS AVA responses of the median model found. This is used to visually inspect the inverted solution for goodness of fit. Figure 3.4 shows the running medians of acoustic impedance and Poisson's ratio, used to check for convergence. The running medians change little after the iteration number has reached $1,000,000$, showing convergence to the posterior distribution. Figure 3.2 shows the marginal distributions of density, P wave velocity and S wave velocity for the basal ice (a-c) and the bed (d-f), with model values and distribution medians marked by black dashed lines and yellow dotted lines, respectively. When viewed as a combination of ρ, α and β, the distributions of bed properties are complicated, being multimodal for α and β. Due to nonuniqueness in the solution space, it is difficult

for the inversion to resolve these variables; the median inverted properties of $\rho_2 = 2778$ kg m^{-3}, $\alpha_2 = 3232$ m s^{-1} and $\beta_2 = 2123$ m s^{-1} are $\sim 13\%$ away from the respective model values (dotted yellow lines compared to dashed black lines in Fig. 3.2d-f).

In contrast, bed properties are better resolved by marginalising the distributions in terms of Z and σ. Figure 3.3 shows the marginal distributions of Poisson's ratio and acoustic impedance, from which the medians and quartiles are drawn. The medians are $Z = (9.07 \pm 0.3)$ kgm^{-2}s^{-1} and $\sigma = 0.13 \pm 0.08$. The inverted basal properties are within 2% of the true values, printed in Table 3.1 ($Z = 9.19$ kgm^{-2}s^{-1} and $\sigma = 0.128$). This demonstrates that the inversion is skilled at recovering known basal acoustic impedances and Poisson's ratios; consequently when comparing the performances of single and joint inversion under different survey parameters, I quote the medians and quartiles of the marginal distributions of Z and σ.

Figure 3.5 shows the posterior distributions of Z and σ as a 2D histogram, along with the known properties of subglacial materials given in Table 3.1. Viewing the distributions in this way is helpful for putting inverted results in the context of other subglacial materials.

In the next section, I explore the performance of the inversion scheme when singly inverting (PP only) and jointly inverting (PP/PS) synthetic AVA data.

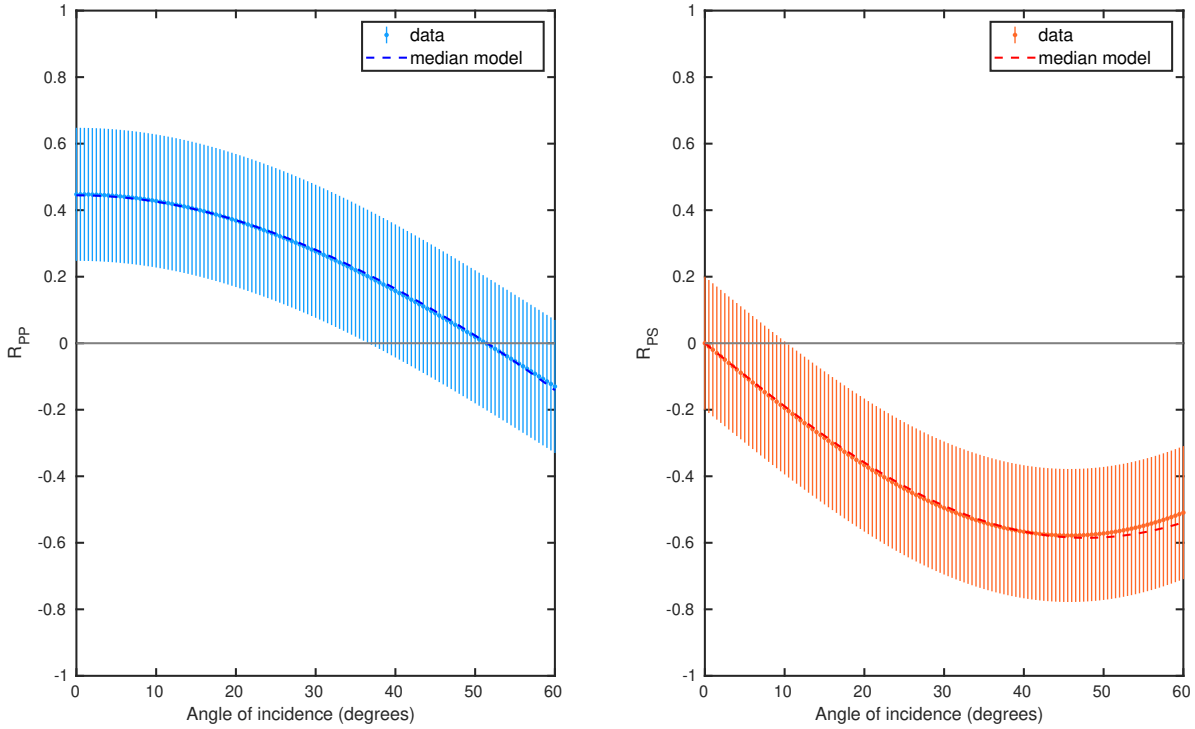

Figure 3.1: Synthetic AVA responses used as inputs to an inversion, simulated for ice overlying lithified sediments (see Table 3.1 for properties). Horizontal grey line marks zero amplitude for reference. The dashed lines are the AVA responses of the median model.

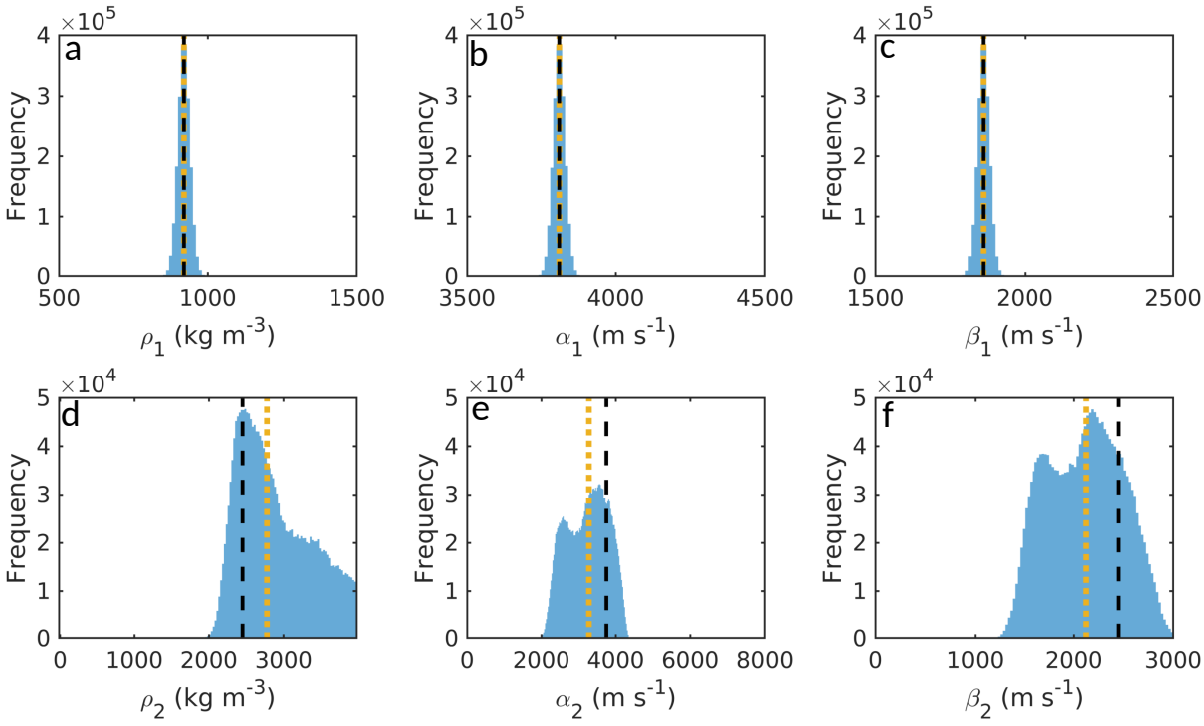

Figure 3.2: Marginal distributions of density ρ, P wave velocity α and S wave velocity β for basal ice (a-c) and the bed (d-f). Model values are indicated by the black dashed lines and distribution medians by the yellow dotted lines. Medians are $\rho_2 = 2778$ kg m^{-3}, $\alpha_2 = 3232$ m s^{-1}, $\beta_2 = 2123$ m s^{-1}.

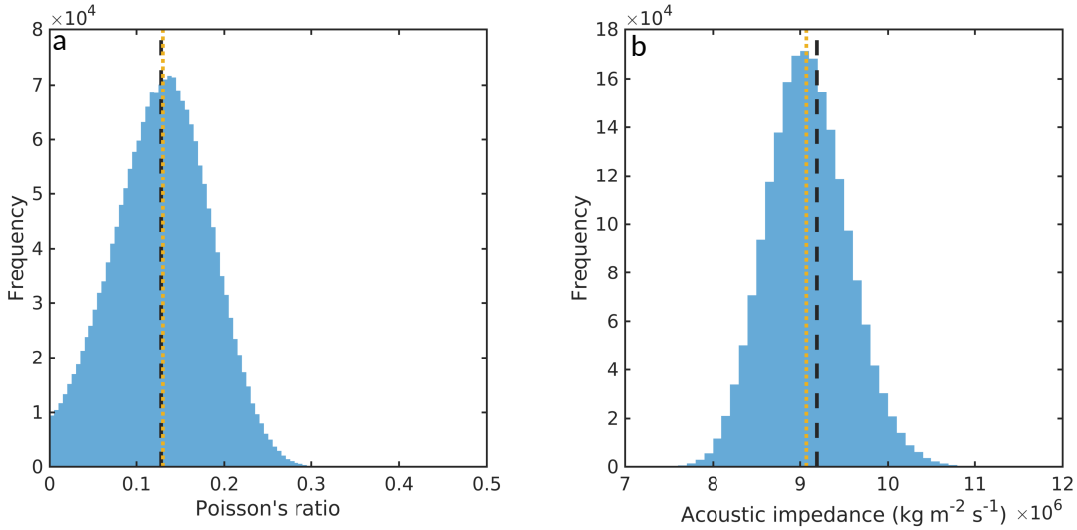

Figure 3.3: Marginal distributions of basal Poisson's ratio and acoustic impedance. The medians of these distributions, along with the 25th and 75th percentiles, are the most representative quantities for interpretative purposes. The percentiles are expressed as an inter-quartile range. (a) $\sigma = 0.13 \pm 0.08$, (b) $Z = (9.07 \pm 0.3)$ kgm^{-2}s^{-1}. In both a and b, the dark grey dashed line indicates the model value and the yellow dotted line indicates the distribution median.

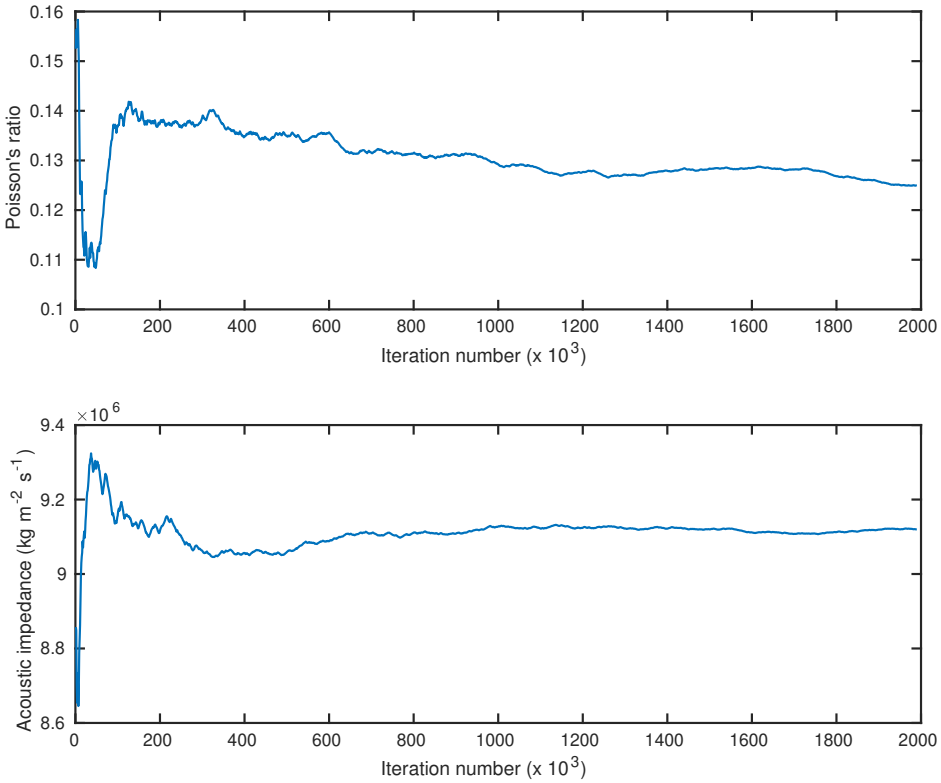

Figure 3.4: Running medians of basal Poisson's ratio and acoustic impedance, used to check an inversion for convergence. The running medians change little after 1 million iterations, demonstrating convergence.

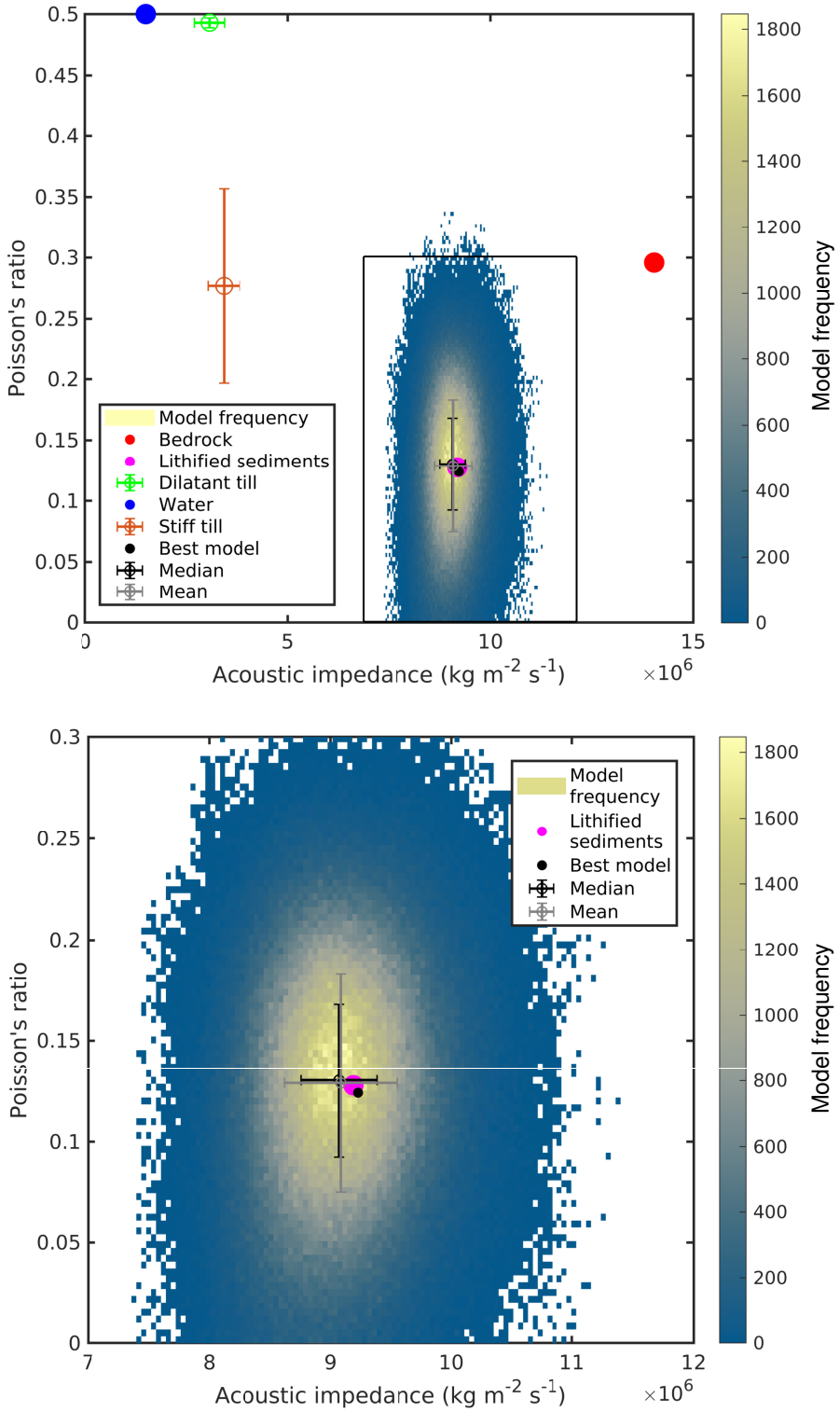

Figure 3.5: 2D posterior distribution in terms of basal acoustic impedance and Poisson's ratio. The coloured dots represent the properties of known basal materials. The grey and black circles with error bars, represent the median and mean models. The best model is represented as the black dot without error bars. Colour bar represents the frequency with which models express given quantities. (a) shows the context of this measurement within the space of known subglacial materials. (b) is a zoom of the box shown in (a), showing the consistency of the mean, median and best model metrics, as well as their accurate recreation of the input model.

Basal material	Inversion type	Max angle (°)	Z true ($\times 10^6$ kg m^{-2}s^{-1})	σ true	Z inverted ($\times 10^6$ kg m^{-2}s^{-1})	σ inverted
Basement	PP	30	14.04	0.3	13.71 ± 1.00	0.331 ± 0.095
Basement	PP	46	14.04	0.3	13.36 ± 0.93	0.385 ± 0.045
Basement	PP/PS	30	14.04	0.3	14.09 ± 0.75	0.290 ± 0.047
Basement	PP/PS	46	14.04	0.3	14.03 ± 0.59	0.319 ± 0.027
Basement	PP/PS/SS	30	14.04	0.3	14.09 ± 0.73	0.303 ± 0.037
Basement	S	46/20	14.04	0.3	14.09 ± 0.55	0.313 ± 0.024
Dilatant till	P	30	3.06	0.49	3.16 ± 0.15	0.460 ± 0.046
Dilatant till	P	60	3.06	0.49	3.09 ± 0.13	0.486 ± 0.010
Dilatant till	PP/PS	30	3.06	0.49	3.05 ± 0.11	0.492 ± 0.004
Dilatant till	PP/PS	60	3.06	0.49	3.03 ± 0.10	0.492 ± 0.002
Dilatant till	PP/PS/SS	30	3.06	0.49	3.06 ± 0.11	0.493 ± 0.001
Dilatant till	PP/PS/SS	60/30	3.06	0.49	3.04 ± 0.10	0.493 ± 0.001
Lithified sediments	P	30	9.19	0.128	8.99 ± 0.52	0.246 ± 0.098
Lithified sediments	P	60	9.19	0.128	9.06 ± 0.43	0.133 ± 0.054
Lithified sediments	PP/PS	30	9.19	0.128	9.29 ± 0.41	0.158 ± 0.056
Lithified sediments	PP/PS	60	9.19	0.128	9.07 ± 0.31	0.130 ± 0.038
Lithified sediments	PP/PS/SS	30	9.19	0.128	9.29 ± 0.39	0.157 ± 0.059
Lithified sediments	PP/PS/SS	60/28	9.19	0.128	9.12 ± 0.30	0.130 ± 0.033
Stiff till	P	30	3.42	0.28	3.36 ± 0.16	0.365 ± 0.102
Stiff till	P	60	3.42	0.28	3.44 ± 0.15	0.264 ± 0.051
Stiff till	PP/PS	30	3.42	0.28	3.44 ± 0.13	0.279 ± 0.049
Stiff till	PP/PS	60	3.42	0.28	3.43 ± 0.10	0.270 ± 0.027
Stiff till	PP/PS/SS	30	3.42	0.28	3.44 ± 0.13	0.276 ± 0.034
Stiff till	PP/PS/SS	60/27	3.42	0.28	3.43 ± 0.10	0.273 ± 0.023
Water	P	30	1.50	0.5	1.57 ± 0.08	0.457 ± 0.060
Water	P	60	1.50	0.5	1.56 ± 0.06	0.498 ± 0.002
Water	PP/PS	30	1.50	0.5	1.49 ± 0.07	0.499 ± 0.001
Water	PP/PS	60	1.50	0.5	1.50 ± 0.05	0.500 ± 0.0002
Water	PP/PS/SS	30	1.50	0.5	1.51 ± 0.07	0.500 ± 0.0001
Water	PP/PS/SS	60/30	1.50	0.5	1.52 ± 0.05	0.500 ± 0.00004

Table 3.3: Results of synthetic tests. Results comparing PP and PP/PS inversions are discussed in 3.4. Results from PP/PS/SS inversions are discussed in Section 3.6

3.4 Inversion performance: PP versus PP/PS joint inversion

In this section I will discuss the performance of PP/PS joint inversion when compared with single inversion. It should be noted that the following observations are taken from experiments with noise-free data; I will explore their robustness to noise in Section 3.5. Table 3.3 summarises the results of the single and joint inversion scenarios for the five bed types. For completeness, Table 3.3 includes the results of PP/PS/SS joint inversion; these results will be discussed in Section 3.6. Figure 3.6 shows the medians and quartiles of the posterior distributions of the single PP and joint PP/PS inversions for the five bed types. The acoustic impedances and Poisson's ratios of the reference materials (Table 3.1) are plotted alongside the inversion results, to enable identification of the basal regime. Figure 3.6 shows that the inversion scheme is effective in retrieving known basal properties and is able to distinguish basal regimes from each other, even for single inversion of data for which $\theta \leqslant 30^\circ$ (Fig. 3.6a). However, given the large errors obtained by narrow single inversion (Fig. 3.6a), interpretation of these results may still be ambiguous. Substrate identification becomes less ambiguous when jointly inverting or adding wider angle data: comparing Figs. 3.6a-d, uncertainties reduce when going from narrow single inversion to wide or joint inversionsm and in general medians approach the known solutions. Furthermore, a comparison of panels b and c shows that narrow joint inversion of $\theta \leqslant 30^\circ$ data can deliver results of comparable quality to those obtained by wide single inversion of $\theta \leqslant 60^\circ$ data. This has implications for future survey design, raising the question of whether it is preferable to expend logistical effort carrying out a spatially large survey or recording three components of data.

In general, then, a converted-wave joint inversion reduces the width of the posterior distribution and brings it closer to the true solution; i.e. joint inversion improves both accuracy and precision when compared with single inversion. It is clear from Figure 3.6 that joint inversion has the potential to reduce ambiguity in glacial substrate identification.

To quantify the improvements joint inversion makes upon single inversion, I evaluate the performance of the inversion scheme in two ways. To indicate precision, I look at half of the inter-quartile range as a percentage of the median - in the following discussion this is referred to as δ_Z or δ_σ, for Z and σ, respectively. To indicate accuracy, I look at the difference between the median and true solution, as a percentage of the true solution - I refer to this as ε_Z or ε_σ. These metrics are displayed in Figure 3.7 for all of the tested bed types. Single (PP) inversion

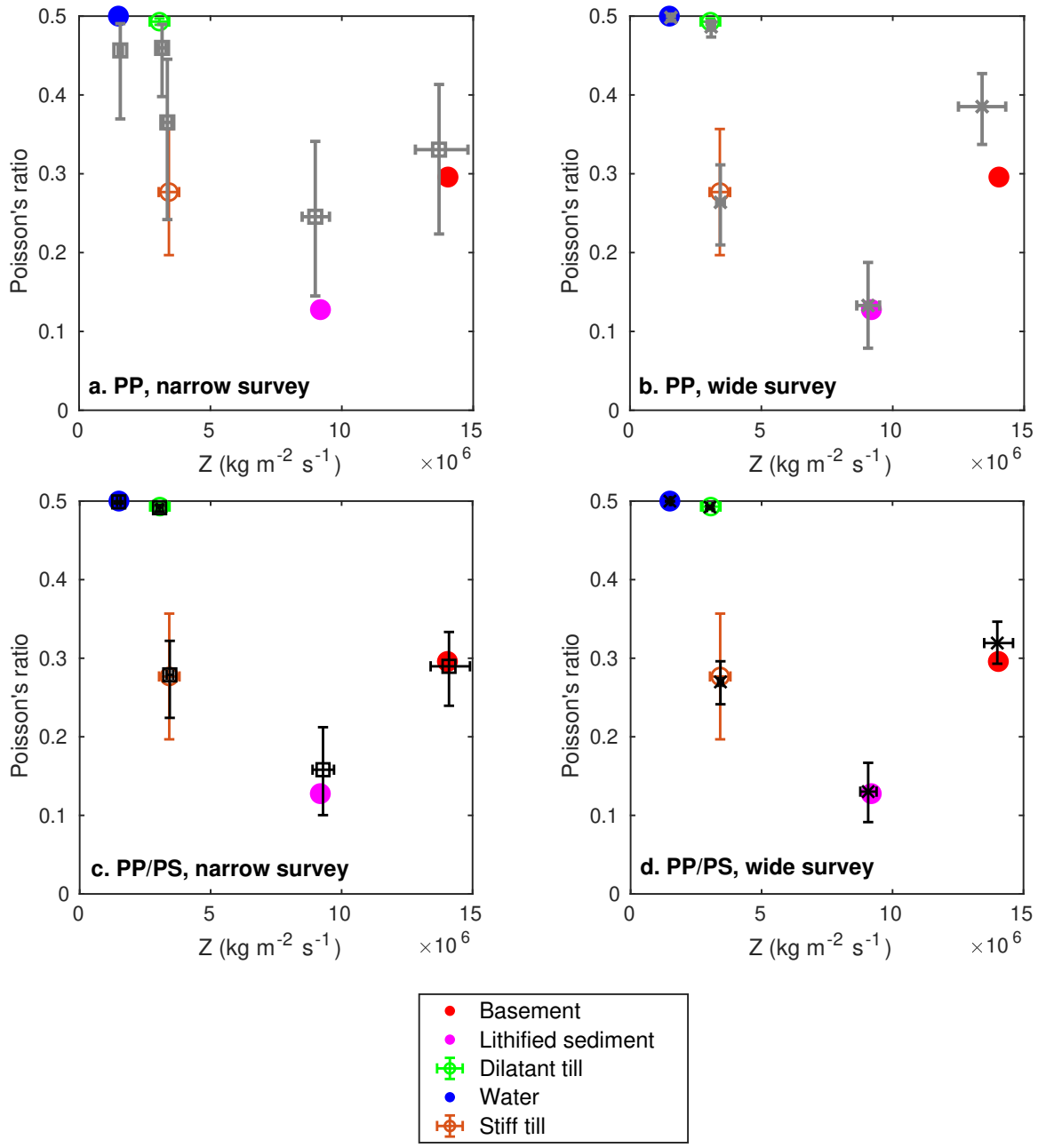

Figure 3.6: Results from synthetic PP and PP/PS joint inversions. (a) and (b) show results for single PP inversion, and (c) and (d) show results from joint PP/PS inversion. Plots on the left (a, c) show the results from the narrow survey, where $\theta < 30°$, and plots on the right (b, d) show results from the wide survey, where $\theta < 60°$ (or $\theta < \theta_{\text{crit}}$). (b) and (c) demonstrate that joint inversion of narrow-angle data can deliver results of comparable precision and accuracy to single inversion wide-angle data.

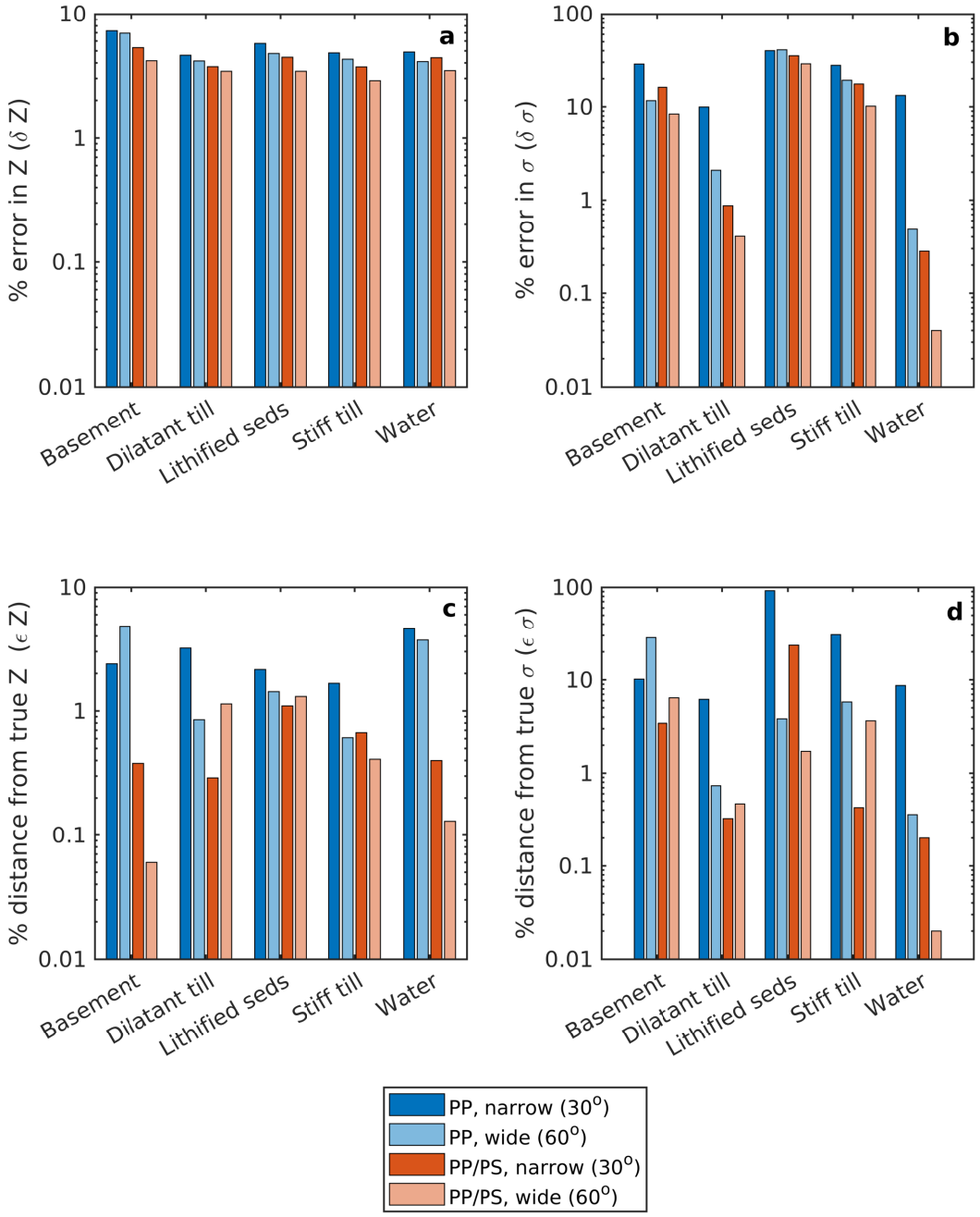

Figure 3.7: Half inter-quartile ranges of posterior distributions (a, b), and the distance of the medians from the true solution (c,d). Note the logarithmic scales and different scales for acoustic impedance (Z) and Poisson's ratio (σ) plots.

results are shown in blue, while joint (PP/PS) inversion results are shown in red. Narrow survey geometries ($\theta \leqslant 30^\circ$) are represented by the darker bars, with lighter bars representing wider survey geometries ($\theta \leqslant 60^\circ$ or $\theta < \theta_{\text{crit}}$). In almost all cases, given the same angular range, jointly inverting PP and PS waves improves both the accuracy and precision of the inversion when compared with inverting PP waves only. In general, narrow joint inversion over $\theta \leqslant 30^\circ$ also performs better than wide single inversion over $\theta \leqslant 60^\circ$, despite these inversions being given approximately the same quantity of data (as suggested by Figure 3.6). This suggests that converted wave AVA data provide different information from PP wave AVA data, particularly in measurements of Poisson's ratio, and joint inversion therefore has value beyond merely providing more data points through the inclusion of a PS AVA curve. In the following discussion, when referring to an average quantity (e.g. δ_Z) across the five bed types tested, this is the median of the five results.

When comparing results for Z, it is apparent that joint inversion offers an improvement in precision over single inversion (Figure 3.7a). Joint inversion is more precise given the same angular range of data (over all bed types tested δ_Z is an average (median) of 24% smaller under joint inversion than single inversion). Furthermore, narrow joint inversion is in most cases more precise than wide single inversion (δ_Z is an average of 10% smaller across all bed types tested). When it is not, the difference is small (i.e. for an ice/water interface, $\delta_Z = 4.11\%$ for wide PP inversion versus 4.42% for narrow PP/PS inversion).

Similar observations are true of the precision in Poisson's ratio (Fig. 3.7b). The degree of improvement by joint inversion is largest for materials with high Poisson's ratios (water, dilatant till) and lowest for those with low Poisson's ratios (lithified sediments). It is greatest for dilatant till and water, for which materials δ_σ is 65% and 91% smaller, respectively, under joint inversion than single inversion, given the same angle range. For both dilatant till and water, when $\theta \leqslant 30^\circ$, by including PS AVA curves δ_σ is reduced from $> 10\%$ to $< 1\%$. Given the same angular range, δ_σ is an average of 49% smaller for joint inversion across all the bed types tested. In general, narrow joint inversion is at least as precise as wide single inversion: δ_σ is an average of 14% smaller for all bed types tested, with the largest difference observed for dilatant till, at 58%.

In certain cases, performing a wider-angle survey will improve the precision more than jointly inverting (e.g. δ_σ for basement, figure 3.7b). However, even in these cases, accuracy is improved more by jointly inverting than by increasing the survey angles (Figure 3.7c). In general, accuracy

is improved in both Z and σ by joint inversion (Figures 3.7c, d), however the extent to which this is the case is more strongly dependent on the subglacial material than is seen for precision.

Joint inversion is in most cases more accurate than single inversion given the same angular range; ε_Z is an average of 47% smaller and ε_σ an average of 68% smaller for joint inversion. This improvement is particularly pronounced for narrow inversions (dark orange bars compared with dark blue bars). In these cases jointly inverting decreases ε_Z by 84% and ε_σ by 95% when compared with single inversion (average across all tested bed types). In general, narrow joint inversion is also more accurate than wide single inversion, for both Z and σ: ε_Z is an average of 65% smaller, and ε_σ an average of 56% smaller, for narrow joint than wide single inversion.

A notable exception to the general observations stated above is that for ice over lithified sediments, increasing the survey range from $\theta \leqslant 30^\circ$ to $\theta \leqslant 60^\circ$ under single inversion improves accuracy in Poisson's ratio far more than jointly inverting over $\theta \leqslant 30^\circ$ (Figure 3.7d) - $\varepsilon_\sigma = 4\%$ for wide single vs 24% for narrow joint inversion). While both of these results are an improvement on narrow single inversion ($\varepsilon_\sigma = 92\%$), the deviation from the general result is striking. I hypothesise that this results from the change in polarity at $\sim 50^\circ$ shown by the AVA curve in question (see Figure 3.1), which is a highly diagnostic feature of AVA data (Anandakrishnan 2003). This zero crossing puts a much tighter constraint on the AVA gradient, which is controlled by the contrast in σ at the interface (see Section 1.3.3), and therefore much reduces the number of plausible models.

It is not always the case that increasing the angular range increases accuracy; for ice over bedrock, accuracy in both Z and σ is significantly worse (by 100% and 180%, respectively) under wide single inversion than narrow joint inversion. This could be an effect of a local minimum which represents a good fit only to the far offset AVA data, and only becomes present when the data extend beyond $\theta \leqslant 30^\circ$. Wide joint inversion is more robust to the effect of this local minimum, providing both improved accuracy and precision than wide single inversion.

Figures 3.7 and 3.6demonstrate that in most cases, extending to converted wave analysis improves an AVA inversion at least as much as extending a survey to 60 degrees. In acquisitions where three component recording is available, this may be easier than performing a very wide-angle survey. For example, where the ice is very thick, which is the case at many Antarctic ice streams, the logistical requirements of obtaining very wide-angle data significantly exceed those of obtaining narrow-angle data. Furthermore, energy is more attenuated at large offsets, which

will either result in poorer-quality data or necessitate the use of larger sources, further adding to the logistical burden. Experiments which include three-component recording for complementary reasons such as the measurement of crystal orientation fabric by shear wave splitting (e.g. Brisbourne et al. 2019) will also benefit from the potential to do converted-wave AVA with little extra logistical effort required.

3.5 Inversion of noisy data

To illustrate the improvement joint PP/PS AVA inversion can make to interpretation of AVA results, I use the example of distinguishing stiff till and dilatant till. While they have similar acoustic impedances (3.42 ± 0.4 kg m^{-2}s^{-1} and 3.06 ± 0.4 kg m^{-2}s^{-1}, respectively), they have different Poisson's ratios (0.28 ± 0.08 and 0.49 ± 0.08). Distinguishing these materials by measurements of the acoustic impedance alone can be difficult, so they are good targets for AVA study. To produce the synthetic AVA curves, I use the properties set out in Table 3.1 and apply a Gaussian perturbation with a standard deviation of 0.2 to each point; this type of noise might result from different coupling from receiver to receiver. The perturbation is chosen to demonstrate the power of joint inversion when applied to poor-quality data; the standard deviation of ± 0.2 represents a reasonable estimate of a large AVA error, and reflects the largest uncertainties in the AVA data presented in Chapter 4. In reality, AVA uncertainties are often smaller than this in Antarctic settings, and uncertainties can be offset dependent (e.g. Peters et al. 2008, and the data presented in Chapter 4 of this thesis). Although this presentation of noisy data relies on a simplified representation of AVA uncertainties, it can nevertheless illustrate the power of the joint inversion method.

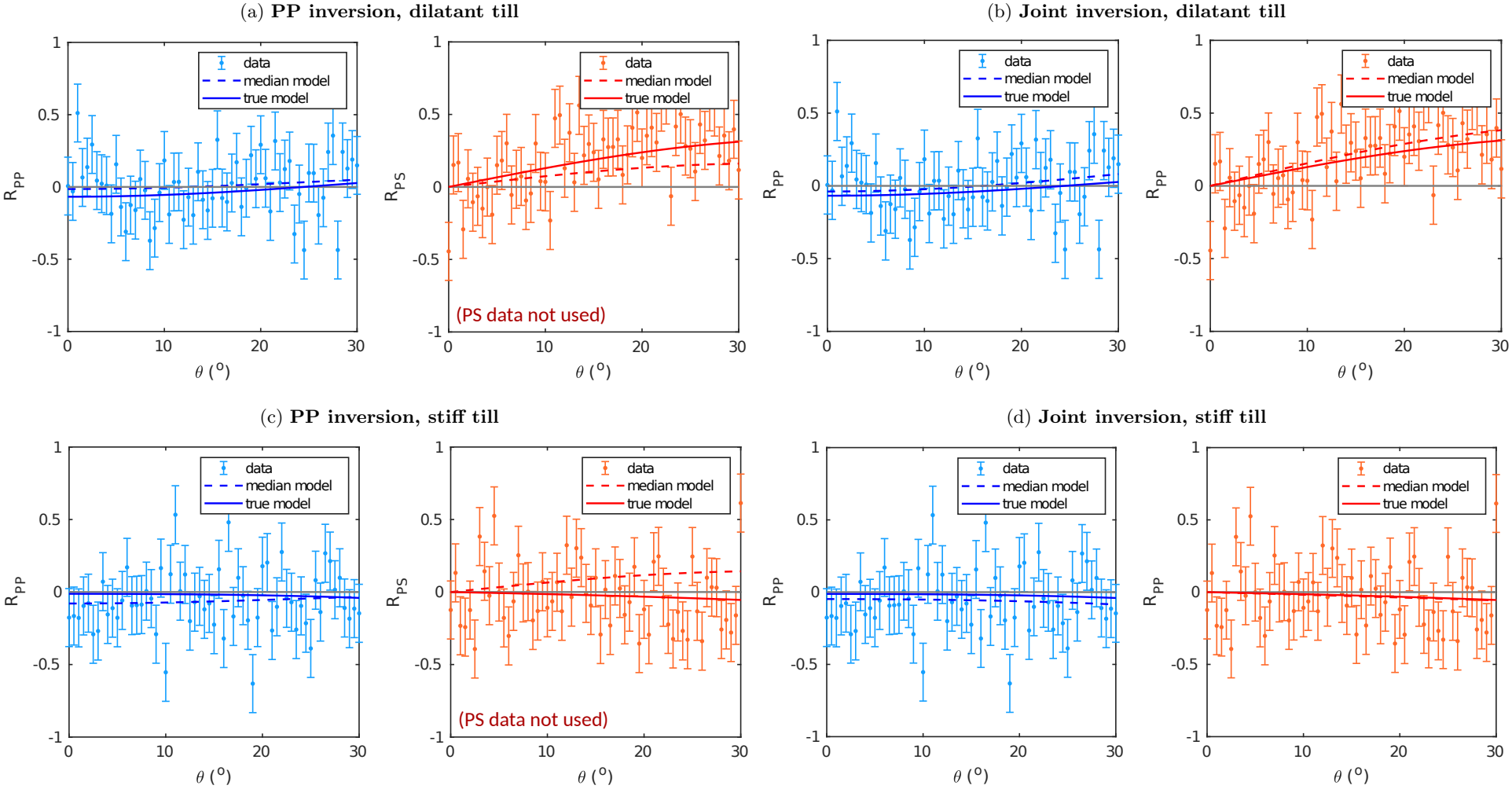

Figure 3.8: Noisy AVA data used for (a) single inversion of PP data for a bed of dilatant till, (b) joint PP/PS inversion, dilatant till, (c) single inversion, stiff till, (d), joint PP/PS inversion, stiff till. Note here that the PS wave data in red are not used as input data in inversions (a) and (c), but the PS AVA curves resulting from the inversions have been simulated (solid and dashed curves) to illustrate the extra information provided by converted waves.

3.5.1 Joint inversion improves an ambiguous interpretation

The first question I ask is whether jointly inverting these noisy data can result in a less ambiguous interpretation than singly inverting. To address this I compare narrow single and joint inversions for the two basal materials. The modelled noisy AVA responses used for the inversion are shown in Figure 3.8. I restrict the maximum incidence angle to 30° to simulate likely acquisition constraints (e.g. Booth et al. 2012; Horgan et al. 2021) and demonstrate the efficacy of the converted-wave method. I run the inversions for $2,000,000$ iterations to ensure convergence, with all other conditions as described in Section 3.4.

Figure 3.8 displays the synthetic data used as the input for the inversions. Additionally, it shows the AVA responses associated with the true solutions (i.e. the unperturbed data, solid line) and the AVA responses associated with the inverted medians (dashed lines). Figures 3.8a and d show the input data used for PP inversion for dilatant till and stiff till, respectively. While the PS AVA responses were not used for these inversions, they are shown alongside the PP data. This is intended to demonstrate that while inverted basal properties obtained by single inversion reproduce a good fit to the PP data, they are inconsistent with the PS data. Figures 3.8b and f show the PP and PS AVA responses associated with the medians resulting from joint inversion. All of the data displayed were used as inputs to these inversions. Comparison of the PP AVA responses associated with the inversion medians for single and joint inversion shows similar inverted PP responses associated with single and joint inversion. In contrast, jointly inverted models reproduce a good fit to the PS data, where singly inverted models do not. This serves as a visual demonstration of the nonuniqueness of the solution space and its constraint by joint inversion: joint inversion rules out models which provide a good fit to the PP data but not to the PS data. Single inversion is unable to distinguish between these models.

The results of the narrow inversions are presented in Table 3.4, along with results from wide inversions which will be discussed later. The posterior distributions are shown in Figure 3.9. Figures 3.9a and b show the posteriors for dilatant till and Figures 3.9c and d show the results for stiff till. Comparing Figures 3.9a and c (PP inversions), it is clear that the distributions for dilatant and stiff till overlap significantly. In this case, identification of a substrate from one of the distributions would be highly ambiguous. In particular, given the distribution shown in Figure 3.9c, a substrate of stiff till would likely be misidentified as dilatant till owing to the high apparent Poisson's ratio. Comparing these distributions with those resulting from

Bed type	Inversion type	Max angle	Z true ($\times 10^6$ kg m^{-2}s^{-1})	σ true	Z inverted ($\times 10^6$ kg m^{-2}s^{-1})	σ inverted
Dilatant till	PP	30°	3.06	0.49	3.41 ± 0.2	0.46 ± 0.05
Dilatant till	PP	60°	3.06	0.49	3.34 ± 0.14	0.48 ± 0.01
Dilatant till	PP/PS	30°	3.06	0.49	3.24 ± 0.12	0.499 ± 0.001
Dilatant till	PP/PS	60°	3.06	0.49	3.20 ± 0.11	0.495 ± 0.001
Stiff till	PP	30°	3.42	0.28	3 ± 0.14	0.42 ± 0.07
Stiff till	PP	60°	3.42	0.28	3.14 ± 0.13	0.29 ± 0.05
Stiff till	PP/PS	30°	3.42	0.28	3.19 ± 0.12	0.19 ± 0.06
Stiff till	PP/PS	60°	3.42	0.28	3.33 ± 0.10	0.20 ± 0.04

Table 3.4: Acoustic impedances and Poisson's ratios obtained from inverting noisy synthetic AVA data. The $0 \leqslant \theta \leqslant 30^\circ$ portions of the noisy AVA responses are shown in Figure 3.8.

joint inversion (Figures 3.9b and d), it is clear that joint inversion would significantly help an interpretation. Under joint inversion, the posterior distributions for dilatant till (b) and stiff till (d) are effectively separated and have moved closer to their respective true solutions. It is unlikely that results from one of these inversions would result in an incorrect interpretation; this shows the clear potential of joint inversion to aid glaciological studies even when data quality is poor.

3.5.2 Robustness to noise: wide single vs narrow joint inversions

The second issue I explore here is concerned with survey planning. In section 3.4, I observed that in many cases narrow joint inversion is more precise and more accurate than wide single inversion. How robust is this observation to noise - might it be preferable to acquire three components of data over a smaller angular range than one component over a larger one?

To address this question, I repeat the tests described in section 3.1.2, comparing four inversions for each bed type: narrow ($\theta \leqslant 30^\circ$) and wide ($\theta \leqslant 60^\circ$) single (PP) and joint (PP/PS) inversions. I compare these for beds of dilatant till and stiff till; the noise model is the same as described in the previous section.

The comparisons between the single and joint inversions are broadly consistent with those reported in Section 3.4. Figure 3.10 shows the medians and quartiles resulting from the inversions. Figure 3.11 shows the precision and accuracy metrics δ_Z, δ_σ, ε_Z and ε_σ for the inversions. Comparison of Figures 3.10b and c shows that, consistent with the earlier results, narrow joint inversion (c) can deliver results of similar quality to wide single inversion (b). In both of these cases an incorrect interpretation would be unlikely for either bed material. Wide single inversion

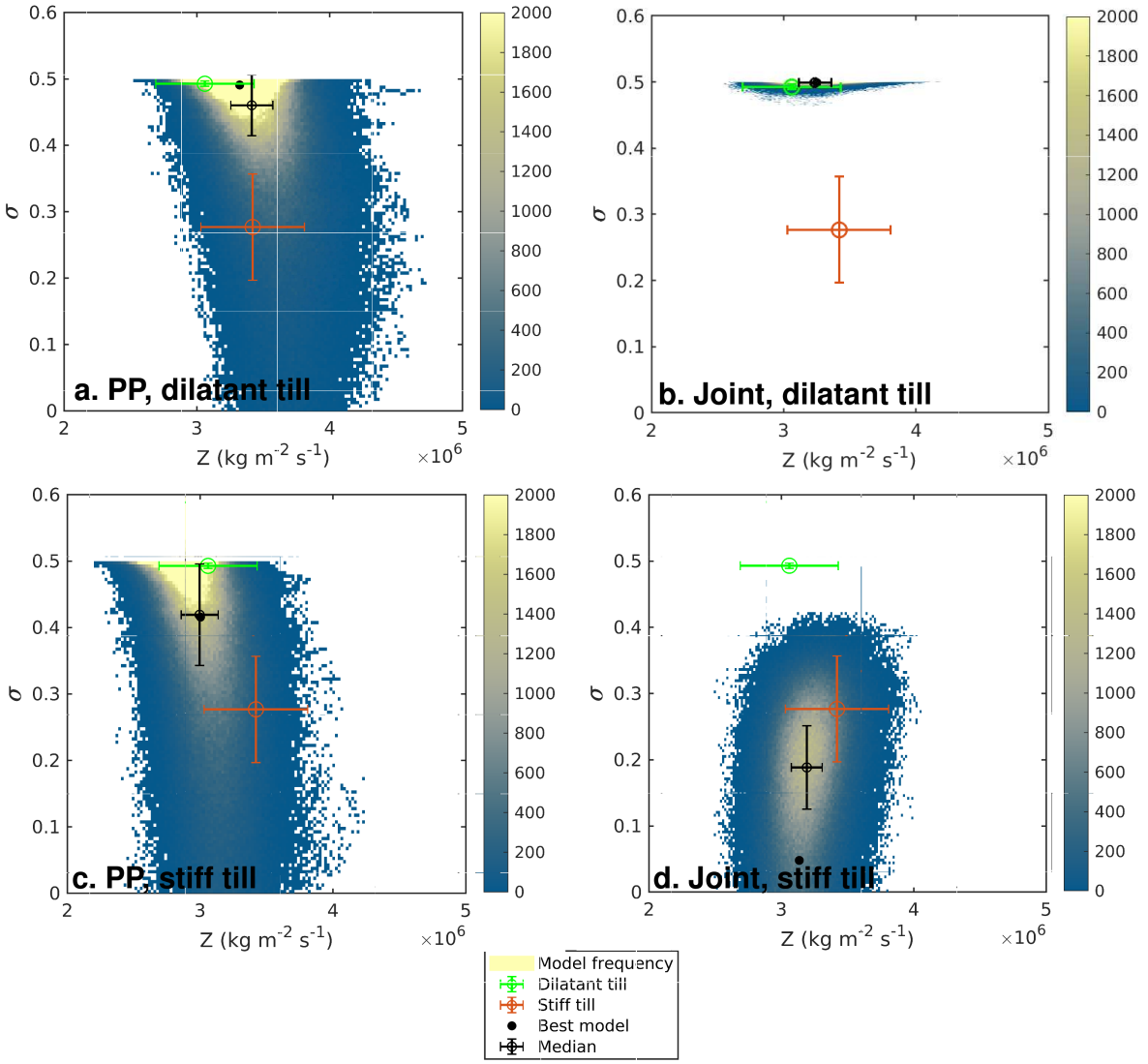

Figure 3.9: Posterior distributions resulting from inverting $\theta \leqslant 30^{\circ}$ synthetic AVA curves for ice over dilatant till (a, b) and ice over stiff till (c, d). The centre of the error bars is the median of the posterior distribution, and the error bars represent the quartiles. The colour bars represent the frequency with which explored models express the given quantities, as in Figure 3.5. The inclusion of PS waves in the inversion separates the overlapping parts of the posterior distributions, enabling identification of the substrates. In the case of (c), the substrate would likely be misidentified as dilatant till. Joint inversion (panel d) rules this out, moving the distribution away from dilatant till properties.

or narrow joint inversion would likely be sufficient to determine the substrate; narrow single inversion would result in an interpretive risk. Wide joint inversion (3.10d), while improving in accuracy and precision on narrow joint inversion, may not improve an interpretation sufficiently to justify the extra logistical effort required for this survey.

Figure 3.11 quantifies these observations; in general, given the same angular range, joint inversion is both more precise and more accurate than single inversion. For narrow inversions, δ_Z is 21% smaller, δ_σ is 59% smaller, ε_Z is 48% smaller, and ε_σ is 53% smaller under joint inversion.

The picture is more complicated for wide inversions. For dilatant till, joint inversion reliably improves both accuracy and precision in Z and σ. For stiff till, the accuracy of joint inversion is $\sim 50\%$ better than the accuracy of single inversion in obtaining Z. However ε_σ is ~ 10 times worse for joint inversion. This is an unusual case due to the extremely small ε_σ obtained by wide single inversion for stiff till (Figure 3.11d). However, inspection of the inverted results plotted next to the true solutions in Figure 3.10 shows both wide single (b) and narrow joint (c) inversions lying within errors obtained by Peters et al. (2007); interpretations resulting from these inversions would be consistent with one another.

While it is clear from Figure 3.11 that joint inversion represents an improvement in constraint of Z when compared with single inversion, the interpretation for σ is less clear, and appears more highly dependent on the interface's AVA response and interaction with the noise model. For dilatant till, both Z and σ are clearly better constrained by joint inversion. For stiff till, Z is better constrained by joint inversion, but the constraint of σ is far better for wide single inversion than any other case. This unpredictability likely arises from the effect of noise on the posterior distribution; the presence of noise in an AVA response does not only broaden the posterior distribution, it also translates the median in the $Z - \sigma$ domain in an unpredictable way. As such, noise represents a fundamental limit to the inversion's capability.

Further tests should be done with more realistic noise models to improve the understanding of the above observations' robustness to noise. With real data, I recommend running inversions which include varying subsections of the recorded AVA responses to check for consistency between the inverted solutions.

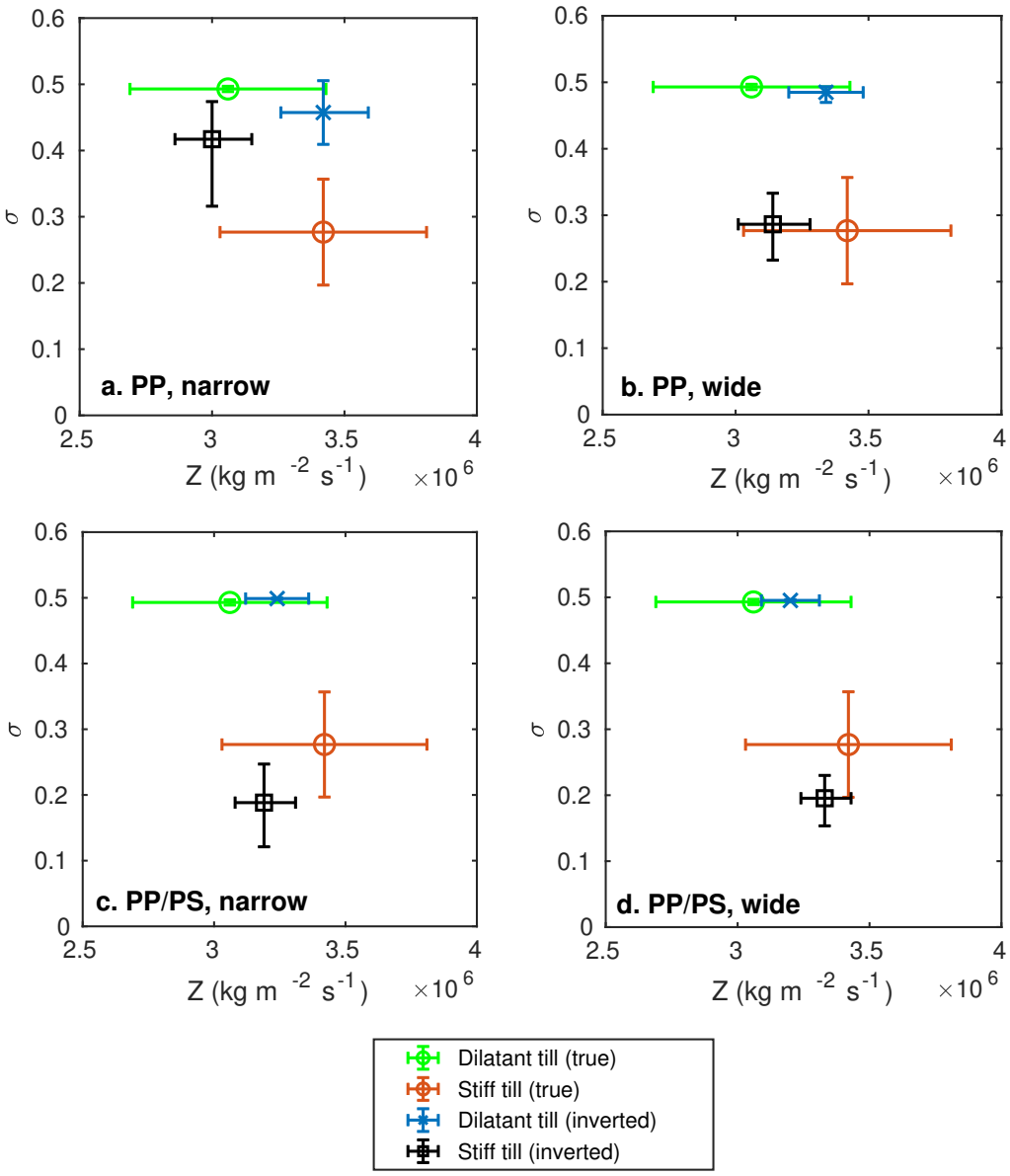

Figure 3.10: Medians and quartiles of posterior distributions resulting from (a) narrow PP inversion, (b) wide PP inversion, (c) narrow joint inversion, (d) wide joint inversion. True solutions and uncertainties (green, orange) are taken from Peters et al. (2007).

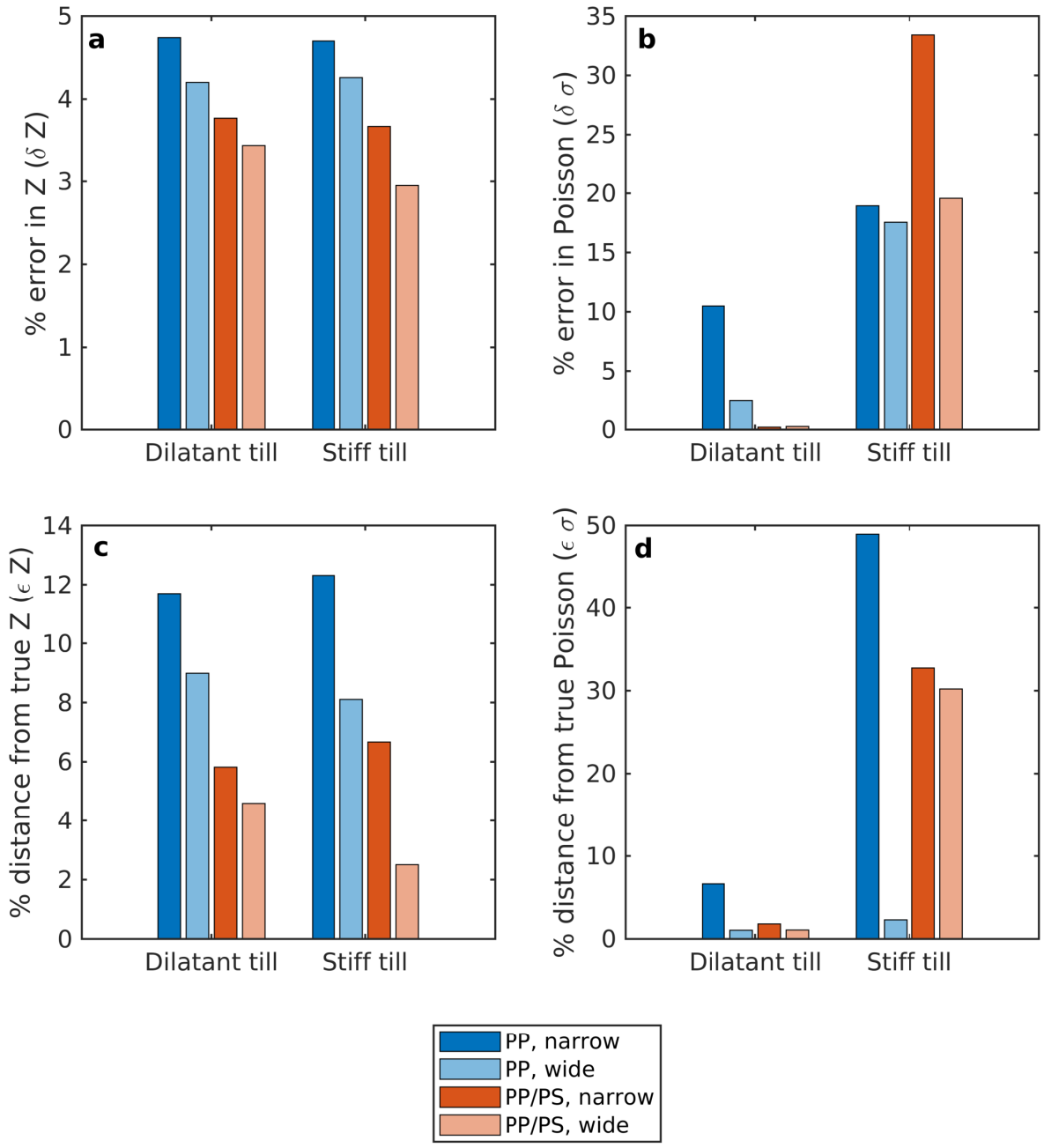

Figure 3.11: Precision and accuracy metrics for noisy inversions for beds of dilatant and stiff till. (a) δ_Z, (b) δ_σ, (c) ε_Z, (d) ε_σ.

3.6 Joint inversion including SS amplitudes

We have seen that joint inversion which includes PS waves can improve constraint of basal properties and reduce ambiguity in interpretations. In a three component acquisition, it is likely that SS waves will also be recorded - can these also help AVA inversions?

To test this, I run inversions which include SS wave AVA responses. I simulate noiseless SS responses for the five previously tested bed materials and cut the SS AVA responses off at the critical angle, as described in section 3.1.2. An S wave incident at the glacier bed goes critical at a much smaller angle than the respective P wave, typically in the region of $20^\circ \leqslant \theta_{\text{crit}} \leqslant 30^\circ$. Therefore for the wide-angle AVA tests, I expand the range only of the PP and PS data, and keep the SS data the same. The results are summarised in table 3.3, along with the results from the PP and PP/PS inversions. In the following discussion, I call PP inversion single inversion, PP/PS double joint inversion and PP/PS/SS inversion triple joint inversion. The accuracy and precision metrics are presented in Figure 3.12. In general, precision and accuracy is improved by inclusion of SS waves. However, the improvement triple inversion makes over double inversion is smaller than the improvement double inversion makes over single inversion.

Triple inversion shows a very slight improvement in precision of Z when compared with double inversion (Figure 3.12a). δ_Z is on average $\sim 4\%$ smaller for triple inversion than double inversion. For comparison, δ_Z is on average $\sim 24\%$ smaller for double inversion than single inversion.

The degree to which precision in σ is improved by triple inversion is greater for materials with high Poisson's ratios, consistent with the observations made in Section 3.4 (Figure 3.12b). For example, δ_σ for narrow triple inversion over dilatant till (high σ) is 4 times smaller than the corresponding δ_σ for narrow double inversion, whereas for lithified sediments (low σ), the precision is similar for the two inversions. However, the materials for which SS waves help to improve δ_σ already have very well constrained Poisson's ratios by double joint inversion: $\delta_\sigma < 1\%$ for both dilatant till and water under joint inversion. Therefore triple joint inversion offers little tangible benefit when compared with double joint inversion.

In some cases, triple inversion improves accuracy when compared with double inversion (Figures 3.12c and d). However, in other cases there is no improvement or the triple inversion accuracy is worse than that for double inversion (e.g. basement, water). These improvements are equivocal; where ε_Z is improved by triple inversion (stiff till, dilatant till), ε_σ is worsened. The converse

is true; where ε_σ is improved, ε_Z is worsened (e.g. basement, water). In any case, double joint inversion is consistently able to obtain results within 1% of the true Z, and within $< 5\%$ of the true σ, so again the inclusion of SS waves, while delivering a hypothetical improvement, will make little difference to the glaciological interpretation arising from a measurement.

An interpretive danger arising from SS AVA data is that of critical refractions. The Zoeppritz equations do not take into account head waves, and therefore can not be used at $\theta > \theta_{\text{crit}}$. The characteristic sharp peaks associated with incident P waves going critical enable their identification. However, the critical peaks in SS AVA responses are often smaller in magnitude and appear at smaller incidence angles (Section 1.3.3, Figure 1.5c). Therefore the potential that a critical peak is not visible above noise and remains unidentified makes the use of real-world SS AVA data in these inversions perilous.

To conclude, while including analysis of SS waves hypothetically has the potential to further improve glaciological AVA inversions, the improvement of triple joint (PP/PS/SS) inversion over double joint (PP/PS) inversion is small compared with the improvement double joint inversion makes over single (PP) inversion. Furthermore, difficulties in processing real SS data, such as poorly constrained S wave attenuation measurements, as well as the difficulty in producing S wave sources, remain barriers to the realisation of this technique. With current standards of data acquisition and processing I consider it unlikely that a result from triple joint inversion would be sufficiently better constrained than a result from double joint inversion to necessitate the time and effort invested in the extra processing required.

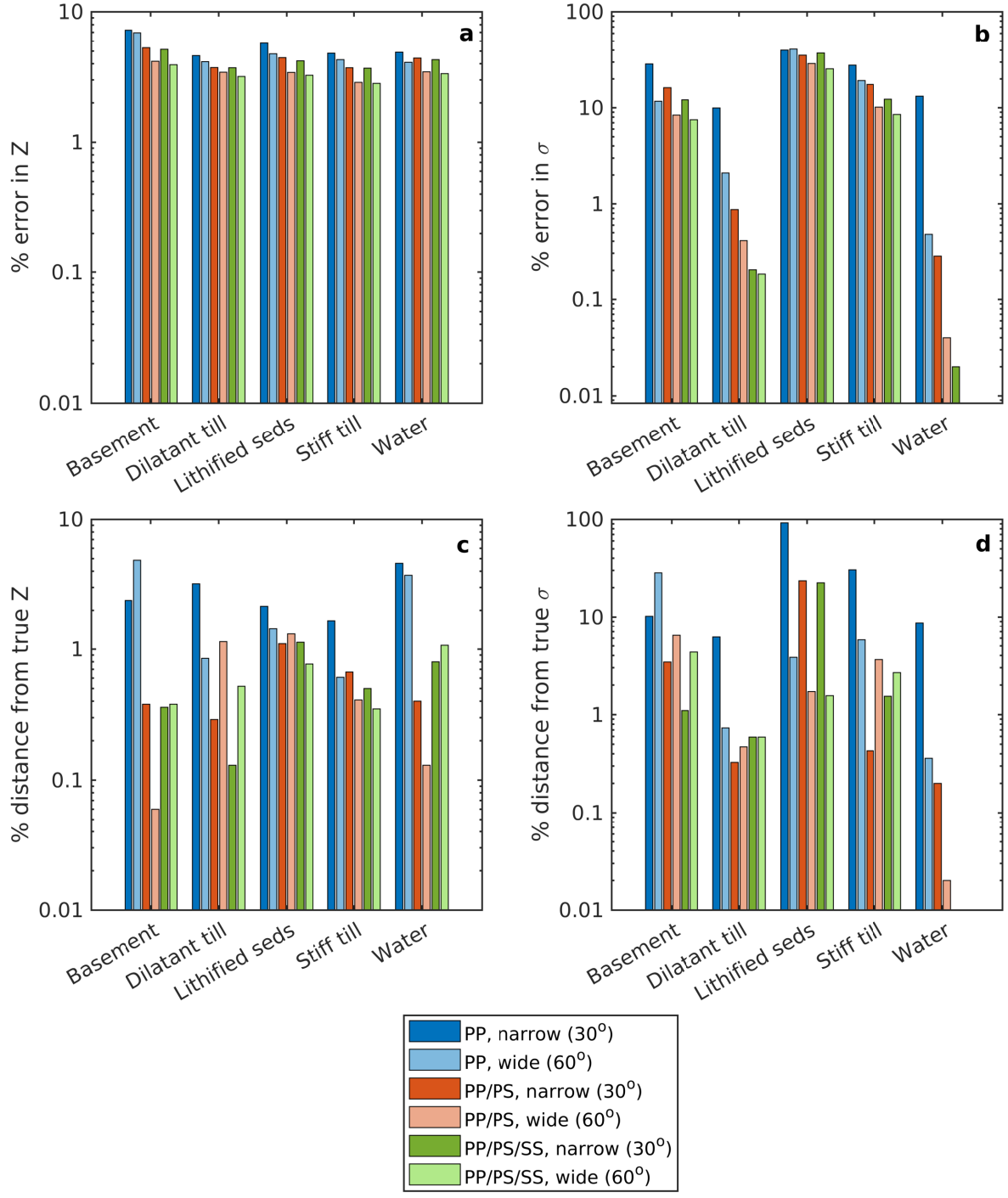

Figure 3.12: Accuracy and precision metrics for noiseless synthetic inversions. (a) δ_Z, (b) δ_σ, (c) ε_Z, (d) ε_σ.

3.7 Conclusions

In this chapter, I have investigated the potential of PP, PS and SS wave joint inversion to improve upon conventional methods of AVA inversion. I have presented a Bayesian Markov-chain Monte-Carlo method which uses the Metropolis-Hastings-Green algorithm to sample from the posterior distribution of models, calculating the likelihood of a model based on forward modelling AVA curves from the exact Knott-Zoeppritz equations. I have tested this inversion scheme on AVA responses from a variety of possible glaciological targets, comparing the performance of single (PP only) inversion, double joint (PP and PS) inversion, and triple joint (PP, PS and SS) on AVA responses which have maximum incidence angles of 30° and 60°.

My results show that in general, converted-wave joint inversion improves upon PP wave single inversion in both accuracy and precision. Joint inversion on AVA data with a maximum incidence angle of 30° performs similarly or favourably when compared with single inversion of data with incidence angles extending to 60°. The degree to which joint inversion improves over single inversion is dependent on the character of the AVA response, so future surveys need to be planned carefully to determine the optimal survey parameters for a particular glaciological target. This should include forward modelling the AVA responses of the possible bed materials and testing the inversion performance for wide single inversion and narrow joint inversion. Depending on the bed conditions and noise present, it may be difficult to predict whether inversion accuracy is better for wide single inversion than narrow joint inversion. In this case either may be sufficient, and the survey should be designed to complement other scientific aims as well as minimise the logistical requirements of the survey.

Extension of the inversion scheme to include SS wave information, while hypothetically able to deliver better-constrained results than PP/PS inversion, makes only a small improvement upon PP/PS inversion. I consider it unlikely that PP/PS/SS inversion of real datasets will lead to meaningfully better-constrained results than PP/PS inversion.

When designing an AVA survey, it may be logistically preferable to record three components using a narrower-angle survey geometry than recording one component with a wide-angle survey. For example, on ice 2.5 km thick, offsets of > 8.5 km would be required to obtain incidence angles of 60°, which may be difficult given competing priorities and limited time in a field deployment. An alternative survey design which may provide the best of both worlds may be to

lay out a standard wide-angle AVA survey, with mostly vertically oriented receivers, but with radially oriented receivers at regular intervals (e.g. every 4th or 5th receiver). In this manner, some PS information would be recorded while minimising the cost to the PP wave dataset.

Converted wave joint inversion may therefore make acquisition of AVA data easier and maximise the utility of acquisitions which include 3-component recording for complementary reasons such as shear wave splitting measurements. This has the potential to simplify acquisitions and optimise planning in time sensitive field deployments.

Chapter 4

Basal conditions at Korff Ice Rise, West Antarctica, from seismic AVA measurements

In this chapter I describe measurements of the basal conditions at Korff Ice Rise (KIR), West Antarctica. I investigate the utility of converted wave joint inversion when applied to a real dataset. I apply the method presented in Chapter 3 to the data and describe the processing to obtain absolute AVA responses, including geometric spreading, attenuation and source amplitude corrections (Section 4.2. For measuring source amplitude, I introduce a correction to the direct-path method of Holland and Anandakrishnan (2009) which takes account of the Q gradient in firn (Chapter 2), and find that the conventional direct-path method underestimates source amplitude by a factor of ~ 1.6 at this location (Section 4.2.3).

Jointly inverting the resultant AVA responses, I find that the bed has an acoustic impedance of $Z = (5.79 \pm 0.26) \times 10^6$ kg m^{-2}s^{-1} and a Poisson's ratio of $\sigma = 0.298 \pm 0.01$. P wave velocity, α, is 4.03 ± 0.05 km s^{-1}, S wave velocity, β, is 2.16 ± 0.06 km s^{-1}, and the density, ρ, is 1436 ± 60 kg m^{-3}. I interpret this response as arising from a bed of partially consolidated/lithified and/or frozen sediment. I will discuss the basal properties and their glaciological implications further in Chapter 5. I investigate the use of joint inversion at this site in a similar manner to that described in Chapter 3, running single and joint inversions both with all available data, and with data which is restricted to incidence angles of $\theta \leqslant 30^\circ$. I find that for a given survey

geometry, uncertainties in Poisson's ratio are 28% smaller under joint inversion than single inversion, but joint inversion does not meaningfully improve constraint of acoustic impedance for this dataset. I discuss a potential pitfall of this dataset owing to a possible misinterpretation of a polarity reversal, and argue that joint inversion is more robust to interpretive errors of this kind (Section 4.5.1). Finally, I make recommendations for future acquisition design.

4.1 Introduction

Chapter 3 shows the potential of joint inversion to aid glaciological AVA experiments. In practice, AVA uncertainties are influenced by source amplitude and attenuation effects being poorly known, but needing to be accounted for (Holland and Anandakrishnan 2009). In this chapter, I apply my method to data from KIR, aiming to determine the bed conditions of the site. KIR is an ice rise in the Weddell Sea sector of West Antarctica which may have ungrounded and regrounded following deglaciation after the last glacial maximum, as discussed in Chapter 1, Section 1.5 (Brisbourne et al. 2019; Kingslake et al. 2016). Establishing whether or not the bed at KIR is frozen has implications for the deglaciation history of the region, and could potentially offer insight into the date of grounding.

The data used for the following analysis are described in Chapter 1, Section 1.6.2. I use data from Acquisition B for the PP wave analysis, and Acquisiton C for the PS wave analysis. Acquisition B used four separate shots of 150 g Pentolite, buried at 20 m depth, recorded on vertically oriented georods. These gathers were then combined into a supergather and displayed in Section 1.6.2. Acquisiton C used four shots of 600 g Pentolite, buried at 20 m depth. The georods were placed alternately radially and transversely. I use the radial component only for the PS wave analysis. For the purposes of the following chapter, the bed is assumed homogeneous and the bed roughness is assumed small. This is considered reasonable given the reflection profile presented in Figure 1.11.

To obtain AVA amplitudes, I pick the start and end of a wavelet, and take the root-mean-square of the amplitude, as recommended by Horgan et al. (2021). Figure 4.1 shows the root-mean-square (RMS) amplitudes of the PP and PS bed reflections as a function of source-receiver offset, with interpreted polarities (i.e. RMS amplitudes are multiplied by -1 for an interpreted negative polarity reflection, as for the PS reflection shown in Figure 4.1b). As previously described in Chapter 1, the equation used for calculating the P wave reflection coefficient from

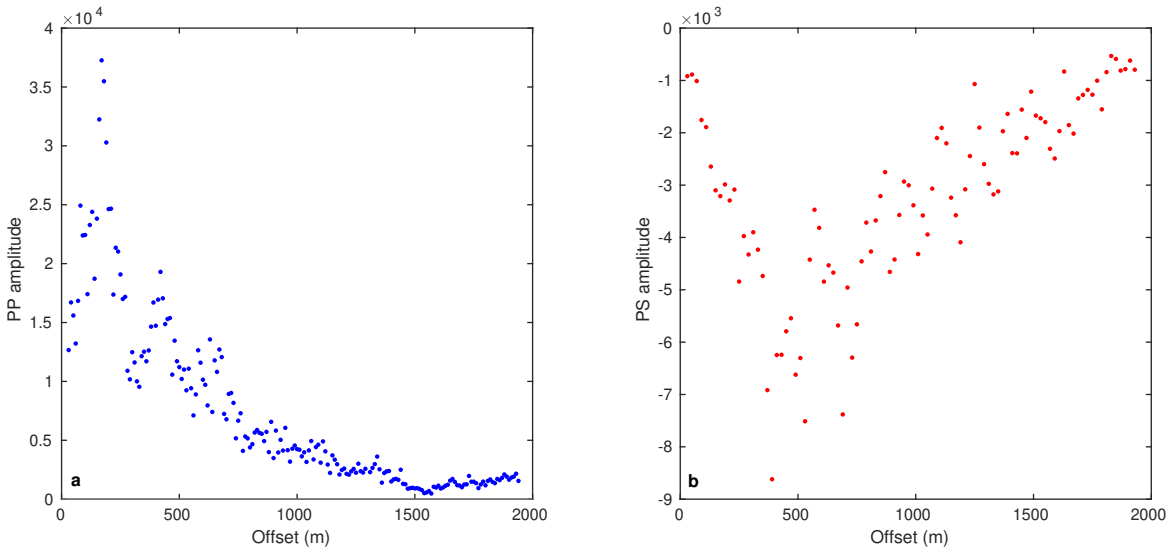

Figure 4.1: Raw RMS amplitudes of (a) PP and (b) PS reflection picks.

these amplitudes is:

$$R_{PP} = \frac{A}{A_0}\frac{1}{\gamma}e^{\pi f t^{*}(x)}, \tag{4.1}$$

where A is the measured amplitude, A_0 is the source amplitude, γ is the geometric spreading factor, f is frequency and $t^* = t/Q$ is the attenuated time of a ray having travel time t and quality factor Q. For the PS converted wave, the P and S portions of the ray path are dealt with separately, and the PS wave reflection coefficient, R_{PS} is:

$$R_{PS} = \frac{A}{A_0}\frac{1}{\gamma_P \gamma_S}e^{\pi f t_P^*}e^{\pi f t_S^*}, \tag{4.2}$$

where γ_P and γ_S are the geometric spreading factors for the P and S wave parts and t_P^* and t_S^* are the attenuated times of the P and S wave parts of the ray path. In the following sections, I describe the stages of data processing necessary for the calculation of each of the terms in Equations 4.1 and 4.2.

4.2 Data processing

ReflexW (www.sandmeier-geo.de) was used to pick wavelet arrival times. MATLAB was used for all further processing.

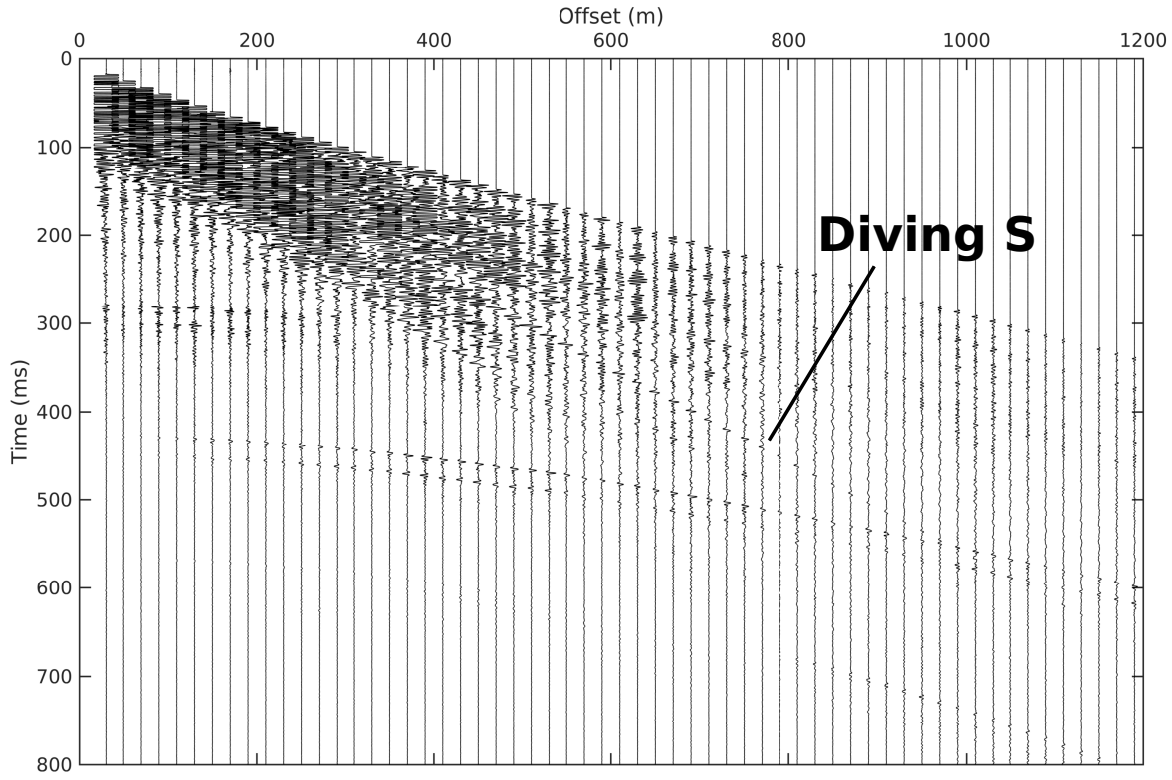

Figure 4.2: Close up of radial component (acquisition C), showing the diving S wave used for WHI

4.2.1 Velocity model and ray tracing to find $\theta(x)$ and reflection points

Wiechert-Herglotz inversion was used to obtain P and S wave velocity models using the method by Kirchner and Bentley (Kirchner and C. R. Bentley 1990), as described in Section 2.2. Figure 4.2 shows radial traces from Acquisition C, with the diving S wave used to pick S wave travel times labelled.

I used the P velocity model from chapter 2. I then assumed a linearly increasing temperature profile from the surface to the bed (as observed by Mulvaney et al. (2021) at the nearby Skytrain Ice Rise). This implies a linearly decreasing velocity profile from the base of firn to the bed, with velocities calculated from the empirical relation by Kohnen (1972). The velocities were tuned to match normal-incidence arrival times of the primary reflection, after Brisbourne et al. (2023). Figure 4.3 shows the P and S wave velocity-depth models used.

To find the incidence angles and reflection points for PP and PS reflections, I traced rays through these velocity profiles. Figure 4.4 shows the reflection points for the four shots in the P wave and S wave record. All of the PP reflection points lie in the same region of $\sim$ 200 m length. Due to the asymmetric ray paths of PS waves and the symmetric progression of offsets, the

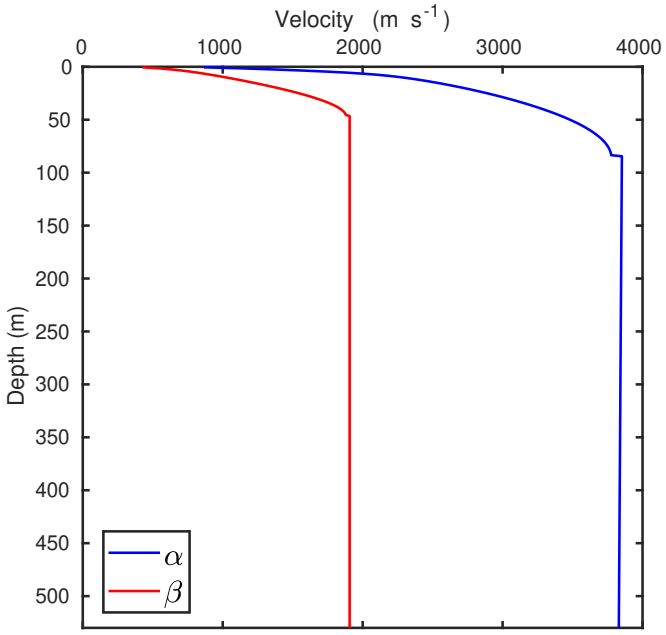

Figure 4.3: Models of P wave velocity, α, and S wave velocity, β, used for ray tracing to find reflection points and incidence angles

PS reflection points are spread over a wider region than those for PP. PS reflection points are marked in red, with the circled numbers denoting the shot for which those reflection points are recorded (e.g. for shot (1) at 960 m, the receivers were laid out between 990 and 1470 m, and reflection points lie between 980 m and 1300 m). The PS reflection points span almost 1 km. Given the observed bed homogeneity, I expect no variation on this scale (Figure 1.11). For a less homogeneous bed, the survey would have to be designed in order to ensure a smaller spread of PS reflection points, or alternatively heterogeneity could be preserved by processing the PS data as individual gathers rather than the supergather presented here.

4.2.2 Geometric correction

I assume spherical spreading inversely proportional to the path length r. Amplitudes are also corrected for the angle of the ray as it reaches the receiver. The geometric correction factor $\gamma(x)$ is therefore

$$\gamma(x) = \frac{1}{r(x)} \cos\theta_{\text{rec}}, \tag{4.3}$$

where $r(x)$ is the path length of the ray and θ_{rec} is the angle of the ray as it reaches the receiver

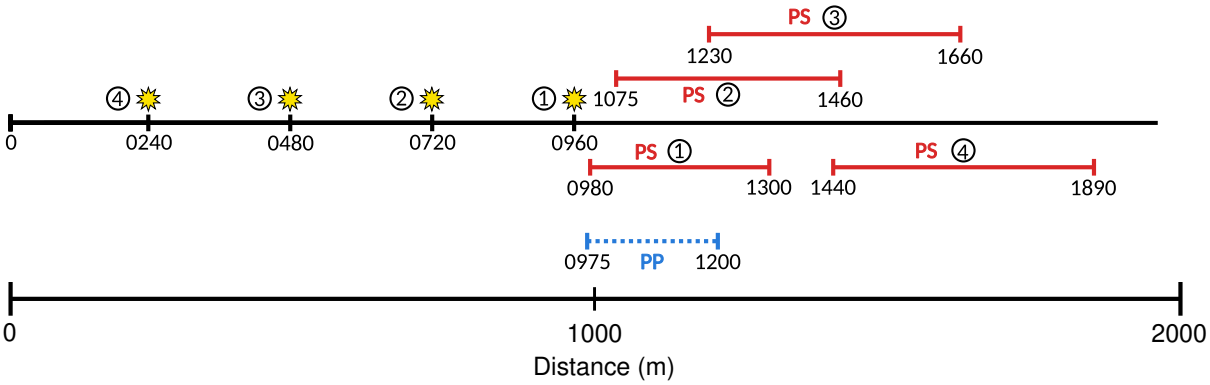

Figure 4.4: Reflection points for PP data (blue) and PS data (Red). Positions of shots along the line are labelled with circled numbers. Reflection points from all four shots in the P wave record fall in the same region. PS reflection points are spread over a wider area of the bed. Distances are in metres measured from the end of the reflection line.

(Zechmann et al. 2018).

4.2.3 Source amplitude

4.2.3.1 Source variability

Prior to further processing, I examine the shot-to-shot variability in source amplitude. The amplitude $A(x)$ of a diving wave emerging at an offset x is:

$$A(x) = A_0 \gamma(x) \mathrm{e}^{\frac{-\pi f}{Qv} r(x)}, \tag{4.4}$$

where A_0 is the source amplitude, $\gamma(x)$ describes geometric spreading, f is frequency, Q is the quality factor, v is wavelet velocity and $r(x)$ is the path length. Taking the natural logarithm of $A(x)$ gives:

$$\ln A(x) = \ln A_0 + \ln \gamma(x) - \frac{\pi f}{Qv} r(x). \tag{4.5}$$

At sufficiently far offsets (here, for $x > 500$ m), $r(x)$ is proportional to x and $\ln A(x)$ is linear with offset. Figure 4.5 shows the natural logarithm of diving wave amplitude as a function of offset, for a) Acquisition B and b) the radial component of Acquisition C. The amplitudes shown are corrected for the angle of the ray as it reaches the receiver, θ_{rec}. For Acquisition B, diving P waves were recorded on vertical georods:

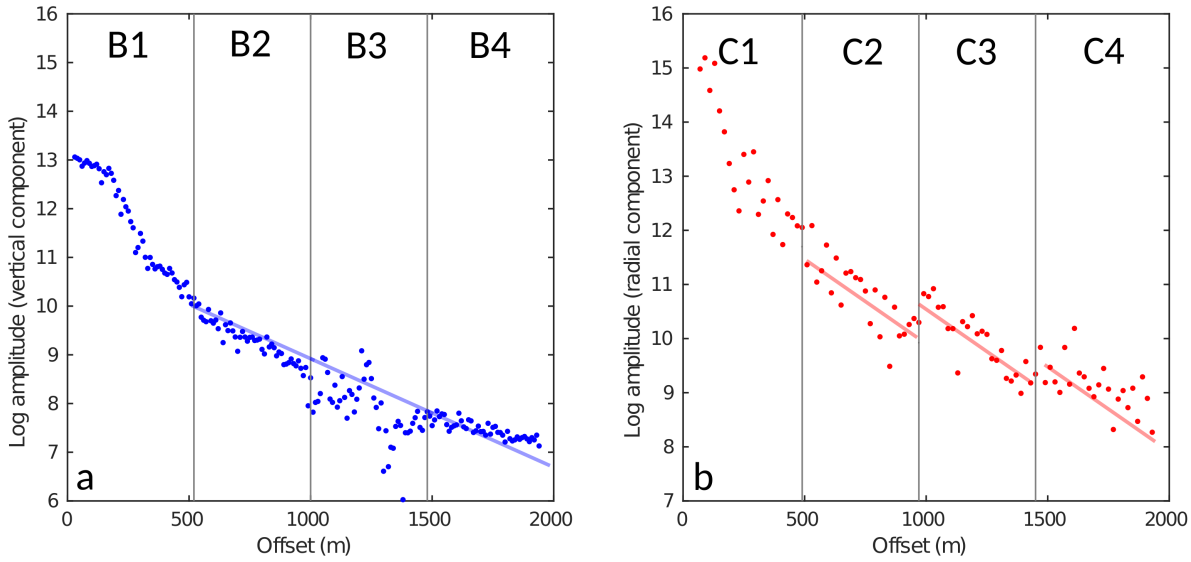

Figure 4.5: RMS amplitudes of the direct P wave recorded from acquisitions (a) B and (b) C. Four shots were used for each acquisition, here labelled (a) B1-B4 and (b) C1-C4. Vertical lines show the boundaries between amplitudes recorded with separate shots. B1-B4 are 150g Pentolite sources and C1-C4 are 600g Pentolite sources.

$$A = \frac{A_v}{\cos\theta_{\text{rec}}}, \tag{4.6}$$

where A is the true amplitude and A_v is the component of amplitude measured by a vertical georod. This is the familiar $\cos\theta$ obliquity term in the geometric correction (Equation 4.3). Since Acquisition C records diving P waves on radially oriented georods, their amplitudes are instead corrected using

$$A = \frac{A_r}{\sin\theta_{\text{rec}}}. \tag{4.7}$$

A is the true amplitude and A_r the component of amplitude measured by a radial georod (a sketch is shown in Figure 4.6).

Discontinuities in the linear trends of Figures 4.5a and b are assumed to result from differences in source size, as for adjacent offsets x_1, x_2,l $\gamma(x_1) \simeq \gamma(x_2)$. Figure 4.5a shows consistent source sizes between shots B1-B4, with continuity between shots. Amplitudes recorded from shot B3 are noisier than B1-B2 and B4. Figure 4.5b shows the amplitudes of the diving P waves recorded on the radial component geophones in Acquisition C. Shots C1 and C2 show good continuity, but shots C3 and C4 are clearly larger than C1 and C2. Consequently I multiply amplitudes

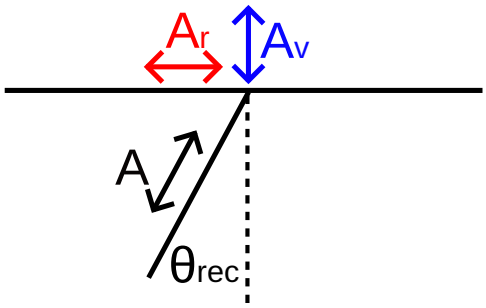

Figure 4.6: Component amplitudes of a diving P wave (black line) incident at the surface with amplitude A, recorded on vertical (blue, amplitude A_v) and radial (red, amplitude A_r) georods. $A_r = A \sin\theta_{rec}$ and $A_v = A \cos\theta_{rec}$, leading to Eqs. 4.6 and 4.7

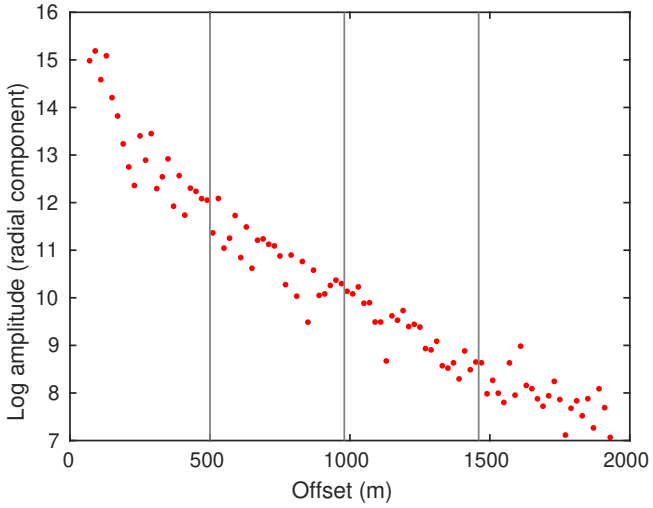

Figure 4.7: Amplitudes of diving waves recorded by Acquisition C, corrected for source size variability and incidence angle θ_{rec}. Amplitude decay is non linear at $x < 500$ m due to the diving waves recorded at these offsets penetrating only into the shallow firn, where velocity increases with depth.

from shot C3 by 0.5 and C4 by 0.2 to ensure continuity. The diving wave amplitudes corrected for source size variability and incidence angle are shown in Figure 4.7. I use these amplitudes to calculate the PS wave source amplitude.

4.2.3.2 PP source amplitude

To measure the source amplitude of the PP reflection (Acquisiton B), I was able to use the multiple-bounce method, which compares the amplitudes A_1 and A_2 of the primary reflection and its first multiple at normal incidence. A_0 is calculated using the equation

$$A_0 = \frac{{A_1}^2}{A_2} \frac{1}{2\gamma_1}, \tag{4.8}$$

where γ_1 is the geometric spreading factor for the primary reflection (Holland and Anandakrishnan 2009). The multiple-bounce method is considered the most reliable method of measuring source amplitude (Horgan et al. 2021). Using this method, the source amplitude for the PP reflection recorded in Acquisition B was measured as $(2.22 \pm 1) \times 10^8$.

4.2.3.3 PS source amplitude

The PP and PS reflections were recorded using different sized sources (see Section 1.6.2), so the source amplitude must be independently constrained for each acquisition. However, Acquisition C included no vertically oriented georods, so the P wave first-order multiple (PPPP) was not recorded. Consequently the source amplitude for Acquisition C was measured using diving P waves measured on radial component georods.

The direct-path method by Holland and Anandakrishnan (2009) is commonly used to estimate source amplitude in cases where multiples are not present (e.g. Clyne et al. 2020; Holland and Anandakrishnan 2009; Muto et al. 2019b). It uses the amplitudes A_1 and A_2 of two diving waves with path lengths r_1 and r_2, which are chosen such that $r_2/r_1 = 2$, to compute A_0:

$$A_0 = \frac{{A_1}^2}{A_2} \frac{\gamma_2}{{\gamma_1}^2}. \tag{4.9}$$

γ_1 and γ_2 are the geometric spreading factors of the two diving waves.

Equation 4.9 assumes that the path-averaged attenuation is the same for the two ray paths. As we have seen, the seismic quality factor Q increases with depth in firn (Chapter 2), so the assumption of Equation 4.9 is not correct. The path-averaged Q, Q_{av}, can be computed by tracing the diving waves through n firn layers of quality factor Q_i, in which the ray spends time t_i, to find the ray's attenuated time, t^*_{tot}. Attenuated time is cumulative along the ray:

$$t^*_{\text{tot}} = \sum_i^n \frac{t_i}{Q_i} = \frac{t_{\text{tot}}}{Q_{\text{av}}}. \tag{4.10}$$

Q_{tot} can then be calculated from t^*_{tot} and t_{tot}. As the source-receiver offset increases, the diving waves penetrate deeper into the firn, and the path-averaged Q experienced by the ray increases. Figure 4.8 shows the path-averaged Q for diving P waves of increasing offset in the firn at KIR. For example, a ray emerging at 600 m experiences an effective $Q = 205$, while a ray emerging

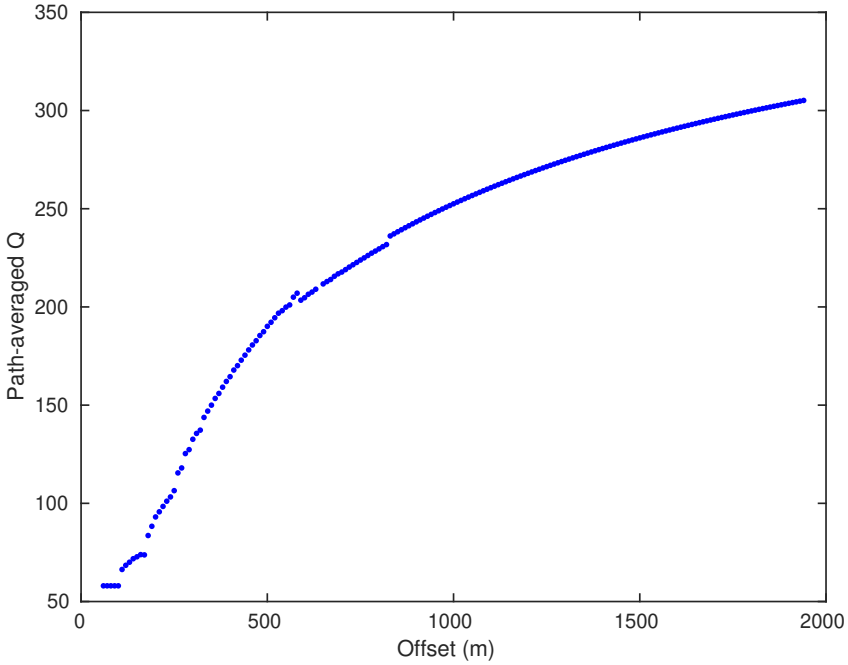

Figure 4.8: Path averaged Q for diving P waves at increasing offsets, given the Q_P versus depth model determined in Chapter 2, determined by ray tracing. 'Steps' in the curve at 100, 170, 560 and 820 m are artefacts resulting from the stepped Q model used.

at 1200 m experiences an effective $Q = 270$, given the Q_P and velocity versus depth models determined in Chapter 2. This is true even for rays which penetrate near to the base of the firn. Consider two rays A and B which penetrate to similar depths in the firn, near to the critical refraction, where the velocity increases only slowly with depth. The further offset ray can emerge at a much larger offset while only penetrating slightly deeper (Figure 4.9). The depth-averaged Q is similar for the two rays since they sample similar portions of the firn column. In contrast, the path-averaged Q for the further offset ray is larger, since this ray spends a greater proportion of its time in the higher-Q deep firn, leading to a larger contribution to the total attenuated time from the deeper firn. Consequently the direct-path method using Equation 4.9 underestimates source amplitude.

To account for attenuation, Equation 4.9 can be modified with an exponential term:

$$A_0 = \frac{{B_1}^2}{B_2} \frac{\gamma_2}{{\gamma_1}^2} e^{\pi f (2t_1^* - t_2^*)}, \tag{4.11}$$

where f is the frequency of the diving wave and t_1^*, t_2^* are the attenuated times of rays 1 and 2, respectively. If Q is assumed equal for rays 1 and 2, and $t_2 = 2t_1$, then $t_2^* = 2t_1^*$ and Equation

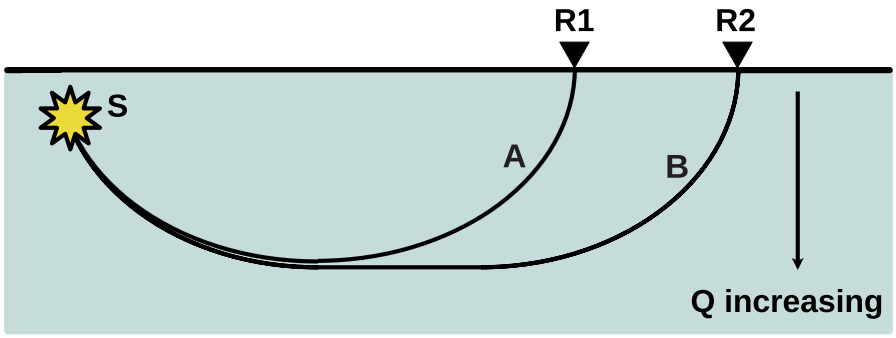

Figure 4.9: Two diving waves which penetrate near to the base of the firn, where velocity increases slowly with depth. As determined in Chapter 2, Q increases with depth. Since rays A and B penetrate to similar depths, their depth-averaged Q is similar. However since ray B spends a larger portion of its time at the base of the firn, its path-averaged Q is larger than that of ray A.

4.11 simplifies to Equation 4.9 (Holland and Anandakrishnan 2009). However, if Q is known not to be constant, the exponential term is significant. Where $r_2 = 2r_1$, the geometric spreading terms reduce to $\gamma_2/\gamma_1^2 = r_1/2$. I call the method using Equation 4.11 the variable-Q direct-path method.

I measure A_0 using pairs of rays at offsets x_1, x_2 with path lengths r_1, r_2 for which $1.995 < \frac{r_1}{r_2} < 2.005$ and $x_1 > 500$ m. This means that for all offset pairs, both rays penetrate close to the base of the firn column. Rays are traced through the velocity and Q models determined in Chapter 2 to estimate t^* for each ray, and a single frequency of $f = 300$ Hz is used.

The constraint of $x_1 > 500$ m is not necessary for the variable-Q direct-path method (Equation 4.11) since this equation makes no assumptions about attenuation, but the conventional direct-path method (Equation 4.9) requires that rays penetrate to the base of the firn so Q can be assumed equal for the two rays. I compute A_0 using the two methods, using the same rays, in order to directly compare results.

Using the conventional direct-path method, the source amplitude is measured as $(2.6 \pm 1.9) \times 10^8$. The variable-$Q$ direct-path method results in a corrected source amplitude of $A_0 = (4.1 \pm 2.9) \times 10^8$, meaning that Equation 4.9 underestimates A_0 by a factor of ~ 1.6. Correspondingly, using the conventional direct-path method with no Q consideration would overestimate reflection coefficients by the same factor.

In all further analysis I use $A_0 = (4.1 \pm 2.9) \times 10^8$ for the source amplitude of the PS wave.

4.2.4 Attenuation correction

In Chapter 2, I detail measurements of attenuation over various depth ranges of the ice column. Despite the depth-dependence of Q, the simplest way of correcting reflection amplitudes for attenuation is to assume an equivalent uniform Q over the entire glacier (2.4). Furthermore, correcting for uniform Q in this way has the advantage of smaller uncertainties than a layer-stripping Q model, which propagates errors through the layers. Consequently I use the primary-multiple measurement of $Q_P = 250 \pm 100$. As I was unable to measure Q_S over the whole ice column, I assume $Q_P/Q_S = 3$, after measurements by Clee et al. (1969), which results in $Q_S = 83 \pm 30$. For the PP reflection I correct amplitudes for a single frequency of $f = 300$ Hz, and for PS, I correct for a single frequency $f = 225$ Hz. These frequencies are determined by inspection of individual reflected wavelet spectra.

4.2.5 Error Analysis

The errors on the reflectivity are assumed to be dominated by the errors in attenuation measurement and source amplitude. I therefore estimate the error in reflectivity δR using the equation:

$$\delta R = R\left[\left(\frac{\pi f r}{v Q^2}\right)^2 (\delta Q)^2 + \frac{1}{{A_0}^2} (\delta A_0)^2 \right]^{1/2}. \tag{4.12}$$

Here, f is the dominant frequency of the wavelet, r is the path length, v is the wave speed, and Q is the quality factor. δQ is the error in the quality factor measurement.

4.3 Corrected AVA responses and inversion setup

The PP and PS AVA responses, corrected by the above source amplitude, geometric spreading and attenuation terms, are shown in Figure 4.10. Incidence angles, obtained by ray tracing, reach 63° for PP and 73° for PS reflections. The solid lines shown in Figure 4.10 represent the median model found by jointly inverting R_{PP} and R_{PS} using all available data. R_{PP} decreases from 0.15 ± 0.1 at close to normal incidence to 0.03 ± 0.03 at 57°, before rising again. R_{PS} has its greatest magnitude of -0.6 ± 0.7 at 45°. The Knott-Zoeppritz fit to the median model shows a critical refraction at 72°, 10° beyond the maximum incidence angle captured by the PP AVA response. This is consistent with the rise in R_{PP} towards 70°, which would be expected from a critical refraction.

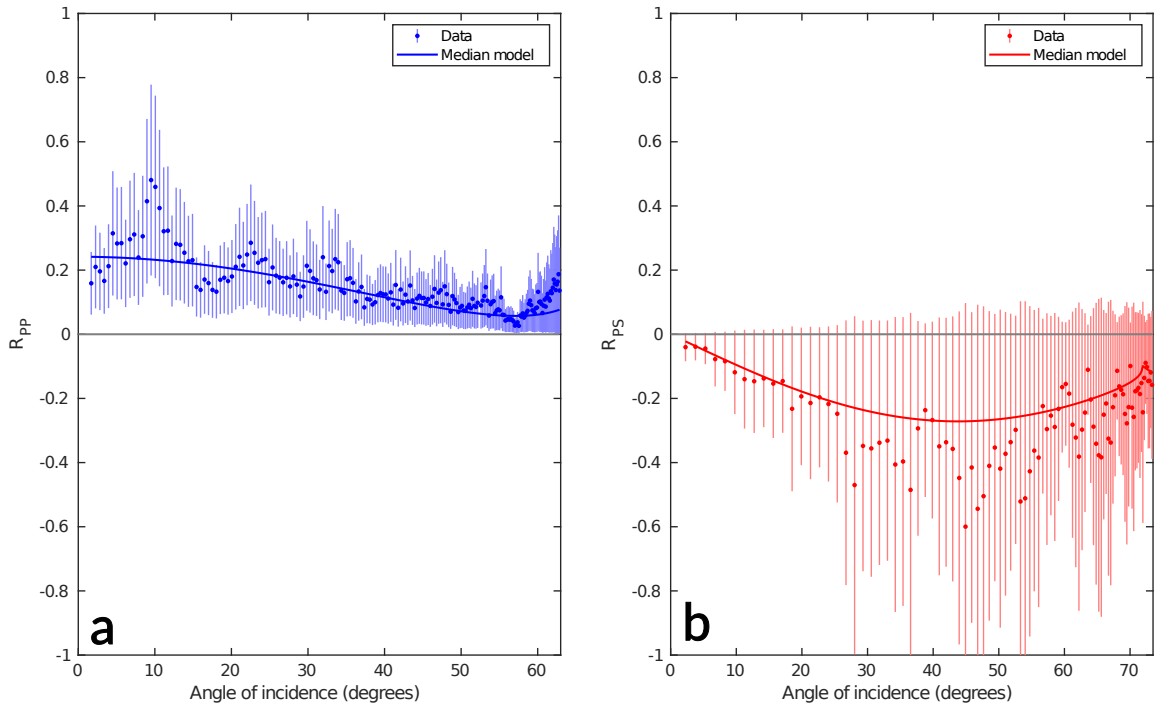

Figure 4.10: a) PP, and b) PS AVA responses at Korff Ice Rise. Solid lines indicate median models from jointly inverting all available data. Cyclical amplitude variations are assumed to result from inhomogeneities in basal properties between Fresnel zones across the area of reflections.

Following the procedure described in Chapter 3, I run four separate inversions of the AVA responses, which invert different subsets of the available data: i) the PP response only, with data for $0 \leqslant \theta \leqslant 30^{\circ}$ only; ii) PP and PS, over $0 \leqslant \theta \leqslant 30^{\circ}$; iii) PP only, using all available data ($\theta \leqslant 63^{\circ}$); and iv) PP and PS, using all available data ($\theta_{PP} \leqslant 63^{\circ}, \theta_{PS} \leqslant 73^{\circ}$).

I run each inversion for $5,000,000$ iterations. The basal ice properties are assumed to be $\alpha_{\text{ice}} = 3830 \pm 50\text{m s}^{-1}$, $\beta_{\text{ice}} = 1906 \pm 50\text{m s}^{-1}$, and $\rho_{\text{ice}} = 920 \pm 50\text{m s}^{-1}$. The basal ice properties are allowed to vary to account for the uncertainty in temperature at the base of the ice column.

4.4 Results

Results of the four inversions are summarised in Table 4.1, which quotes the medians and inter-quartile ranges of output marginal distributions for P wave velocity, S wave velocity, density, acoustic impedance and Poisson's ratio of the basal material. Figure 4.11 shows marginal distributions of acoustic impedance and Poisson's ratio as 2D histograms.

Inversion type	Extent	α (km s^{-1})	β (km s^{-1})	ρ (kg m^{-3})	Z ($\times 10^6$ kg m^{-2}s^{-1})	σ
PP	30°	3.4 ± 1	1.76 ± 0.7	1650 ± 600	5.59 ± 0.30	0.299 ± 0.075
PP/PS	30°	3.3 ± 1	1.85 ± 0.65	1740 ± 640	5.69 ± 0.27	0.255 ± 0.055
PP	All data	4.02 ± 0.07	2.15 ± 0.08	1418 ± 60	5.69 ± 0.26	0.300 ± 0.014
PP/PS	All data	4.03 ± 0.05	2.16 ± 0.06	1436 ± 60	5.79 ± 0.26	0.298 ± 0.010
PP/PS	All data	2.53 ± 0.4	1.04 ± 0.24	2150 ± 350	5.44 ± 0.23	0.40 ± 0.018

Table 4.1: Results from all inversions of Korff AVA responses. All results quoted are medians $\pm$ inter-quartile range of marginal distributions. Results quoted in the final row are obtained from data interpreted to have a polarity reversal at 57°, discussed in Section 4.5.1.

For the $0-30°$ inversions (panels a and c), acoustic impedance is well constrained but Poisson's ratio is not. In constraining acoustic impedance Z, single and joint inversion perform comparably, with the uncertainty in Z 10% smaller in the case of joint inversion ($Z = (5.69 \pm 0.27) \times 10^6$ kg m^{-2}s^{-1} for joint inversion vs $Z = (5.59 \pm 0.3) \times 10^6$ kg m^{-2}s^{-1} for single inversion). In contrast, joint inversion constrains Poisson's ratio σ significantly better than single inversion does, with the uncertainty in σ 27% smaller under joint inversion ($\sigma = 0.255 \pm 0.055$ for joint inversion vs $\sigma = 0.299 \pm 0.075$ for single inversion).

When all available data were used, both acoustic impedance and Poisson's ratio were better constrained than in the restricted angle case, for single and joint inversion. However, the improvement in constraint of Z by including the wide-angle data was small. When comparing wide-angle joint inversion with wide-angle single inversion, I find no meaningful improvement in constraint of acoustic impedance ($Z = (5.79 \pm 0.26) \times 10^6$ kg m^{-2}s^{-1} for joint inversion vs $Z = (5.69 \pm 0.26) \times 10^6$ kg m^{-2}s^{-1} for single inversion). While extending the inversion to wide angles does little to improve constraint of Z, it significantly improves constraint of σ. Using all the available data, the uncertainty in σ is $\sim$ 80% smaller for both single and joint inversions than when θ is restricted. Consistent with the 30° inversions, joint inversion of the wide-angle data produces a result with an uncertainty in σ 28% smaller than that for single inversion.

Results from wide-angle and restricted-angle inversions are consistent with each other. This demonstrates the robustness of the inversion, indicating that far offset amplitudes and near offset amplitudes are consistent with one another for both PP and PS waves.

In all further analysis, I use the results from joint inversion of all data. Marginal distributions of α, β and ρ for basal ice and he subglacial material are shown in Figure 4.12, with medians indicated by the dashed lines. In this case, velocities and density of the subglacial material are

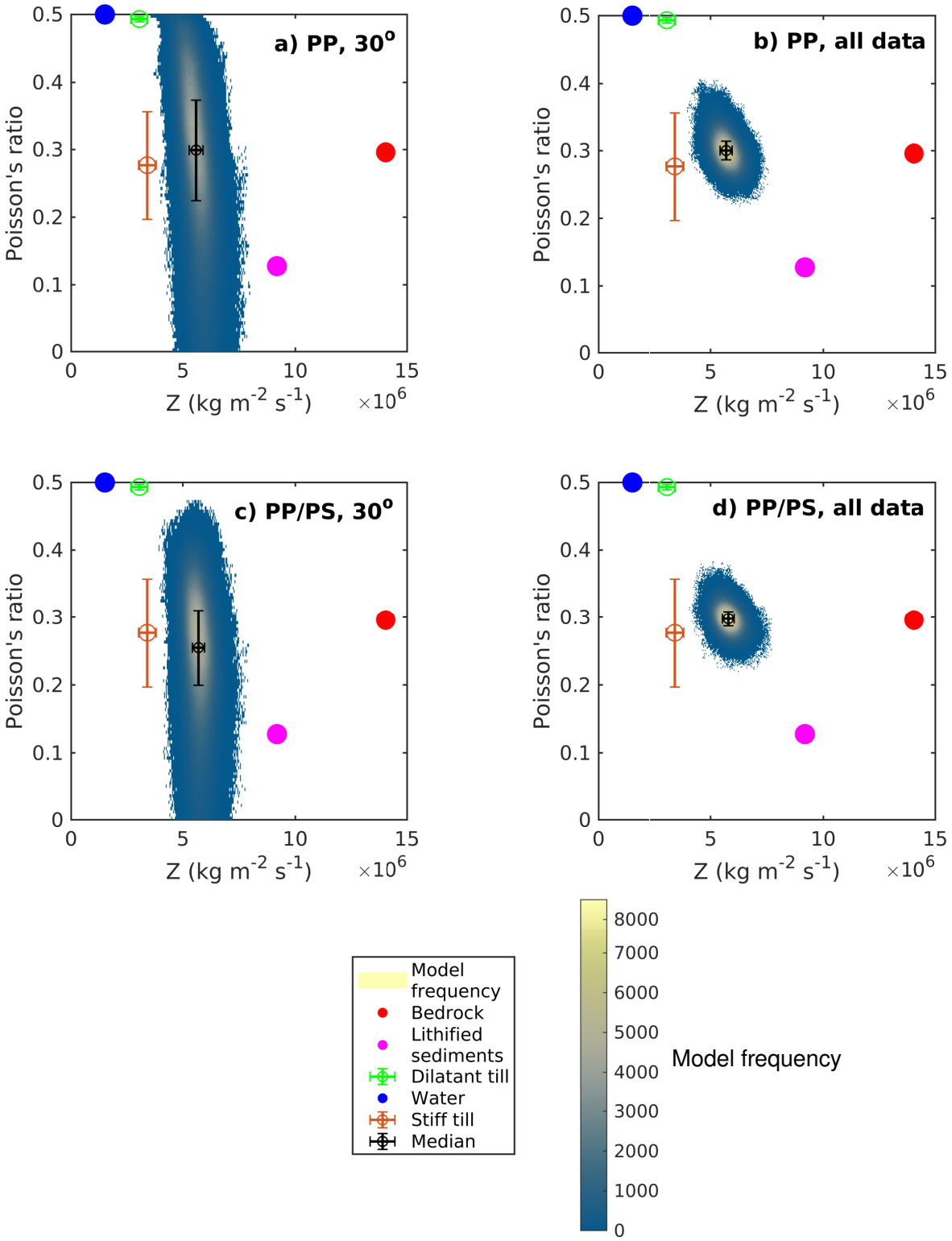

Figure 4.11: Inverted bed properties at Korff Ice Rise. a) PP-only inversion, using $\theta \leqslant 30°$. b) PP-only inversion, using all available data. c) Joint PP/PS inversion, using $\theta \leqslant 30°$. b) Joint PP/PS inversion, using all available data.

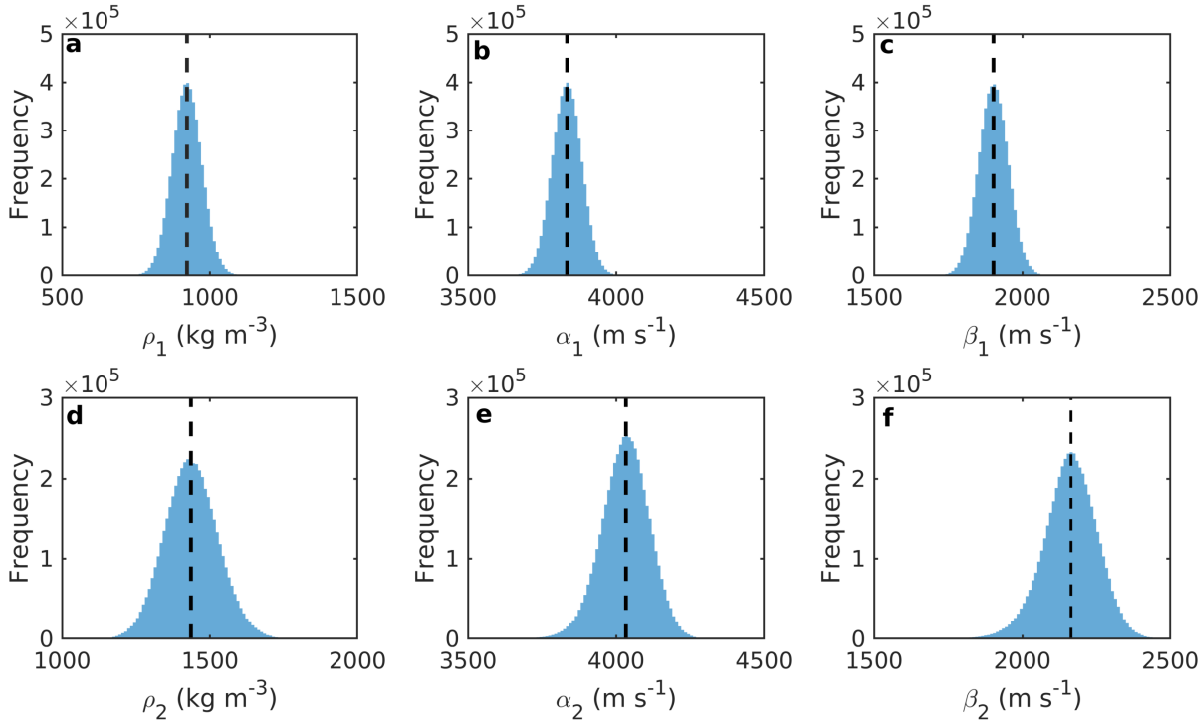

Figure 4.12: Histograms showing marginal distributions of explored model properties, of basal ice (a-c) and the bed (d-f). Vertical dashed lines indicate medians of the distributions. Density, P wave velocity and S wave velocity are all well constrained in this case. These distributions are those resulting from joint inversion of all data.

very well constrained, which should help in identifying the subglacial material; in Chapter 5 I will make a more detailed interpretation of these properties. Marginal distributions of Z and σ are shown in Figure 4.13, with the medians indicated.

4.5 Discussion

Taking the result from joint inversion of all available data, the subglacial material has an acoustic impedance of $Z = (5.79 \pm 0.26) \times 10^6$ kg m^{-2}s^{-1} and a Poisson's ratio of $\sigma = 0.298 \pm 0.01$. This rules out many common glacial substrates such as dilatant till and bedrock (e.g. of igneous origin), and makes a bed of fully lithified sediments unlikely (see Table 3.1). I also rule out pooling of liquid water at the bed in this location. The properties are closest to those of stiff till previously reported by Peters et al. (2008), although the higher acoustic impedance implies greater consolidation and/or freezing. I therefore interpret the response as that originating from partially consolidated/lithified or frozen sediments. I will expand on this interpretation and discuss it further in Chapter 5. I intend to use the following section to discuss the subtleties and limitations of the geophysical inversion described in this chapter.

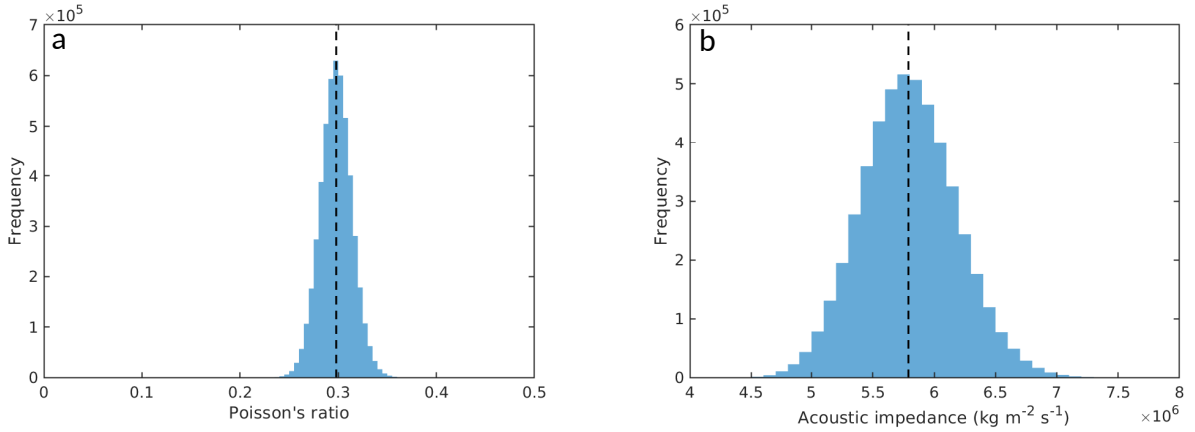

Figure 4.13: Histograms of marginal distributions of basal (a) Poisson's ratio and (b) Acoustic impedance resulting from joint inversion of all data, also shown in Figure 4.11. Dashed lines indicate the distribution medians.

4.5.1 A polarity reversal at 57°?

As demonstrated in Chapter 3, and shown by other authors (Anandakrishnan 2003), a polarity reversal in an AVA response is highly diagnostic; if correctly interpreted, it can be a powerful piece of information for identifying subglacial substrates. However, it presents a risk to AVA analysis if the polarity is ambiguous and a polarity reversal may be misinterpreted.

Figure 4.14 shows the supergather for all vertical georods in Acquisition B, with enlarged views of wavelets at offsets 720 m, 1550 m and 1930 − 1950 m. The polarity of the PP reflection is ambiguous at offsets > 1550 m. The amplitude of the reflection decreases to a minimum at ∼ 1550 m (∼ 56°), whereafter it increases. At near offsets, the wavelet is a clear 'white-black-white' polarity. At ∼ 1550 m, the wavelet is still the same polarity but becomes difficult to distinguish above noise. Looking at the furthest offsets, 1930−1950 m, the polarity is ambiguous due to interference from refracted waves (red arrow, Figure 4.14): the largest amplitude portion of the wavelet is the second white portion. The red and blue crosses in Figure 4.14 indicate possible picks of where the wavelets begin and end: it is possible to interpret the polarity as 'white-black-white' (red picks), or alternatively, 'black-white-black' (blue picks). In the previous sections, I have interpreted the red picks as correct, and interpret the the large white amplitude and following significant black tail as resulting from interference. However, an alternative interpretation is that of a polarity reversal in the AVA response at intermediate offsets, which would imply the blue picks are correct.

How should we interpret the wavelet in question? To illustrate the effect of misinterpreting the

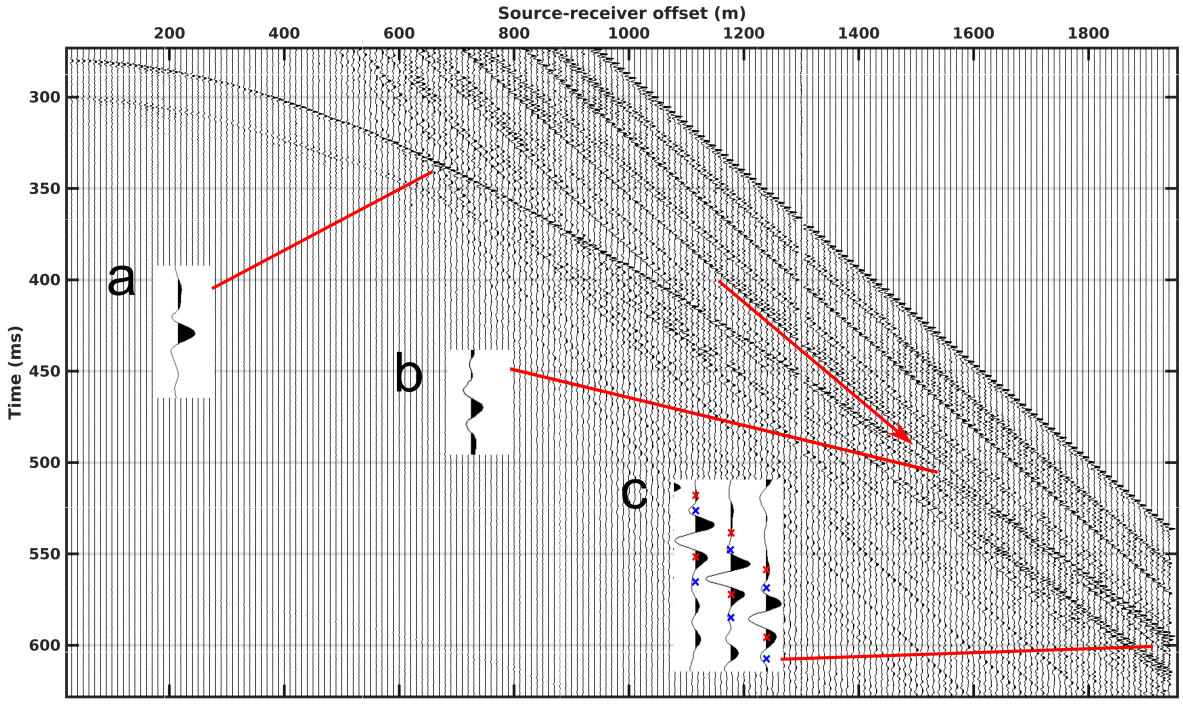

Figure 4.14: PP reflection, with enlarged wavelets from a) 720 m, b) 1550 m, c) 1930 – 1950 m. Red and blue crosses indicate candidate locations for picking the wavelet at far offsets, with red picks indicating no polarity reversal and blue picks indicating a reversal. The red arrow indicates refracted waves which interfere with the reflection. Note that traces are normalised so apparent amplitudes are not to scale.

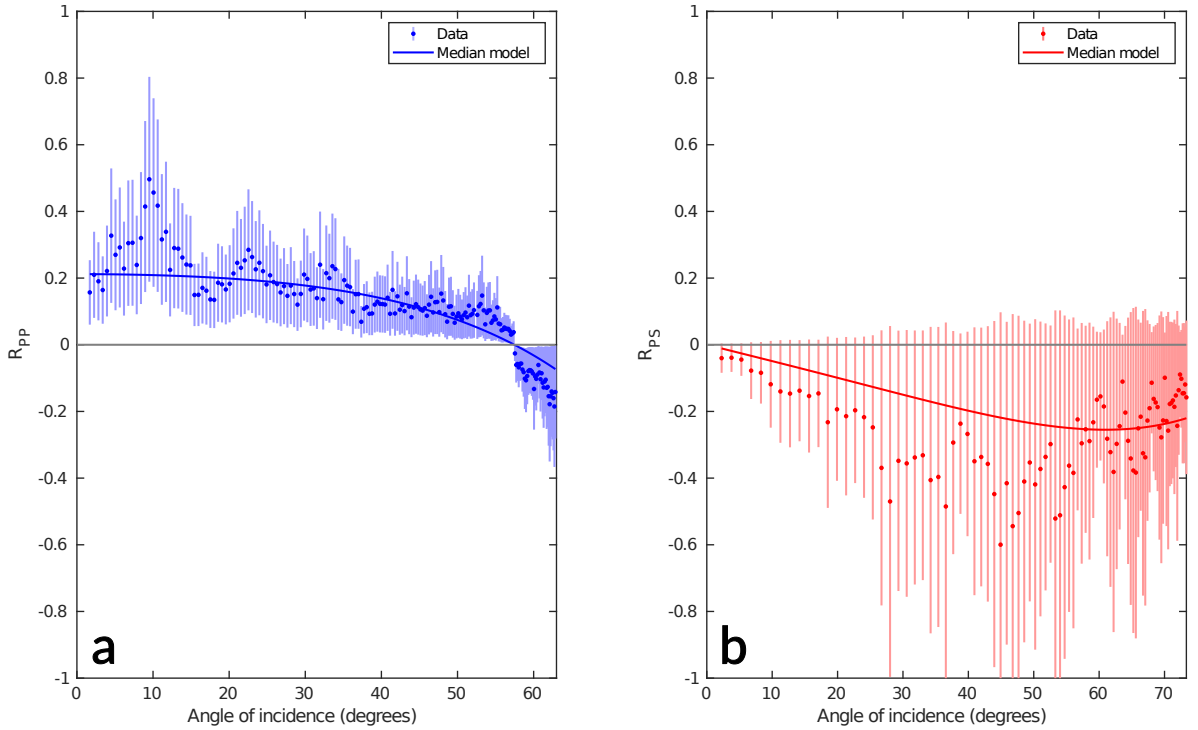

Figure 4.15: AVA responses of a) PP waves, reinterpreted with a polarity reversal at 57°, and b) PS waves. Solid lines show the AVA response of the median inverted model (joint inversion using all data).

present data, I interpret a polarity reversal at 1580 m (57.4°) and jointly invert the resultant PP AVA response along with the previously presented PS response (inversion parameters are as described in section 4.3). Figure 4.15 shows the reinterpreted PP and PS AVA data and the AVA responses of the median inverted model. While the inversion captures the character of the PP response excellently due to the forcing of the polarity reversal, the character of the PS response is not captured as accurately. In particular, the data show the magnitude of R_{PS} increasing to a maximum at $\sim 40^{\circ}$ followed by a decrease at larger angles; the inverted model displays R_{PS} increasing in magnitude to a maximum at $\sim 60^{\circ}$ (Figure 4.15b). This contrasts with the inverted model obtained when no polarity reversal is interpreted (Figure 4.10b), which shows the maximum magnitude of R_{PS} at $\sim 40^{\circ}$. Given the nature of source amplitude and attenuation corrections, if amplitudes of an AVA response are mis-estimated, it is more likely that absolute amplitudes are incorrect while preserving the character of an AVA response than the character being incorrect with correct absolute amplitudes. Qualitative inspection of the AVA responses shown in Figure 4.15 therefore highlights an inconsistency between the PP and PS AVA responses which indicates an incorrect interpretation.

Figure 4.16 shows the posterior distributions of Z and σ for the reversed-polarity case, which are summarised in the final row of Table 4.1. The acoustic impedance of $Z = (5.44 \pm 0.23)$ kg m^{-2}s^{-1} is consistent with the result from the correctly interpreted case (Figure 4.11d); however, the reversed-polarity AVA responses imply a much higher Poisson's ratio of $\sigma = 0.4 \pm 0.018$. This higher Poisson's ratio indicates a higher porosity than that obtained by inverting the correct AVA curves, and may potentially imply a thin-layer response at the bed. Booth et al. (2012) describe measurements of high acoustic impedance and high Poisson's ratio as diagnostic of thin-layer effects, as these measurements point to opposing substrate porosities.

To assess the potential for misinterpretation, it is useful to compare this result to the results obtained by the restricted-angle single and joint inversions reported in Section 4.4 (Figures 4.11a and 4.11c). The polarity reversal, occurring at 57°, is irrelevant to these inversions. The median of the restricted-angle single inversion (Fig. 4.11a) indeed points to a different Poisson's ratio to the reversed-polarity inversion, but the inversion does not rule out Poisson's ratios of $\sigma = 0.4$ or more, the distribution being relatively flat. If converted-wave information was unavailable, the new information provided by the polarity reversal may not be interpreted as inconsistent with the narrow-angle data.

In contrast, the posterior distribution resulting from the restricted-angle joint inversion constrains Poisson's ratio better than single inversion, ruling out out very high Poisson's ratios. This posterior distribution is more clearly inconsistent with the distribution obtained by joint inversion of the PP response containing a polarity reversal, and the misinterpretation of polarity would more likely be identified. Joint inversion is in this case more robust to misinterpretation of polarities due to the inconsistency of these results.

This example highlights the potential pitfalls of an interpretation which places too much emphasis on a polarity reversal, especially one where the amplitudes are small.

4.5.2 The value of joint inversion

For the AVA responses presented in this chapter, joint inversion improves constraint of bed properties when compared with single inversion, given the same angular range. The improvement is small for constraint of Z, but joint inversion constrains σ more precisely than single inversion, with uncertainties in $\sigma \sim 28\%$ smaller for joint inversion. The improvement in constraint of σ is greater when increasing the angular range than it is by the inclusion of PS inversion. This is

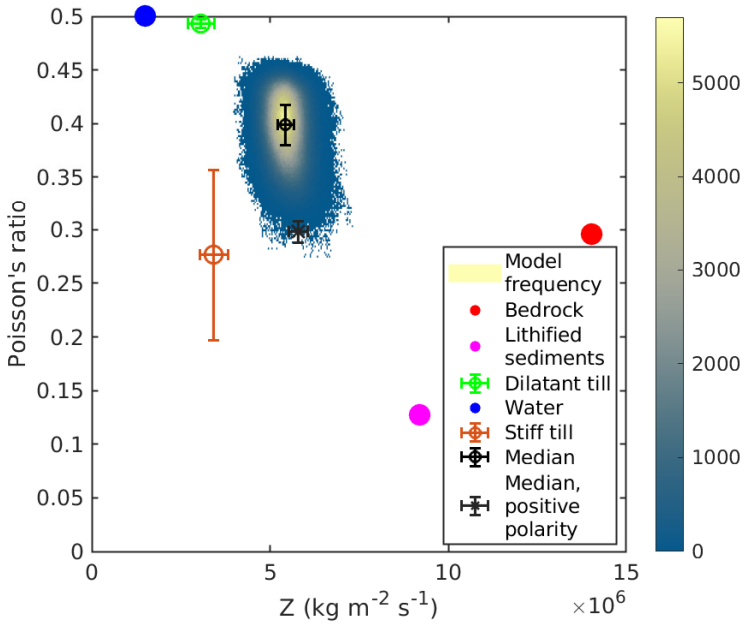

Figure 4.16: Posterior distribution of acoustic impedance and Poisson's ratio obtained from joint inversion of the reinterpreted AVA responses shown in Figure 4.15. Grey cross indicates the median obtained from the inversion when a polarity reversal is not interpreted.

consistent with the findings of Chapter 3: joint inversion improves constraint of bed properties given the same angular range, but the extent to which it does this depends on the character of the AVA response, and there are some characters of AVA response for which large angles provide more information than converted waves. In Chapter 3, the case of a polarity reversal at a large angle was identified as one for which the benefit of joint inversion is secondary to that of obtaining large angles; the data presented for KIR demonstrate that there are also other cases for which this is true. However, since *a priori* knowledge of the AVA response is rarely available, and the angular range obtained is often limited by logistical constraints, I suggest that the value of the joint inversion framework is the technique's reliable improvement upon single inversion for a given survey geometry, and its robustness to interpretive pitfalls such as the polarity reversal discussed in Section 4.5.1. A valuable extension to this work would be to validate the method where the interface characteristics are well known; for example, on an ice shelf, where an ice-water interface is guaranteed (e.g. Horgan et al. 2021).

4.5.3 Attenuation considerations

A limitation of my analysis is that I had to assume the S-wave quality factor, Q_S. Englacial measurements of Q_S are scarce, and collocated measurements of Q_P and Q_S at a wider variety of

locations are desirable to inform our understanding of their physical relationship. This may also provide a basis for assuming Q_S values where acquisition constraints render their measurement impossible.

An acquisition designed to measure Q_S over the whole ice column could use the primary S wave reflection, SS, and its multiple, SSSS (as described for P waves in Section 2.2.2). An explosive source buried in the firn would be required to generate S wave energy from close-to-source P-to-S conversions; the source would need to be very large in order to generate sufficient S wave energy to record S wave multiples with an acceptable signal-to-noise ratio. Furthermore, the ice would need to be relatively thin, so that a) the SSSS wave arrives before the recording finishes, and b) the SSSS wave is recorded with a good signal-to-noise ratio. Experiments using three-component nodes to record the wavefield are good candidates for including a number of large shots as an additional experiment to measure Q_S, due to the existing three-component capability and continuous recording.

To measure Q_S in firn, a dedicated S wave source such as stacked hammer blows (e.g. King and Jarvis 2007) could be used at the surface, combined with the layer stripping method described in Chapter 2. This method has recently been applied to attenuation measurements by Picotti et al. (2023).

4.5.4 Effect of source amplitude on reflectivity measurements

Source amplitude is a large contributor to the uncertainty in R_{PP} and R_{PS}. For the data presented here, source amplitude had to be measured twice, by different methods, due to the nature of the acquisition (i.e. separate acquisitions were used for vertical and radial components). In future, acquisitions should have collocated vertical and radial geophones which record the same shot, so A_0 need only be measured once.

The variable-Q direct-path method (Section 4.2.3, Equation 4.11) introduces a correction to the standard direct-path method which accounts for the varying effective attenuation experienced by diving waves travelling in the firn column. Other authors have used the standard direct path method (Equation 4.9) to measure seismic reflection amplitudes and deduce the presence of subglacial water (e.g. Muto et al. 2019a; Muto et al. 2019b). When I compare the source amplitudes obtained by the standard and modified methods, I find that the standard method underestimates source amplitude by a factor of ~ 1.6, and therefore would overestimate the

reflectivity by the same factor. Note that the factor of 1.6 is derived from diving wave travel times and the $Q(z)$ relationship measured in Chapter 2, and will not necessarily be the same for other locations, where accumulation and firn structure will be different. However, the general argument remains that as long as there is a Q gradient in the firn column, the source amplitude will be underestimated by the standard direct-path method. This may lead to errors in interpretation of glacial substrates.

As an example of this, Muto et al. (2019a; 2019b) present reflectivity and acoustic impedance measurements from Thwaites Glacier, West Antarctica, derived using the direct-path method for source amplitude. A stacked and migrated seismic section, reflectivities and acoustic impedances are shown in Figure 4.17 (Figure taken from Muto et al. (2019a)). They interpret seven locations of subglacial water pooling along their profile, at which the reflectivity $R = -0.4$ lies within their quoted uncertainties. Assuming they overestimate the magnitude of R by the factor 1.6, when the reflection coefficients are rescaled, there remain only four locations at which $R = -0.4$ lies within the uncertainties. Therefore, I suggest that existing studies which interpret subglacial water in this way and use the direct-path method (e.g. Clyne et al. 2020) may overestimate the prevalence of subglacial water. Note that this is a very approximate calculation, and a more comprehensive reinterpretation of the results from Thwaites Glacier would require a consideration of the differing velocity and attenuation structures of the firn column in an area of much higher accumulation than KIR (Arthern et al. 2006).

Horgan et al. (2021) established that the direct-path is the least reliable method for measuring A_0 and recommend the use of multiples to measure source amplitude. However, where multiples are not recorded, the direct-path method must be used; in this case it is essential to consider Q variability in the firn. This underlines the need for designing acquisitions to record good-quality multiples, given the increased complexity of attenuation measurements in firn compared with those involving multiples.

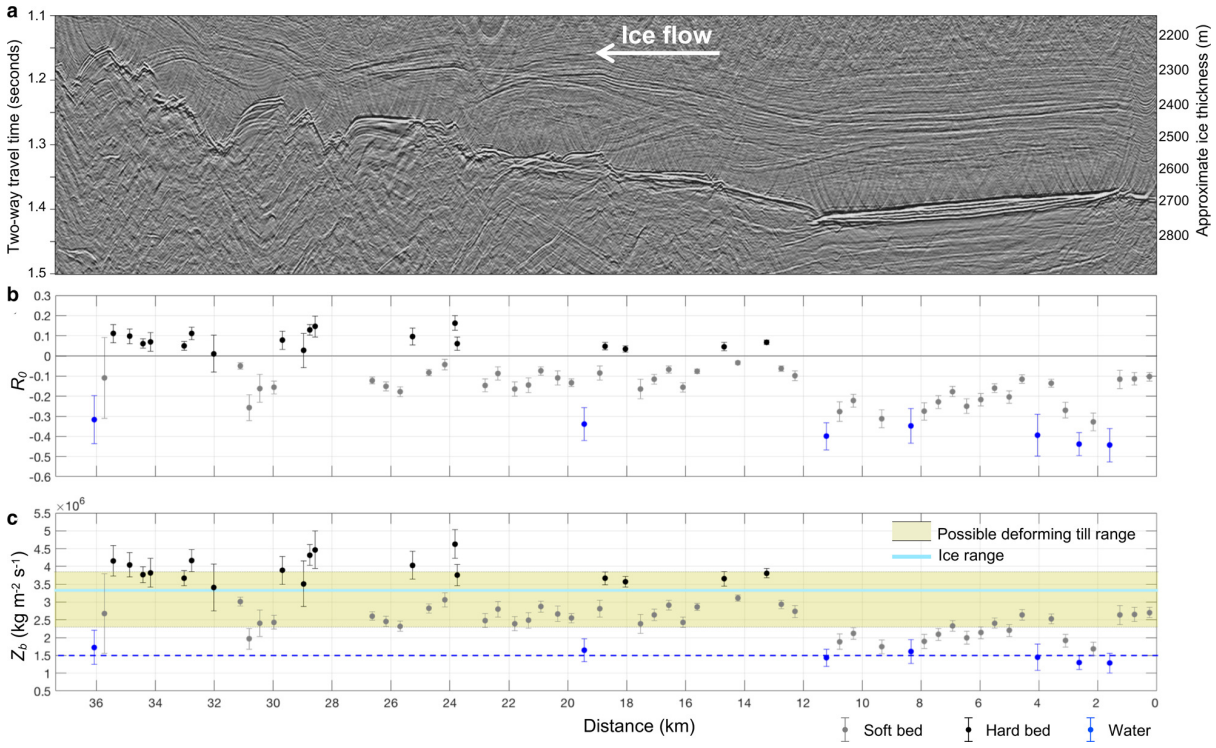

Figure 4.17: a) Stacked and migrated seismic section, b) normal-incidence reflectivities and c) acoustic impedances from a portion of Thwaites Glacier, West Antarctica, taken from Muto et al. (2019a). Blue data points in c) are where subglacial water is interpreted. Light and dark grey points are where they interpret a soft bed and hard bed, respectively. The reflectivities presented here were calculated using the direct-path method for source amplitude, and therefore may overestimate the true reflectivities.

4.6 Conclusions

In this chapter, I have presented measurements of the basal properties of Korff Ice Rise, West Antarctica (KIR), derived using amplitude-versus-angle analysis and an inversion scheme I described and investigated in Chapter 3. I describe the processing steps used to obtain absolute amplitudes and AVA responses, including geometric, attenuative and source amplitude corrections. I introduce a modified source amplitude correction which takes account of the quality factor gradient in firn, and compare it to the standard direct-path method by Holland and Anandakrishnan (2009), and find that for the Q gradient at KIR, the standard method significantly underestimates source amplitude.

Using joint inversion, I find that the bed has an acoustic impedance of $Z = (5.79 \pm 0.26) \times 10^6$ kg m^{-2}s^{-1} and a Poisson's ratio of $\sigma = 0.298 \pm 0.01$. I interpret this response as arising from a bed of partially consolidated and/or frozen sediments; this interpretation will be discussed further in Chapter 5. I evaluate the performance of the joint inversion scheme and find that for a given survey geometry, joint inversion performs better than single inversion, particularly in the constraint of Poisson's ratio. For this substrate, joint inversion does not meaningfully improve constraint of acoustic impedance. I also find that for the PP and PS AVA responses at KIR, obtaining wide-angle data ($\sim 60^\circ - 70^\circ$) for single inversion improves inversion precision more than including PS wave amplitudes for a narrow survey (where $\theta \leqslant 30^\circ$). I discuss a potential interpretive pitfall concerning a polarity reversal at large offsets, and argue that joint inversion is more robust to errors of this nature. I suggest that the value of the joint inversion framework lies in its reliable improvement over single inversion given a similar survey geometry and its robustness to possible interpretive errors.

Chapter 5

Synthesis

This chapter has four parts. In the first part, I will make a more detailed interpretation of the geophysical measurements reported in Chapter 4. In the second part, I will place these observations into their wider palaeoglaciological context and discuss possible explanations for the observations. In the third part, I will frame the importance of the novel methodological developments and make recommendations for future acquisitions. Finally, I will identify future work needed to address knowledge gaps left by my analysis, both geophysical and glaciological.

5.1 Further geophysical interpretation

5.1.1 Density and porosity of subglacial material

The acoustic impedance $Z = (5.79 \pm 0.26) \times 10^6$ kg m^{-2}s^1 and Poisson's ratio $\sigma = 0.298 \pm 0.01$ of the basal material at KIR, obtained by joint inversion of the PP and PS waves, suggest a bed composed of partially consolidated and/or frozen sediments. In this section I aim to interpret the results in more detail, noting that the marginal distributions of P wave velocity α, S wave velocity β and density ρ resulting from the inversion are well constrained: $\alpha = 4.03 \pm 0.05$ km s^{-1}, $\beta = 2.16 \pm 0.06$ km s^{-1}, and $\rho = 1.44 \pm 0.06$ g cm^{-3}.

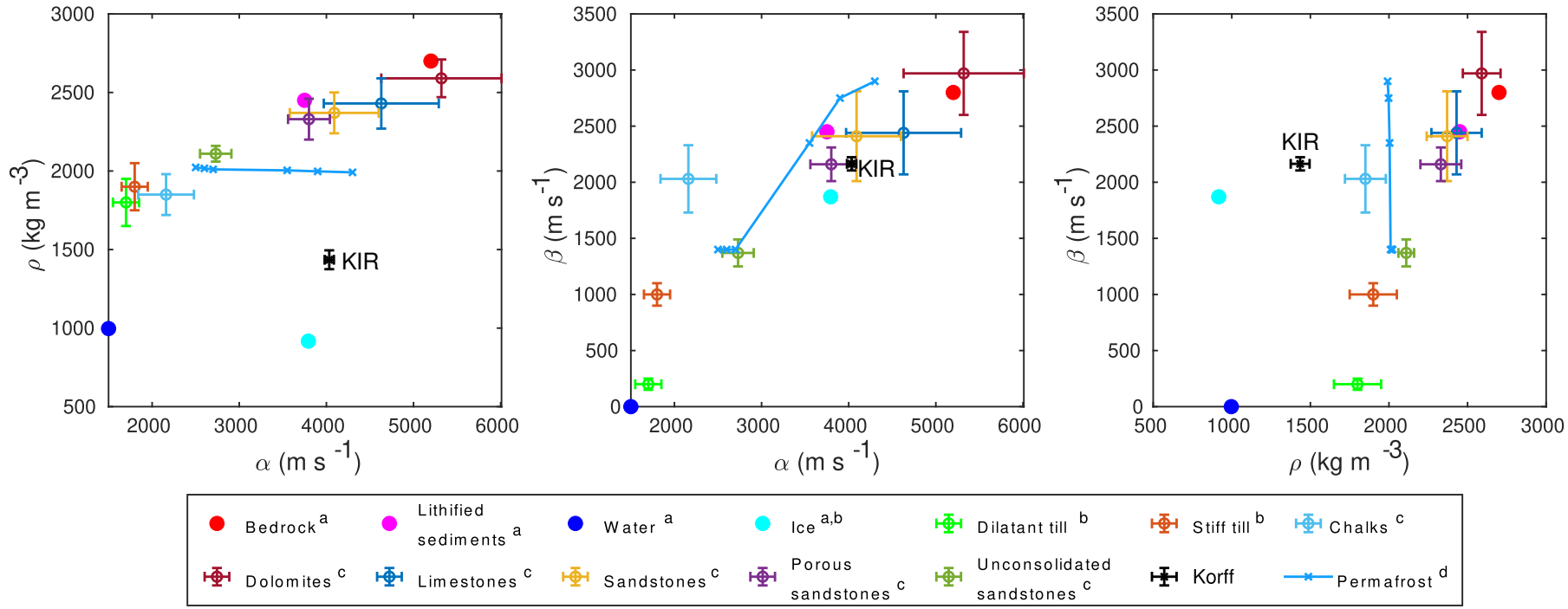

Figure 5.1: (a) P wave velocity and density, (b) P wave velocity and S wave velocity, and (c) density and S wave velocity plotted for ice, water and various rock and sediment types. Properties observed at KIR are plotted alongside. Properties are taken from [a]Peters et al. 2008, [b]Peters et al. 2007, [c]Mavko et al. 2009, [d]Johansen et al. 2003.

To view these results within the context of other materials, I plot them alongside properties of various rocks (Mavko et al. 2009), glacial substrates (Peters et al. 2007; Peters et al. 2008) and permafrost (Johansen et al. 2003). Figure 5.1 shows the densities, P and S wave velocities of these materials, displayed in three separate plots which show (a) ρ against α, (b) β against α, and (c) β against ρ. Viewed alongside these rock properties, the material observed at KIR appears unusual. In particular, sedimentary rocks with similar velocities to that observed at KIR (e.g. sandstones, porous sandstones) have much higher densities (e.g. $\rho = 2200 - 2500$ kg m^{-3} for porous sandstones, Figure 5.1). This precludes an interpretation of consolidated to lithified sediments at KIR. The low density implies a high porosity. A pore fill of free water and/or air would be associated with a low β. The observation of high velocities coincident with low density is therefore consistent with a subglacial material composed of a high-porosity matrix, with a significant part of the pore space occupied by ice; i.e. a partially to completely frozen bed.

The porosity ϕ of a composite material consisting of a mineral with density of ρ_m and another material occupying the pore space with density ρ_p can be calculated using:

$$\phi = \frac{\rho_m - \rho}{\rho_m - \rho_p} \tag{5.1}$$

where ρ is the bulk density of the material (Mavko et al. 2009). We can put upper and lower bounds on the porosity of the subglacial material at KIR if we assume the end-member cases of the pore space being entirely occupied by saline water or entirely occupied by ice, and calculating ϕ for each case. There are many possibilities for the mineral density ρ_m, and the present analysis is inevitably limited by the choice. However sediment cores retrieved in the Weddell Sea exhibit high proportions of sand and silt (Hillenbrand et al. 2012), and direct sampling of the bed at Berkner Island retrieved fine sand (Mulvaney et al. 2007). This suggests that quartz, which has density $\rho_m = 2.65$ g cm^{-3}, is a reasonable mineral choice. Using densities of ice and brine of $\rho_{\text{ice}} = 0.917$ g cm^{-3} and $\rho_{\text{brine}} = 1.04$ g cm^{-3}, porosities of $\phi = 0.75 \pm 0.04$ and $\phi = 0.7 \pm 0.03$ are estimated for an entirely unfrozen bed and for an entirely frozen bed, respectively.

These porosities are much higher than those observed elswhere subglacially: porosities of $\phi = 0.3 - 0.45$ are typical for dilatant sediments beneath ice streams (e.g. Blankenship et al. 1986; Blankenship et al. 1987; Brisbourne et al. 2017; Christianson et al. 2014; Dow et al. 2013;

A. M. Smith 1997a). A porosity of $0.7 - 0.75$ implies that the subglacial material is mostly composed of ice and/or brine, a seemingly improbable subglacial scenario. It is possible that the material underlying the ice is composed of much lower density minerals, which, combined with a relatively high porosity (but still < 0.7), would result in the observed density. Indeed, densities as low as $1.4 - 1.6$ g cm^{-3} have been observed upstream of the Thwaites Glacier grounding zone (James Smith, personal communication). A bed consisting of a high-porosity glaciomarine sediment composed of low density minerals and saturated with ice and/or brine is therefore a possible explanation for the low density observed at KIR.

An alternative interpretation for the low density is that the observed seismic reflection is from a layer of entrained basal debris at the base of the ice column. This would be a mixture of ice and mineral grains which was either part of the ice shelf before grounding, having been entrained perhaps at an upstream rumple, or entrained during streaming flow closely upstream. If the bed at present is unfrozen or in a transient state of freezing, there may be brine present in this mixture, originating from a glaciomarine sediment which was saturated with saline water prior to grounding. To resolve the degree of freezing of this hypothesised mixture, it is useful to predict its mechanical properties and compare these with the inverted model from KIR.

5.1.2 Using rock physics to constrain the degree of freezing

Rock physics approaches can be used to predict the bulk properties of a material from the volume fractions and properties of its individual constituents, namely bulk modulus K and shear modulus μ (Mavko et al. 2009). The Hashin-Shtrikman (HS) bounds (Hashin and Shtrikman 1963) describe the theoretical maximum and minimum values that K and μ can take for a given porosity, regardless of grain or pore shape. A porosity of zero represents a case in which the volume is entirely occupied by the stiffer material (in this case quartz), and a porosity of one represents the case in which the volume is entirely occupied by the weaker material (water, brine, or a mixture). The HS bounds are calculated using the equations:

$$K^{\mathrm{HS}\pm} = K_1 + \frac{f_2}{(K_2 - K_1)^{-1} + f_1(K_1 + \frac{4}{3}\mu_1)^{-1}}, \tag{5.2}$$

$$\mu^{\mathrm{HS}\pm} = \mu_1 + \frac{f_2}{(\mu_2 - \mu_1)^{-1} + \frac{2f_1(K_1+2\mu_1)}{5\mu_1(K_1+\frac{4}{3}\mu_1)}}, \tag{5.3}$$

where K_1 and K_2 are the bulk moduli of the two constituents, μ_1 and μ_2 are the shear moduli of the constituents, and f_1 and f_2 are the volume fractions of the individual constituents. The maximum and minimum bounds are calculated by interchanging the indices 1 and 2 (Mavko et al. 2009).

To constrain the degree of freezing of the hypothesised quartz-ice-brine mixture, I calculate the HS bounds for three cases: (a) a quartz-brine mixture (e.g. entirely unfrozen marine sediment), (b) a quartz-ice-brine mixture (partially frozen/transient state), and (c) a quartz-ice mixture (entirely frozen). For the quartz-ice-brine mixture, I first calculate the predicted properties of an ice-brine mixture, composed of 80% ice and 20% brine, using the Voigt-Reuss-Hill average M_{VRH}, which combines the Voigt upper bound M_V and Reuss lower bound M_R:

$$M_{\mathrm{V}} = \sum_{i=1}^{N} f_i M_i, \tag{5.4}$$

$$\frac{1}{M_{\mathrm{R}}} = \sum_{i=1}^{N} \frac{f_i}{M_i}, \tag{5.5}$$

$$M_{\mathrm{VRH}} = \frac{M_V + M_R}{2}. \tag{5.6}$$

In Eqs. 5.4-5.6, the modulus M can be either K or μ. If one of the constituents is a fluid, M_R is defined as zero (Hill 1952; Mavko et al. 2009). The associated velocities are calculated using the standard equations

$$\beta = \sqrt{\frac{\mu}{\rho}} \tag{5.7}$$

$$K = \alpha^2 \rho + \frac{4}{3}\mu. \tag{5.8}$$

The properties used to model the Hashin-Shtrikman bounds are summarised in Table 5.1.

Figure 5.2 shows the HS bounds for the bulk and shear moduli of (a) the quartz-brine mixture, (b) the quartz-ice-brine mixture and (c) the quartz ice mixture. The crosses represent the bulk and shear moduli of the reflector at KIR ($K = 14.4 \pm 0.9$ GPa and $\mu = 6.7 \pm 0.4$ GPa) plotted at the porosity implied by the inverted density of 1.44 g cm^{-3}. $\phi = 0.75 \pm 0.04$ for the quartz-brine mixture, $\phi = 0.71 \pm 0.04$ for quartz-ice-brine, and $\phi = 0.7 \pm 0.03$ for quartz-ice. Figure 5.3 shows

Material	K (GPa)	μ (GPa)	α (km s^{-1})	β (km s^{-1})	ρ (g cm^{-3})
Quartz	36	45	6.02	4. 12	2.65
Ice	8.9	3.2	3.79	1.87	0.917
Brine	2.2	0	1.45	1.04	0
Ice-brine mixture (80/20)	3.78	1.28	2.41	1.17	0.94
KIR	14.4 ± 0.9	6.7 ± 0.4	4.03 ± 0.05	2.16 ± 0.06	1.44 ± 0.06

Table 5.1: Properties used to model Hashin-Shtrikman bounds. The properties for an ice-brine mixture of 80% ice, 20% brine were calculated using a Voigt-Reuss-Hill average.

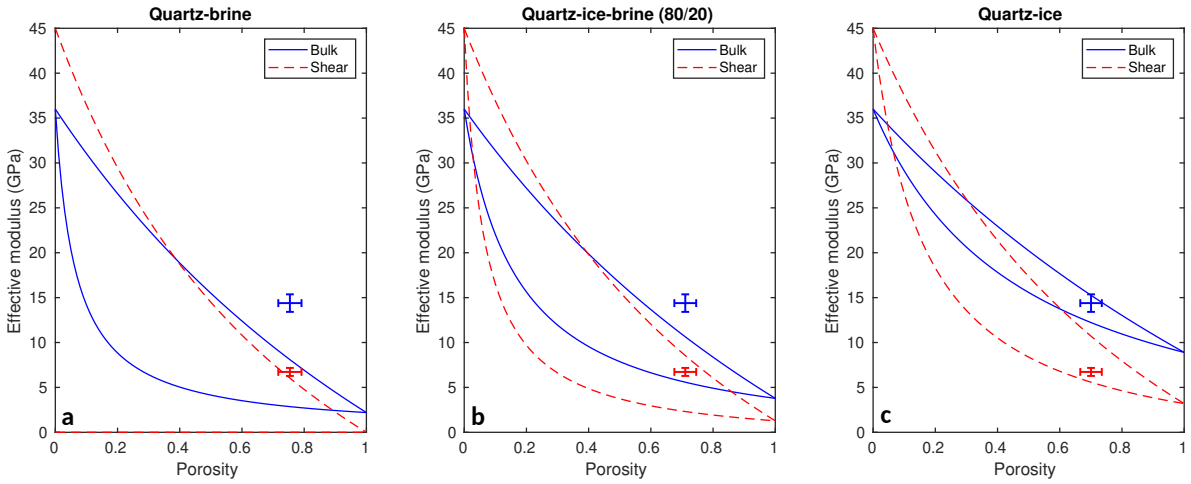

Figure 5.2: Predicted limits of bulk and shear moduli for (a) a quartz-brine mixture, (b) a quartz-brine-ice mixture, (c) a quartz-ice mixture. Crosses are the observed properties at KIR, at the porosities implied by the measured density. Blue = bulk, red = shear.

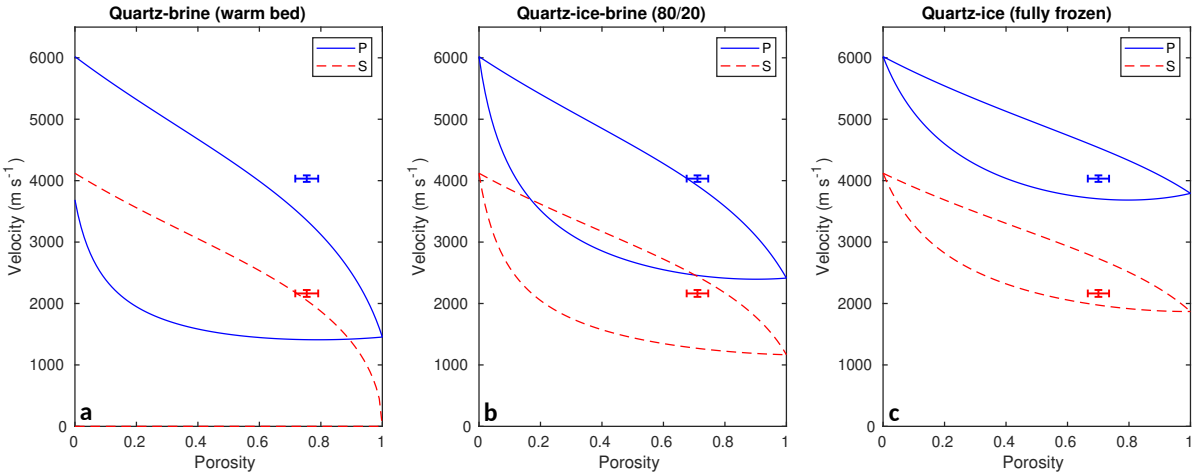

Figure 5.3: Predicted limits of P (blue) and S (red) wave velocity for (a) a quartz-brine mixture, (b) a quartz-brine-ice mixture, (c) a quartz-ice mixture. Crosses are the observed P (blue) and S (red) wave velocities at KIR, plotted at the porosities implied by the measured density of $\rho = 1.44$ g cm^{-3}.

the HS bounds for P and S wave velocity which result from the moduli calculated for the three scenarios.

The bulk and shear for the basal material at KIR both lie outside the HS bounds calculated for a quartz-brine mixture (Figure 5.2a). The HS bounds calculated for the mostly frozen quartz-ice-brine mixture are consistent with the shear modulus and S wave velocity at KIR, but inconsistent with the bulk modulus and P wave velocity (Figs. 5.2b and 5.3b). The only scenario tested for which the observed properties of the base-ice reflector at KIR lie within the possible HS bounds is the scenario of a fully frozen bed (Figs. 5.2c and 5.3c).

This analysis rules out the hypothesis of warm, highly porous, low density saturated subglacial sediments underlying the ice rise, and lends weight to the interpretation of the observed 'base-ice' reflection at KIR originating from a layer of entrained debris within the basal ice. The absence of visible reflections beneath this horizon suggests a continuous transition from debris-rich ice to frozen sediments with depth.

5.2 Glaciological interpretation

5.2.1 KIR and hypotheses of post-LGM grounding line retreat

In this section I will interpret my geophysical observations in the context of the glacial history of KIR and the broader Weddell Sea region. The present-day grounding line in the Weddell Sea sector is hypothesised to have originated in one of two ways (See section 1.5.2). After the last glacial maximum (LGM), either the grounding line retreated monotonically to the present day position (e.g. Hillenbrand et al. 2014), or the grounding line underwent a period of rapid retreat, followed by a more recent advance (e.g. Bradley et al. 2015; Kingslake et al. 2018; Siegert et al. 2013).

Work by previous authors (Brisbourne et al. 2019; Kingslake et al. 2016) has established that ice flow reorganised at KIR around 2.5 ka before present, based on observations of stratigraphy and crystal orientation fabric (COF). Brisbourne et al. (2019) detected a COF above 200 m depth which is consistent with present-day divide flow, and a COF below 230 m depth consistent with a previous episode of ice flow from the south. This indicates that prior to divide formation, ice flowing over the present day location could have been (a) grounded and sliding over a warm bed, (b) weakly grounded as an ice rumple, or (c) entirely ungrounded as an ice shelf. In the

following section, I will evaluate the consistency of my observations with each of these scenarios.

I model the likely temperature evolution of KIR after grounding in order to constrain its possible date of formation. Given that my previous analyses (Section 5.1.2) suggest that the bed at KIR is likely frozen, the question arises of how long the bed takes to freeze. In other words, what is the most recent date of grounding consistent with a frozen bed, and is this consistent with the stratigraphy and COF at KIR?

5.2.2 Modelling the age-temperature-depth relationship at KIR

To provide context to my geophysical measurements, I model the time evolution of the temperature-depth profile at KIR, using a 1D age-depth-temperature model supplied by Carlos Martín (British Antarctic Survey) and reported in a previous study by Jordan et al. (2018). The conceptual framework is that of an ice shelf with steady-state temperature profile grounding on the seabed: following grounding, the ice-bed interface will cool. The timescale on which the bed freezes will inform the glaciological interpretation of my geophysical results.

The model solves the heat equation from an initial temperature profile $T_0(z)$ to a solution at the present time t_p:

$$\rho(z)c(T)\left(\frac{\partial T}{\partial t} + w(z)\frac{\partial T}{\partial z}\right) - \frac{\partial}{\partial z}\left(k(T)\frac{\partial T}{\partial z}\right) = 0. \tag{5.9}$$

where T is temperature, z is elevation, $\rho(z)$ is the density and $w(z)$ is the vertical velocity. $k(T)$ is the thermal conductivity and $c(T)$ is the specific heat capacity. These vary with temperature (Ritz 1987):

$$c(T) = (146.3 + 7.253\ T)\ \text{J kg}^{-1}\ \text{K}^{-1}, \tag{5.10}$$

$$k(T) = 9.828e^{-0.0057\ T}\ \text{W m}^{-1}\ \text{K}^{-1}. \tag{5.11}$$

In the above two equations, temperatures are in Kelvin. $w(z)$ takes the form:

$$w(z,t) = -m + [-a + m]\eta(z), \tag{5.12}$$

Model parameter	Symbol	Value
Accumulation rate[a]	a	0.56 m a^{-1}
Surface temperature[a]	T_s	-29°C
Ocean temperature[b]	$T(0,0)$	-2.3°C
Geothermal heat flux[c]	Q_G	60 ± 20 mW m^{-2}

Table 5.2: Parameters used to determine temperature model boundary conditions. [a]taken from KIR automatic weather station data. [b]taken from Nicholls and Jenkins (1993). [c]taken from Burton-Johnson et al. (2020).

where m is the basal melt rate, here assumed zero, a is the accumulation rate, and $\eta(z)$ is the shape function, which depends entirely on ice rheology. This takes a form following the shallow ice approximation (Hutter 1983):

$$\eta(s) = 1 - s\left(\frac{n+2}{n+1} - \frac{s^{n+1}}{n+1}\right), \tag{5.13}$$

where s is the normalised depth, $s = \frac{H-z}{H}$, for ice thickness H. n is a rheological factor which is set to $n = 3$ (Cuffey and Paterson 2010). The boundary conditions are set as:

$$T(z, t=0) = T_0(z), \tag{5.14}$$

$$T(z=H, t) = T_s(t), \tag{5.15}$$

$$\left.\frac{\partial T}{\partial z}\right|_{z=0} = -\frac{Q_G}{k}, \tag{5.16}$$

where $T_0(z)$ is an initial temperature profile, T_s is the surface temperature, and Q_G is the geothermal heat flux. The initial ice temperature profile is set based on the steady-state temperature of an ice shelf given a surface accumulation of $a = 0.56$ m a^{-1}, a surface temperature of $T_s = 29$°C and an initial basal temperature of $T(0,0) = -2.3$°C, where it is in contact with the ocean. Surface temperature and accumulation are taken from automatic weather station data at the field site, and the ocean temperature is taken from measurements by Nicholls and Jenkins (1993). The initial seabed temperature is based on the steady state temperature given a geothermal heat flux of 60 mW m^{-2} (Burton-Johnson et al. 2020) and a temperature of -2.3°C. The values used to calculate boundary conditions are summarised in Table 5.2.

Figure 5.4 shows modelled temperature profiles for KIR, displayed at intervals of 2 ka after grounding, with the geothermal heat flux, Q_G, set to 60 mW m^{-2}. The bed cools rapidly

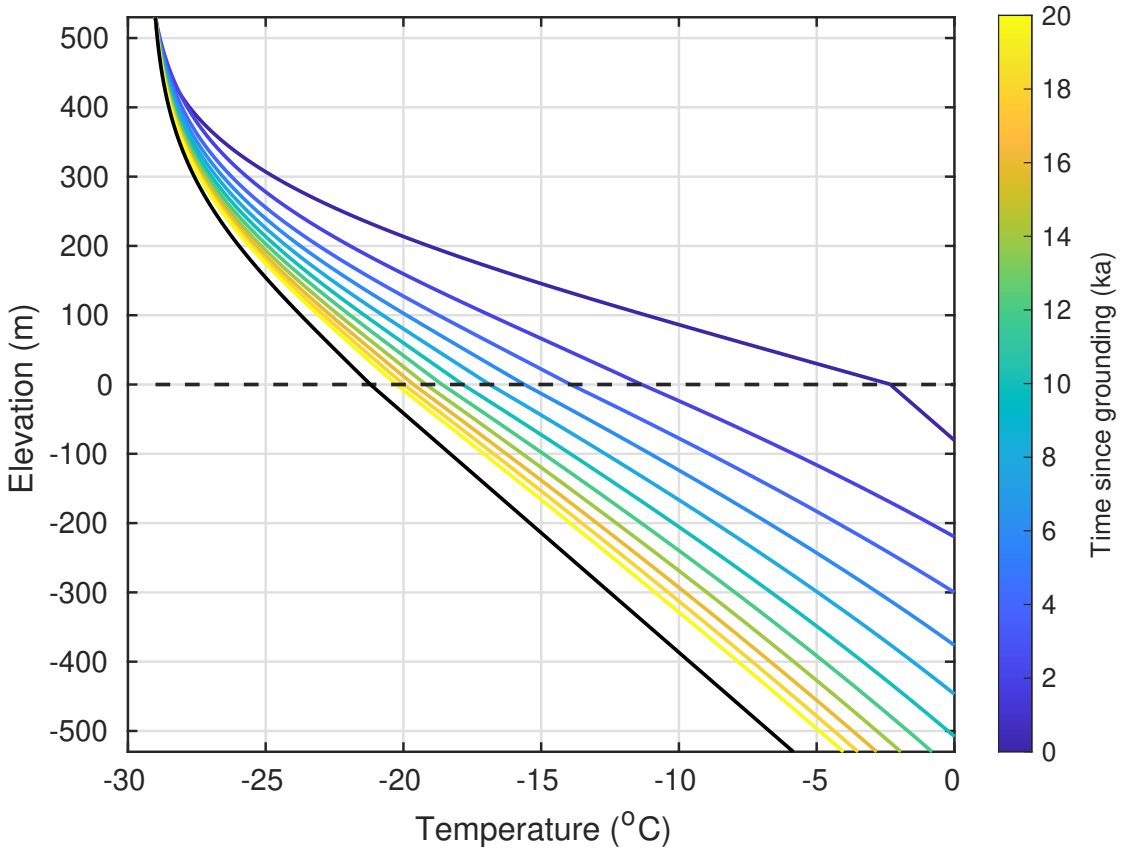

Figure 5.4: Modelled temperature profiles of KIR at intervals of 2 ka after grounding. The solid black line is the steady state profile. Dashed line at zero elevation indicates the ice-bed interface. Basal temperature at each time is given by the intersection of the dashed line with the temperature profile. Black solid line indicates the steady state temperature profile.

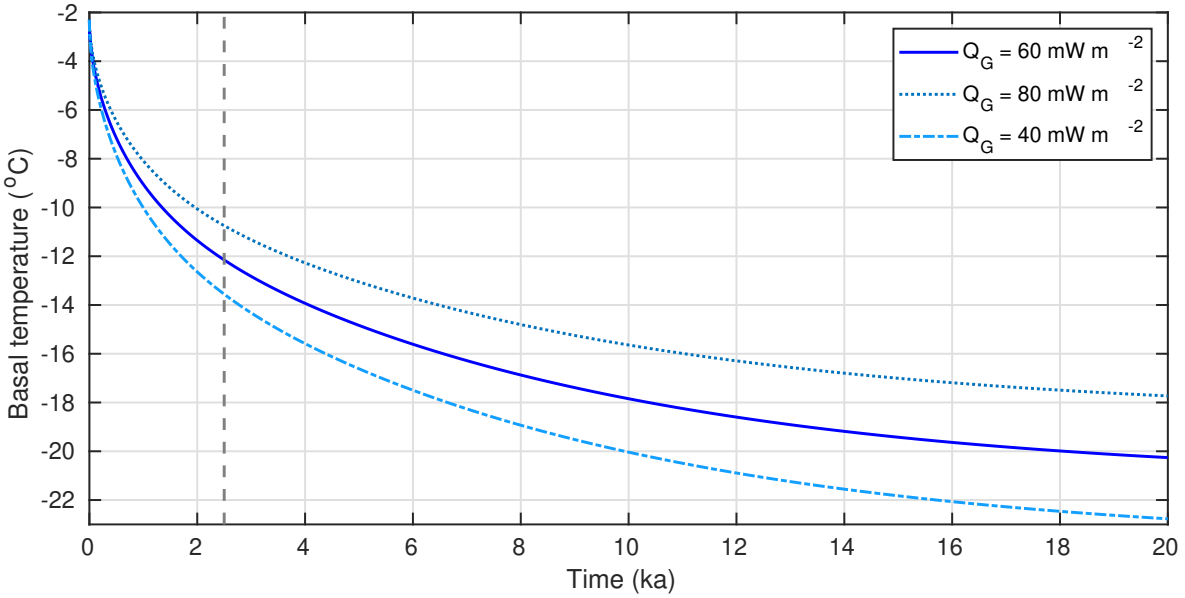

Figure 5.5: Modelled basal temperature of KIR as a function of time, for geothermal heat fluxes of 40 mW m^{-2}, 60 mW m^{-2} and 80 mW m^{-2}. $t = 0$ is the time of grounding. Vertical dashed line is at $t = 2.5$ ka, the likely length of time that has elapsed between flow reorganisation and the present day (Brisbourne et al. 2019; Kingslake et al. 2016). If KIR was ungrounded prior to flow reorganisation, and reorganisation coincided with grounding, the current basal temperature would be -12 ± 1.5°C.

at first - the basal temperature reaches ~ -10°C after 2 k annum (ka). The rate of cooling then gradually decreases, with the basal ice eventually reaching the steady-state temperature of -21°C (shown where the black line intersects the dashed line at 0 m elevation).

The largest source of uncertainty for dating ice rises based on temperature is geothermal heat flux (Montelli and Kingslake 2023). To account for this, I run the model three times, for $Q_G = 40$ mW m^{-2}, $Q_G = 60$ mW m^{-2} and $Q_G = 80$ mW m^{-2}. Figure 5.5 shows the basal temperature as a function of time after grounding for each of these scenarios; after 2.5 ka, the basal temperature is -12 ± 1.5°C. This means that in order for the bed to be unfrozen, KIR must have formed very recently; the basal temperature reaches -5°C after only 160 ± 50 years. In light of this modelling, my observation of a bed which is likely frozen is consistent with divide formation 2.5 ka before present. However, since the initial cooling is so fast, it is not possible to put further constraints on the timing of divide formation using this technique.

5.2.3 Formation hypotheses for KIR

The seismic observations can be explained if prior to the present flow regime, KIR was weakly grounded as a rumple, following rapid grounding line retreat and readvance. During grounding

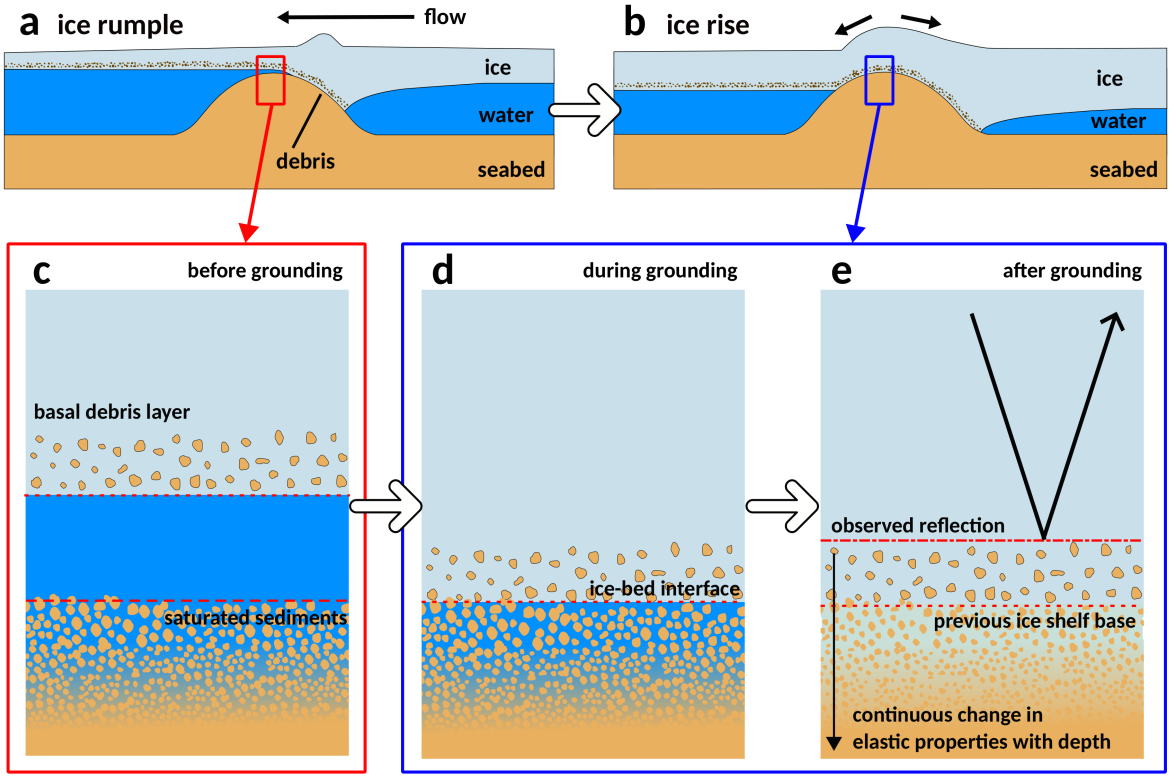

Figure 5.6: Possible stages of formation explaining the seismic observations. (a) debris is entrained in the basal ice at the stoss side of the rumple and is carried to the lee side. (b) GIA or ice thickening initiates grounding line readvance and divide flow. The lee side ice grounds, bringing the debris-rich basal ice into contact with high-porosity sediments. (c) cross-section of basal ice, ocean cavity and seafloor sediments prior to grounding. (d) during grounding, the debris-rich basal ice comes into contact with the saturated sediments and the water in the sediment pore space begins to freeze. (e) the water occupying the pore space has frozen, resulting in a continuous change of elastic properties with depth.

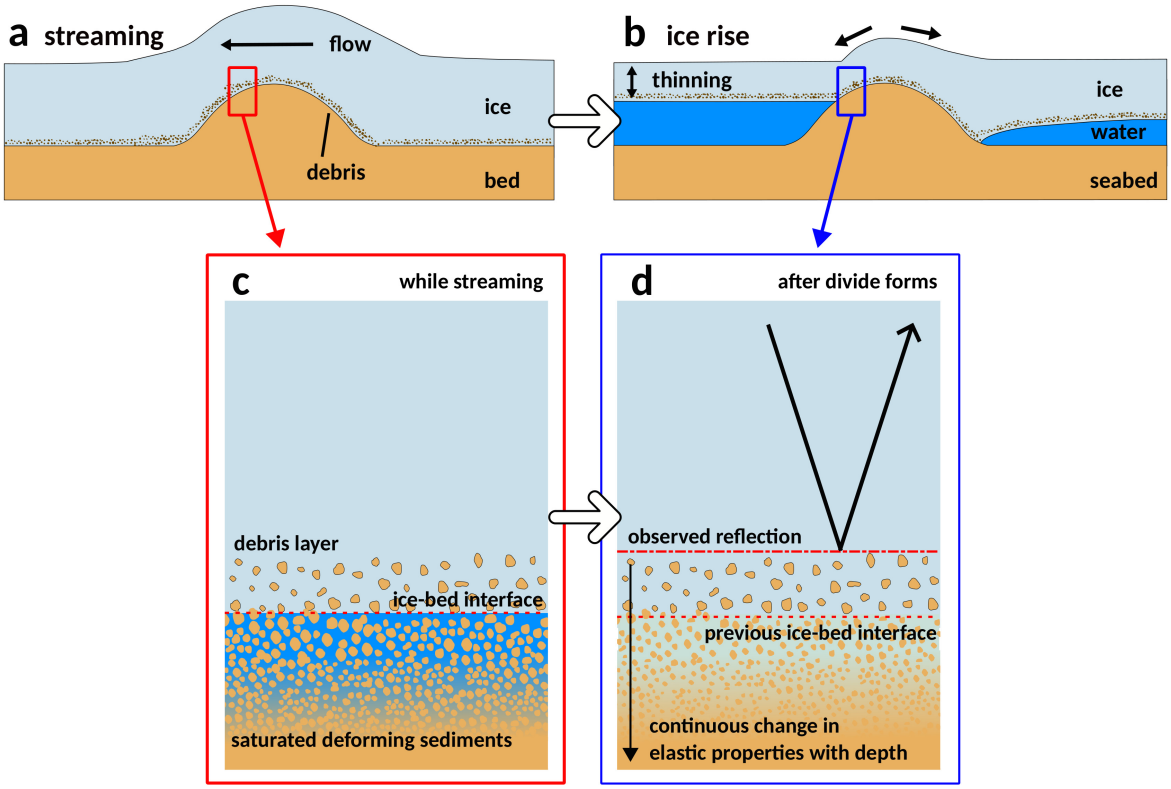

Figure 5.7: Possible origin of the current subglacial conditions in a monotonic grounding line retreat scenario. (a, c) during streaming flow, debris is entrained in a basal layer while flowing over dilatant sediments. (b,d) If subglacial water persists during flow stagnation, water in the pore space freezes after grounding, leading to an ill-defined transition betweeen the basal debris layer and the frozen subglacial sediment.

line retreat, the grounded area may have retreated upstream of the basal high point (Henry et al. 2022), ungrounding at the seismic field site. Figure 5.6 shows a schematic of the hypothesised formation stages of KIR, and the associated basal conditions. During flow as a rumple (Fig. 5.6a, c), debris is entrained in the basal ice on the stoss side of the rumple and transported to the lee side. The seabed is composed of saturated glaciomarine sediments. During grounding line readvance (Fig. 5.6d) the basal debris layer comes into contact with these sediments. After grounding, these sediments freeze. The transition between dirty basal ice and frozen subglacial sediments is not well-defined, and there is now a continuous transition of elastic properties with depth. The observed 'ice-bed' reflection comes from the top of the basal debris layer; due to the continuous transition with depth, no futher subglacial reflections are observed at KIR. This hypothesis of formation is consistent with my observations.

It is important to note that while this physical scenario can explain the seismic observations, it can not unequivocally rule out grounded streaming flow followed by monotonic grounding line

retreat. Fig 5.7 shows the potential steps of formation in a monotonic retreat scenario - retreat of the grounding line, stagnation of streaming flow, and commencement of divide flow. During streaming flow, KIR may have been underlain by dilatant sediments (Fig. 5.7c). If subglacial water persisted during stagnation, then this basal water would freeze, leading to the same physical conditions as in the retreat/readvance scenario. However, stagnation of streaming flow is associated with dewatering and stiffening of subglacial sediments (e.g. during the stagnation of Kamb Ice Stream, Anandakrishnan and Alley 1997; Catania et al. 2006). If this were the case, the observed seismic response at KIR would be that of a stiff sediment bed or an associated thin-layer response. It is unclear how or why subglacial water would persist during stagnation, so while it cannot be ruled out, monotonic grounding line retreat less easily explains the seismic observations.

5.2.4 Thin layer effects

The presence of thin layering at the ice-bed interface can lead to interference between reflections from the top and bottom of the thin layer, altering the apparent results of AVA inversions (Booth et al. 2012). A thorough interpretation of glaciological AVA results must therefore consider thin layer interpretations which may be consistent with observations but result in contradictory conclusions.

The Hashin-Shtrikman analysis (Section 5.1.2) strongly supports the interpretation of a cold bed, implying that grounding occurred sufficiently long ago for the bed to freeze. This is consistent with previous observations, which date a change in flow regime to $\sim$ 2.5 ka before present (Kingslake et al. 2016; Brisbourne et al. 2019). It is nevertheless worth considering if a thin layer response from a warm bed may be consistent with the observed reflectivity, as this would signal an anomalously high geothermal heat flux or more recent grounding.

Shortly after grounding, water or brine would occupy the pore space immediately under the ice base, as in Figure 5.6d. In this case, the observation of a subglacial reflector or a thin-layer response originating from the interference between the clean ice-debris layer reflection and the debris layer-wet sediment reflection would be expected. Booth et al. (2012) interpret that in a thin layer AVA response, the apparent acoustic impedance is dominated by the acoustic impedance of the lower layer and the apparent Poisson's ratio is dominated by the Poisson's ratio of the upper layer. Consequently, if there were a thin layer of debris-rich basal ice overlying

water or brine saturated sediments, we would likely see an acoustic impedance in the region of 3×10^6 kg m^{-2}s^{-1}, much lower than the inverted acoustic impedance at KIR of $(5.79 \pm 0.26) \times 10^6$ kg m^{-2}s^{-1}.

Another plausible thin layer scenario for a warm bed would be that of a thin layer composed of ice, brine and debris, overlying a bed of stiff sediments or crystalline bedrock. My inverted acoustic impedance is far too low to accommodate bedrock underneath the basal ice, so this is ruled out. I do, however, observe an acoustic impedance plausible in consolidated sediments, so this scenario merits further consideration. If the bed was warm enough to accommodate significant basal melting, the basal debris layer would likely not be fully frozen, but would be a mixture of ice, debris and water. The apparent Poisson's ratio would likely be higher than the σ I observe, due to the liquid in the thin layer. This scenario is also inconsistent with my observations, so a warm bed can be ruled out.

Stagnation of streaming flow is associated with dewatering and stiffening of subglacial sediments (Anandakrishnan and Alley 1997; Catania et al. 2006). A plausible subglacial environment resulting from monotonic grounding line retreat could therefore be characterised by a cold bed, with a thin layer of debris-rich basal ice overlying stiff sediments. In this scenario, the apparent Z would likely be similar to Z for the stiff sediments, and the apparent σ would be similar to that of the basal debris layer. This would be consistent with our results. Consequently, this scenario can not be ruled out. However, thin layer responses are often characterised by the apparent Z and σ contradicting each other (Booth et al. 2012); since the argument invoked in Section 5.2.3 fully explains the observed properties at KIR, they are not contradictory, so I consider the model of a basal debris layer overlying frozen marine sediments with an ill-defined boundary between the two the most convincing interpretation. Full-waveform modelling of the AVA responses associated with a basal debris layer (e.g. Booth et al. 2012) is necessary if more detailed interpretations are to be drawn.

5.2.5 Do these results tell us more about the recent history of the Weddell Sea Sector?

The observation of a frozen bed at KIR is consistent with flow reorganisation $\sim$ 2.5 ka before present. The analysis presented in Section 5.2.2 demonstrates that by 2.5 ka after grounding, the bed is frozen. Due to the rapid cooling of the ice-bed horizon when an ice shelf grounds,

the observation of a cold bed at KIR does not in and of itself provide much insight into the recent history of the ice sheet. The utility of seismic methods to date ice rise formation is fundamentally limited by the indirect dependence of elastic properties on basal temperature. In the context of West Antarctica, improved seismic techniques such as converted-wave AVA will primarily be of value in refining maps of the basal properties underneath ice streams.

Based on the scenarios discussed in Section 5.2.3, I consider the most likely interpretation that of partial ungrounding as a rumple followed by regrounding. This scenario is indistinguishable at the present day from a complete ungrounding, as during regrounding the ice would have passed through an intermediate rumple stage. Previous authors (Kingslake et al. 2018; Wearing and Kingslake 2019) have proposed complete ungrounding at Henry ice rise (HIR); however, the bathymetric high occupied by KIR is higher than that at HIR (see Fig. 1.8), so complete ungrounding is less likely to have occurred at KIR. The observations reported at KIR lend weight to the rapid retreat/readvance hypothesis; however, it is not possible to rule out the hypothesis of monotonic retreat unequivocally.

These observations imply an ill-defined boundary between the glacier and a frozen bed, both seismically and glaciologically. Functionally, should the ice-bed interface here be considered the inferred position of the ice base at grounding, or should it be considered the top of the basal debris layer from which the reflection is observed? This may not matter for the current glaciological context, because the ice is slow moving; however, it may have implications for future seismic measurements where basal debris is present. In ice streams, the quantity and character of debris in basal ice potentially has significant effects on the slip mechanisms (e.g. Hudson et al. 2023). Poorly defined transitions between basal ice, debris layers and sediment beds could also potentially have significant effects on observed reflectivities. This highlights the need for further work on both the geophysical and glaciological properties of basal debris layers.

5.2.6 Can measurements of permafrost be used as an analog for a frozen glacier bed?

When attempting to identify whether an AVA response could result from a frozen glacier bed, a natural comparison to make is with permafrost, i.e. frozen soils in polar regions. Johansen et al. (2003) model the P and S wave velocities of permafrost for varying degrees of porosity, saturation and freezing. Here I discuss their results for fully saturated permafrost with a porosity of 0.38.

Frozen fraction	α (km s^{-1})	β (km s^{-1})	ρ (kg m^{-3})	Z (10^6 kg m^{-2} s^{-1})	σ
0	2.5	1.4	2023	5.09	0.272
0.2	2.6	1.4	2017	5.29	0.296
0.4	2.7	1.4	2010	5.49	0.316
0.6	3.55	2.35	2004	7.22	0.11
0.8	3.9	2.75	1998	7.94	0.0056
1.0	4.3	2.9	1992	8.75	0.0828

Table 5.3: Properties calculated for 38% porosity permafrost saturated with water/ice. Velocities are from Johansen et al. (2003). I calculate Z and σ from their published results, with densities calculated using Eq. 5.1.

I calculate Z and σ for each of their measurements - the values are displayed in Table 5.3. 'Frozen fraction' refers to the fraction of the water occupying the pore space which is frozen; e.g. fully saturated permafrost with a frozen fraction of 0.2 is composed of 62% quartz, 30.4% water and 7.6% ice by volume.

Figure 5.8 shows the calculated Z and σ of permafrost alongside the previously discussed subglacial materials. The properties exhibit a sharp change as the frozen fraction passes the threshold of 0.4, clearly separating 'less frozen' and 'more frozen' materials. When viewed in isolation, the observed Z and σ at KIR appear to place KIR in the 'less frozen' category. However, this masks the very low density and high velocity implied by the reflection observed at KIR, and would be an incorrect interpretation. The interpretation of the reflection at KIR as coming from a basal debris layer explains the apparent contradiction with the properties reported by Johansen et al (2003); the observed reflection does not come from a permafrost-like material, it comes from an overlying layer. The material with origins in frozen marine sediments (i.e. the palaeo seabed) may well display properties similar to Johansen et al.'s 'more frozen' permafrost; however, the overlying debris layer and continuous elastic transition with depth means that this cannot be observed. This illustrates a potential interpretive danger with using AVA to identify frozen glacier beds. Direct comparison with reported properties of permafrost is not appropriate in light of the presence of basal debris layers, and attempts to draw interpretations from these comparisons may lead to incorrect conclusions.

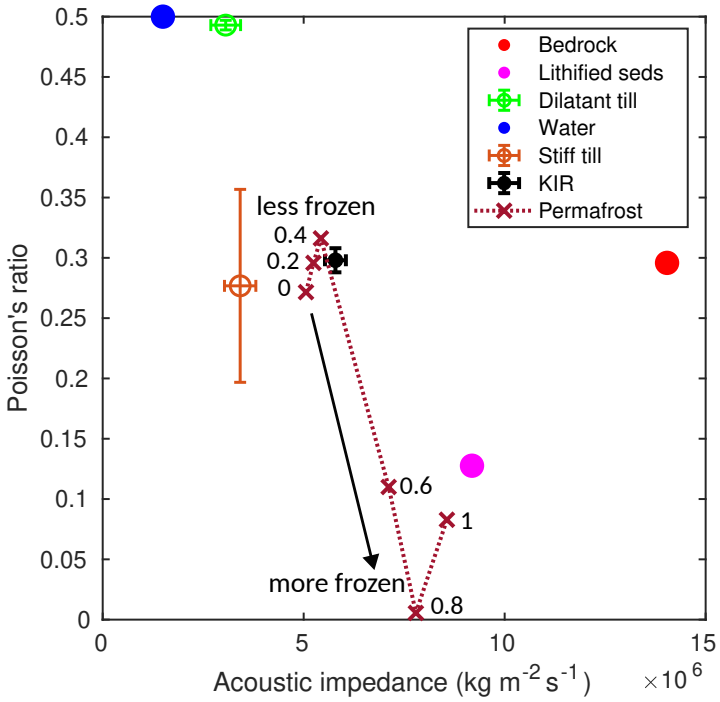

Figure 5.8: Properties of permafrost, calculated from Johansen et al. (2003), and plotted alongside previously discussed glacier bed properties. Number labels beside crosses indicate the frozen fraction. A sudden transition in properties is observed when the frozen fraction reaches > 0.4, clearly separating 'less frozen' and 'more frozen' permafrost. Superficial comparison of these properties with Z and σ observed at KIR would lead to KIR being classified as 'less frozen'. This interpretation is incorrect and masks the low density and high velocity at KIR. In light of the interpretation of a basal debris layer at KIR, this illustrates the potential dangers of interpreting an AVA result on this basis.

5.3 Improved techniques for the glaciological toolbox

5.3.1 Importance of improved techniques

Chapter 2 describes a method of measuring seismic Q which can be used in cases where multiple reflections are not observed. This method will enable more accurate constraint of reflection amplitudes. Furthermore, it will aid future seismic studies of firn structure using techniques such as full waveform inversion, which currently do not take account of firn's attenutative structure (Pearce et al. 2023a).

In Section 2.4 I discussed the effect of correcting for a variable $Q(z)$ model on AVA amplitudes, and found that compared to a uniform $Q(z)$ correction, the more detailed variable-Q correction makes little difference to the corrected AVA amplitudes at incidence angles $< 50^{\circ}$. However, this analysis ignored the effect of Q on measurement of source amplitude, and therefore masked the true value of the Q in firn method. In cases where multiples are not observed, both Q and source amplitude A_0 must be estimated using diving waves. Crucially, the commonly-used method by Holland and Anandakrishnan (2009) assumes that effective path-averaged Q can be considered equal for two diving waves which penetrate to similar depths at the base of the firn but emerge at different offsets. The results presented in Chapter 2 demonstrate this is not the case. In Section 4.2.3 I calculate A_0 both using the direct-path method by Holland and Anandakrishnan (2009) and by a method I call the variable-Q direct path method, which takes account of the firn's $Q(z)$ gradient. I find that the conventional direct-path method underestimates A_0 by a factor of ~ 1.6, for the $Q(z)$ model observed at KIR. Therefore reflectivities estimated using this method may be significantly overestimated. The chief importance of accounting for the Q gradient in firn is therefore not through its direct effect on the attenuation correction, but through the effect of Q on source amplitude correction.

Chapter 3 demonstrated that PP/PS joint inversion in general performs better in both accuracy and precision than single PP inversion, given the same survey geometry. Furthermore, in many cases jointly inverting PP and PS data acquired using a narrow survey geometry (where $\theta < 30^{\circ}$) can deliver more accurate and precise results than singly inverting PP data from a wide survey geometry ($\theta < 60^{\circ}$). This demonstrates that the information converted waves provide goes beyond the mere provision of extra data points. Chapter 4 also demonstrates that joint inversion is more robust to the interpretive pitfall of an ambiguous polarity reversal, due to the

contradictory PP and PS AVA curves resulting from a misinterpretation.

5.3.2 Acquisition recommendations

Given finite logistical constraints, is it preferable to do a wide-angle survey or a three-component survey over a narrower angular range? In principle, given the results presented in Chapter 3, if no prior information was available about the substrate, it would be preferable to expend logistical resources acquiring three-component data. However, as Chapter 4 demonstrates, there exist glaciological scenarios for which obtaining wide-angle data improves constraint of bed properties more than three-component analysis does. In the case of the data acquired at KIR, the constraint of density provided by the wide-angle data is what enabled the interpretation as a basal debris layer; the density as constrained by joint inversion over $\theta < 30^\circ$ ($\rho = 1740 \pm 640$ kg m^{-3}) would not rule out a reflection from an ice/stiff sediment interface, and the reflection would likely have been interpreted as such. The observation of narrow joint inversion being preferable to wide single inversion has yet to be confirmed with a real dataset. More work is required, and more three-component AVA datasets must be acquired in glacial environments, to fully understand the potential and limitations of converted wave joint inversion.

In Chapter 3, I highlighted the logistical advantage of performing a two or three component AVA survey over a narrower spatial range on very thick ice. On an ice stream 2.5 km thick, source-receiver offsets of 9 km are required to obtain $\theta_{PP} = 60^\circ$. In contrast, offsets of 3 km are required for $\theta_{PP} = 30^\circ$, and offsets of 2.2 km are needed for $\theta_{PS} = 30^\circ$. There is a clear logistical benefit to performing a three component AVA survey in this case. The possibility is also raised of whether shorter-offset PS wave data may be better quality than long-offset PP wave data, since they propagate for a much shorter distance.

Recalling Equation 1.2 (Section 1.3), we can compare the factor $\Gamma = \gamma e^{-\frac{\pi f}{Q v} r}$, which combines amplitude losses from geometric spreading and attenuation, for a ray A emerging at an offset of 2.2 km (incidence angle $\sim 30^\circ$, total path length ~ 5.5 km) with that for a ray B emerging at an offset of 9 km (incidence angle $\sim 60^\circ$, path length ~ 10 km). Assuming $Q_P = 300$, $f = 300$ Hz, and $v = 3.8$ km s^{-1}, ray B, the PP wave, has $\Gamma_B = 2.6 \times 10^{-8}$. Because of the asymmetric PS ray path, the converted wave has a P ray path length of 2.9 km and an S ray path length of 2.6 km. Assuming for the converted wave $Q_P = 300$, $Q_S = 100$, $f = 225$ Hz, $v_p = 3.8$ km s^{-1} and $v_s = 1.9$ km s^{-1}, the amplitude factor is $\Gamma_B = 1.9 \times 10^{-9}$. Therefore the amplitude loss for

a PS wave emergent at 2.2 km is 14 times greater than those for a PP wave emergent at 9 km offset. In this case, PS waves emergent at 2.2 km may have a worse signal-to-noise ratio than PP waves emergent at 9 km, despite being logistically easier to acquire. This underlines my reluctance to recommend sacrificing PP coverage for PS coverage if acquisition of wide-angle data is logistically feasible.

Acquisition of radial-component data need not always come at the expense of vertical-component data. When experiments plan to use equipment such as seismic nodes, joint inversion represents a way to maximise the value of an AVA dataset. Furthermore, if a survey also aims to acquire data suitable for shear wave splitting analysis, as was the case for the KIR dataset, designing a survey with converted wave analysis in mind need not be detrimental to vertical acquisition.

If undertaking a conventional georod acquisition, one way to obtain PS wave data at minimal cost to the PP dataset would be to bury most georods vertically as for a single-component acquisition, but orient some georods radially at regular intervals (e.g. every 4th or 5th georod). This way, a relatively small number of PP data points is sacrificed, and the potential value added of the acquired PS data may outstrip the value lost by the sparser coverage of the PP dataset. This acquisition design would have the added benefit of acquiring PP and PS data with the same source, meaning that the same source amplitude correction could be used for both AVA datasets.

In future, acquisitions should record for a long enough record length and use a sufficiently powerful source to acquire P wave multiples from the bed. These multiples can then be used to measure the source amplitude A_0 and bulk Q of the ice column. While this was possible for the PP data at KIR, the source amplitude correction for the PS data was more challenging and required measurement of diving wave amplitudes. While it is possible to measure A_0 from diving waves, as I showed in Section 4.2.3, accurate measurement of A_0 requires a correction to account for the depth-dependence of Q in the firn column. Chapter 2 presents a method for measuring Q in firn; however, these measurements are far more time consuming, and accumulate more errors, than a simple measurement of A_0 and Q from ice-bed multiples.

Nevertheless, the work reported in this thesis demonstrates a comprehensive strategy for Q and A_0 corrections for acquisitions which do not record multiples: Q_P can be constrained using layer-stripping and the resulting $Q_P(z)$ model used to accurately measure A_0 from diving P waves. This represents an improvement on previous measurement techniques, for which attenuation

must either be assumed based on likely ice temperature (A. M. Smith 1997a) or measured from the decay of diving waves reaching close to the base of the firn (Horgan et al. 2011; Peters 2009). The latter measurement is sensitive to the attenuation at a single depth, so the assumption that this is constant throughout the ice column is unlikely to be correct. The variable-Q direct path correction I introduce connects the layer-stripping Q method to its usefulness for AVA.

If possible, S wave Q should be measured at the field site to ensure accurate Q corrections are applied to the PS data. There are two ways to accomplish this. The first is to use a very large source to generate high amplitude S waves, and a long record length to ensure the S wave multiple is recorded. This is only feasible where the ice is sufficiently thin that the reflected S waves do not attenuate to amplitudes too low to be recorded. The alternative way S wave Q could be measured would be an acquisition based on the expanding-spread refraction acquisition A (Section 1.6.1), with radially oriented georods placed at progressively increasing offset intervals. An S wave source (e.g. King and Jarvis 2007; Picotti et al. 2023) would enable Q_S to be estimated by layer stripping.

5.4 Future Work

5.4.1 Geophysical challenges

Impact of basal debris on the ice-bed reflection

One of the most significant questions arising from this work is that of the impact of basal debris layers on the ice-bed reflection. Measurements of the normal-incidence reflection coeffcient R_0 are commonly used to infer basal acoustic impedance Z_{bed}, leading to interpretations about substrate stiffness. Commonly these are separated into 'stiff till' and 'dilatant till' to represent different mechanisms of basal motion - basal sliding vs pervasive till deformation (e.g. A. M. Smith 1997b; Vaughan et al. 2003). These measurements assume that the acoustic impedance of the basal ice Z_{ice} is known, and that the reflectivity arises from an interface between two half-spaces. The acoustic impedance of the bed is then calculated using:

$$Z_{\text{bed}} = \frac{1 + R_0}{1 - R_0} Z_{\text{ice}}. \tag{5.17}$$

I interpret a basal debris layer of unknown thickness at KIR, likely entrained during an earlier

episode of flow on the stoss side of the bathymetric high where it is currently grounded (Section 5.2.3). This layer has approximately 30% debris by volume (Section 5.1.2), which significantly raises Z in the basal ice. This interpretation raises the possibility that routine measurements of the subglacial environment underestimate Z_{ice}.

A weak reflection with a negative polarity at normal incidence is characteristic of dilatant till underlying the glacier. However, in these measurements, if Z_{ice} is raised by the presence of entrained basal debris, a polarity reversal may be observed where stiffer materials underlie the glacier. The acoustic impedances of stiff till and dilatant till that I have used throughout this thesis are $Z_{\text{stiff till}} = 3.42 \times 10^6$ kg m^{-2}s^{-1} and $Z_{\text{dilatant till}} = 3.06 \times 10^6$ kg m^{-2}s^{-1} (Peters et al. 2007). Z_{ice} therefore need only be raised by a factor of 1.12 for a bed of stiff till to result in a polarity reversal. Assuming this change in Z_{ice} comes entirely from a change in density, a volume fraction of 6% basal debris is required for a stiff bed to result in a polarity reversal at normal incidence. Hence, ignoring basal debris may result in misinterpretations of stiff/soft bed locations, resulting in incorrect conclusions about ice slip mechanisms and incorrect boundary conditions being fed into models. At Rutford ice stream, Hudson et al. (2023) interpret icequake source mechanisms as originating from the differing interactions between entrained clasts and the basal material: these observations, as well as laboratory studies (Zoet et al. 2013) suggest that basal debris may have a significant influence on glacier slip. Therefore, failing to account for basal debris in seismic observations may have wide implications for glacier models.

If interference occurs at this thin layer, this would further complicate an interpretation of normal-incidence reflection amplitudes. The effect of basal debris layers on measurements of basal acoustic impedance therefore represents a currently unexplored interpretive risk to glaciological seismic studies. Further work to better understand the effect of basal debris should include modelling the interference effects of a basal debris layer and investigating the sensitivity of AVA and normal-incidence reflectivity measurements to such a layer. Comparison with direct sampling is also desirable to quantify the distribution and composition of likely debris layers; this would inform future analysis of seismic data and enable the refinement of workflows to account for basal debris.

Anisotropy

In the analyses presented in this thesis, I have not accounted for anisotropy. However, glacier ice is highly anisotropic and anisotropy associated with crystal orientation fabric (COF) has been observed at KIR (Brisbourne et al. 2019). Significant converted wave energy is present on the transverse component (See Fig. 1.16, which would not be expected from a horizontal planar bed and an isotropic propagating medium. This raises the possibility that either the bed at KIR is obliquely dipping or the PS wave is polarised by the COF. The splitting of PS wave energy potentially means that the radial-component PS AVA amplitudes reported in Chapter 4 do not accurately describe the true amplitude of the PS waves. Brisbourne et al. (Brisbourne et al. 2019) inferred a COF model consistent with the splitting of shear waves observed at KIR: polarisation of PS waves should be modelled using this COF to understand the effect this may have on the AVA measurements.

Additionally, AVA experiments were performed at KIR both parallel to the ice divide (line K01, reported here) and obliquely to the divide (called lines K02 and K03). Further experiments are desirable to test the robustness of single and joint inversion at various orientations to the COF, and investigate possible anisotropy in the basal debris layer.

Other further work

Nonstandard survey geometries should be synthetically tested, or tested by downsampling existing data, to determine the optimal geometry for hybrid vertical/radial acquisitions, following my reccommendations in Section 5.3.2. This will enable future survey planning by determining how many PP data points it is worth sacrificing for PS coverage. A similar question which remains to be answered is how robust joint inversion is to varying patterns of offsets acquired. The AVA responses in both my synthetic tests and analysis of real data were densely sampled, at angular intervals of 0.5° for synthetic data, $\sim 0.3°$ for PP at KIR, and 0.75° for PS at KIR). Many AVA datasets are not this densely sampled - it is common to obtain data points every degree (e.g. Hofstede et al. 2018). Furthermore, data may be acquired at irregular intervals, with clusters of data points separated by gaps (e.g. Hofstede et al. 2023). Gonzalez et al. (2020) report data obtained at intervals of 2° between 20° and 40° only, due to interference from groundroll at close offsets. Therefore it is desirable to test the robustness of both single and joint inversion to more sparsely or irregularly sampled AVA curves, and investigate any benefit

joint inversion may have in this case.

Further investigation of the robustness of the inversion to varying noise models is also desirable. The noise model I chose was intended to demonstrate the efficacy of joint inversion to reduce interpretative ambiguity even when faced with very noisy data 3.5. An investigation of more realistic noise models would therefore further inform our understanding of the robustness of joint inversion.

Glaciological AVA inversions can display cyclical amplitude increases and decreases such as those observed in the PP data reported in Chapter 4. This has also been observed at Rutford ice stream (Alex Brisbourne, personal communication) and other locations in Antarctica (Huw Horgan, personal communication). These peaks are assumed to result from inhomogeneities in the basal properties between Fresnel zones over the length of the reflection area. Further experiments should investigate the robustness of AVA inversions to these features. The observation of these cyclic features in an AVA response interpreted to be that of a basal debris layer also raises the question of whether these features could be related to the presence of basal debris; an investigation of this would therefore also be desirable.

If the full potential of converted and shear wave methods is to be realised, more widespread measurements of S wave Q in polar ice are essential. Q_S is difficult to measure due to the large S wave source and long record length required to record S wave multiples; the layer-stripping method offers a way to address this shortfall. Concurrent measurements of P wave Q and S wave Q are desirable. The relationship between Q_P, Q_S and temperature in firn and ice is currently unknown. A better understanding of this relationship will aid further seismic reflection studies where it is not possible to measure Q_S, allowing better informed assumptions to be made.

Joint inversion of multiple geophysical quantities (e.g. Killingbeck et al. 2020) can be a powerful means of investigating subglacial conditions. In future, inversion of seismic reflectivity could be combined with other measurements, such as that of radar reflectivity (e.g. Schlegel et al. 2022), to further investigate basal processes of glaciers and ice sheets.

As discussed previously, thin layering at the ice-bed interface complicates interpretations of glaciological AVA responses (Booth et al. 2012). A full investigation into thin layering was beyond the scope of this thesis; however, further study would help to understand the effect of thin layering on PS AVA responses.

5.4.2 Further constraint of Holocene ice dynamics in the Weddell Sea sector

It remains ambiguous whether the current grounding line in the Weddell Sea sector has arisen from a monotonic retreat since the LGM or from a rapid retreat and readvance. The ability of seismic reflectivity methods to constrain the region's history based on inferences of basal temperature is limited, due to the low geothermal heat fluxes in the region resulting in rapid cooling of the bed after grounding.

However, the interpretation described in Section 5.2.3 offers a glimpse of a retreat/readvance scenario, as my seismic observations are consistent with frozen, soft marine sediments underlying the debris layer at KIR, which may have been deposited at a time prior to the onset of the current flow regime. The other ice rises in the region from which ice cores have been obtained are Berkner Island, Fletcher Promontory and Skytrain ice rise (Mulvaney et al. 2007; Mulvaney et al. 2014; Mulvaney et al. 2021). Fletcher Promontory and Skytrain ice rise are promontory-type ice rises near to the current grounded ice extent, and are less likely to have ungrounded than HIR and KIR (Kingslake et al. 2018). The only ice rise in the region at which the basal material has been sampled is Berkner Island, which is known to be long-term stable (Matsuoka et al. 2015). KIR and HIR are therefore the most promising candidates for further basal investigation due to their possible ungrounding during rapid retreat/readvance. Direct sampling and analysis of the bed at either KIR or HIR could therefore add valuable information which could corroborate or rule out retreat/readvance. Since HIR is more likely to have ungrounded after the LGM than KIR, due to the lower elevation of its bathymetric high, I suggest that HIR is the priority site for further investigation.

Borehole temperature measurements at KIR and HIR (e.g. Bindschadler et al. 1990) remain a promising way to constrain ice sheet history; comparison of the two sites may give clues as to the differences between their recent dynamics. Additionally, analysis of ice cores linking water isotopes to elevation (e.g. Goursaud et al. 2021) may provide important information about Holocene ice thickness.

Chapter 6

Conclusions

6.1 Seismic attenuation in firn

- I have presented a method which successfully constrains the depth-attenuation relationship in firn, which combines a modified spectral-ratio method with a stochastic method of error propagation.
- Q increases with depth in firn.
- This method offers a strategy for constraining Q in seismic reflection experiments which do not record multiples. The measurement of $Q(z)$ in firn also enables improved constraint of source amplitude.

6.2 Joint inversion of PP, PS and SS reflection amplitudes

- In general, joint inversion of PP and PS wave amplitudes improves the precision and accuracy of AVA inversions, compared with PP inversion of data with the same angular range.
- Joint inversion has the potential to reduce ambiguity in glaciological AVA interpretations.
- The extent to which joint inversion improves upon single inversion is dependent on the character of the AVA responses and the properties of the substrate.
- In many cases, PP/PS inversion of data with an angular range of $0 - 30^{\circ}$ can deliver comparable or improved results when compared with PP inversion of data with an angular

range of $0-60^{\circ}$. Joint inversion therefore has the potential to reduce the logistical burden of wide-angle AVA surveys.

- Joint inversion of PP, PS and SS amplitudes improves upon joint PP/PS inversion in precision and accuracy, however PP/PS inversion constrains bed properties sufficiently well that inclusion of SS data into analyses is unlikely to improve interpretations, given the likely uncertainties introduced by the measurement of SS amplitudes.

- To maximise the potential of joint inversion, future acquisitions should be planned to acquire PS wave data at minimal cost to PP data coverage.

- Future acquisitions should aim to record ice-base multiples for constraint of Q and source amplitude.

- Concurrent measurements of Q_P and Q_S in glacial ice and firn are needed to inform their relationship and enable their use in further AVA measurements.

6.3 Bed conditions at KIR

- Analysis of PP and PS AVA responses at KIR shows the reflection to arise from a material with an acoustic impedance of $Z = (5.79 \pm 0.26) \times 10^6$ kg m^{-2}s^1 and a Poisson's ratio of $\sigma = 0.298 \pm 0.01$. The P wave velocity α, S wave velocity β and density ρ resulting from the inversion are $\alpha = 4.03 \pm 0.05$ km s^{-1}, $\beta = 2.16 \pm 0.06$ km s^{-1}, and $\rho = 1.44 \pm 0.06$ g cm^{-3}, respectively.

- Joint inversion improved constraint in bed properties at KIR when compared with single inversion. The improvement was modest; however, joint analysis of PP and PS wave data was observed to be more robust to the interpretive pitfall of an ambiguous polarity reversal; confidence in the PP wave data was improved by corroboration with the PS AVA response.

- The inverted properties are consistent with a reflection from a layer of entrained debris at the ice base.

- The implied presence of basal debris highlights that the ice-bed interface is more complex than seismic studies commonly assume. The possibility of entrained debris should be accounted for in future studies of basal reflectivity.

6.4 Ice flow reorganisation in the Weddell Sea sector after the LGM

- The observations at KIR are consistent with a reflection from a debris-rich basal ice layer overlying frozen sediments, with a poorly-defined boundary between the two.
- Modelling of basal temperatures at KIR is consistent with a frozen bed at 2.5 ka after grounding.
- The implication of a basal debris layer at KIR is consistent with a previous episode of grounding line retreat and weak ungrounding as an ice rumple, followed by regrounding at the lee side of the bathymetric high.
- Monotonic grounding line retreat is not ruled out by the observations, but is considered less likely due to the implied presence of frozen basal water occupying the sediment pore space, which requires persistence of subglacial water during streaming flow stagnation.
- Direct sampling of the bed at KIR will help distinguish between monotonic retreat and retreat/readvance scenarios.

References

Agnew, R. S., Clark, R. A., Booth, A. D., Brisbourne, A. M., and Smith, A. M. (2023). "Measuring seismic attenuation in polar firn: method and application to Korff Ice Rise, West Antarctica". In: *Journal of Glaciology*, pp. 1–12. DOI: 10.1017/jog.2023.82.

Aki, K. and Richards, P. G. (2002). *Quantitative seismology*. University Science Books, Sausalito, CA, USA.

Alley, R. B., Holschuh, N., MacAyeal, D. R., Parizek, B. R., Zoet, L., Riverman, K., Muto, A., Christianson, K., Clyne, E., Anandakrishnan, S., Stevens, N., and GHOST Collaboration (2021). "Bedforms of Thwaites Glacier, West Antarctica: Character and Origin". In: *Journal of Geophysical Research: Earth Surface* 126.12, e2021JF006339. DOI: 10.1029/2021JF006339.

Alley, R. B., Spencer, M. K., and Anandakrishnan, S. (2007). "Ice-sheet mass balance: assessment, attribution and prognosis". In: *Annals of Glaciology* 46, pp. 1–7. DOI: 10.3189/172756407782871738.

Alsuleiman, A. (2018). *Measuring seismic attenuation for the firn layer in Antarctica*. Unpublished BSc. Geophysical Sciences dissertation, School of Earth and Environment, University of Leeds.

Anandakrishnan, S. (2003). "Dilatant till layer near the onset of streaming flow of Ice Stream C, West Antarctica, determined by AVO (amplitude vs offset) analysis". In: *Annals of Glaciology* 36, pp. 283–286. DOI: 10.3189/172756403781816329.

Anandakrishnan, S. and Alley, R. B. (1997). "Stagnation of Ice Stream C, West Antarctica by water piracy". In: *Geophysical Research Letters* 24.3, pp. 265–268. DOI: 10.1029/96GL04016.

Arthern, R. J., Winebrenner, D. P., and Vaughan, D. G. (2006). "Antarctic snow accumulation mapped using polarization of 4.3-cm wavelength microwave emission". In: *Journal of Geophysical Research: Atmospheres* 111.D6. DOI: 10.1029/2004JD005667.

Bamber, J. L., Riva, R. E. M., Vermeersen, B. L. A., and LeBrocq, A. M. (2009). "Reassessment of the Potential Sea-Level Rise from a Collapse of the West Antarctic Ice Sheet". In: *Science* 324.5929, pp. 901–903. DOI: 10.1126/science.1169335.

Båth, M. (1974). *Developments in solid Earth Geophysics: spectral analysis in Geophysics*. Elsevier Scientific Publishing Company.

Bayes, T. (1764). "An Essay Toward Solving a Problem in the Doctrine of Chances". In: *Philosophical Transactions of the Royal Society of London* (53), pp. 370–418.

Bentley, C. R. (1971). "Seismic Evidence for Moraine within the Basal Antarctic Ice Sheet". In: *Antarctic Research Series*. Ed. by A.P. Crary. Washington, D. C.: American Geophysical Union, pp. 89–129. DOI: 10.1029/AR016p0089.

Bentley, C. R. and Kohnen, H. (1976). "Seismic refraction measurements of internal friction in Antarctic ice". In: *Journal of Geophysical Research* 81.8, pp. 1519–1526. DOI: 10.1029/JB081i008p01519.

Bentley, M. J., Fogwill, C. J., Le Brocq, A. M., Hubbard, A. L., Sugden, D. E., Dunai, T. J., and Freeman, S. P.H.T. (2010). "Deglacial history of the West Antarctic Ice Sheet in the Weddell Sea embayment: Constraints on past ice volume change". In: *Geology* 38.5, pp. 411–414. DOI: 10.1130/G30754.1.

Bentley, M. J., Ó Cofaigh, C., Anderson, J. B., Conway, H., Davies, B., Graham, A. G.C., Hillenbrand, C-D, Hodgson, D. A., Jamieson, S. S.R., Larter, R. D., Mackintosh, A., Smith, J. A., Verleyen, E., Ackert, R. P., Bart, P. J., Berg, S., Brunstein, D., Canals, M., Colhoun, E. A., Crosta, X., Dickens, W. A., Domack, E., Dowdeswell, J. A., Dunbar, R., Ehrmann, W., Evans, J., Favier, V., Fink, D., Fogwill, C. J., Glasser, N. F., Gohl, K., Golledge, N. R., Goodwin, I., Gore, D. B., Greenwood, S. L., Hall, B. L., Hall, K., Hedding, D. W., Hein, A. S., Hocking, E. P., Jakobsson, M., Johnson, J. S., Jomelli, V., Jones, R. S., Klages, J. P., Kristoffersen, Y., Kuhn, G., Leventer, A., Licht, K., Lilly, K., Lindow, J., Livingstone, S. J.,

Massé, G., McGlone, M. S., McKay, R. M., Melles, M., Miura, H., Mulvaney, R., Nel, W., Nitsche, F. O., O'Brien, P. E., Post, A. L., Roberts, S. J., Saunders, K. M., Selkirk, P. M., Simms, A. R., Spiegel, C., Stolldorf, T. D., Sugden, D. E., van der Putten, N., van Ommen, T., Verfaillie, D., Vyverman, W., Wagner, B., White, D. A., Witus, A. E., and Zwartz, D. (2014). "A community-based geological reconstruction of Antarctic Ice Sheet deglaciation since the Last Glacial Maximum". In: *Quaternary Science Reviews* 100. Reconstruction of Antarctic Ice Sheet Deglaciation (RAISED), pp. 1–9. DOI: 10.1016/j.quascirev.2014.06.025.

Bindschadler, R. A., Roberts, E. P., and Iken, A. (1990). "Age of Crary Ice Rise, Antarctica, Determined from Temperature-Depth Profiles". In: *Annals of Glaciology* 14, pp. 13–16. DOI: 10.3189/S0260305500008168.

Bingham, R. G. and Siegert, M. J. (2007). "Radio-Echo Sounding Over Polar Ice Masses". In: *Journal of Environmental and Engineering Geophysics* 12.1, pp. 47–62. DOI: 10.2113/JEEG12.1.47.

Blankenship, D. D., Bentley, C. R., Rooney, S. T., and Alley, R. B. (1986). "Seismic measurements reveal a saturated porous layer beneath an active Antarctic ice stream". In: *Nature* 322.6074, pp. 54–57. DOI: 10.1038/322054a0.

Blankenship, D. D., Bentley, C. R., Rooney, S. T., and Alley, R. B. (1987). "Till beneath ice stream B: 1. Properties derived from seismic travel times". In: *Journal of Geophysical Research: Solid Earth* 92.B9, pp. 8903–8911. DOI: 10.1029/JB092iB09p08903.

Booth, A. D., Christoffersen, P., Schoonman, C., Clarke, A., Hubbard, B., Law, R., Doyle, S.H., Chudley, T. R., and Chalari, A. (2020). "Distributed Acoustic Sensing of Seismic Properties in a Borehole Drilled on a Fast-Flowing Greenlandic Outlet Glacier". In: *Geophysical Research Letters* 47.13. DOI: 10.1029/2020GL088148.

Booth, A. D., Clark, R. A., Kulessa, B., Murray, T., Carter, J., Doyle, S., and Hubbard, A. (2012). "Thin-layer effects in glaciological seismic amplitude-versus-angle (AVA) analysis: implications for characterising a subglacial till unit, Russell Glacier, West Greenland". In: *The Cryosphere* 6.4, pp. 909–922. DOI: 10.5194/tc-6-909-2012.

Booth, A. D., Emir, E., and Diez, A. (2016). "Approximations to seismic AVA responses: Validity and potential in glaciological applications". In: *Geophysics* 81.1, WA1–WA11. DOI: 10.1190/geo2015-0187.1.

Bougamont, M., Christoffersen, P., Hubbard, A. L., Fitzpatrick, A. A., Doyle, S. H., and Carter, S. P. (Sept. 2014). "Sensitive response of the Greenland Ice Sheet to surface melt drainage over a soft bed". In: *Nature Communications* 5.1, p. 5052. DOI: 10.1038/ncomms6052.

Bradley, S. L., Hindmarsh, R. C.A., Whitehouse, P. L., Bentley, M. J., and King, M. A. (2015). "Low post-glacial rebound rates in the Weddell Sea due to Late Holocene ice-sheet readvance". In: *Earth and Planetary Science Letters* 413, pp. 79–89. DOI: 10.1016/j.epsl.2014.12.039.

Brisbourne, A. M., Martín, C., Smith, A. M., Baird, A. F., Kendall, J. M., and Kingslake, J. (2019). "Constraining Recent Ice Flow History at Korff Ice Rise, West Antarctica, Using Radar and Seismic Measurements of Ice Fabric". In: *Journal of Geophysical Research: Earth Surface* 124.1, pp. 175–194. DOI: 10.1029/2018JF004776.

Brisbourne, A. M., Smith, A. M., Rivera, A., Zamora, R., Napoleoni, F., Uribe, J. A., and Ortega, M. (2023). "Bathymetry and bed conditions of Lago Subglacial CECs, West Antarctica". In: *Journal of Glaciology*, pp. 1–10. DOI: 10.1017/jog.2023.38.

Brisbourne, A. M., Smith, A. M., Vaughan, D. G., King, E. C., Davies, D., Bingham, R. G., Smith, E. C., Nias, I. J., and Rosier, S. H. R. (2017). "Bed conditions of Pine Island Glacier, West Antarctica". In: *Journal of Geophysical Research: Earth Surface* 122.1, pp. 419–433. DOI: 10.1002/2016JF004033.

Burton-Johnson, A., Dziadek, R., and Martín, C. (2020). "Review article: Geothermal heat flow in Antarctica: current and future directions". In: *The Cryosphere* 14.11, pp. 3843–3873. DOI: 10.5194/tc-14-3843-2020.

Carpenter, E. W., Bullard, E. C., and Penney, W. G. (1966). "A quantitative evaluation of teleseismic explosion records". In: *Proceedings of the Royal Society of London. Series A. Mathematical and Physical Sciences* 290.1422, pp. 396–407. DOI: 10.1098/rspa.1966.0058.

Castagna, J. P. and Backus, M. M. (1993). "AVO analysis—Tutorial and review". In: *Offset-dependent reflectivity: theory and practice of AVO analysis*, pp. 3–36.

Catania, G. A., Scambos, T. A., Conway, H., and Raymond, C. F. (2006). "Sequential stagnation of Kamb Ice Stream, West Antarctica". In: *Geophysical Research Letters* 33.14. DOI: 10.1029/2006GL026430.

Červený, V. (1966). "On Dynamic Properties of Reflected and Head Waves in the n-layered Earth's Crust". In: *Geophysical Journal of the Royal Astronomical Society* 11.1, pp. 139–147. DOI: https://doi.org/10.1111/j.1365-246X.1966.tb03496.x.

Christensen, N. I. (1989). "Seismic velocities". In: *Practical Handbook of Physical Properties of Rocks and Minerals*. Ed. by R. S. Carmichael. Boca Raton, Fla.: CRC press.

Christianson, K., Peters, L. E., Alley, R. B., Anandakrishnan, S., Jacobel, R. W., Riverman, K. L., Muto, A., and Keisling, B. A. (2014). "Dilatant till facilitates ice-stream flow in northeast Greenland". In: *Earth and Planetary Science Letters* 401, pp. 57–69. DOI: 10.1016/j.epsl.2014.05.060.

Clark, C. D., Knight, J. K., and Gray, J. T. (2000). "Geomorphological reconstruction of the Labrador Sector of the Laurentide Ice Sheet". In: *Quaternary Science Reviews* 19.13, pp. 1343–1366. DOI: 10.1016/S0277-3791(99)00098-0.

Clee, T. E., Savage, J. C., and Neave, K. G. (1969). "Internal friction in ice near its melting point". In: *Journal of Geophysical Research* 74.4, pp. 973–980. DOI: 10.1029/JB074i004p00973.

Clyne, E. R., Anandakrishnan, S., Muto, A., Alley, R. B., and Voigt, D. E. (2020). "Interpretation of topography and bed properties beneath Thwaites Glacier, West Antarctica using seismic reflection methods". In: *Earth and Planetary Science Letters* 550, p. 116543. DOI: 10.1016/j.epsl.2020.116543.

Crane, J. M., Lorenzo, J. M., Shen, J., and White, C. D. (2018). "The competing effects of stress and water saturation on *in situ* Q for shallow (¡ 1 m), unconsolidated sand, evaluated with a modified spectral ratio method". In: *Near Surface Geophysics* 16.2, pp. 104–117. DOI: 10.3997/1873-0604.2017048.

Cuffey, K. and Paterson, W. S. B. (2010). *The physics of glaciers*. 4th ed. Oxford: Elsevier.

Dasgupta, R. and Clark, R. A. (1998). "Estimation of Q from surface seismic reflection data". In: *Geophysics* 63.6, pp. 2120–2128. DOI: 10.1190/1.1444505.

DeConto, R. M. and Pollard, D. (2016). "Contribution of Antarctica to past and future sea-level rise". In: *Nature* 531.7596, pp. 591–597. DOI: 10.1038/nature17145.

Dow, C. F., Hubbard, A., Booth, A. D., Doyle, S. H., Gusmeroli, A., and Kulessa, B. (2013). "Seismic evidence of mechanically weak sediments underlying Russell Glacier, West Greenland". In: *Annals of Glaciology* 54.64, pp. 135–141. DOI: 10.3189/2013AoG64A032.

Favier, L. and Pattyn, F. (2015). "Antarctic ice rise formation, evolution, and stability". In: *Geophysical Research Letters* 42.11, pp. 4456–4463. DOI: 10.1002/2015GL064195.

Fretwell, P., Pritchard, H. D., Vaughan, D. G., Bamber, J. L., Barrand, N. E., Bell, R., Bianchi, C., Bingham, R. G., Blankenship, D. D., Casassa, G., Catania, G., Callens, D., Conway, H., Cook, A. J., Corr, H. F. J., Damaske, D., Damm, V., Ferraccioli, F., Forsberg, R., Fujita, S., Gim, Y., Gogineni, P., Griggs, J. A., Hindmarsh, R. C. A., Holmlund, P., Holt, J. W., Jacobel, R. W., Jenkins, A., Jokat, W., Jordan, T., King, E. C., Kohler, J., Krabill, W., Riger-Kusk, M., Langley, K. A., Leitchenkov, G., Leuschen, C., Luyendyk, B. P., Matsuoka, K., Mouginot, J., Nitsche, F. O., Nogi, Y., Nost, O. A., Popov, S. V., Rignot, E., Rippin, D. M., Rivera, A., Roberts, J., Ross, N., Siegert, M., Smith, A. M., Steinhage, D., Studinger, M., Sun, B., Tinto, B. K., Welch, B. C., Wilson, D., Young, D. A., Xiangbin, C., and Zirizzotti, A. (2013). "Bedmap2: improved ice bed, surface and thickness datasets for Antarctica". In: *The Cryosphere* 7.1, pp. 375–393. DOI: 10.5194/tc-7-375-2013.

Gonzalez, L. F. (2020). *Active Seismic Studies in Lemon Creek Valley Glacier, Juneau, Alaska: Characterization of Subglacial Sediments to Understand Glacier Dynamics.* Unpublished MSc. dissertation, Department of Geological Sciences, University of Texas at El Paso.

Goursaud, S., Holloway, M., Sime, L., Wolff, E., Valdes, P., Steig, E. J., and Pauling, A. (2021). "Antarctic Ice Sheet Elevation Impacts on Water Isotope Records During the Last Interglacial". In: *Geophysical Research Letters* 48.6. e2020GL091412 2020GL091412, e2020GL091412. DOI: https://doi.org/10.1029/2020GL091412.

Green, P. J. (1995). "Reversible jump Markov chain Monte Carlo computation and Bayesian model determination". In: *Biometrika* 82.4, pp. 711–732. DOI: 10.1093/biomet/82.4.711.

Gudmundsson, G. H., Krug, J., Durand, G., Favier, L., and Gagliardini, O. (2012). "The stability of grounding lines on retrograde slopes". In: *The Cryosphere* 6.6, pp. 1497–1505. DOI: 10.5194/tc-6-1497-2012.

Gusmeroli, A., Clark, R. A., Murray, T., Booth, A. D., Kulessa, B., and Barrett, B. E. (2010). "Seismic wave attenuation in the uppermost glacier ice of Storglaciären, Sweden". In: *Journal of Glaciology* 56.196, pp. 249–256. DOI: 10.3189/002214310791968485.

Harper, J. T., Humphrey, N. F., Meierbachtol, T. W., Graly, J. A., and Fischer, U. H. (2017). "Borehole measurements indicate hard bed conditions, Kangerlussuaq sector, western Greenland Ice Sheet". In: *Journal of Geophysical Research: Earth Surface* 122.9, pp. 1605–1618. DOI: 10.1002/2017JF004201.

Hashin, Z. and Shtrikman, S. (1963). "A variational approach to the theory of the elastic behaviour of multiphase materials". In: *Journal of the Mechanics and Physics of Solids* 11.2, pp. 127–140. DOI: 10.1016/0022-5096(63)90060-7.

Hastings, W. K. (1970). "Monte Carlo sampling methods using Markov chains and their applications". In: *Biometrika* 57.1, pp. 97–109. DOI: 10.1093/biomet/57.1.97.

He, Y-X., He, G., Yuan, S., Zhao, J., and Wang, S. (2022). "Bayesian Frequency-Dependent AVO Inversion Using an Improved Markov chain Monte Carlo Method for Quantitative Gas Saturation Prediction in a Thin Layer". In: *IEEE Geoscience and Remote Sensing Letters* 19, pp. 1–5. DOI: 10.1109/LGRS.2020.3046283.

Henry, A. C. J., Drews, R., Schannwell, C., and Višnjević, V. (2022). "Hysteretic evolution of ice rises and ice rumples in response to variations in sea level". In: *The Cryosphere* 16.9, pp. 3889–3905. DOI: 10.5194/tc-16-3889-2022.

Hepburn, D. (2016). *Estimation of the seismic attenuation in firn through use of the Wiechert-Herglotz Inversion and spectral ratio methods*. Unpublished MSc. Exploration Geophysics dissertation, School of Earth and Environment, University of Leeds.

Herglotz, G. (1907). "Über das Benndorfsche problem der fortpflanzungsgeschwindigkeit der erdbebenstrahlen (On the Benndorf problem of propagation velocity of earthquake rays)". In: *Zeitschrift für Geophysik* 8, pp. 145–147.

Hill, R. (1952). "The Elastic Behaviour of a Crystalline Aggregate". In: *Proceedings of the Physical Society. Section A* 65.5, p. 349. DOI: 10.1088/0370-1298/65/5/307.

Hillenbrand, C.-D., Bentley, M. J., Stolldorf, T. D., Hein, A. S., Kuhn, G., Graham, A. G.C., Fogwill, C. J., Kristoffersen, Y., Smith, J. A., Anderson, J. B., Larter, R. D., Melles, M., Hodgson, D. A., Mulvaney, R., and Sugden, D. E. (2014). "Reconstruction of changes in the Weddell Sea sector of the Antarctic Ice Sheet since the Last Glacial Maximum". In: *Quaternary Science Reviews* 100. Reconstruction of Antarctic Ice Sheet Deglaciation (RAISED), pp. 111–136. DOI: 10.1016/j.quascirev.2013.07.020.

Hillenbrand, C.-D., Melles, M., Kuhn, G., and Larter, R. D. (2012). "Marine geological constraints for the grounding-line position of the Antarctic Ice Sheet on the southern Weddell Sea shelf at the Last Glacial Maximum". In: *Quaternary Science Reviews* 32, pp. 25–47. DOI: 10.1016/j.quascirev.2011.11.017.

Hinkel, J., Aerts, J. C. J. H., Brown, S., Jiménez, J. A., Lincke, D., Nicholls, R. J., Scussolini, P., Sanchez-Arcilla, A., Vafeidis, A., and Appeaning Addo, K. (2018). "The ability of societies to adapt to twenty-first-century sea-level rise". In: *Nature Climate Change* 8.7, pp. 570–578. DOI: 10.1038/s41558-018-0176-z.

Hodgson, D. A., Bentley, M. J, Schnabel, C., Cziferszky, A., Fretwell, P., Convey, P., and Xu, S. (2012). "Glacial geomorphology and cosmogenic 10Be and 26Al exposure ages in the northern Dufek Massif, Weddell Sea embayment, Antarctica". In: *Antarctic Science* 24.4, pp. 377–394.

Hofstede, C., Christoffersen, P., Hubbard, B., Doyle, S. H., Young, T. J., Diez, A., Eisen, O., and Hubbard, A. (2018). "Physical Conditions of Fast Glacier Flow: 2. Variable Extent of Anisotropic Ice and Soft Basal Sediment From Seismic Reflection Data Acquired on Store Glacier, West Greenland". In: *Journal of Geophysical Research: Earth Surface* 123.2, pp. 349–362. DOI: 10.1002/2017JF004297.

Hofstede, C., Wilhelms, F., Neckel, N., Fritzsche, D., Beyer, S., Hubbard, A., Pettersson, R., and Eisen, O. (2023). "The Subglacial Lake That Wasn't There: Improved Interpretation From Seismic Data Reveals a Sediment Bedform at Isunnguata Sermia". In: *Journal of Geophysical Research: Earth Surface* 128.10. e2022JF006850 2022JF006850, e2022JF006850. DOI: 10.1029/2022JF006850.

Holland, C. W. and Anandakrishnan, S. (2009). "Subglacial seismic reflection strategies when source amplitude and medium attenuation are poorly known". In: *Journal of Glaciology* 55.193, pp. 931–937. DOI: 10.3189/002214309790152528.

Hollmann, H., Treverrow, A., Peters, L. E., Reading, A. M., and Kulessa, B. (2021). "Seismic observations of a complex firn structure across the Amery Ice Shelf, East Antarctica". In: *Journal of Glaciology* 67.265, pp. 777–787. DOI: 10.1017/jog.2021.21.

Horgan, H. J., Anandakrishnan, S., Alley, R. B., Burkett, Peter G., and Peters, L. E. (2011). "Englacial seismic reflectivity: imaging crystal-orientation fabric in West Antarctica". In: *Journal of Glaciology* 57.204, pp. 639–650. DOI: 10.3189/002214311797409686.

Horgan, H. J., Anandakrishnan, S., Jacobel, R. W., Christianson, K., Alley, R. B., Heeszel, D. S., Picotti, S., and Walter, J. I. (2012). "Subglacial Lake Whillans — Seismic observations of a shallow active reservoir beneath a West Antarctic ice stream". In: *Earth and Planetary Science Letters* 331-332, pp. 201–209. DOI: 10.1016/j.epsl.2012.02.023.

Horgan, H. J., Haastrecht, L. van, Alley, R. B., Anandakrishnan, S., Beem, L. H., Christianson, K., Muto, A., and Siegfried, M. R. (2021). "Grounding zone subglacial properties from calibrated active-source seismic methods". In: *The Cryosphere* 15.4, pp. 1863–1880. DOI: 10.5194/tc-15-1863-2021.

Hubbard, B., Luckman, A., Ashmore, D. W., Bevan, S., Kulessa, B., Kuipers Munneke, P., Philippe, M., Jansen, D., Booth, A. D., Sevestre, H., Tison, JL., O'Leary, M., and Rutt, I. (2016). "Massive subsurface ice formed by refreezing of ice-shelf melt ponds". In: *Nature Communications* 7.1, p. 11897. DOI: 10.1038/ncomms11897.

Hudson, T. S., Kufner, S. K., Brisbourne, A. M., Kendall, J. M., Smith, A. M., Alley, R. B., Arthern, R. J., and Murray, T. (July 2023). "Highly variable friction and slip observed at

Antarctic ice stream bed". In: *Nature Geoscience* 16.7, pp. 612–618. DOI: 10.1038/s41561-023-01204-4.

Hutter, K. (1983). *Theoretical Glaciology*. Springer Dordrecht.

Jamieson, S. S. R., Vieli, A., Livingstone, S. J., Ó Cofaigh, Colm, Stokes, C., Hillenbrand, C.-D., and Dowdeswell, J. A. (2012). "Ice-stream stability on a reverse bed slope". In: *Nature Geoscience* 5.11, pp. 799–802. DOI: 10.1038/ngeo1600.

Jarvis, E. P. and King, E. C. (1993). "The seismic wavefield recorded on an Antarctic ice shelf". In: *Journal of Seismic Exploration* 2, pp. 69–86.

Johansen, T. A., Digranes, P., Schaack, M. van, and Lønne, I. (2003). "Seismic mapping and modeling of near-surface sediments in polar areas". In: *GEOPHYSICS* 68.2, pp. 566–573. DOI: 10.1190/1.1567226.

Jordan, T. A., Martín, C., Ferraccioli, F., Matsuoka, K., Corr, H., Forsberg, R., Olesen, A., and Siegert, M. (2018). "Anomalously high geothermal flux near the South Pole". In: *Scientific Reports* 8.1, p. 16785. DOI: 10.1038/s41598-018-35182-0.

Killingbeck, S. F., Booth, A. D., Livermore, P. W., Bates, C. R., and West, L. J. (2020). "Characterisation of subglacial water using a constrained transdimensional Bayesian transient electromagnetic inversion". In: *Solid Earth* 11.1, pp. 75–94. DOI: 10.5194/se-11-75-2020.

Killingbeck, S. F., Livermore, P. W., Booth, A. D., and West, L. J. (2018). "Multimodal Layered Transdimensional Inversion of Seismic Dispersion Curves With Depth Constraints". In: *Geochemistry, Geophysics, Geosystems* 19.12, pp. 4957–4971. DOI: 10.1029/2018GC008000.

King, E. C. and Jarvis, E. P. (2007). "Use of Shear Waves to Measure Poisson's Ratio in Polar Firn". In: *Journal of Environmental and Engineering Geophysics* 12.1, pp. 15–21. DOI: 10.2113/JEEG12.1.15.

Kingslake, J., Martín, C., Arthern, R. J., Corr, H. F. J., and King, E. C. (2016). "Ice-flow reorganization in West Antarctica 2.5 kyr ago dated using radar-derived englacial flow velocities". In: *Geophysical Research Letters* 43.17, pp. 9103–9112. DOI: 10.1002/2016GL070278.

Kingslake, J., Scherer, R. P., Albrecht, T., Coenen, J., Powell, R. D., Reese, R., Stansell, N. D., Tulaczyk, S., Wearing, M. G., and Whitehouse, P. L. (2018). "Extensive retreat and re-advance of the West Antarctic Ice Sheet during the Holocene". In: *Nature* 558.7710, pp. 430–434. DOI: 10.1038/s41586-018-0208-x.

Kirchner, J. F. and Bentley, C. R. (1990). "RIGGS III: Seismic Short-Refraction Studies Using an Analytical Curve-Fitting Technique". In: *Antarctic Research Series*. Ed. by Charles R. Bentley and Dennis E. Hayes. Washington, D. C.: American Geophysical Union, pp. 109–126. DOI: 10.1029/AR042p0109.

Kjartansson, E. (1979). "Constant Q -wave propagation and attenuation". In: *Journal of Geophysical Research* 84.B9, p. 4737. DOI: 10.1029/JB084iB09p04737.

Knott, C. G. (1899). "Reflexion and refraction of elastic waves with seismological applications". In: *Philosophical magazine* (48).

Kohnen, H. (1972). "Über die Beziehung zwischen seismischen Geschwindigkeiten und der Dichte in Firn und Eis". In: *Zeitschrift für Geophysik* 38.5, pp. 925–935.

Kufner, S.-K., Brisbourne, A. M., Smith, A. M., Hudson, T. S., Murray, T., Schlegel, R., Kendall, J. M., Anandakrishnan, S., and Lee, I. (2021). "Not all Icequakes are Created Equal: Basal Icequakes Suggest Diverse Bed Deformation Mechanisms at Rutford Ice Stream, West Antarctica". In: *Journal of Geophysical Research: Earth Surface* 126.3, e2020JF006001. DOI: 10.1029/2020JF006001.

Kuipers Munneke, P., Ligtenberg, S. R. M., Van Den Broeke, M. R., and Vaughan, D. G. (2014). "Firn air depletion as a precursor of Antarctic ice-shelf collapse". In: *Journal of Glaciology* 60.220, pp. 205–214. DOI: 10.3189/2014JoG13J183.

Kulessa, B., Booth, A. D., O'Leary, M., McGrath, D., King, E. C., Luckman, A. J., Holland, Paul R., Jansen, D., Bevan, S. L., Thompson, Sarah S., and Hubbard, B. (2019). "Seawater softening of suture zones inhibits fracture propagation in Antarctic ice shelves". In: *Nature Communications* 10.1, p. 5491. DOI: 10.1038/s41467-019-13539-x.

Kulessa, B., Hubbard, A. L., Booth, A. D., Bougamont, M., Dow, C. F., Doyle, S. H., Christoffersen, P., Lindbäck, K., Pettersson, R., Fitzpatrick, A. A. W., and Jones, G. A. (2017).

"Seismic evidence for complex sedimentary control of Greenland Ice Sheet flow". In: *Science Advances* 3.8, e1603071. DOI: 10.1126/sciadv.1603071.

Kuroiwa, D. (1964). "Internal Friction of Ice. III : The Internal Friction of Natural Glacier Ice". In: *Contributions from the Institute of Low Temperature Science* 18, pp. 49–62.

Kurt, H. (2007). "Joint inversion of AVA data for elastic parameters by bootstrapping". In: *Computers & Geosciences* 33.3, pp. 367–382. DOI: 10.1016/j.cageo.2006.08.012.

Kyrke-Smith, T. M., Gudmundsson, G. H., and Farrell, P. E. (2017). "Can Seismic Observations of Bed Conditions on Ice Streams Help Constrain Parameters in Ice Flow Models?" In: *Journal of Geophysical Research: Earth Surface* 122.11, pp. 2269–2282. DOI: 10.1002/2017JF004373.

Labedz, C. R., Bartholomaus, T. C., Amundson, J. M., Gimbert, F., Karplus, M. S., Tsai, V. C., and Veitch, S. A. (2022). "Seismic Mapping of Subglacial Hydrology Reveals Previously Undetected Pressurization Event". In: *Journal of Geophysical Research: Earth Surface* 127.3. e2021JF006406 2021JF006406, e2021JF006406. DOI: 10.1029/2021JF006406.

Lakes, R. (1987). "Foam Structures with a Negative Poisson's Ratio". In: *Science* 235.4792, pp. 1038–1040. DOI: 10.1126/science.235.4792.1038.

Le Brocq, A. M., Bentley, M. J., Hubbard, A., Fogwill, C. J., Sugden, D. E., and Whitehouse, P. L. (2011). "Reconstructing the Last Glacial Maximum ice sheet in the Weddell Sea embayment, Antarctica, using numerical modelling constrained by field evidence". In: *Quaternary Science Reviews* 30.19, pp. 2422–2432. DOI: 10.1016/j.quascirev.2011.05.009.

Liner, C. L. (2012). *Elements of seismic dispersion: A somewhat practical guide to frequency-dependent phenomena*. Society of Exploration Geophysicists, DISC Series 15.

Lu, J., Yang, Z., Wang, Y., and Shi, Y. (2015). "Joint PP and PS AVA seismic inversion using exact Zoeppritz equations". In: *GEOPHYSICS* 80.5, R239–R250. DOI: 10.1190/geo2014-0490.1.

Luh, P. C. (1993). "Wavelet attenuation and bright-spot detection". In: *Offset-dependent reflectivity: Theory and practice of AVO analysis: Investigations in Geophysics* 8, pp. 190–198.

Lyons, J. B., Ragle, R. H., and Tamburi, A. J. (1972). "Growth and Grounding of the Ellesmere Island Ice Rises". In: *Journal of Glaciology* 11.61, pp. 43–52. DOI: 10.3189/S0022143000022474.

MacAyeal, D. R. and Thomas, R. H. (1980). "Ice–shelf Grounding: Ice and Bedrock Temperature Changes". In: *Journal of Glaciology* 25.93, pp. 397–400. DOI: 10.3189/S0022143000015252.

Margrave, G.F. and Lamoureux, M.P. (2019). *Numerical Methods of Exploration Seismology: With Algorithms in MATLAB®*. Cambridge University Press.

Matsuoka, K., Hindmarsh, R. C. A., Moholdt, G., Bentley, M. J., Pritchard, H. D., Brown, J., Conway, H., Drews, R., Durand, G., Goldberg, D., Hattermann, T., Kingslake, J., Lenaerts, J. T.M., Martín, C., Mulvaney, R., Nicholls, K. W., Pattyn, F., Ross, N., Scambos, T., and Whitehouse, P. L. (2015). "Antarctic ice rises and rumples: Their properties and significance for ice-sheet dynamics and evolution". In: *Earth-Science Reviews* 150, pp. 724–745. DOI: 10.1016/j.earscirev.2015.09.004.

Matsuoka, K., Skoglund, A., Roth, G., Pomereu, J. de, Griffiths, H., Headland, R., Herried, B., Katsumata, K., Le Brocq, A., Licht, K., Morgan, F., Neff, P. D., Ritz, C., Scheinert, M., Tamura, T., Van de Putte, A., Broeke, M. van den, Deschwanden, A. von, Deschamps-Berger, C., Van Liefferinge, B., Tronstad, S., and Melvær, Y. (2021). "Quantarctica, an integrated mapping environment for Antarctica, the Southern Ocean, and sub-Antarctic islands". In: *Environmental Modelling & Software* 140, p. 105015. DOI: 10.1016/j.envsoft.2021.105015.

Mavko, G., Mukerji, T., and Dvorkin, J. (2009). "Seismic wave propagation". In: *The Rock Physics Handbook: Tools for Seismic Analysis of Porous Media*. 2nd ed. Cambridge University Press, pp. 81–168. DOI: 10.1017/CBO9780511626753.004.

Mercer, J. H. (1978). "West Antarctic ice sheet and CO2 greenhouse effect: a threat of disaster". In: *Nature* 271.5643, pp. 321–325. DOI: 10.1038/271321a0.

Metropolis, N., Rosenbluth, A. W., Rosenbluth, M. N., Teller, A. H., and Teller, E. (1953). "Equation of State Calculations by Fast Computing Machines". In: *The Journal of Chemical Physics* 21.6, pp. 1087–1092. DOI: 10.1063/1.1699114.

Montelli, A. and Kingslake, J. (2023). "Geothermal heat flux is the dominant source of uncertainty in englacial-temperature-based dating of ice rise formation". In: *The Cryosphere* 17.1, pp. 195–210. DOI: 10.5194/tc-17-195-2023.

Mouginot, J., Rignot, E., Scheuchl, B., and Millan, R. (2017). "Comprehensive Annual Ice Sheet Velocity Mapping Using Landsat-8, Sentinel-1, and RADARSAT-2 Data". In: *Remote Sensing* 9.4. DOI: 10.3390/rs9040364.

Mouginot, J., Scheuchl, B., and Rignot, E. (2012). "Mapping of Ice Motion in Antarctica Using Synthetic-Aperture Radar Data". In: *Remote Sensing* 4.9, pp. 2753–2767. DOI: 10.3390/rs4092753.

Mulvaney, R., Alemany, O., and Possenti, P. (2007). "The Berkner Island (Antarctica) ice-core drilling project". In: *Annals of Glaciology* 47, pp. 115–124. DOI: 10.3189/172756407786857758.

Mulvaney, R., Rix, J., Polfrey, S., Grieman, M., Martìn, C., Nehrbass-Ahles, C, Rowell, I., Tuckwell, R., and Wolff, E. (2021). "Ice drilling on Skytrain Ice Rise and Sherman Island, Antarctica". In: *Annals of Glaciology* 62.85-86, pp. 311–323. DOI: 10.1017/aog.2021.7.

Mulvaney, R., Triest, J., and Alemany, O. (2014). "The James Ross Island and the Fletcher Promontory ice-core drilling projects". In: *Annals of Glaciology* 55.68, pp. 179–188. DOI: 10.3189/2014AoG68A044.

Muto, A., Alley, R. B., Parizek, B. R., and Anandakrishnan, S. (2019a). "Bed-type variability and till (dis)continuity beneath Thwaites Glacier, West Antarctica". In: *Annals of Glaciology* 60.80, pp. 82–90. DOI: 10.1017/aog.2019.32.

Muto, A., Anandakrishnan, S., Alley, R. B., Horgan, H. J., Parizek, B. R., Koellner, S., Christianson, K., and Holschuh, N. (2019b). "Relating bed character and subglacial morphology using seismic data from Thwaites Glacier, West Antarctica". In: *Earth and Planetary Science Letters* 507, pp. 199–206. DOI: 10.1016/j.epsl.2018.12.008.

Nicholls, K. W. and Jenkins, A. (1993). "Temperature and salinity beneath Ronne Ice Shelf, Antarctica". In: *Journal of Geophysical Research: Oceans* 98.C12, pp. 22553–22568. DOI: 10.1029/93JC02601.

Nolan, M. and Echelmeyer, K. (1999). "Seismic detection of transient changes beneath Black Rapids Glacier, Alaska, U.S.A.: II. Basal morphology and processes". In: *Journal of Glaciology* 45.149, pp. 132–146. DOI: 10.3189/S0022143000003117.

O'Connell, R. J. and Budiansky, B. (1978). "Measures of dissipation in viscoelastic media". In: *Geophysical Research Letters* 5.1, pp. 5–8. DOI: 10.1029/GL005i001p00005.

O'Doherty, R. F. and Anstey, N. A. (1971). "REFLECTIONS ON AMPLITUDES". In: *Geophysical Prospecting* 19.3, pp. 430–458. DOI: 10.1111/j.1365-2478.1971.tb00610.x.

Pan, X.-O., Zhang, G.-Z., Zhang, J.-J., and Yin, X.-Y. (2017). "Zoeppritz-based AVO inversion using an improved Markov chain Monte Carlo method". In: *Petroleum Science* 14.1, pp. 75–83. DOI: 10.1007/s12182-016-0131-4.

Parizek, B. R., Christianson, K., Anandakrishnan, S., Alley, R. B., Walker, R. T., Edwards, R. A., Wolfe, D. S., Bertini, G. T., Rinehart, S. K., Bindschadler, R. A., and Nowicki, S. M. J. (2013). "Dynamic (in)stability of Thwaites Glacier, West Antarctica". In: *Journal of Geophysical Research: Earth Surface* 118.2, pp. 638–655. DOI: 10.1002/jgrf.20044.

Pearce, E., Booth, A. D., Rost, S., Sava, P., Konuk, T., Brisbourne, A., Hubbard, B., and Jones, I. (2023a). "A synthetic study of acoustic full waveform inversion to improve seismic modelling of firn". In: *Annals of Glaciology*, pp. 1–5. DOI: 10.1017/aog.2023.10.

Pearce, E., Booth, A. D., Rost, S., Sava, P., Konuk, T., Brisbourne, A., Hubbard, B., and Jones, I. (2023b). "Characterising ice slabs in firn using seismic full waveform inversion, a sensitivity study". In: *Journal of Glaciology*, pp. 1–15. DOI: 10.1017/jog.2023.30.

Peters, L. E. (2009). *A seismic investigation of basal conditions in glaciated regions*. Unpublished PhD thesis, Pennsylvania State University Graduate School.

Peters, L. E. and Anandakrishnan, S. (2007). "Subglacial conditions at a sticky spot along Kamb Ice Stream, West Antarctica". In: *Antarctica: A Keystone in a Changing World - Online Proceedings for the 10th International Symposium on Antarctic Earth Sciences*. Open-File Report. Reston, VA: U.S. Geological Survey. DOI: 10.3133/ofr20071047SRP097.

Peters, L. E., Anandakrishnan, S., Alley, R. B., and Smith, A. M. (2007). "Extensive storage of basal meltwater in the onset region of a major West Antarctic ice stream". In: *Geology* 35.3, p. 251. DOI: 10.1130/G23222A.1.

Peters, L. E., Anandakrishnan, S., Alley, R. B., and Voigt, D. E. (2012). "Seismic attenuation in glacial ice: A proxy for englacial temperature". In: *Journal of Geophysical Research: Earth Surface* 117.F2. DOI: 10.1029/2011JF002201.

Peters, L. E., Anandakrishnan, S., Alley, R. B., Winberry, J. P., Voigt, D. E., Smith, A. M., and Morse, D. L. (2006). "Subglacial sediments as a control on the onset and location of two Siple Coast ice streams, West Antarctica". In: *Journal of Geophysical Research: Solid Earth* 111.B1. DOI: 10.1029/2005JB003766.

Peters, L. E., Anandakrishnan, S., Holland, C. W., Horgan, H. J., Blankenship, D. D., and Voigt, D. E. (2008). "Seismic detection of a subglacial lake near the South Pole, Antarctica". In: *Geophysical Research Letters* 35.23, p. L23501. DOI: 10.1029/2008GL035704.

Picotti, S., Carcione, J. M., and Pavan, M. (2023). "Seismic attenuation in Antarctic firn". In: *The Cryosphere Discussions* 2023, pp. 1–28. DOI: 10.5194/tc-2023-19.

Prasad, M. and Meissner, R. (1992). "Attenuation mechanisms in sands: Laboratory versus theoretical (Biot) data". In: *Geophysics* 57.5, pp. 710–719. DOI: 10.1190/1.1443284.

Quan, Y. and Harris, J. M. (1997). "Seismic attenuation tomography using the frequency shift method". In: *Geophysics* 62.3, pp. 895–905. DOI: 10.1190/1.1444197.

Ramos, A. C. B. and Castagna, J. P. (2001). "Useful approximations for converted-wave AVO". In: *GEOPHYSICS* 66.6, pp. 1721–1734. DOI: 10.1190/1.1487114.

Reese, R., Gudmundsson, G. H., Levermann, A., and Winkelmann, R. (2018). "The far reach of ice-shelf thinning in Antarctica". In: *Nature Climate Change* 8.1, pp. 53–57. DOI: 10.1038/s41558-017-0020-x.

Rignot, E, Mouginot, J., and Scheuchl., B. (2017). *MEaSUREs InSAR-Based Antarctica Ice Velocity Map, Version 2*. DOI: 10.5067/D7GK8F5J8M8R.

Rist, M. A., Sammonds, P. R., Murrell, S. A. F., Meredith, P. G., Oerter, H., and Doake, C. S. M. (1996). "Experimental fracture and mechanical properties of Antarctic ice: preliminary results". In: *Annals of Glaciology* 23, pp. 284–292. DOI: 10.3189/S0260305500013550.

Ritz, C. (1987). "Time dependent boundary conditions for calculating of temperature fields in ice sheets". In: *The Physical Basis of Ice Sheet Modeling. International Association of Hydrological Sciences Press, Institute of Hydrology, Wallingford, Oxfordshire UK. 1987. p 207-216.*

Robin, G. de Q. (1958). "Glaciology III: Seismic Shooting and Related Investigations". In: *Norwegian–British–Swedish Antarctic Expedition, 1949–52, Scientific Results* 5.

Ross, N., Bingham, R. G., Corr, H. F. J., Ferraccioli, F., Jordan, T. A., Le Brocq, A., Rippin, D. M., Young, D., Blankenship, D. D., and Siegert, M. J. (2012). "Steep reverse bed slope at the grounding line of the Weddell Sea sector in West Antarctica". In: *Nature Geoscience* 5.6, pp. 393–396. DOI: 10.1038/ngeo1468.

Röthlisberger, H. (1972). *Seismic exploration in cold regions, CRREL Monograph 11-A 2a.* Hanover, New Hampshire: Cold Regions Research and Engineering Laboratory.

Scambos, T.A., Haran, T.M., Fahnestock, M.A., Painter, T.H., and Bohlander, J. (2007). "MODIS-based Mosaic of Antarctica (MOA) data sets: Continent-wide surface morphology and snow grain size". In: *Remote Sensing of Environment* 111.2, pp. 242–257. DOI: 10.1016/j.rse.2006.12.020.

Schlegel, R., Diez, A., Löwe, H., Mayer, C., Lambrecht, A., Freitag, J., Miller, H., Hofstede, C., and Eisen, O. (2019). "Comparison of elastic moduli from seismic diving-wave and ice-core microstructure analysis in Antarctic polar firn". In: *Annals of Glaciology* 60.79, pp. 220–230. DOI: 10.1017/aog.2019.10.

Schlegel, R., Murray, T., Smith, A. M., Brisbourne, A. M., Booth, A. D., King, E. C., and Clark, R. A. (2022). "Radar Derived Subglacial Properties and Landforms Beneath Rutford Ice Stream, West Antarctica". In: *Journal of Geophysical Research: Earth Surface* 127.1. e2021JF006349 2021JF006349, e2021JF006349. DOI: 10.1029/2021JF006349.

Schoenberger, M. and Levin, F. K. (1974). "Apparent attenuation due to intrabed multiples". In: *Geophysics* 39.3, pp. 278–291. DOI: 10.1190/1.1440427.

Schoof, C. (2007). "Ice sheet grounding line dynamics: Steady states, stability, and hysteresis". In: *Journal of Geophysical Research: Earth Surface* 112.F3. DOI: 10.1029/2006JF000664.

Sheriff, R. E. and Geldart, L. P. (1995). *Exploration seismology*. Cambridge University Press.

Shuey, R. T. (1985). "A simplification of the Zoeppritz equations". In: *Geophysics* 50.4, pp. 609–614. DOI: 10.1190/1.1441936.

Siegert, M. J., Kingslake, J., Ross, N., Whitehouse, P. L., Woodward, J., Jamieson, S. S. R., Bentley, M. J., Winter, K., Wearing, M., Hein, A. S., Jeofry, H., and Sugden, D. E. (2019). "Major Ice Sheet Change in the Weddell Sea Sector of West Antarctica Over the Last 5,000 Years". In: *Reviews of Geophysics* 57.4, pp. 1197–1223. DOI: 10.1029/2019RG000651.

Siegert, M. J., Makinson, K., Blake, D., Mowlem, M., and Ross, N. (2014). "An assessment of deep hot-water drilling as a means to undertake direct measurement and sampling of Antarctic subglacial lakes: experience and lessons learned from the Lake Ellsworth field season 2012/13". In: *Annals of Glaciology* 55.65, pp. 59–73. DOI: 10.3189/2014AoG65A008.

Siegert, M. J., Ross, N., Corr, H., Kingslake, J., and Hindmarsh, R. (2013). "Late Holocene ice-flow reconfiguration in the Weddell Sea sector of West Antarctica". In: *Quaternary Science Reviews* 78, pp. 98–107. DOI: 10.1016/j.quascirev.2013.08.003.

Siegert, M. J., Ross, N., Li, J., Schroeder, D. M., Rippin, D., Ashmore, D., Bingham, R., and Gogineni, R. (2016). "Subglacial controls on the flow of Institute Ice Stream, West Antarctica". In: *Annals of Glaciology* 57.73, pp. 19–24. DOI: 10.1017/aog.2016.17.

Slichter, L. B. (1932). "The Theory of the Interpretation of Seismic Travel-Time Curves in Horizontal Structures". In: *Physics* 3.6, pp. 273–295. DOI: 10.1063/1.1745133.

Smith, A. M. (1986). "Ice rumples on Ronne Ice Shelf, Antarctica". In: *British Antarctic Survey Bulletin* 72, pp. 47–52.

Smith, A. M. (1997a). "Basal conditions on Rutford Ice Stream, West Antarctica, from seismic observations". In: *Journal of Geophysical Research: Solid Earth* 102.B1, pp. 543–552. DOI: 10.1029/96JB02933.

Smith, A. M. (1997b). "Variations in basal conditions on Rutford Ice Stream, West Antarctica". In: *Journal of Glaciology* 43.144, pp. 245–255. DOI: 10.3189/S0022143000003191.

Smith, A. M. (2007). "Subglacial Bed Properties from Normal-Incidence Seismic Reflection Data". In: *Journal of Environmental and Engineering Geophysics* 12.1, pp. 3–13. DOI: 10.2113/JEEG12.1.3.

Smith, A. M., Jordan, T. A., Ferraccioli, F., and Bingham, R. G. (2013). "Influence of subglacial conditions on ice stream dynamics: Seismic and potential field data from Pine Island Glacier, West Antarctica". In: *Journal of Geophysical Research: Solid Earth* 118.4, pp. 1471–1482. DOI: 10.1029/2012JB009582.

Smith, A. M., Murray, T., Davison, B. M., Clough, A. F., Woodward, J., and Jiskoot, H. (2002). "Late surge glacial conditions on Bakaninbreen, Svalbard, and implications for surge termination". In: *Journal of Geophysical Research: Solid Earth* 107.B8, ESE 1-1-ESE 1–16. DOI: 10.1029/2001JB000475.

Smith, A. M., Murray, T., Nicholls, K.W., Makinson, K., Adalgeirsdóttir, G., Behar, A.E., and Vaughan, D.G. (2007). "Rapid erosion, drumlin formation, and changing hydrology beneath an Antarctic ice stream". In: *Geology* 35.2, pp. 127–130. DOI: 10.1130/G23036A.1.

Smith, A. M., Woodward, J., Ross, N., Bentley, M. J., Hodgson, D. A., Siegert, M., and King, E. C. (2018). "Evidence for the long-term sedimentary environment in an Antarctic subglacial lake". In: *Earth and Planetary Science Letters* 504, pp. 139–151. DOI: 10.1016/j.epsl.2018.10.011.

Smith, E. C., Smith, A. M., White, R. S., Brisbourne, A. M., and Pritchard, H. D. (2015). "Mapping the ice-bed interface characteristics of Rutford Ice Stream, West Antarctica, using microseismicity". In: *Journal of Geophysical Research: Earth Surface* 120.9, pp. 1881–1894. DOI: 10.1002/2015JF003587.

Spetzler, J. and Snieder, R. (2004). "The Fresnel volume and transmitted waves". In: *Geophysics* 69.3, pp. 653–663. DOI: 10.1190/1.1759451.

Stolldorf, T., Schenke, H.-W., and Anderson, J. B. (2012). "LGM ice sheet extent in the Weddell Sea: evidence for diachronous behavior of Antarctic Ice Sheets". In: *Quaternary Science Reviews* 48, pp. 20–31. DOI: 10.1016/j.quascirev.2012.05.017.

Teng, T.-L. (1968). "Attenuation of body waves and the Q structure of the mantle". In: *Journal of Geophysical Research (1896-1977)* 73.6, pp. 2195–2208. DOI: 10.1029/JB073i006p02195.

Thomas, R. H. (1979). "Ice Shelves: A Review". In: *Journal of Glaciology* 24.90, pp. 273–286. DOI: 10.3189/S0022143000014799.

Ting, T. C. T. and Chen, T. (Feb. 2005). "Poisson's ratio for anisotropic elastic materials can have no bounds". In: *The Quarterly Journal of Mechanics and Applied Mathematics* 58.1, pp. 73–82. DOI: 10.1093/qjmamj/hbh021.

Toverud, T. and Ursin, B. (2005). "Comparison of seismic attenuation models using zero-offset vertical seismic profiling (VSP) data". In: *Geophysics* 70.2, F17–F25. DOI: 10.1190/1.1884827.

Ursenbach, C. (2005). "Can multicomponent or joint AVO inversion improve impedance estimates?" In: *SEG Technical Program Expanded Abstracts 2003*, pp. 161–164. DOI: 10.1190/1.1817612.

Vaughan, D. G., Smith, A. M., Nath, P. C., and Meur, E. le (2003). "Acoustic impedance and basal shear stress beneath four Antarctic ice streams". In: *Annals of Glaciology* 36, pp. 225–232. DOI: 10.3189/172756403781816437.

Veitch, S. A., Karplus, M., Kaip, G., Gonzalez, L. F., Amundson, J. M., and Bartholomaus, T. C. (2021). "Ice thickness estimates of Lemon Creek Glacier, Alaska, from active-source seismic imaging". In: *Journal of Glaciology* 67.265, pp. 824–832. DOI: 10.1017/jog.2021.32.

Voigt, D. E., Peters, L. E., and Anandakrishnan, S. (2013). "'Georods': the development of a four-element geophone for improved seismic imaging of glaciers and ice sheets". In: *Annals of Glaciology* 54.64, pp. 142–148. DOI: 10.3189/2013AoG64A432.

Wearing, M. G. and Kingslake, J. (2019). "Holocene Formation of Henry Ice Rise, West Antarctica, Inferred From Ice-Penetrating Radar". In: *Journal of Geophysical Research: Earth Surface* 124.8, pp. 2224–2240. DOI: 10.1029/2018JF004988.

Weertman, J. (1957). "On the Sliding of Glaciers". In: *Journal of Glaciology* 3.21, pp. 33–38. DOI: 10.3189/S0022143000024709.

Wiechert, E. (1910). "Bestimmung des Weges der Erdbebenwellen im Erdinnern. I. Theoretisches (Raypath Determination of earthquakes waves in the Earth's interior, I. Theory)". In: *Physikalische Zeitschrift* 11, pp. 294–304.

Wingham, D. J. (2000). "Small fluctuations in the density and thickness of a dry firn column". In: *Journal of Glaciology* 46.154, pp. 399–411. DOI: 10.3189/172756500781833089.

Winter, K., Woodward, J., Ross, N., Dunning, S. A., Bingham, R. G., Corr, H. F. J., and Siegert, M. J. (2015). "Airborne radar evidence for tributary flow switching in Institute Ice Stream, West Antarctica: Implications for ice sheet configuration and dynamics". In: *Journal of Geophysical Research: Earth Surface* 120.9, pp. 1611–1625. DOI: 10.1002/2015JF003518.

Yilmaz, O. (2001). *Seismic data analysis: processing, inversion and interpretation of seismic data*. Society of Exploration Geophysicists.

Young, T. J., Agnew, R. S., Hunt, M., Pearce, E., and Karplus, M. (2023). *Eastwind Glacier Geophysical Surveys ON Top Of Antarctic iceShelf Transition (EGGS On TOAST). Data set.* DOI: 10.7914/JAH0-9856.

Zechmann, J. M., Booth, A. D., Truffer, M., Gusmeroli, A., Amundson, J. M., and Larsen, C. F. (2018). "Active seismic studies in valley glacier settings: strategies and limitations". In: *Journal of Glaciology* 64.247, pp. 796–810.

Ziolkowski, A. and Fokkema, J. T. (1986). "Tutorial: The progressive attenuation of high-frequency energy in seismic reflection data". In: *Geophysical Prospecting* 34.7, pp. 981–1001. DOI: https://doi.org/10.1111/j.1365-2478.1986.tb00509.x.

Zoeppritz, K. (1919). "VII b. Über Reflexion und Durchgang seismischer Wellen durch Unstetigkeitsflächen". In: *Nachrichten von der Gesellschaft der Wissenschaften zu Göttingen, Mathematisch-Physikalische Klasse* 1919, pp. 66–84.

Zoet, L. K., Carpenter, B., Scuderi, M., Alley, R. B., Anandakrishnan, S., Marone, C., and Jackson, M. (2013). "The effects of entrained debris on the basal sliding stability of a glacier". In: *Journal of Geophysical Research: Earth Surface* 118.2, pp. 656–666. DOI: https://doi.org/10.1002/jgrf.20052.

Zoet, L. K. and Iverson, N. R. (2020). "A slip law for glaciers on deformable beds". In: *Science* 368.6486, pp. 76–78. DOI: 10.1126/science.aaz1183.

Appendix A

Appendices

A.1 Derivation

This is a derivation of Equation 2.5 seen in the main text. Here superscripts denote rays, and subscripts denote quasi-layers in the firn; e.g. t_2^B is the time ray B spends in layer 2, and Q_2 is the quality factor in that layer. m^B, A is the gradient obtained from the logarithm of the spectral ratio $S^B(f)/S^B(A)$, where $S^B(f)$ is the spectrum of a wavelet following the path of ray B, and $S^A(f)$ is the spectrum of a wavelet following the path of ray A. Figure 2.3b shows two rays A and B, which reach the bottom of firn quasi-layers 1 and 2, with quality factors Q_1 and Q_2, respectively. These rays would be used to calculate Q in the interval between their maximum penetration depths, i.e. Q_2. The difference in their attenuated times is:

$$\begin{aligned}\delta t^{*B,A} &= t^{*B} - t^{*A} \\ &= \left(\frac{t_1^B}{Q_1} + \frac{t_2^B}{Q_2}\right) - \frac{t_1^A}{Q_1}.\end{aligned}$$

Assuming Q_1 is known, rearranging for Q_2 gives:

$$Q_2 = t_2^B \left[\delta t^{*B,A} + \frac{t_1^A - t_1^B}{Q_1}\right]^{-1}$$

where $\delta t^{*B,A}$ is computed from the spectral ratio gradient $m = -\pi\delta t^*$. Consider a ray C which penetrates to the base of a third layer; by a similar argument,

$$Q_3 = t_3^C \left[\delta t^{*C,B} + \frac{t_1^B - t_1^C}{Q_1} + \frac{t_2^B - t_2^C}{Q_2} \right]^{-1} \tag{A.1}$$

To calculate Q_n in an arbitrary layer n, we would use the spectral ratio gradient calculated from two rays X and Y, one of which (Y) has penetrated to the base of layer n, and one of which (X) has penetrated to the base of layer $n-1$. By extension of Equation A.1, Q_n is:

$$Q_n = t_n^Y \left[\frac{m^{Y,X}}{-\pi} + \sum_{i=1}^{n-1} \frac{t_i^X - t_i^Y}{Q_i} \right]^{-1}.$$

A.2 Data examples

Here we show examples of the wavelets, spectral amplitudes and spectral ratios relied upon for each of our measurements. In each figure, the legend indicates the source-receiver offsets of the traces used. In spectral ratio plots, the vertical grey lines indicate the bandwidth over which the gradient is measured. Figure A.2.1 shows the relevant wavelets for the measurement of Q_{1d} in the 12 m thick top layer. Figure A.2.2 shows the wavelets and associated spectra for the critical refraction measurement, for Q_{crit} at the base of the firn column. An independent measurement of Q near the surface, Q_{1pg} was made using the primary reflection, PP, and its source ghost, pPP. Figure A.2.3 (a-d) shows these wavelets and their spectra, and Figure A.2.4a shows the associated spectral ratios, along with the bandwidth of measurement. A measurement was also made over the entire ice column of Q_{tot}, using the primary and its first multiple (PPPP). These wavelets and spectra are shown in Figure A.2.3 (e, f), with associated spectral ratios in Figure A.2.4b. Finally, a third measurement was made of Q close to the surface, Q_{1mg}, from the first multiple and its ghost, pPPPP. Figure A.2.5 shows these wavelets, their spectra and associated spectral ratios. Table A.2.1 shows the bandwidth used for each measurement.

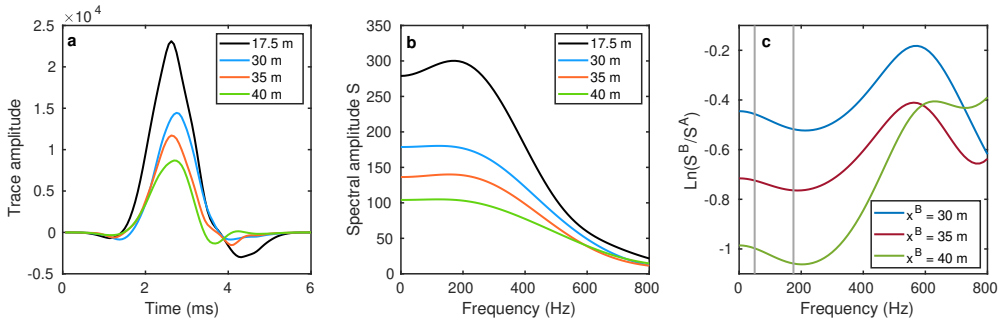

Figure A.2.1: a) Wavelets, b) spectra and c) logarithmic spectral ratios of diving waves used for the calculation of Q_{1d} in the uppermost layer (12 m thick). The spectral ratios are approximately linear within the chosen bandwidth of $200 - 450$ Hz, indicated in c) by the grey vertical lines. The legends in a) and b) indicate source-receiver offsets of traces and their associated spectra. In c), S^A is always the spectrum of the reference trace, at 17.5 m offset. x^B is the source-receiver offset of the comparison trace, with spectrum S^B, used to obtain the spectral ratio.

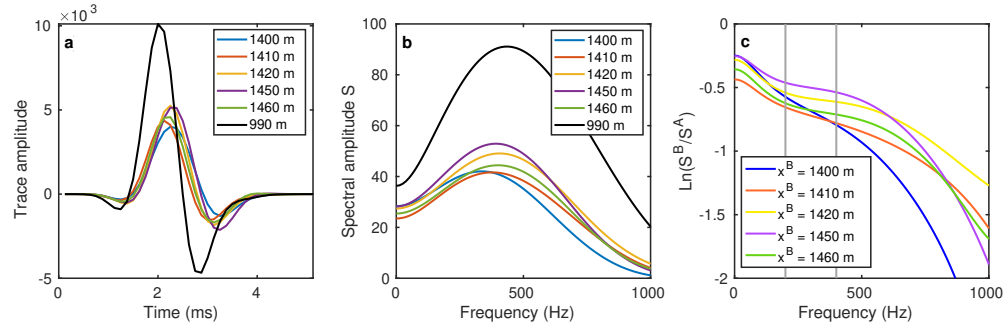

Figure A.2.2: a) Wavelets, b) spectra and c) logarithmic spectral ratios of critically refracted waves used for the calculation of Q at the base of the firn column, Q_{crit}. Legends a) and b) indicate source-receiver offsets of traces. The reference trace, which has spectrum S^A, is at 990 m offset. Legend c) refers to the source-receiver offset of the comparison trace, x^B, used to obtain the spectral ratio.

Table A.2.1: Bandwiths used for each spectral ratio measurement

Measurement	Frequency range (Hz)
Q_{1d} in uppermost layer (direct wave)	50 - 175
Q_{1pg} in uppermost layer from PP/pPP	200 - 300
Q_{1mg} in uppermost layer from PPPP/pPPPP	100 - 250
Q_{2-4} from layer stripping	200 - 450
Q_{crit} from critical refraction	200 - 400
Q_{tot} from primary and first multiples	200 - 350

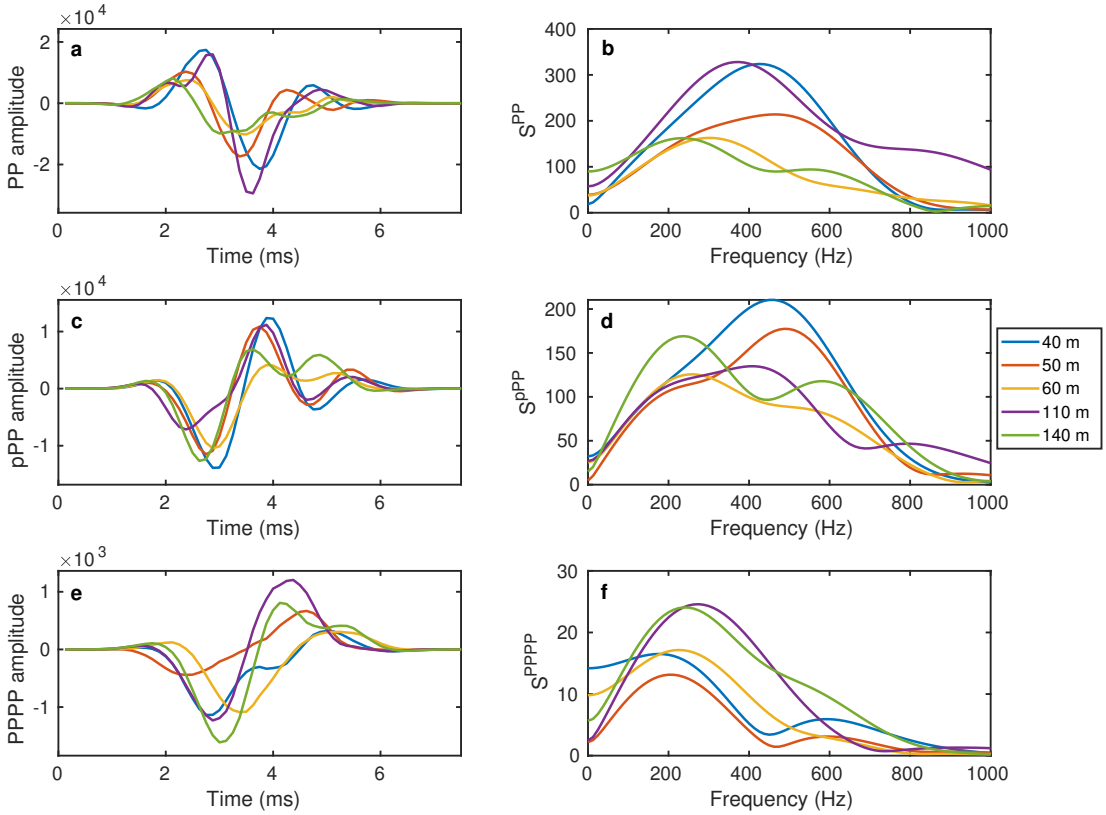

Figure A.2.3: Wavelets and spectra recorded from buried-shot data. Primary reflection PP (a, b), its ghost pPP (c, d), and its first multiple PPPP (e, f).

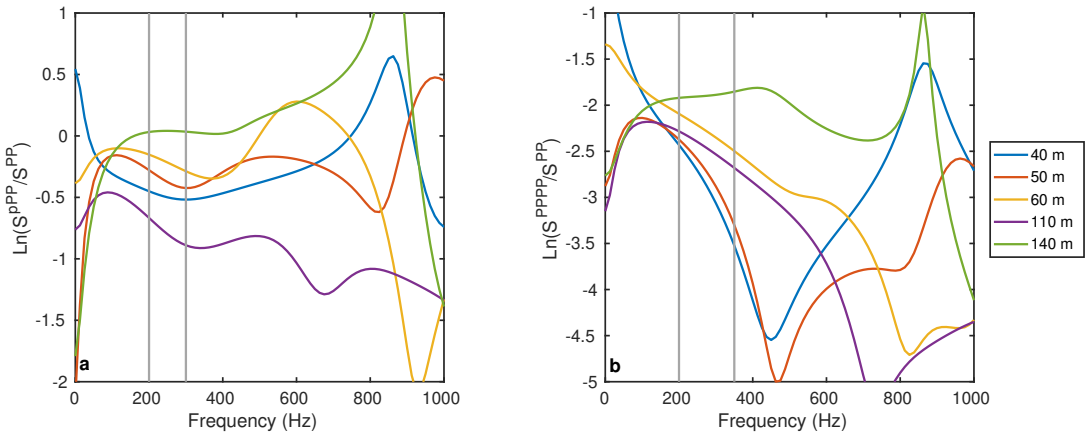

Figure A.2.4: a) Logarithmic spectral ratios of the primary (PP) and first multiple reflections (PPPP), used for the calculation of Q_{tot}. b) Logarithmic spectral ratios of the primary and its ghost (pPP), used for the calculation of $Q_{1\text{pg}}$. Legend indicates source-receiver offset.

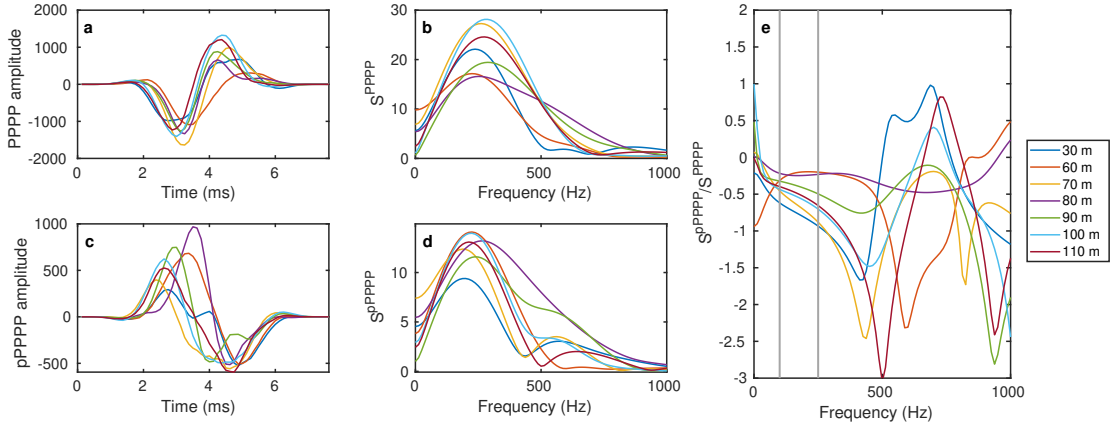

Figure A.2.5: a) Wavelets and b) spectra of the first multiple (PPPP) used for calculation of $Q_{1\mathrm{mg}}$. c) Wavelets and d) spectra of the first multiple ghost (pPPPP) used for calculation of $Q_{1\mathrm{mg}}$. e) Logarithmic spectral ratios used to calculate $Q_{1\mathrm{mg}}$. Legend indicates source-receiver offset of each ghost/multiple pair.